UNIVERSITÀ
DEGLI STUDI
DI PADOVA

Sede Amministrativa: Università degli Studi di Padova

DIPARTIMENTO DI INGEGNERIA DELL'INFORMAZIONE

SCUOLA DI DOTTORATO DI RICERCA IN INGEGNERIA DELL'INFORMAZIONE

INDIRIZZO: SCIENZA E TECNOLOGIA DELL'INFORMAZIONE

CICLO XXV

TITOLO DELLA TESI:

ELECTRICAL MODELING AND EXPERIMENTAL STUDIES OF SENSING SYSTEMS FOR BIOLOGICAL AND BIOMEDICAL APPLICATIONS

Direttore della Scuola: Ch.mo Prof. Matteo Bertocco

Coordinatore d'indirizzo: Ch.mo Prof. Carlo Ferrari

Supervisore: Ch.mo Prof. Alessandro Paccagnella

Dottorando

Matteo Scaramuzza

Delibera 4.b della riunione del Collegio dei docenti della Scuola di dottorato di ricerca in Ingegneria dell'Informazione del **21 MAGGIO 2013 ore 14.30.**

La riunione convocata con posta elettronica del 23 aprile 2013 (All. A) si è tenuta nell'Aula Magna "Antonio Lepschy" DEI/A, Dipartimento di Ingegneria dell'Informazione.

Presenti:
Federico Avanzini, Leonardo Badia, Alessandro Beghi, Matteo Bertocco, Andrea Bevilacqua, Sergio Canazza, Ruggero Carli, Luca Corradini, Chiara Dalla Man, Nicola Laurenti, Emanuele Menegatti, Andrea Neviani, Enrico Pagello, Enoch Peserico, Silvano Pupolin, Giovanni Sparacino, Giorgio Spiazzi, Paolo Tenti, Francesco Ticozzi, Giuseppe Vallone, Pietro Zanuttigh. dottorandi: Riccardo Bonetto, Chiara Fabris.

Assenti giustificati:
Andrea Bagno, Antonio D. Capobianco, Claudio Cobelli, Barbara Di Camillo, Boris Kovatchev, Gaudenzio Meneghesso, Piergiorgio Nicolosi, Gianluca Nucci, Alessandro Paccagnella, Morten Pedersen, Michele Rossi, Giorgio Satta, Gianna Toffolo, Federico Turkheimer, Giovanni Verzellesi, Paolo Villoresi, Harald Wimmer, Enrico Zanoni, Michele Zorzi.

Assenti:
Alessandra Bertoldo, Gianfranco Bilardi, Giancarlo Calvagno, Andrea Cester, Guido Maria Cortelazzo, Augusto Ferrante, Carlo Ferrari, Lorenzo Finesso, Gabriele Manduchi, Paolo Mattavelli, Claudio Narduzzi, Luca Palmieri, Michele Pavon, Gianluigi Pillonetto, Luca Schenato, Maria Francesca Susin, Lorenzo Vangelista, Stefano Vassanelli, Sandro Zampieri.

Presiede la seduta il Direttore della Scuola Prof. Matteo Bertocco, svolge le funzioni di segretario il Prof. Giovanni Sparacino.

Le deliberazioni prese in questa seduta, sono state redatte, lette e approvate seduta stante.

Ordine del giorno

1. Approvazione verbale seduta precedente (30 gennaio 2013)
2. Comunicazioni
3. Programmazione della Scuola
4. Valutazione dell'attività svolta dai dottorandi Nicola Dalla Pozza e Matteo Scaramuzza, 25^ ciclo, indirizzo Scienza e tecnologia dell'informazione, in proroga (6 mesi), ammissione all'esame finale
5. Proposta al rettore della commissione per l'esame finale per i dottorandi Nicola Dalla Pozza e Matteo Scaramuzza in proroga (6 mesi), 25^ ciclo, indirizzo Scienza e tecnologia dell'informazione, ammissione all'esame finale
6. Commissioni esame finale 26^ ciclo
7. Pratiche studenti

Punto 4. Valutazione dell'attività svolta dai dottorandi Nicola Dalla Pozza e Matteo Scaramuzza, 25^ ciclo, indirizzo Scienza e tecnologia dell'informazione, in proroga (6 mesi), ammissione all'esame finale

Il direttore ricorda al Collegio le modalità approvate circa l'ammissibilità dei dottorandi **all'esame finale**.

Illustra al collegio il risultato della valutazione condotta dalla commissione sulla base della bozza della tesi e della presentazione dell'attività triennale svolta.
Sulla base della valutazione della Commissione (All. 4.1e 4.2), il Collegio propone all'unanimità l'ammissione all'esame finale gli studenti Nicola Dalla Pozza e Matteo Scaramuzza e predispone la loro presentazione come di seguito riportata

.....omissis.....

Presentazione e giudizio finale sull'attività svolta da **Matteo Scaramuzza** nell'ambito del XXV ciclo, Scuola di Dottorato di Ricerca in Ingegneria dell'Informazione, Indirizzo Scienza e Tecnologia dell'Informazione.

Negli anni accademici 2009/2010, 2010/2011 e 2011/2012 il dottor **Matteo Scaramuzza** ha frequentato presso il Dipartimento di Ingegneria dell'Informazione dell'Università di Padova la Scuola di Dottorato di Ricerca in Ingegneria dell'Informazione, XXV ciclo, Indirizzo Scienza e Tecnologia dell'Informazione.

Il candidato dichiara quanto segue:

Parte 1 Didattica

Corsi seguiti.

- Dose, effect threshold.
- Project management.
- Bioelectromagnetics.
- Applied linear algebra.
- Statistical methods.

Seminari seguiti al DEI o in altre sedi.

- Advanced course on "Electrical characterization of nano scale samples & bio-chemical interfaces. Methods and electronic instrumentation", Prof. Sampietro, Milano, 16-19 Novembre 2010.
- "Performance Trends and Limitations of Electronic Energy Processing Systems", Prof. Johann Kolar.
- "Factors impacting Processor Design -- A view from the field", Dr. Pratap Pattnaik.
- "Interfaccia chip-cervello per comunicazione bidimensionale ad alta risoluzione", Prof. Vassanelli.
- "Computational problems in cancer genomics", Prof. Upfal.
- "Può l'informazione modificare il cervello?", Prof. Maffei.
- "Microfluidic technology for biomedical applications", Dr. Elvassore.
- Corso di formazione sulla banca dati brevettuale ORBIT, Servizio di Trasferimento Tecnologico dell'Università di Padova, 14 Giugno 2011.
- "Brain models: from functional mapping through the connectome to self-organized criticality", Dr. Turkheimer.
- "Nanoelectrode and Nanofluidic Based Assays of Ion Channels, Mitochondria Membrane Potential, and Apoptosis", Prof. P. Burke.
- "Motion, Geometry and Metadata for Multimedia Compression and Delivery", Prof. D. Taubman.
- "Polymer Networks for Bioengineered Surfaces - New Bioanalytical Devices and Blood Compatible Materials", Prof. J. Rühe.
- "Mechanisms of muscle atrophy in disuse", Prof. M. Sandri, Dipartimento di Biotecnologie Università di Padova.

Partecipazione a Conferenze Internazionali.

- Biosensors 2010, 20th Anniversary World Congress on Biosensors, 26-28 May 2010, Glasgow, UK.

- PRIME 2010, 6th Conference on Ph.D. Research in Microelectronics & Electronics, 18 – 21 July 2010 Berlin Institute of Technology, Berlin, Germany.
- Biosensing Technology 2011, 10-12 October 2011, Amsterdam, The Netherlands.

Partecipazione a manifestazioni.

- *ExpoSanità* (Bologna, 16-19 Maggio 2012).
- *MedTech Italy* (Modena, 2-3 Ottobre 2012).

Attività di co-relatore.

- Affiancamento di studenti durante il periodo di tesi.
  - Tesi triennale "Studio sui biosensori per la rivelazione del lattato".
  - Tesi specialistica "Caratterizzazione e validazione di un biosensore per la rilevazione di acido lattico".
- Attività di co-relatore.
  - co-relatore della tesi triennale "Tecniche di trasduzione di segnali biometrici in riabilitazione funzionale".
  - co-relatore della tesi specialistica "Studio, progettazione e sviluppo di un sistema elettronico per la misura di segnali biometrici della mano finalizzato ad applicazioni riabilitative".

Parte 2 Ricerca

Titolo definitivo della tesi:
Electrical modeling and experimental studies of sensing systems for biological and biomedical applications.

Supervisore: Prof. Alessandro Paccagnella.

Durante il Dottorato ho affrontato la tematica della trasduzione elettrica di segnali generati da sistemi biologici: ho misurato questi sistemi con tecniche voltammetriche e di spettroscopia di impedenza elettrochimica, raccogliendo dati utili alla loro caratterizzazione elettrica. Ho inoltre elaborato questi dati sperimentali per ricavarne modelli elettrici predittivi della risposta elettrica a diversi stimoli applicati. Con questi obiettivi ho approfondito lo studio delle caratteristiche elettriche dell'interfaccia elettrochimica fra elettrodi metallici e differenti materiali biologici (cellule, enzimi, DNA), e la rispettiva modellizzazione elettrica sia a parametri concentrati che pseudo-distribuiti.

Questa attività, iniziata durante il mio periodo di Tesi specialistica, ha portato all'implementazione di un modello elettrico basato su tre diversi software (COMSOL, MATLAB e HSPICE) in grado di simulare il comportamento elettrico dell'interfaccia elettrodo/elettrolita/materiale biologico. La geometria della cella elettrochimica da simulare viene scomposta in una mesh di circuiti equivalenti infinitesimi, i cui parametri elettrici sono funzione della distanza euclidea dall'elettrodo di lavoro. Sfruttando la consolidata analisi con modelli elettrici concentrati, ho determinato le leggi di variazione spaziale dei parametri elettrici equivalenti del sistema, che sono state quindi implementate nel sistema di simulazione combinato.

La flessibilità offerta dal sistema combinato di simulazione consente di tenere in considerazione anche gli elementi parassiti del banco di misura e della cella elettrochimica: attraverso la modellizzazione elettrica di misure di spettroscopia a vuoto e con elettroliti ad elevata conducibilità, è possibile ricavare dei parametri correttivi da applicare, in fase di simulazione, per compensare l'influenza degli elementi parassiti e identificare senza ambiguità il contributo dell'interfaccia elettrochimica.

Nel corso del Dottorato ho realizzato le misure di spettroscopia d'impedenza elettrochimica necessarie a progettare e validare il sistema di simulazione presso il laboratorio BioDevices del Dipartimento di Ingegneria dell'Informazione. Queste misure sono state eseguite su dispositivi commerciali tipo MEA (Multi Electrodes Array) e su prototipi di substrati polimerici creati con un innovativo processo industriale che ho

contribuito a mettere a punto all'interno di una collaborazione con la Next Step Engineering (spin off del Dipartimento di Ingegneria dell'Informazione dell'Università di Padova). Questa attività di ottimizzazione ha portato alla stesura di un brevetto italiano, attualmente in fase di deposito, di cui l'Università di Padova sarà co-titolare.

Grazie a questo processo produttivo industriale vengono realizzati dispositivi microfluidici con elettrodi metallici integrati (oro, argento, alluminio) idonei alle costruzione di sensori elettrochimici per applicazioni biologiche e biomediche, che ho utilizzato nel corso del mio dottorato per eseguire misure su diversi elettroliti con mediatori redox, cellule in adesione e cinetiche enzimatiche. A partire dai risultati ottenuti con questi dispositivi, ho eseguito studi approfonditi sulle tecniche di modellizzazione dell'impedenza elettrica di sistemi eterogenei del tipo metallo/elettrolita e dei relativi fenomeni elettrochimici d'interfaccia (resistenza di trasferimento di carica, capacità del doppio strato elettrochimico, impedenze di diffusione).

Nel corso del mio Dottorato ho potuto approfondire lo studio dell'interfaccia elettrochimica in diversi ambiti scientifici. Durante il primo anno ho infatti partecipato al Progetto di Eccellenza della Fondazione CARIPARO "MISCHA: MIcrofluidics laboratory for Scientific and teCHnological Applications" (Dipartimenti coinvolti: DEI, DISCC, DIP, DII), focalizzato sull'approfondimento delle conoscenze sulla microfluidica e sulla realizzazione di dispositivi microelettronici/microfluidici per applicazioni in ambito chimico e biologico. In questo progetto mi sono occupato di caratterizzare sperimentalmente e modellizzare la risposta elettrica di dispositivi microelettronici/microfluidici mediante spettroscopia di impedenza, e di eseguire test di adesione ed elettroporazione cellulare su superfici d'oro con stima dell'efficienza di trasfezione attraverso osservazioni al microscopio a fluorescenza.

Nel corso del secondo anno ho partecipato al Progetto di Ateneo 2010-2012 "Design and validation of a biosensor to monitor myogenic cell growth in vitro" (Dipartimenti coinvolti: DEI, ex-DAFU), che ha avuto come obiettivo lo sviluppo di un sensore microelettronico, basato sulle reazioni metaboliche di cellule muscolari geneticamente modificate, per rilevare la presenza di sostanze ipertrofiche e anabolizzanti in campioni liquidi, sia di origine animale che umana. Il biosensore elettronico che ho contribuito a sviluppare quantifica la percentuale di lattato presente nei campioni attraverso misure voltammetriche, sfruttando le reazioni di ossidoriduzione che coinvolgono l'enzima lattato ossidasi. Con la collaborazione del DAFU ho sviluppato un protocollo di funzionalizzazione di elettrodi d'oro con lattato ossidasi che garantisse la ripetibilità e la stabilità delle misure voltammetriche nel tempo. La modellizzazione elettrica equivalente delle risposte amperometriche mi ha permesso di quantificare il grado di copertura enzimatica della zona attiva, valutando l'efficacia dei protocolli di deposizione testati. Le performance del biosensore per lattato sono state verificate in termini di limite di sensibilità e intervallo di linearità, utilizzando soluzioni racemo di acido lattico a diverse concentrazioni.

Durante l'ultimo anno del mio Dottorato ho potuto ampliare il concetto di trasduzione elettrica di segnali biometrici, contribuendo a sviluppare un prototipo di protesi sensorizzata per il Veteran Affairs Hospital di Palo Alto (CA, USA), in collaborazione con il Dott. Quarta della Stanford University (CA, USA) e la Wetware Concepts (spin off Università di Padova), nell'ambito del programma statunitense di studio sulla rigenerazione dei nervi della spina dorsale post-trauma indotta con cellule staminali. Questa protesi, nella forma di un guanto, consente di misurare la forza impressa da ciascun dito della mano di un paziente grazie a diversi sensori polimerici. Ciascuno di questi sensori è stato caratterizzato elettricamente presso il laboratorio BioDevices del DEI. Analogamente, ho progettato e realizzato la circuiteria di controllo e acquisizione dei dati nel nostro Dipartimento. Un software dedicato, sviluppato dal gruppo di ricerca cui appartengo, consente di acquisire i dati in tempo reale provenienti dalla protesi oppure di guidare il paziente attraverso numerosi esercizi assistiti, che abbiamo sviluppato in collaborazione con il team di Chirurgia della mano e Riabilitazione del Veteran Affairs Hospital durante il mio periodo di permanenza a Stanford. La protesi consente di monitorare il decorso della riabilitazione dei pazienti, verificando l'efficacia o meno di un particolare protocollo di riabilitazione in modo quantitativo.

Ho contribuito inoltre a perfezionare il prototipo di guanto sensorizzato in collaborazione con le equipe mediche del Prof. Piccione (IRCCS Ospedale Riabilitativo San Camillo, Lido di Venezia) e del Dott. Bertagnoni (Unità Spinale e Gravi Cerebrolesioni, Ospedale San Bortolo, Vicenza). Questo interazione ha portato allo sviluppo di un sistema elettronico a retroazione basato su biofeedback fisici, in grado sia di misurare la forza sviluppata dalla mano dell'utilizzatore, mappandone la distribuzione superficiale, che di interfacciarsi con le strumentazioni mediche e cliniche già esistenti, quali ad esempio elettroencefalografi ed elettromiografi, in

modo da fornire dati di forza esercitata correlabili alle tecniche di indagine di riferimento. Per questa attività ho curato direttamente la progettazione sia della circuiteria di controllo del sistema che delle interfacce software di misura, di training e di gaming presso il laboratorio BioDevices del DEI.

Parte 3 Pubblicazioni

Elenco pubblicazioni su rivista internazionale:

- A. Ferrario, **M. Scaramuzza**, E. Pasqualotto, A. De Toni, A. Paccagnella, "Coadsorption optimization of DNA in binary self-assembled monolayer on gold electrode for electrochemical detection of oligonucleotide sequences", Journal of Electroanalytical Chemistry (2012), doi: http://dx.doi.org/10.1016/j.jelechem.2012.11.029
- **M. Scaramuzza**, A. Ferrario, E. Pasqualotto, A. De Toni, "Development of an electrode/electrolyte interface model based on pseudo-distributed elements combining COMSOL, MATLAB and HSPICE", Procedia Chemistry 6 (2012) 69 – 78.
- E. Pasqualotto, A. Ferrario, **M. Scaramuzza**, A. De Toni, M. Maschietto, "Monitoring electropermeabilization of adherent mammalian cells through electrochemical impedance spectroscopy", Procedia Chemistry 6 (2012) 79 – 88.
- Ferrario, **M. Scaramuzza**, E. Pasqualotto, A. De Toni, A. Paccagnella, "Development of a disposable gold electrodes-based sensor for electrochemical measurements of cDNA hybridization", Procedia Chemistry 6 (2012) 36 – 45.

Elenco pubblicazioni su convegno internazionale:

- **M. Scaramuzza**, A. Ferrario, E. Pasqualotto, G. Rosati, A. De Toni, M. Quarta, A. Paccagnella, C. Reggiani, "Low-cost enzyme-based biosensor for lactic acid amperometric detection. Electrical modeling and validation for clinical and food processing applications", Proceedings of the International Conference on Biomedical Electronics and Devices, pp. 380-383.
- G. Rosati, **M. Scaramuzza**, A. Ferrario, A. De Toni, M. Quarta, A. Paccagnella, C. Reggiani, "Low-cost enzyme-based biosensor for detection of lactic acid in clinical and food-processing applications", Proceedings of Nanotech Italy (November 2011, Venice, Italy).
- M. Perino, T. Ongarello, P. Zilio, E. Pasqualotto, **M. Scaramuzza**, A. De Toni, F. Romanato, "Design, fabrication and testing of a biosensor using plasmonic gratings", Proceedings of the International Conference on Micro and Nano Engineering (September 2011, Berlin, Germany).
- M. Perino, E. Pasqualotto, T. Ongarello, **M. Scaramuzza**, P. Zilio, A. De Toni, F. Romanato, "Plasmonic grating based biosensor: design, fabrication and testing", Proceedings of Nanotech Italy (November 2011, Venice, Italy).
- Ferrario, **M. Scaramuzza**, A. De Toni, L. Odorizzi, C. Ress, C. Collini, E. Morganti and L. Lorenzelli, "Advanced electrical characterization of an innovative microelectronic/microfluidic device", Proceedings of Biosensors (Glasgow, UK, 2010).
- **Scaramuzza, M.**; Ferrario, A.; De Toni, A., "Development of an innovative electrolytes characterization approach using a combined COMSOL/MATLAB/HSPICE system", Ph.D. Research in Microelectronics and Electronics (PRIME), 2010 Conference on , vol., no., pp.1-4, 18-21 July 2010.

Brevetti italiani attualmente in fase di deposito, come inventore:

- "Metodo e apparato per definire e mantenere l'orientazione di dischi polimerici all'interno di processi produttivi industriali di supporti ottici di immagazzinamento dati digitali", co-titolarità Università di Padova e Next Step Engineering srl (spin off Dip. Ingegneria dell'Informazione).
- Sistema indossabile e portabile per la misura di parametri biometrici della mano e la generazione di biofeedback fisici.
- Accessorio endoscopico per il prelievo multiplo e continuo di campioni bioptici del tratto gastro-intestinale, co-titolarità Università di Padova e Next Step Endoscopy srl (spin off del Dipartimento di Scienze Chirurgiche e Gastroenterologiche) (in fase di perfezionamento).

Il Collegio prende atto di quanto esposto e osserva che durante i tre anni della Scuola di Dottorato il dott. **Matteo Scaramuzza** si è impegnato con dedizione e profitto nella sua attività di ricerca e di studio, evidenziando un'ottima capacità di lavorare sia in maniera autonoma che all'interno di un gruppo di ricerca. Il Collegio unanime riconosce la notevole assiduità del candidato, le sue ottime capacità nella ricerca e gli originali risultati conseguiti. **Pertanto il collegio lo ammette all'esame finale.**

Letto, approvato e sottoscritto
Padova, 21/05/2013

Il Direttore
Matteo Bertocco

Il Segretario
Giovanni Sparacino

Allegato 4.2
Collegio docenti
21 Maggio 2013

DEI
DIPARTIMENTO DI
INGEGNERIA DELL'INFORMAZIONE

UNIVERSITÀ
DEGLI STUDI
DI PADOVA

via Gradenigo, 6/B
35131 Padova, Italy
tel +39 049 8277600
fax +39 049 8277699
info@dei.unipd.it
www.dei.unipd.it

CF 80006480281
P.IVA 00742430283

Al Collegio dei Docenti della
Scuola di Dottorato in
Ingegneria dell'Informazione
Padova, 7 maggio 2013

OGGETTO: *Parere sull'ammissibilità dello studente di dottorato Scaramuzza Matteo all'esame finale.*

La commissione si è riunita il 7 maggio 2013 alle ore 15.00 in sala videoconferenze DEI/A per assistere ad una presentazione tenuta dal dottorando Matteo Scaramuzza relativa all'attività di ricerca da lui svolta nel triennio di studi in via di conclusione. Il dottorando ha lavorato nell'ambito dei biosensori per applicazioni biologiche e biomediche.

L'attività di ricerca svolta da Matteo Scaramuzza si è incentrata sullo studio di sistemi di trasduzione elettrica di segnali biologici. Attraverso misure elettrochimiche, sia di impedenza elettrica che di tipo voltammetrico, ha caratterizzato elettricamente il comportamento di diverse tipologie di biosensori: un biosensore amperometrico per la rilevazione di eventi di ibridazione di DNA, un biosensore basato su enzimi catalitici per la quantificazione della concentrazione di acido lattico in campioni liquidi e un biosensore per il monitoraggio della crescita di cellule e la loro conseguente elettroporazione.

Lo studente ha inoltre utilizzato differenti tipi di modelli elettrici equivalenti per interpretare i dati raccolti dalle misure, identificando parametri utili sia alla valutazione dell'efficacia dei protocolli di funzionalizzazione biologica degli elettrodi, che all'ottimizzazione dei protocolli di misura. Ha inoltre sviluppato un modello elettrico dell'interfaccia microelettrodo/elettrolita basato su elementi equivalenti pseudo-distribuiti, che comprende l'influenza sia della geometria della cella elettrochimica che gli elementi parassiti del sistema di misura.

Infine, lo studente ha contribuito a progettare e realizzare un sistema indossabile di misura della forza impressa dalla mano. Questo sistema, con forma di guanto, è dotato di un'interfaccia software che acquisisce in tempo reale i segnali generati dai sensori di forza e interagisce con l'utilizzatore in un ambiente di *gaming*. Lo studente ha realizzato un sistema di sincronizzazione dei dati acquisiti dal guanto sensorizzato con quelli rilevati da un elettroencefalografo a 64 canali, riuscendo in questo modo a correlarne le epoche con i dati di forza.

La qualità dei risultati ottenuti è documentata anche dalle pubblicazione di cui il dottorando è coautore, tra cui 1 lavoro su rivista, 9 lavori su atti di conferenze internazionali e 3 brevetti in fase di deposito.

Dall'analisi della bozza della tesi emerge che l'ossatura della stessa è già ben delineata per cui, tenuto conto del materiale già disponibile nelle pubblicazioni di cui il dottorando è coautore, lo stato di avanzamento del lavoro è giudicato dalla commissione pienamente il linea con l'obiettivo di completare la versione definitiva entro fine luglio 2013.

Complessivamente, la commissione formula un giudizio pienamente positivo sull'attività di ricerca svolta da Matteo Scaramuzza e ne propone l'ammissione all'esame finale.

Il supervisore del dottorando

Prof. A. Paccagnella

Prof.ssa A. Bertoldo

Prof. A. Neviani

Table of contents

Abstract

Italiano

L'argomento principale dell'attività di ricerca che ho svolto durante il mio periodo di Dottorando in Scienza e Tecnologia dell'Informazione è stato la rilevazione di fenomeni di interazione biologica tramite trasduttori elettrici, ovverosia lo studio di dispositivi elettronici per applicazioni biosensoristiche.

Ho studiato diversi aspetti del processo di trasduzione elettrica allo scopo di ottimizzare la rilevazione delle interazioni biologiche e migliorare le caratteristiche dei biosensori, quali ad esempio la selettività e la risposta in frequenza. Ho iniziato il mio lavoro di Tesi studiando le classiche teorie delle interfacce elettrochimiche fra elettrodi metallici e campioni liquidi, ad esempio la teoria del doppio strato di Helmholtz e la dispersione in frequenza di Warburg, per approfondire i meccanismi di trasferimento di carica elettrica in ambienti eterogenei.

La modellizzazione elettrica a parametri equivalenti dei dati elettrochimici sperimentali è fondamentale per giungere a una loro interpretazione attendibile: il flusso di cariche elettriche attraverso un'interfaccia elettrochimica è il risultato di numerosi contributi, ciascuno dei quali può essere modellizzato utilizzando circuiti elettrici equivalenti con specifiche impedenze. Collegando questi circuiti equivalenti secondo appropriate topologie è possibile simulare la risposta in frequenza di complesse celle elettrochimiche.

Durante il mio periodo di Tesi ho continuato a sviluppare il sistema di simulazione che avevo iniziato a implementare durante il mio periodo di Tesi di Laurea Specialistica: con questo sistema è possibile simulare la risposta elettrica di un sistema elettrodo/elettrolita utilizzando un metodo a elementi pseudo-distribuiti, cioè un'interconnessione finita di circuiti elettrici equivalenti locali la cui topologia viene determinata a partire dalla mesh della geometria della cella elettrochimica. Ciascun circuito elettrico locale può essere formato da diversi elementi elettrici, sia attivi che passivi, con una propria topologia. Il valore di ciascun elemento elettrico locale è determinato con funzioni matematiche ricavate da misure elettrochimiche sperimentali.

Questo approccio di simulazione basato sulla mesh consente di preservare le informazioni geometriche legate alla forma degli elettrodi e della cella elettrochimica, che risultano particolarmente importanti quando è necessario simulare elettrodi in flusso oppure biosensori con componenti microfluidiche.

Le simulazioni e le tecniche di modellizzazione elettrica risultano importanti anche qualora sia necessario progettare il layout di un biosensore. Durante la mia attività di Dottorato ho utilizzato sia biosensori disponibili commercialmente che dispositivi custom: in entrambi i casi, l'interpretazione dei dati sperimentali ottenuti da biosensori con layout differenti è stata eseguite con tecniche di modellizzazione elettrica equivalente, al fine di valutare la distribuzione del campo elettromagnetico fra gli elettrodi e l'influenza degli elementi parassiti del sistema di misura e del dispositivo, quali ad esempio le capacità di cross-talk e le impedenze elettriche dei contatti elettrici.

Durante il mio periodo di Dottorato ho contribuito a sviluppare, in collaborazione con lo spin off dell'Università di Padova Next Step Engineering, un innovativo processo di produzione industriale che consente di creare dispositivi ibridi microelettronici/microfluidici idonei ad applicazioni biologiche all'interno di una singola linea produttiva automatizzata. Con questo processo ho prodotto i dispositivi custom che ho utilizzato per la mia attività sperimentale. Il processo di produzione è oggetto di un brevetto italiano attualmente in fase di deposito, di cui sono uno degli inventori, che ho scritto e sottomesso durante i sei mesi di proroga della discussione finale della Tesi che ho richiesto.

La possibilità di utilizzare i biosensori elettrochimici custom per applicazioni biomediche e biologiche è stata verificata utilizzando misurazioni di spettroscopia di impedenza elettrochimica, tecniche voltammetriche e amperometriche: le curve di calibrazione dei vari dispositivi sono state ottenute utilizzando elettroliti standard per le varie applicazioni, cioè soluzioni con conducibilità elettrica e potenziali ossido-riduttivi noti, e l'influenza di interferenti in soluzione è stata valutata misurando matrici più complesse composte da vari elettroliti con sostanze disciolte.

Le applicazioni biologiche dei biosensori custom sono state sviluppate in collaborazione con altri Dipartimenti dell'Università degli Studi di Padova e con centri di ricerca:

- un biosensore per il monitoraggio dell'ibridazione di sequenze di DNA è stato sviluppato in collaborazione con l'Ospedale San Bortolo (Vicenza, Italia);

- un biosensore enzimatico per la rilevazione di acido lattico è stato studiato in collaborazione con il Dipartimento di Scienze Biomediche (Università di Padova, Italia) e con il Dipartimento di Scienze Anatomiche e Istologiche (Università Sapienza, Roma, Italia);
- un biosensore per monitorare la crescita cellulare e studiare il fenomeno di elettropermeabilizzazione della membrana cellulare è stato sviluppato in collaborazione con il Dipartimento di Scienze Biomediche (Università di Padova, Italia).

Nell'ultimo periodo della mia attività di Dottorato ho studiato un'altra applicazione della trasduzione elettrica di segnali biometrici. In collaborazione con lo spin off dell'Università di Padova Wetware Concepts e con il Dr. Marco Quarta dell'Università di Stanford, ho contribuito a sviluppare un prototipo di guanto sensorizzato per la trasduzione elettrica della forza esercitata da mani umane. Questo prototipo permette di monitorare il processo di riabilitazione funzionale di pazienti con deficit sia lievi che severi, permettendo la valutazione quantitativa dell'efficacia dei protocolli di riabilitazione.

Inoltre, ho contribuito a sviluppare ulteriormente il prototipo, in collaborazione con l'I.R.C.C.S. Ospedale San Camillo (Venezia, Italia) e con l'Ospedale San Bortolo (Vicenza, Italia), in un sistema basato su biofeedback in grado di misurare la forza esercitata da un paziente e di correlarla con dati provenienti da altri strumenti medici, quali elettroencefalografi ed elettromiografi.

English

The core of my research activity during the Ph.D. period has been the detection of biological interactions phenomena using electrical transducers, i.e. biosensors.

I have studied different aspects of the electrical transduction process, in order to optimize the detection by improving biosensors selectivity and frequency response. I have started my Thesis work by studying the fundamental theories of electrochemical interfaces between biosensor electrodes and liquid samples, e.g., Helmholtz double layer and Warburg frequency dispersion, in order to understand the electron transfer mechanisms in wet environment.

The equivalent electrical modeling plays an important role in interpreting experimental electrochemical data. The net flow of electrical charges across an electrochemical interface is the result of several contributions: each of these processes can be modeled using a lumped parameters equivalent electrical circuit with a peculiar electrical impedance. By connecting these equivalent circuits in suitable networks, the frequency response of a complex electrochemical cell can be predicted.

During my Ph.D. period I have further developed a simulation system that I started to implement during my Laurea Thesis: with this simulation system the electrical response of an electrode/electrolyte system is predicted using a pseudo-distributed method, i.e. with an interconnection of basic equivalent electrical circuits derived from the geometrical mesh of the simulated system. Each basic equivalent electrical circuit can have different electrical elements and custom topologies. The value of each electrical element, both passive (e.g., resistors and capacitors) and active (e.g., current generators), is determined through mathematical functions elaborated from experimental electrochemical measurements. This mesh-based approach permits to retain the geometrical information of cell and electrodes layout, that is particularly useful when simulating in-flow channel electrodes and microfluidic biosensors.

Simulations and equivalent modeling techniques are also useful when designing biosensors layout. During my Ph.D. activity I used commercial biosensors and custom devices: in both cases, the interpretation of experimental data obtained from biosensors with different layouts have been performed by using equivalent electrical circuits modeling techniques, in order to assess the electromagnetic field distribution between

electrodes and the influence of parasitics elements, like cross-talk capacitances and tracks intrinsic impedances.

During my Ph.D. period I have contributed to develop, in collaboration with Next Step Engineering (University of Padova spin off), an innovative industrial process that allows to create microelectronic/microfluidic hybrid devices within a single, well-established, production line. With this process I have manufactured all the custom devices I used for my experimental activity. Moreover, this industrial process is the object of an Italian patent that is now pending: I have asked for a six months procrastination of my final discussion in order to write and submit the Italian patent for this innovation as one of the inventors.

The feasibility of custom biosensors to biomedical and biological applications have been tested using impedance spectroscopy, voltammetric and amperometric measurements: electrical calibration curves have been obtained with standard electrolytes, i.e. solutions with knows electrical conductivity or redox potential, and relevant interferents species have been identified by measuring more complex solutions with various electrolytes and diluted substances.

The biological application of custom biosensors have been developed in collaboration with other Departments of the University of Padova and Research Centers:

- a genosensor for monitoring DNA hybridization has been developed in collaboration with San Bortolo Hospital (Vicenza, Italy);
- an enzyme-modified biosensor for the detection of lactic acid has been studied with the Department of Biomedical Sciences (University of Padova, Italy) and Sapienza University (Roma, Italy);
- a biosensor for both monitoring cells growth and studying electropermeabilization has been developed in collaboration with the Department of Biomedical Sciences (University of Padova, Italy).

Recently, during the last part of my Ph.D., I studied another application of the electrical transduction of biological signals. In collaboration with Wetware Concepts (University of Padova spin off) and Dr. Quarta from Stanford University, I have contributed to develop a prototype of sensorized glove for the electrical transduction of force signals exerted by human hands. This prototype allows to monitor the functional rehabilitation process of patients with both mild and severe impairments, enabling the quantitative assessment of the functional rehabilitation protocol effectiveness.

I have also contributed to further develop the prototype, in collaboration with I.R.C.S.S. San Camillo hospital (Venezia, Italy) and San Bortolo hospital (Vicenza, Italy), into a biofeedback system able to both measure the force exerted by patients hands and to correlate these data with those gathered from other medical equipments, e.g., electroencephalographs and electromyographs.

Introduction

This Thesis is focused on characterization and modeling studies of electrical biosensors devices for biological and biomedical applications. One of the most important part of these devices is the electrochemical interface between sensing electrodes and liquid samples, and the interactions with the biological material used for modify the electrodes features, i.e., the functionalization.

A fundamental aspect of each activity presented in this Thesis is the strong relationship between experimental measurements and electrical modeling techniques: as will be described throughout the Thesis, each different application consists of both experimental tests and modeling studies, in order to gain insights on functionalization features and charge transfer process at the electrodes surfaces.

Chapter 1 introduces the fundamental theories of the electrochemical interfaces between metal electrodes and electrolytes and describes the basic processes that take place in an electrochemical biosensing device, e.g., reduction-oxidation reactions, adsorption and diffusion of ionic species. The major electrochemical measurements techniques are also described, i.e., electrochemical impedance spectroscopy, cyclic voltammetry and double-pulse voltammetry, along with the classical modeling methodologies developed to analyze these data. In fact, the modeling technique with lumped-parameters equivalent electrical circuits is described, and the frequency behavior of noticeable circuit topologies is analyzed.

Chapter 2 outlines a pseudo-distributed approach to biosensors modeling: this kind of model has been developed starting from impedances network models using a dynamic mesh and the features of three well-known simulation software packages, i.e., COMSOL Multiphysics, MATLAB (MathWorks, 2007) and HSPICE (Synopsys, 2003), combined in a single simulation system. By performing electrochemical impedance spectroscopy measurements and relative modeling with a specific technique, mathematical laws for local impedance variations can be evaluated and implemented in the simulation system. With these functions, the model is able both to simulate the electrical impedance of electrochemical cells and to take into account the effects of devices parasitics elements.

Next Chapters deal with biosensors applications to biological interactions detection. Custom biosensors have been studied to achieve different goals, and various electrical modeling techniques have been used to analyze data originated from each application.

In Chapter 3 and 4, a DNA hybridization sensor and a lactic acid enzyme-based sensor are described, respectively. In both cases, the lumped-parameters electrical modeling enables the in-depth study of the biological functionalization layers and the consequent optimization of the electrodes modification processes, in order to enhance biosensors performance, e.g., intensity of the detection signals and selectivity. In the cells-based biosensor described in Chapter 5, the electrical modeling of electrochemical impedance spectroscopy measurements has been used both to monitor cells growing process and to optimize cells electroporation protocol, by means of specific equivalent electrical circuits related to cells inner structure.

In Chapter 6 the object of the electrical transduction is shifted from biological to biometrical signals. In this Chapter a force-sensing glove for functional rehabilitation applications is described: this glove embeds commercial piezoresistive force sensors, enabling the assessment of force exerted by subjects hands and the quantitative evaluation of functional rehabilitation protocols effectiveness. The complete force measurement system also includes a real time force visualization and gaming software, in order to create a biofeedback loop that enhance the perception of the exerted force. Moreover, a synchronization system has been developed to correlate acquired force data with other kinds of data gathered from different medical equipment, e.g., electroencephalographs or electromyographs.

Chapter 1. Electrochemical interfaces: measurements and modeling

1.1 Introduction and fundamental equations

A solution is a homogeneous mixture of at least two components in a single phase: the solute is the component that dissolves in another substance, i.e. the solvent. Some substances dissolved in water produce solutions that are capable to conduct electric currents: this happens when the solute generates electrically charged ions that are hydrates by solvent water dipoles. These hydrate ions are free to move inside the solution when subjected to electromagnetic fields: positive ions are attracted by the cathode while negative ions migrate toward the anode, generating a flux of electric current between the two electrodes. The solutes that dissolved in water produce ions not present among the original reagents are called electrolytes, and ions generation process is called ionization [1].

By placing in contact an electrically charged metal with an electrolyte, electrochemical reactions take place. These reactions involves electrons transfer, and therefore electric current, between electrode and electrolyte: the name of these reactions, i.e. reduction-oxidation reactions (or redox), is related to the two complementary processes that take place at the electrodes of an electrochemical cell, where the acquisition of an electron by an ion is defined reduction, while the loss of one electron is called oxidation.

The electrons transfer at the interface between electrode and electrolyte modifies the ionic concentration and therefore in this region arises a lack of electroneutrality, i.e. the electrolyte that surrounds the electrode is at a different electric potential than bulk solution. The electrode potential is related to the concentration of electroactive species at its surface by the Nernst equation:

$$E = E^0 + \frac{2.3RT}{nF}\log\frac{C_O(0,t)}{C_R(0,t)} \quad , \tag{1.1.1}$$

where E^0 is the standard potential for the redox reaction, R is the universal gas constant (8.314 J K^{-1} mol^{-1}), T is the Kelvin temperature, n is the number of electrons transferred in the reaction and F is the Faraday constant [2]. The current resulting from a change in

oxidation state of electroactive species is defined as faradaic current because it obeys Faraday's law, i.e. the reaction of 1 mole of substance involves a change of n·F Coulombs, and therefore it represents a direct measure of the redox reaction rate.

Simple reactions involve only mass transport of the electroactive species to the electrode surface, the electron transfer across the interface and the transport of the product back to the bulk solution. The net rate of the reaction, and therefore the measured current, can be limited either by reactants mass transport or by electron transfer rate. When the whole reaction is controlled by the rate at which the reactants reach the electrode surface, i.e. with a fast redox process at the electrode surface, the current is said to be mass transport-limited. These reactions are called nernstian or reversible, due to the fact that they obey thermodynamic relationship [2].

When the faradaic current is controlled by the rate of electron transfer at the interface between electrode and electrolytes, the relationship between current and applied potential is represented by the Butler-Volmer equation:

$$i = i_0 \left(e^{-\alpha \frac{nF\eta}{RT}} - e^{(1-\alpha)\frac{nF\eta}{RT}} \right) \quad , \tag{1.1.2}$$

where i_0 is the exchange current, α is the symmetry factor that takes into account the difference between the oxidation and reduction energy barriers, and η is known as the overpotential, i.e. the difference between the voltage applied to the electrode and the equilibrium voltage that leads to the generation of the current i [2].

The total current across the electrode/electrolyte interface is the sum of the faradaic currents, i.e. the currents generated by redox reactions, and the non-faradaic currents, i.e. those currents that do not obey the Faraday's law.

When the electrode and the electrolyte are placed in contact, they are in a condition of electroneutrality. The interfacial electrochemical reactions cause an electrons transfer, and therefore electromagnetic field, that influences future redox reactions by contrasting reduction and accelerating oxidation. These concurrent reactions will reach a condition of equilibrium, resulting in a net flux of current across the interface equal to zero.

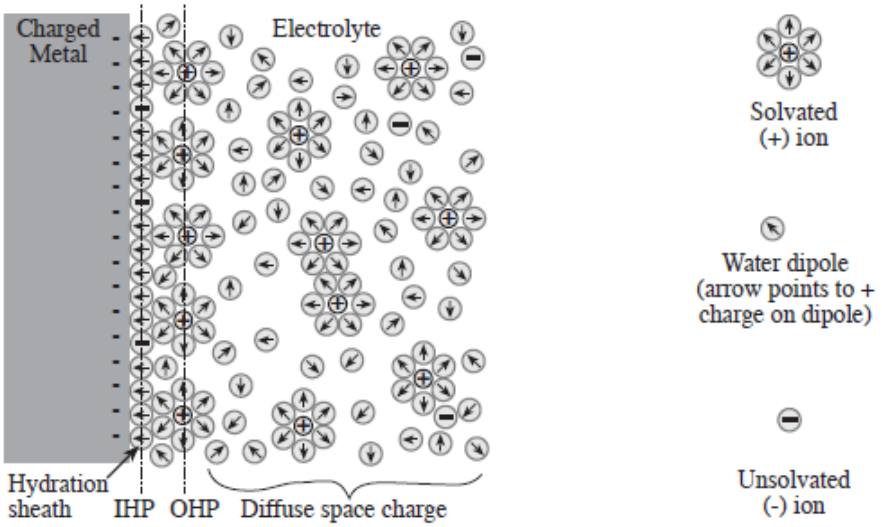

Figure 1.1-1. Schematic representation of the electrified interface between electrode and electrolyte [3].

As depicted in Figure 1.1-1 [3], the electric field generated by redox reactions has a fundamental impact on the electrolyte: this electromagnetic force orients the water dipole, therefore creating a sheet onto the electrode surface called hydratation sheath. Some ions can be specifically adsorbed by the metal surface, resulting in a charge distribution within the sheath. The locus of adsorbed electrical charges onto the electrode surface is known as Inner Helmholtz Plane (IHP). Among the IHP and the bulk solution lie the solvated ions that are generated by electrons transfer at the interface. The plane where these non-specifically adsorbed charges accumulate is called Outer Helmholtz Plane (OHP).

The result of the interfacial chemical reactions, charge adsorption and dipole orientation is the creation of the Electrical Double Layer (EDL), that represents a useful and well-known charge distribution model of an electrically charged conductive surface placed in contact with an aqueous electrolyte.

The first electrical model adopted for the EDL is due to Helmholtz (1879, [4]): in this interpretation, the solvated ions charge is concentrated onto a rigid sheath corresponding to the OHP, and its value is equal and opposite to the charge stored in the electrode. The oriented water dipoles accumulated on the IHP act as a dielectric between the two charged regions, and therefore the interface behavior will be purely capacitive. This capacitance is determined by electrolyte dielectric permittivity $\varepsilon_0\varepsilon_r$, by interface area and by OHP distance from the electrode d_{OHP}:

$$C_H = \frac{\varepsilon_0 \varepsilon_r}{d_{OHP}} \quad , \tag{1.1.3}$$

where C_H is the capacitance per unit of area (F/m^2), ε_0 is the vacuum permittivity and ε_r is the electrolyte relative permittivity. The main approximation of this model is the assumption of rigid and facing sheaths for the electrode charge layer and the OHP.

The Gouy-Chapman model (1910, [5]) takes into account the migration of solvated ions toward the bulk solution: by considering the solvated ions as non-localized, these are free to migrate toward the bulk solution under the influence of both the electrical field generated by the charge accumulated over the electrode and the thermal agitation. This migration process ends when the electrical field generated by the migrating solvated ions compensate the electrode charge. As a result in this region, known as diffuse layer, the combined effects of thermal and electrical forces reach an equilibrium and create an ionic charge distribution that extends the Helmholtz space charge region toward the bulk solution with the same total electrical charge.

This diffuse layer model can modify its electrical capacitance as a function of the ions migration: for little applied voltages, i.e. less than 50 mV, the voltage drop across the space charge region is

$$V(x) = V_0 e^{-\frac{x}{L_D}} \quad , \tag{1.1.4}$$

where x is the distance from the electrode, V_0 is the electrode potential (i.e. for x = 0) and L_D is the Debye length, that describes the potential spatial decaying. This length can be interpreted as the characteristic thickness of the diffuse layer:

$$L_D = \sqrt{\frac{\varepsilon_0 \varepsilon_r V_t}{2 n^0 z^2 q}} \quad , \tag{1.1.5}$$

where $V_t = kT/q$ is the thermal potential, n_0 is the ionic concentration in the electrolyte bulk, z is the ions valence number and q is the electron electrical charge [6].

The differential capacitance per unit area (F/m^2) can be evaluated as

$$C_G = \frac{\varepsilon_0 \varepsilon_r}{L_D} \cosh\left(\frac{z V_0}{2 V_t}\right) \quad , \tag{1.1.6}$$

where the first term represents the capacitance of two conductive plates separated by the distance L_D, that is modulated by the second hyperbolic term that takes into account the effect of the mobile charges in the diffuse layer.

The electrical model based on the theory of Gouy-Chapman usually overestimates the value of the interface capacitance: from experimental measurements the value of

this capacitance is less related to the applied potential than (1.1.6). Furthermore, the capacitance is also related to the ionic concentration of the electrolyte.

The EDL theory by Stern (1924, [3]) combines the Helmholtz model with Gouy-Chapman one, taking into account both a sheath of ions related to the OHP and a diffuse layer of ionic electrical charges. In this model the interface capacitance C_I is given by the series of the Helmholtz capacitance C_H with the Gouy-Chapman one C_G:

$$\frac{1}{C_I} = \frac{1}{C_H} + \frac{1}{C_G} \quad , \tag{1.1.7}$$

where C_H and C_G are described by (1.1.3) and (1.1.6), respectively. The potential drop described in (1.1.7) is approximately linear between the electrode surface and the OHP, and becomes exponential between the OHP and the bulk solution (see Figure 1.1-2) [3]. Increasing the voltage applied to the electrode the electric forces dominate over the thermal ones and the ions of the diffuse layer are attracted toward the interface: this influences the hyperbolic term in (1.1.6), increasing the capacitance C_G. As a result, the series that composes C_I is dominated by the lower term, i.e. C_H, and the resulting capacitance becomes similar to (1.1.3). Conversely, for low applied voltages and diluted solutions, the total interface capacitance is dominated by C_G.

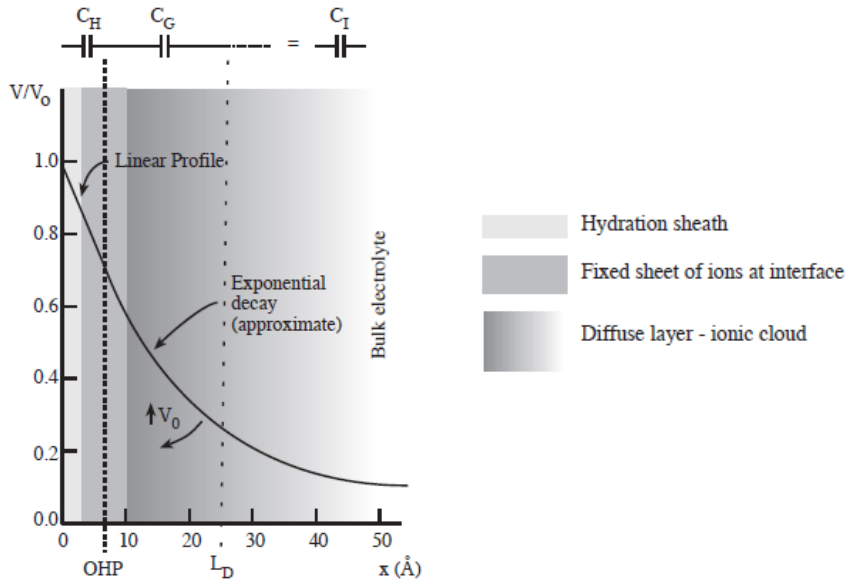

Figure 1.1-2. Schematic representation of the potential profile in the interface region. In the proximity of the electrode surface, the oriented water dipoles cause a linear voltage drop, while far from the OHP the decay is almost exponential. This decay becomes sharper as V_0 is increased. The position of LD shifts toward the electrode surface as the ionic concentration increases [3].

The interface capacitance is related to the electrolyte concentration as described in (1.1.6): by increasing the molar concentration, L_D decreases and therefore C_G increases. This situation is described in Figure 1.1-3, where is also considered the variation of the applied voltage: when a null potential is applied to a physiological system, C_H and C_G reach a similar value, i.e. about 0.14 pF/μm^2, generating a net capacitance of about 0.07 pF/μm^2 [3]. When the null polarization condition is modified, e.g. during electrochemical measurements, the effective thickness of the diffused layer decreases and therefore C_H dominates C_I. This capacitance increases to the maximum imposed by Helmholtz capacitance, i.e. about 0.14 pF/μm^2.

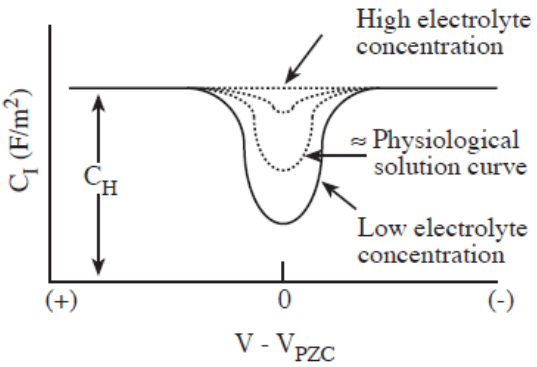

Figure 1.1-3.Behavior of interfacial capacitance C_I as a function of both the electrolyte concentration and the applied potential. By increasing the electrolyte concentration the contribution of C_G is less significant and the total capacitance tends to the fixed value of C_H. Similarly, when the applied potential shifts from the Potential of Zero Charge (PZC), i.e., the potential that reset the charge stored in the electrode, C_I tends to C_H with the trend showed in (1.1.6) [3].

1.2 Electrochemical measurement techniques

The electrochemical cells are heterogeneous systems where elements of different nature coexist and interact, e.g., metal electrodes, saline solutions and living biological materials. In order to investigate all the physical and chemical mechanisms that arise from these interactions, two broad measurement techniques have been used, i.e., impedance-based and voltammetric techniques.

The impedance-based techniques [7], like the electrochemical impedance spectroscopy, evaluate the electrical impedance of the electrochemical system by applying low oscillatory signals between a working and a reference electrode. On the other hand, the voltammetric techniques [1], like cyclic voltammetry or double pulse voltammetry, rely on voltage signals with specific patterns applied from the working to the reference electrode. These potential stimulations trigger electrochemical events, and therefore cause redox currents to flow between working and reference electrodes. A third electrode, defined as counter electrode, provides all the electrons needed by the redox reactions.

1.2.1 Electrochemical impedance spectroscopy

The measurement of the electrical impedance of an electrochemical system using the electrochemical impedance spectroscopy (EIS) technique is based on the transfer function (TF) method, i.e., the system under investigation is perturbed with a sinusoidal voltage input and the correspondent voltage response is measured at the output. If the system is linear, the response is also sinusoidal with the same frequency and different phase and amplitude. The ratio between the measured output and the applied input voltage determines the complex transfer coefficient of the specific applied frequency. The dependence of these coefficients on the frequency defines system transfer function TF. If the frequency range is sufficiently large, the TF describes entirely the dynamic properties of the linear system. Moreover, if the system is in a steady-state condition at the measured frequencies, the output will be in the same stationary condition.

Due to the intrinsic non-linear behavior of the electrochemical systems, a local application of the theory of linear systems is needed. This approach allows the approximation of non-linear system using linear terms [8]: for electrochemical systems the local analysis is implemented by deriving the TF with small amplitudes perturbation signals applied to the steady-state systems, and then taking into account only the linear component of the response. Typically, a perturbation current is applied as an input and the resulting voltage is collected as an output signal. Therefore the TF is identified as a frequency-dependent electrical impedance.

The real electrochemical reaction cells act as large, heterogeneous statistical systems, with the influence of distributed parameters at both macroscopic and microscopic scale. Furthermore, the systems can exhibit non-linear and non-steady state behavior due to both mass and energy transfer processes that could take place during the small-signals perturbation. For these reasons, a widespread methodology has been developed in order to correctly perform EIS measurements [8].

The main requirement that the system should satisfy is the linearity, that can be achieved by keeping the amplitude of the perturbing signal small enough to maintain the system in its steady-state condition. By doing so, the evaluation of the TF coefficients will be time-independent. The control of the environmental parameters is also of crucial importance: during an electrochemical experiment it will be necessary to condition parameters like pH and temperature, in order to reduce the influence of induced chemical phenomena.

Beside these measurement bench conditions, other electrochemical hypothesis have to be verified through a correct definition of the measurement protocol: for example, the faradaic and non-faradaic currents have to be independent process taking place at the electrode surface [6], where the direction of the electrical charge fluxes is only orthogonal to the interface; the electrolyte solution has to be in electroneutrality condition. This means that the total charge density in every infinitesimal volume is zero, therefore the only changes in local ionic concentration in the electrolyte are due to diffusion and charge transfer phenomena, not to mass-related effects like convection or migration.

If the electrochemical experiment fulfills all these hypothesis, the interpretation of EIS data can be accomplished by identifying a suitable equivalent electrical model, that should be of physical type, i.e., it should describe the chemical properties of the

processes taking place in the reactions. The equivalent model can be derived a priori starting from theoretical considerations, or can be constructed starting from the experimental data. By applying the technique known as Structural Modeling [8], the overall electrochemical impedance can be constructed in the frequency domain using specific elements (see Section 1.3). These elements are interconnected with specific topologies in accordance with the behavior of the system under measurement, and each element describes a single physical or chemical process. Therefore, the complete equivalent model can be created as an electrical circuit with impedance matching the EIS experimental data.

1.2.2 Cyclic voltammetry

The Cyclic Voltammetry (CVM) technique consists in the application of a triangular voltage pattern to the electrochemical system, and in the measurements of the corresponding flowing current. The main parameters of the stimulus pattern are the peak-to-peak amplitude, the slew rate, i.e., the scan rate, and the number of sweeps, that are usually defined through a potentiostat connected to the electrochemical cell.

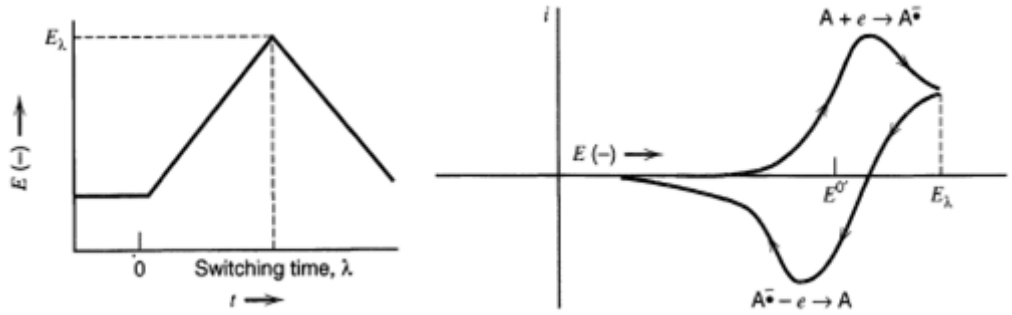

Figure 1.2-1. Typical voltage stimulation for CVM measurements (left). Example of voltammogram with oxidation (i > 0) and reduction (i < 0) redox currents (right) [1].

The CVM technique enables to gather information about the redox processes, e.g., electrons transfer reactions kinetics and surface adsorption processes. It allows also a fast identification of both redox potentials of electroactive species and mediators effectiveness on the overall redox process. Typically, during the forward scan the

cathodic current increases as the applied potential is increased toward the reduction potential. The cathodic current decreases when the applied potential is larger than the reduction potential. When the applied potential reaches the switching point for E_λ, the reverse scan starts and the species generated during the cathodic scan are re-oxidized at the working electrode. Similarly to the forward scan, an anodic peak can be found for applied voltages close to the electroactive species oxidation potentials.

The peaks in the CVM measurement are peculiar of the electroactive species in solution, because they are related to the formation of the diffusion layers at the electrode: varying the applied potential cause a correspondent variation in the concentration of the redox species, and therefore the peak current corresponds to the diffusion-controlled condition.

The CVM scan could provide useful information about the intrinsic nature of the electrochemical processes taking place in the reaction cell, e.g., the reversibility of the system. A system is said to be reversible if all the electrochemical reactions are reversible, i.e., their kinetics is fast, the mass transport phenomena are slow and the diffusion is the dominant process. In this case, the inversion of the potential scan causes the inversion of the redox reactions, without the generation of new reactions with new products or species. Otherwise, if the electrons transfer is slow, the system is said to be irreversible, and CVM measurements can provide useful information in distinguishing the two kind of systems [1].

For reversible systems at room temperature, peaks position with respect to voltage axis does not depend on scan rate but only on the number of electrons involved in the redox reaction, i.e.,

$$\Delta E_p = E_{p,a} - E_{p,c} = \frac{59\ \mathrm{mV}}{n} \quad , \tag{1.2.1}$$

where n is the number of involved electrons, $E_{p,a}$ is the potential of the anodic current peak and $E_{p,c}$ is the potential of the cathodic one. Moreover, if the system is reversible then

$$\left|E_p - E_{p/2}\right| = \frac{56.5\ \mathrm{mV}}{n} \quad , \tag{1.2.2}$$

where $E_{p/2}$ is the voltage corresponding to half the peak current and E_p is the current peak voltage. If the system is irreversible, (1.2.2) becomes

$$\left|E_p - E_{p/2}\right| = \frac{47.7\ \mathrm{mV}}{\alpha} \quad , \tag{1.2.3}$$

where α is the reaction transfer coefficient at the electrode.

The formal potential of redox couples E^O in a reversible system can be evaluated as

$$E^o = \frac{E_{p,a} + E_{p,c}}{2} \quad . \tag{1.2.4}$$

The ratio between the peak currents in a reversible system is unitary:

$$\frac{i_{p,c}}{i_{p,a}} = 1 \quad . \tag{1.2.5}$$

In a reversible system, the magnitude of peak currents is directly proportional to the redox species concentrations and to the square root of the scan rate, following the Randles – Sevcik equation [1]:

$$i_p = (2.69 \times 10^5) AC\sqrt{n^3 D\, v} \quad , \tag{1.2.6}$$

with A electrode area, D diffusion coefficient, v scan rate and C concentration of electroactive species. In a irreversible system, (1.2.6) becomes

$$i_p = (2.99 \times 10^5) AC\sqrt{\alpha\, D\, v} \quad , \tag{1.2.7}$$

where α is the reaction transfer coefficient at the electrode.

1.2.3 Differential pulse voltammetry

The Differential Pulse Voltammetry (DPV) technique is a voltammetric measurement that can minimize the effect of the non-faradaic component of the flowing current, enabling higher sensitivity and therefore the detection of extremely small amount of electroactive chemicals. Moreover, the faradaic current is extracted from the current measurements and so reactions taking place at the electrode surface can be observed more precisely.

During a typical DPV measurement (see Figure 1.2-2), the potential applied to the electrochemical cell is scanned with a series of pulses of 50 ms each. Each potential pulse is fixed at a small amplitude ΔE, i.e., from 10 to 100 mV, and is superimposed on a slowly changing base potential. The current is measured at two specific instants for each pulse, the first just before the application of the pulse i(τ') and the second at the end of the pulse i(τ). The rejection of the non-faradaic component of the current is due to the difference between these two measurements, properly selected to allow for the decay of the non-faradaic current. These "differential" current values are collected for each pulse and then plotted against the applied base potential.

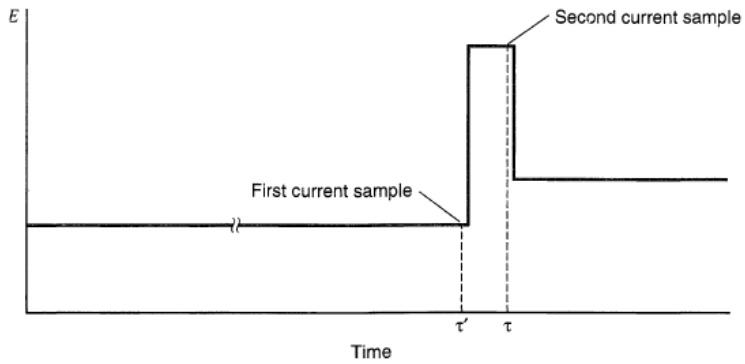

(a)

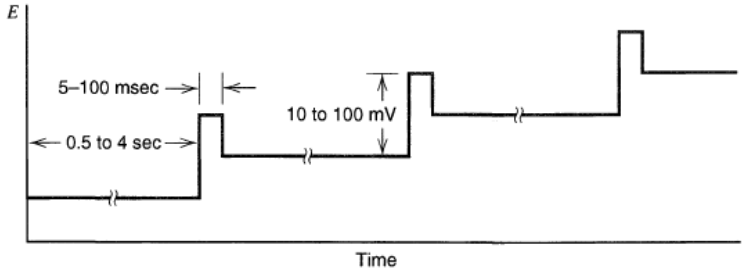

(b)

Figure 1.2-2. Schematization of a single voltage pulse applied during DPV measurements (a); typical DPV stimulation pattern (b) [1].

When the applied base potential is much different from the formal potential of the electrode $E^{0'}$, no faradaic current flows during the time before the pulse, and the change in potential related to the pulse is too small to stimulate the faradaic process. Therefore the difference between i(τ') and i(τ) is close to zero for the faradaic component. Similarly, when the base potential force the system in the diffusion-limited current region, the electroactive species are reduced during the waiting period at the maximum possible rate. The pulse cannot increase this rate further, hence the difference between i(τ') and i(τ) is again close to zero. Only when the applied base potential reaches the region of $E^{0'}$ of a reversible system, an appreciable faradaic "differential" current can be observed. Only in potential regions where an applied small potential perturbation causes a sizable difference in current flow, the DPV technique shows a response.

The DPV response can be treated analytically obtaining, for a reversible system, the following relationships. The "differential" faradaic current δi can be expressed as

$$\delta i = i(\tau) - i(\tau') = \frac{nFA\sqrt{D_O}C_O^*}{\sqrt{\pi(\tau - \tau')}}\left[\frac{P_A(1-\sigma^2)}{(\sigma + P_A)(1+\sigma P_A)}\right] , \qquad (1.2.8)$$

where n is the number of electrons involved in the electrochemical reaction, F is the Farad constant, A is the electrode active area, D_O is the diffusion coefficient of the oxidized species with bulk concentration C_O^*. The two parameters

$$\sigma = \exp\left(\frac{nF}{RT}\frac{\Delta E}{2}\right) \ , \tag{1.2.9}$$

$$P_A = \sqrt{\frac{D_O}{D_R}}\exp\left[\frac{nF}{RT}\left(E + \frac{\Delta E}{2} - E^{0'}\right)\right] \ , \tag{1.2.10}$$

are related to the potential peak height and to the disequilibrium of diffusion coefficients, respectively.

The maximum of the "differential" faradaic current can be observed for $P_A = 1$, and so the height of the current peak $(\delta i)_{max}$ can be obtained from (1.2.8) and is equal to

$$(\delta i)_{max} = \frac{nFA\sqrt{D_O}C_O^*}{\sqrt{\pi(\tau - \tau')}}\left(\frac{1-\sigma}{1+\sigma}\right) \ . \tag{1.2.11}$$

1.3 Equivalent electrical circuit modeling

The data gathered from electrochemical measurements, both spectroscopy and voltammetry, need equivalent modeling to be correctly interpreted: in fact, by using suitable models all the different concurrent phenomena can be recognized and analyzed. Often is possible to gain information from EIS data by observing their locus in the complex plane: by confronting data curves with those of fundamental equivalent electrical models is possible to recognize the dominant process in the measured sample and therefore which could be the correct model to adopt.

The capacitive behavior of the electrochemical interface has been the first investigated aspect of the electrode/electrolyte systems [4]. The electrical impedance of an ideal capacitor C is given by $Z_C(\omega) = (j\omega C)^{-1}$, therefore the frequency-independent feature is the -90° phase while its modulus varies as $(\omega C)^{-1}$ (see Figure 1.3-1).

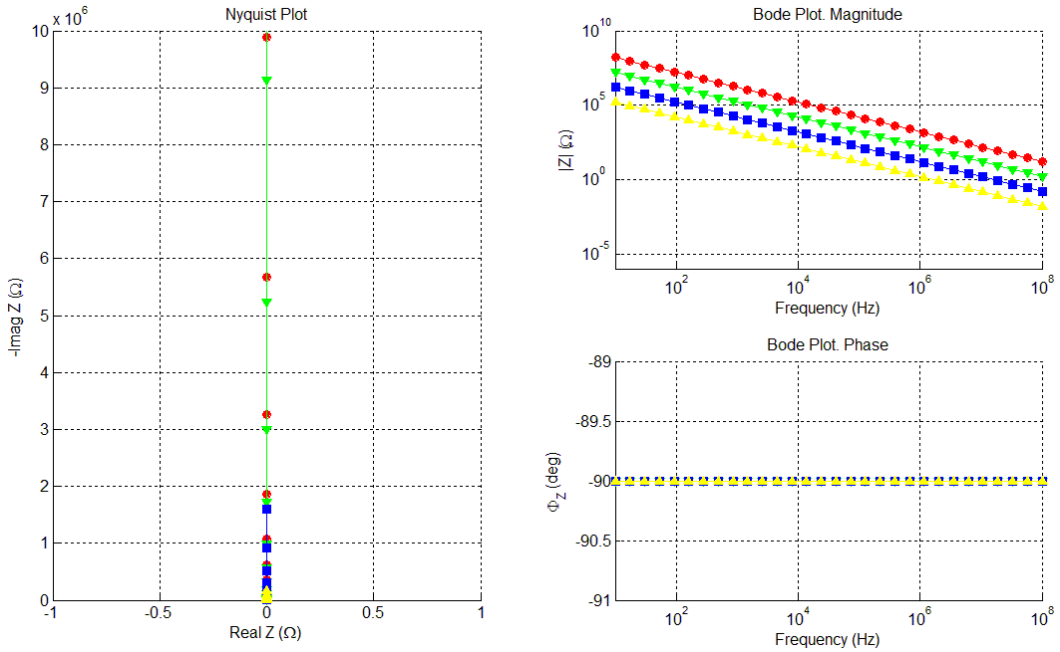

Figure 1.3-1. Impedance of an ideal capacitor: 10 nF (yellow), 100 nF (blue), 1 pF (green), 0.1 pF (red).

When a proper potential is applied to an electrode, a net flow of electric current can be measured across the Electrical Double Layer (EDL), and so a resistive path must be considered along with the electrochemical capacitance. The electrical impedance of an ideal resistor R is given by $Z_R(\omega) = R$, so its real part is equal to the nominal value and the

imaginary part is zero: as frequency varies, these characteristics are constant so this impedance has a punctual representation in Nyquist plane (see Figure 1.3-2).

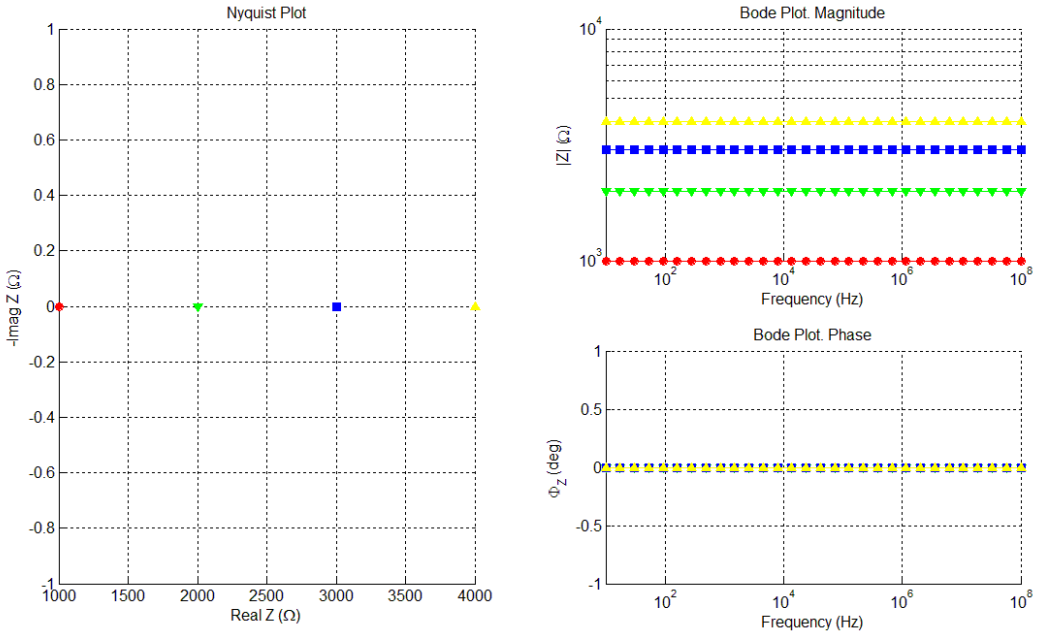

Figure 1.3-2. Impedance of an ideal resistor: 1 kΩ (red), 2 kΩ (green), 3 kΩ (blue), 4 kΩ (yellow).

When the electrochemical system is in dynamic equilibrium, there is a constant flux of charges of both types across the interface but the net flux is null. In this situation the electromagnetic field generates the equilibrium voltage V_0. When a potential V is applied to the electrode, it perturbs this situation of equilibrium: the difference $V - V_0$ is called overpotential η and it represents the sum of four different overpotentials:

$$\eta = \eta_t + \eta_d + \eta_r + \eta_c \quad , \tag{1.3.1}$$

where η_t is due to the charge transfer across the EDL, η_d is related to the diffusion of reagents from and to the electrode, η_r depends on the chemical reactions that take place at the electrode and η_c is related to metal atoms exchange between the electrode and the corresponding ions in solution through the crystallization process [3]. When an electrode is driven around its equilibrium potential the dominant term in (1.3.1) is η_t , resulting in an electric current manly composed by charge transfer across the EDL. The term η_d related to reagents exchange becomes relevant as the applied voltage increases and the EDL voltages strays from equilibrium. For applications to biological systems, overpotentials due to chemical reactions and crystallization are not significant [9].

When metal and electrolyte are in equilibrium the reduction and oxidation currents are balanced. The absolute value of this current is called exchange current density J_0 and its value depends on the electrode material, on the nature of the electrolyte and on the specific redox reactions between charged metal and solution. These reactions make difficult the evaluation of J_0, that is often derived from measurements of electrode/electrolyte systems around the equilibrium potential [6]. If J_0 is known, the total current can be evaluated using the Butler-Volmer formula (1.1.2) for applied potentials near the equilibrium.

To derive an analytical formulation for the resistive path in parallel to the EDL capacitance, a small signal approximation in linear regime can be applied to (1.1.2) [10], obtaining the charge transfer resistance R_{ct} [3]

$$R_{ct} = \frac{V_t}{zJ_0} \quad . \tag{1.3.2}$$

This formulation is valid under the hypothesis of small perturbations applied to the electrode (< 50 mV) and for non-rectifying systems (β = 0.5), that is common during electrochemical impedance spectroscopy measurements. The resulting current can be evaluated using Ohm's law:

$$J = \frac{\eta_t}{R_{ct}} = \frac{J_0 z \eta_t}{V_t} \quad . \tag{1.3.3}$$

The magnitude of J_0 is an important feature of the metal electrode: in fact, if J_0 is high the correspondent value of R_{ct} will be low, and therefore a small overpotential will cause a large current across the interface. The extremization of this situation is known as ideally non-polarizable interface. Conversely, an ideally polarizable interface exhibits a purely capacitive behavior without any charge transfer process (see Section 1.4).

When the overpotential η_t dominates the resistive part of electrode impedance charge, one of the simplest models for the EDL electrical behavior is represented by the R_{ct} (1.3.2) in parallel with the capacitance C_l (1.1.7) [4]. Otherwise, other equivalent elements must be considered to predict the electrical behavior of the electrode/electrolyte system impedance.

A common situation is when the current density through the electrode surface is high enough to reduce the reagents diffusion rate from the bulk solution to the electrode. In this case the current across the interface is diffusion-limited and the dominant overpotential component is η_d. In usual equivalent electrical model this diffusion-related impedance is placed in series to R_{ct}, due to the fact that diffusion and charge transfer

have to take place consecutively, i.e. reagents diffuse toward the interface where they contribute to redox reactions.

When a sinusoidal potential is applied to the electrode, as during electrochemical impedance spectroscopy measurements (see Section 1.2), the ions at the interface migrate under the applied electrical field. In this way a variable ionic concentration is generated at the OHP. By increasing the stimulus frequency the ions are less affected by migration effect so the contribution of the diffuse layer becomes less significant and R_{ct} tends to zero.

In 1899 Warburg analytically describes this frequency-dependent impedance as:

$$|Z_W| = \frac{k}{\sqrt{f}} \ , \tag{1.3.4}$$

where k is a constant related to the mobility of ions involved in the charge transfer process and f is the stimulus frequency. This impedance is intended as a parallel between a resistance R_W and a capacitance C_W, both dependent on the applied voltage [3]:

$$R_W = \frac{10^3 V_t}{z^2 q n^0 \sqrt{\pi f D}} \ , \tag{1.3.5}$$

$$C_W = \frac{1}{2\pi R_W} \ , \tag{1.3.6}$$

$$Z_W = \left(\frac{1}{R_W} + j2\pi C_W\right)^{-1} \ , \tag{1.3.7}$$

where f is the frequency and D is the ionic diffusion coefficient. These formulation are valid for electrochemical systems operating at the equilibrium point and when the diffusion is dominated by a single ionic species. The influence of frequency in the Warburg impedance can be derived by substituting (1.3.5) and (1.3.6) in (1.3.7) obtaining:

$$|Z_W| = \sqrt{2} R_W \ , \tag{1.3.8}$$

$$\theta_{Z_W} = -45° \ . \tag{1.3.9}$$

The module of the Warburg impedance is proportional to its resistive part and has a constant phase as frequency varies. The same features can be found in a uniformly distributed transmission line of finite length [7]: this emphasizes the suitability of the Warburg impedance in modeling diffusive phenomena.

In a more general form than (1.3.7), the Warburg impedance can be defined as

$$Z_W = \frac{k'}{\sqrt{\omega}} \tanh\left(\delta\sqrt{\frac{j\omega}{D}}\right)(1-j) \quad , \tag{1.3.10}$$

where $\omega = 2\pi f$ is the angular frequency, δ is the diffusion region thickness, D is the diffusion coefficient of the diffusing particle and k' is a coefficient evaluated as

$$k' = \frac{V_t}{n^2 FA\sqrt{2}}\left(\frac{1}{C_O^*\sqrt{D_O}} + \frac{1}{C_R^*\sqrt{D_R}}\right) \quad , \tag{1.3.11}$$

where V_t is the thermal voltage; F is the faraday constant; A is the electrode surface; n is the number of electrons involved in the reactions; D_O and D_R are diffusion coefficients for oxidizing and reducing species, respectively; and C_O^* and C_R^* their concentrations in bulk solution.

The formulation in (1.3.10) is valid for a diffusion process in finite dimension medium. If the electrode is located at an infinite distance from the bulk solution, i.e., $\delta \to \infty$, the Warburg impedance become

$$Z_W = \frac{k'}{\sqrt{\omega}}(1-j) \quad . \tag{1.3.12}$$

The Nyquist diagram for (1.3.12) is depicted in Figure 1.3-3: from this diagram can be seen a locus with a constant slope of 45°, while from Bode diagrams can be observed that the phase shift is frequency-independent and the modulus magnitude increases as frequency decreases.

If the electrochemical reactions rate is low, the value of R_{ct} will be high and will dominate the resistive part of the measured impedance. This will vary as $1/(2\pi f)$ like a parallel between a resistance and a capacitance. Otherwise, if the reaction rate is high, the diffusion-limited components dominate the resistive path across the interface, and therefore the measured impedance will vary as $1/(f)^{1/2}$, as stated by (1.3.5).

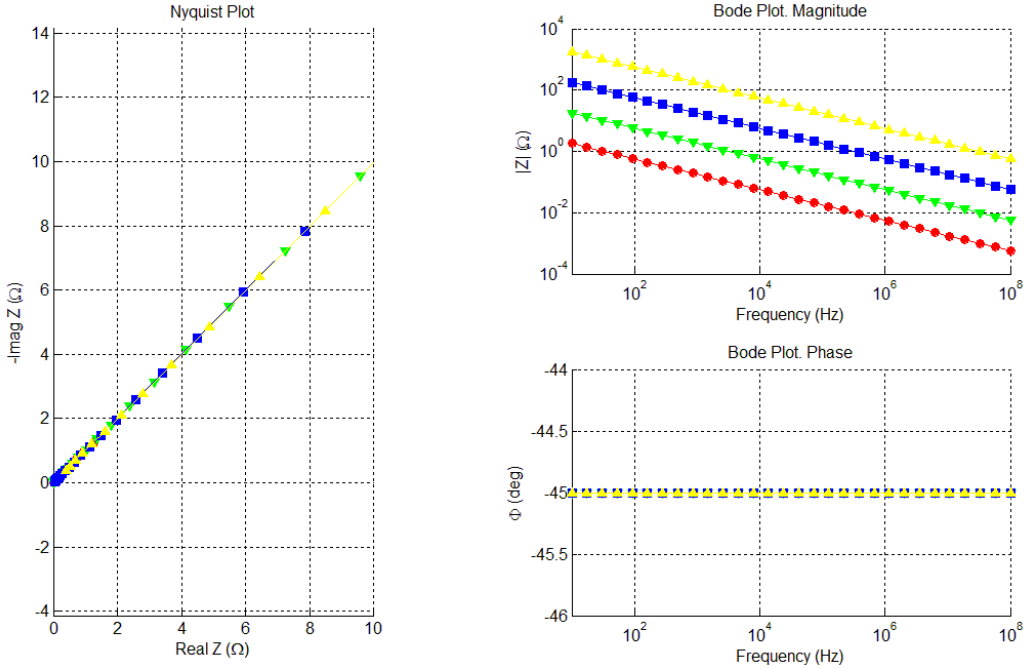

Figure 1.3-2. Impedance of the Warburg element for different values for k': 10 (red), 100 (green), 1000 (blue), 10000 (yellow).

When other aspects of the electrochemical system are significant, e.g. the fractal nature of the electrode surface and the influence of its asperities, the Warburg impedance can be generalized with a Constant Phase Element (CPE) [11]. This impedance has been introduced by Cole and Cole in 1941 and can be written as

$$Z_{CPE} = \frac{1}{Y_0}\omega^{-n}\left(\cos\frac{n\pi}{2} - j\sin\frac{n\pi}{2}\right) \quad , \tag{1.3.13}$$

where Y_0 is a constant, $\omega = 2\pi f$ is the angular frequency and n is a number ranging from zero to one that can be experimentally evaluated using electrochemical impedance spectroscopy [12]. For n = 1 a purely capacitive behavior can be obtained. Similarly to the Warburg impedance, CPE has a constant phase as frequency varies that is equal to $n\pi/2$. Similarly to the Warburg impedance, when the CPE-like behavior is exhibit by a homogeneous layer with finite thickness diffusion, (1.3.13) can be generalized as

$$Z_{BCPE} = \frac{\tanh[R_0 A(j\omega)^n]}{A(j\omega)^n} \quad , \tag{1.3.14}$$

that is the analytical expression of the bounded CPE (see Figure 1.3-4) [13].

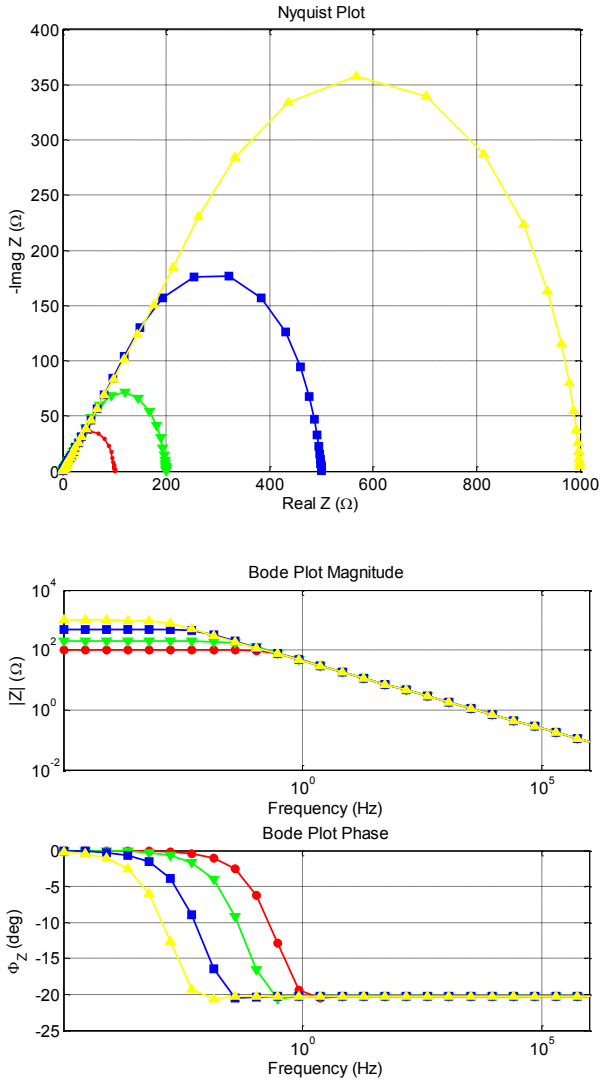

Figure 1.3-4. Impedance of the bounded CPE element for different values of R_0: 100 Ω (red), 200 Ω (green), 500 Ω (blue), 1000 Ω (yellow). Other parameters: n=0.45, A=0.01.

Another fundamental electrical model is the one for ions propagation in solution between the localized working electrode and a distant reference electrode. This phenomenon is modeled as an electrical resistance and its valued is obtained by integrating spherical areas with increasing radius. This spreading resistance is estimated as [6]

$$R = \frac{L}{\sigma A} \quad , \tag{1.3.15}$$

where σ is the electrolyte conductivity, L is the diffusion length and A is the transversal area through which the current flows.

The value of the spreading resistance (1.3.15) is deeply affected by electrode geometry. The planar working electrodes used in biological applications usually are manufactured using microelectronic etching processes, therefore they exhibit round or rectangular shape [14]. For a circular electrode with radius r with a single side exposed to electrolyte, the spreading resistance is given by [6]:

$$R_s = \frac{1}{4\sigma r} = \frac{\sqrt{\pi}}{4\sigma\sqrt{A}} \ , \tag{1.3.16}$$

where A is the circular electrode area. For a rectangular electrode of length l and width w the spreading resistance is given by [6]:

$$R_s = \frac{\ln\left(4\frac{l}{w}\right)}{\sigma\pi l} \ . \tag{1.3.17}$$

1.4 Basic transfer functions

1.4.1 Fundamental topologies

For the usual electrochemical impedance spectroscopy data interpretation, the basic equivalent electrical circuits described in Section 1.3 are combined in widely accepted topologies: these topologies exhibit very peculiar Nyquist diagrams that allow fast estimation of noticeable electrochemical parameters. For example, the main feature of an ideally polarizable electrode is the complete absence of electrochemical reactions on its surface. For this system, the electrical model of the electrode/electrolyte interface can be assumed as the Helmholtz capacitance C_{dl} with a spreading resistance in series (1.4.1), with frequency behavior depicted in Figure 1.4-1.

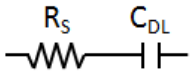

$$Z(\omega) = R_s + \frac{1}{j\omega C_{dl}} \tag{1.4.1}$$

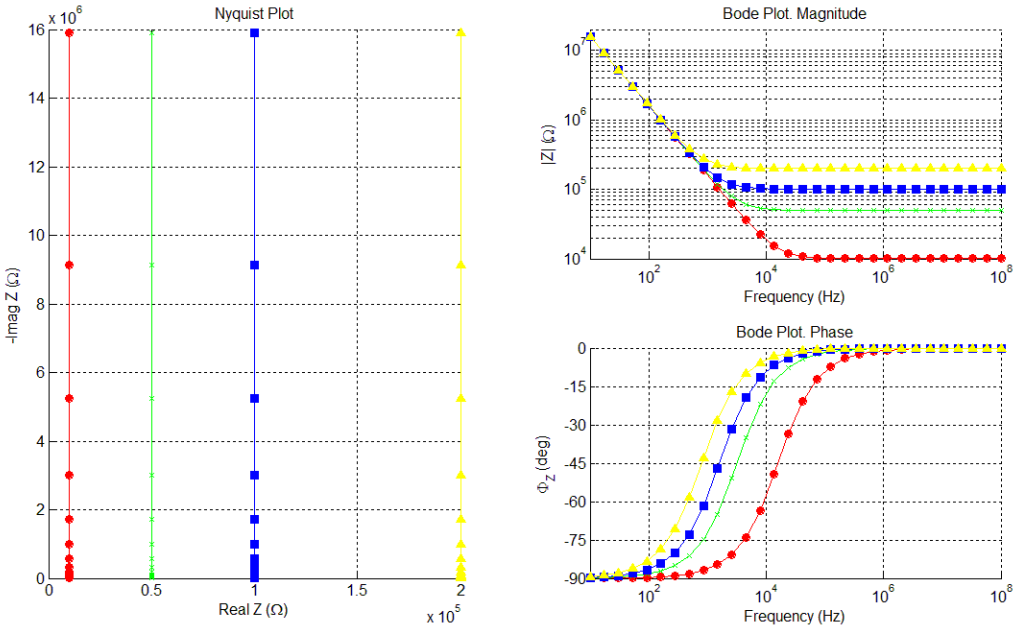

Figure 1.4-1. Ideally polarizable electrode impedance for different values of R_s: 10 kΩ (red), 50 kΩ (green), 100 kΩ (blue), 200 kΩ (yellow).

If a charge transfer process takes place at the electrochemical interface, a simple model can be obtained from the ideally polarizable electrode by adding the charge transfer resistor R_{ct} in parallel to the double layer capacitance C_{dl} (1.4.2). The

correspondent Nyquist diagram of Figure 1.4-2 shows a semicircle of radius R_{ct} / 2 that intercepts the real axis in two points, one is equal to Rs for $\omega \rightarrow \infty$ and the other is equal to $R_s + R_{ct}$ for $\omega \rightarrow 0$, with ω angular frequency.

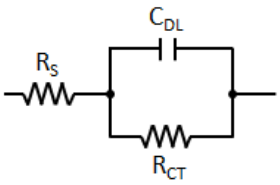

$$Z(\omega) = R_s + \frac{R_{ct}\frac{1}{j\omega C_{dl}}}{R_{ct} + \frac{1}{j\omega C_{dl}}} \tag{1.4.2}$$

The maximum value on the imaginary axis is reached at the angular frequency of ω_0, that is defined by the relationship:

$$\omega_0 = \frac{1}{R_{ct}C_{dl}} = \frac{1}{\tau} \tag{1.4.3}$$

where τ is related to the relaxation time of the system.

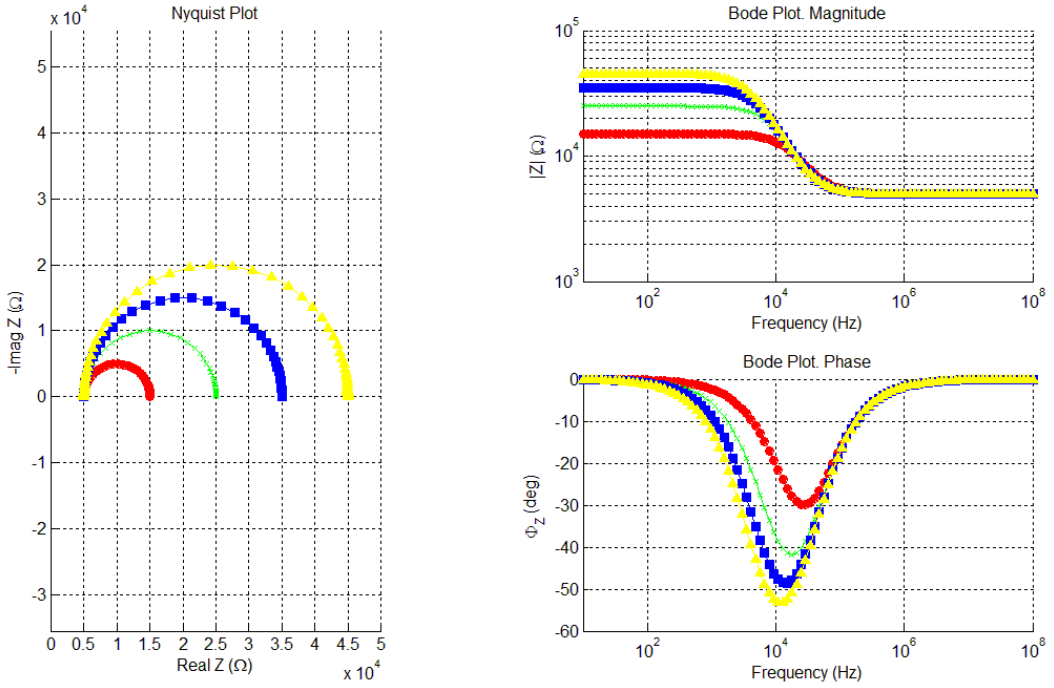

Figure 1.4-2. Impedance of a polarizable electrode with charge transfer process for different values of R_{ct}: 10 kΩ (red), 20 kΩ (green), 30 kΩ (blue), 40 kΩ (yellow). Other parameters: R_s = 5 kΩ.

A widely-accepted equivalent electrical model for an electrochemical system comprehensive of electrode, interfacial sheaths and electrolyte is described by (1.4.4):

thanks to the Warburg element Z_W, this model simulates the behavior of a polarizable electrode in presence of a low frequencies diffusion-limited reactions at its surface [6].

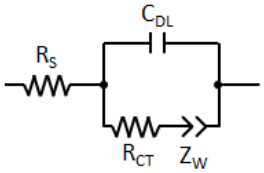

$$Z(\omega) = R_s + \frac{[R_{ct} + Z_W(\omega)]\frac{1}{j\omega C_{dl}}}{R_{ct} + Z_W(\omega) + \frac{1}{j\omega C_{dl}}} \qquad (1.4.4)$$

The frequency behavior of the equivalent impedance, depicted in Figure 1.4-3, is composed of a circular arc for high frequencies and a straight line for low frequencies: as the frequency increase, the Warburg impedance becomes less significant and the overall impedance is dominated by the parallel between R_{ct} and C_{dl}, because at these frequencies the charge transfer processes dominates on diffusive phenomena.

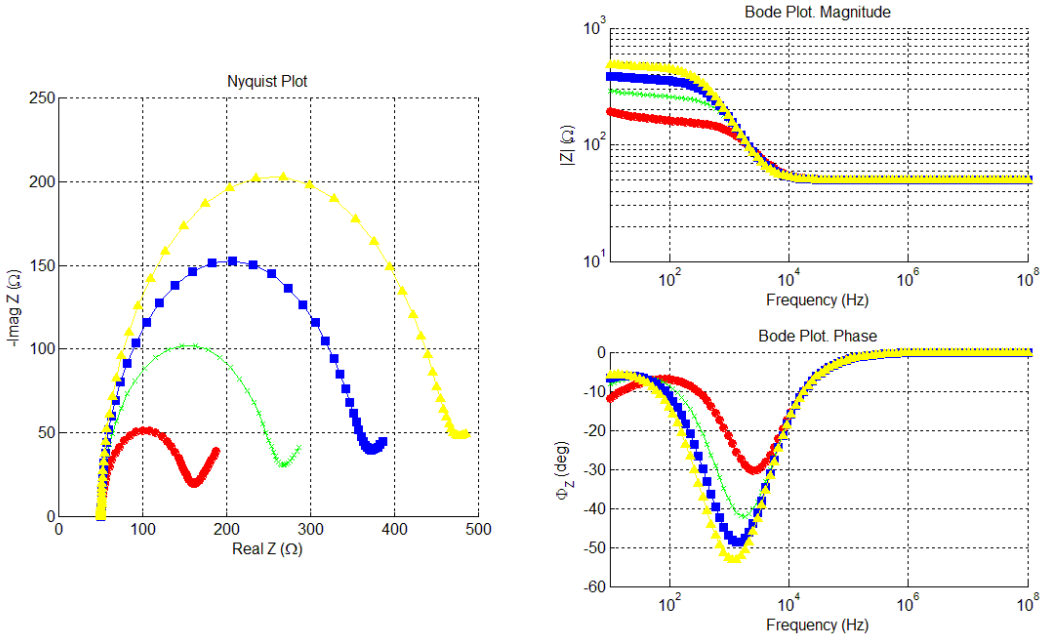

Figure 1.4-3. Frequency dependence of the impedance (1.4.4) for different values of R_{ct}: 100 Ω (red), 200 Ω (green), 300 Ω (blue), 400 Ω (yellow). Other parameters: R_s = 50 Ω, k' = 300.

Figure 1.4-4 describes the application of equivalent electrical models to electrochemical impedance spectroscopy experimental data analysis. For these measurements, phosphate buffer saline (PBS, i.e., NaCl 137 mM, KCl 2.7 mM, Na_2HPO_4 10 mM, KH_2PO_4 2 mM with pH 7.4) electrolyte has been measured using a gold microelectrode as working electrode (15 μm radius) and a silver/silver chloride reference electrode. The experimental data exhibit a behavior similar to that described for impedance (1.4.4) and therefore, using a least squares fitting process [23], the

equivalent circuit parameters values can be obtained. These values well approximate the real data, with a good prediction for impedance magnitude and a 3 % error for impedance phase, so can be concluded that in this example the observed electrochemical process has been a polarizable electrode with a diffusion-limited reactions taking place.

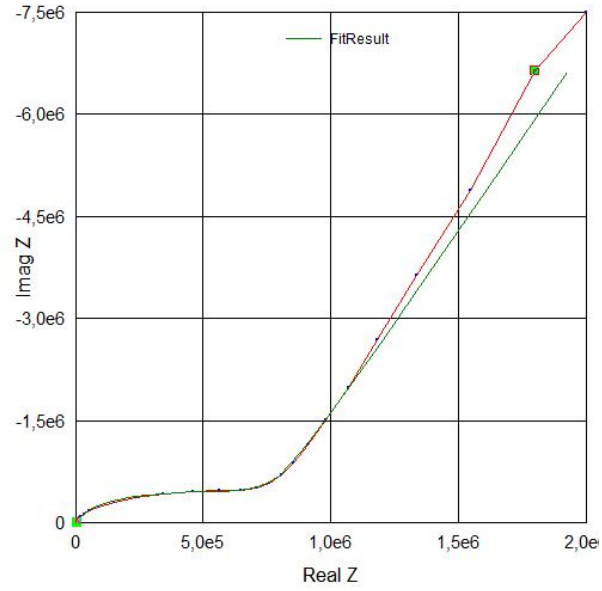

(a)

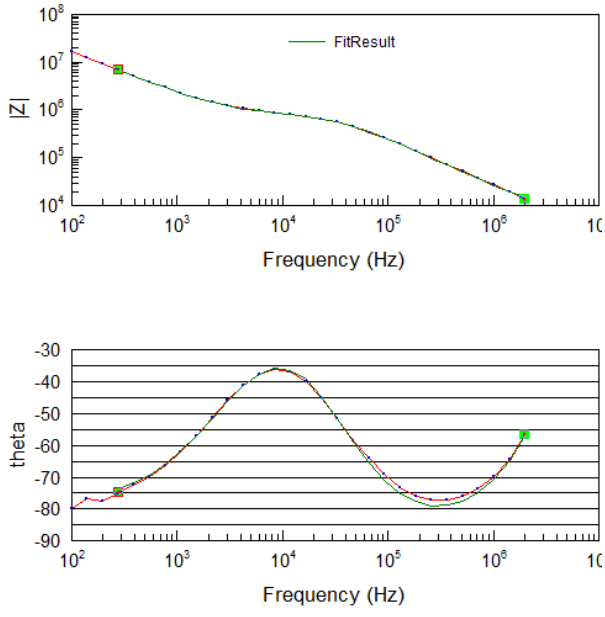

(b)

Figure 1.4-4. EIS data of one microelectrode in contact with PBS saline solution and silver/silver chloride reference electrode (red). Data fitting with (1.4.4) (green) using ZVIEW (Scribner) software: Nyquist (a) and Bode (b) plots.

1.4.2 Two electrodes systems

The electrical response of a two electrodes system under electrical stimulation can be interpreted using the equivalent electrical circuit of Figure 1.4-5 (a) [15], where three general electrical impedances are shown. By assumption, the electrical behavior of the electrode/electrolyte interface is identical for both electrodes of the measurement cell, so its whole equivalent electrical impedance Z_E is given by

$$Z_E(\omega) = Z_P(\omega) + Z_S(\omega) + Z_P(\omega) = Z_S + 2Z_P \,, \tag{1.4.5}$$

where Z_S is the impedance related to the sample inside the measurement cell, Z_P is the polarization impedance of one electrode and ω is the angular frequency.

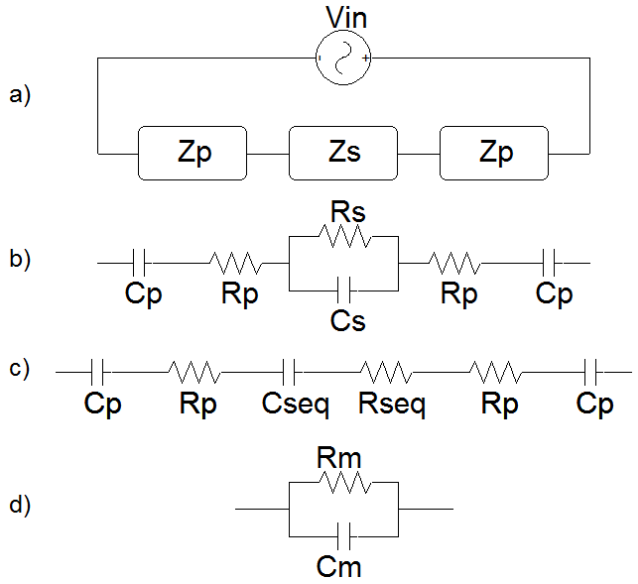

Figure 1.4-5. (a) Schematic representation of electrode/electrolyte/electrode system impedance. (b) Typical equivalent electrical models. (c) Series equivalents. (d) Electrolyte impedance model.

When Z_S and Z_P are described by the circuits shown in Figure 1.4-5 (b), the expressions for sample and polarization impedances become:

$$Z_P = R_P + jX_{C_P} = R_P - j\frac{1}{\omega C_P} \,, \tag{1.4.6}$$

$$Y_S(\omega) = \frac{1}{Z_S(\omega)} = G_S + jB_{C_S} = \frac{1}{R_S} + j\omega C_S \,, \tag{1.4.7}$$

where R_P and C_P are the polarization resistance and capacitance, respectively; X_{CP} is the reactance of C_P; R_S, C_S are the equivalent electrical resistance and capacitance of the sample and G_S, B_S are their respective conductance and susceptance.

By using (1.4.6) and (1.4.7) in (1.4.5) it is possible to write the measurement cell equivalent impedance as:

$$Z_E = Z_S + 2Z_P = \\ = \frac{2R_S C_S R_P C_P s^2 + (2R_S C_S + 2R_P C_P + R_S C_P)s + 2}{j\omega C_P(1 + R_S C_S)} . \quad (1.4.8)$$

If the assumption that $Z_P << Z_S$ holds, this transfer function exhibits one zero located at the frequency

$$f_z = \frac{1}{2\pi R_S C_P} , \quad (1.4.9)$$

and two poles, one in the origin due to C_P and the other one at the frequency

$$f_p = \frac{1}{2\pi R_S C_S} , \quad (1.4.10)$$

which is related only to the electrolyte that fills the cell. For example, if the measurement cell has opposite and facing electrodes and the chamber has a cylindrical or parallelepipedic shape, the electrolyte equivalent electrical parameters R_S and C_S are known:

$$R_S = \frac{1}{\sigma}\frac{h}{\Sigma} , \quad (1.4.11)$$

$$C_S = \varepsilon_0 \varepsilon_r \frac{\Sigma}{h} , \quad (1.4.12)$$

where σ is the sample electrical conductivity, ε_r denotes its relative permittivity, ε_0 is the absolute electrical permittivity and h is the distance between the two electrodes of area Σ. By substitution of (1.4.11) and (1.4.12) in (1.4.10) it can be found that

$$f_p = \frac{1}{2\pi\varepsilon_0}\frac{\sigma}{\varepsilon_r} , \quad (1.4.13)$$

therefore the high frequency pole of (1.4.8) depends only on the tested sample and not on cell geometrical characteristics: for example, considering the sample to be a common bulk electrolyte for biological applications with electrical conductivity σ = 1.2 S/m and relative permittivity ε_r = 72.3 [16], the pole frequency become $f_p \cong 300$ MHz.

In order to express the sample impedance Z_S in a convenient formulation its series synthesis Z_{Seq} can be performed using a resistive part R_{Seq} and a reactive part X_{CSeq}:

$$Z_{Seq}(\omega) = R_{Seq} + jX_{C_{Seq}} = \frac{G_S}{|Y_S|^2} - j\frac{B_{C_S}}{|Y_S|^2} \,. \tag{1.4.14}$$

Referring to the equivalent electrical circuit of Figure 1.4-5 (b), it can be obtained:

$$Z_{Seq}(\omega) = \frac{R_S}{1 + (\omega R_S C_S)^2} - j\omega R_S R_{Seq} C_S \quad , \tag{1.4.15}$$

and by simplifying the resulting series depicted in Figure 1.4-5 (c) the equivalent impedance Z_{Teq} can be found as:

$$\begin{aligned} Z_{Teq}(\omega) = R_{Teq} + jX_{C_{Teq}} = \\ = \left(R_{Seq} + 2R_P\right) + j\left(X_{C_{Seq}} + 2X_{C_P}\right) \,. \end{aligned} \tag{1.4.16}$$

To evaluate the correspondence between polarization impedance and sample equivalent elements of Figure 1.4-5 (b) and instrument results expressed in terms of the parallel impedance of Figure 1.4-5 (d), the parallel synthesis of (1.4.16) can be performed obtaining

$$Y_M(\omega) = G_M + jB_{C_M} = \frac{1}{R_M} + j\omega C_M = \frac{R_{Teq}}{\left|Z_{Teq}\right|^2} - j\frac{X_{C_{Teq}}}{\left|Z_{Teq}\right|^2} \,. \tag{1.4.17}$$

where G_M and B_{CM} are the conductance and the susceptance of R_M and C_M respectively and Y_M is the admittance of the measured impedance Z_M. By solving the equality between last two members of (1.4.17) it can be obtained:

$$R_M = \frac{\left(2R_P + R_{Seq}\right)^2 + \left(\frac{2}{\omega C_P} - X_{C_{Seq}}\right)^2}{2R_P + R_{Seq}} \,, \tag{1.4.18}$$

$$C_M = \frac{\frac{2}{\omega C_P} - X_{C_{Seq}}}{\omega\left[\left(2R_P + R_{Seq}\right)^2 + \left(\frac{2}{\omega C_P} - X_{C_{Seq}}\right)^2\right]} \,, \tag{1.4.19}$$

where the resistance R_{Seq} and the reactance X_{CSeq} are given in (1.4.15).

The above expressions relates the resulting overall impedance obtained from electrochemical impedance spectroscopy measurements to the relevant equivalent electrical parameters of both sample and polarization impedance.

Equations (1.4.18) and (1.4.19) can be simplified by applying the following two hypothesis:

$$Z_P \ll Z_S \,, \tag{1.4.20}$$

$$f \ll f_p = \frac{1}{2\pi R_S C_S} \,. \tag{1.4.21}$$

The first assumption is not restricting [15] because if the polarization impedance is larger than the sample one its presence would shield the sample response, making the sensor useless. Also the second assumption is not limiting because it sets the frequency upper limit to (1.4.10), whose common values are much higher than the interesting frequencies.

Using the above assumptions, (1.4.18) and (1.4.19) reduce to

$$R_{M1} = \frac{1+\alpha^2}{\alpha^2} R_S + 2R_P = \beta_1 R_S + 2R_P \,, \tag{1.4.22}$$

$$C_{M1} = \frac{\alpha^2}{1+\alpha^2} C_S + \frac{1}{1+\alpha^2}\frac{C_P}{2} = \frac{1}{\beta_1} C_S + \frac{\beta_2}{2} C_P \,, \tag{1.4.23}$$

where the function $\alpha(\omega)$ is given by

$$\alpha(\omega) = \frac{\omega R_S C_P}{2} \tag{1.4.24}$$

and the behavior of functions β_1 and β_2 is depicted in Figure 1.4-6.

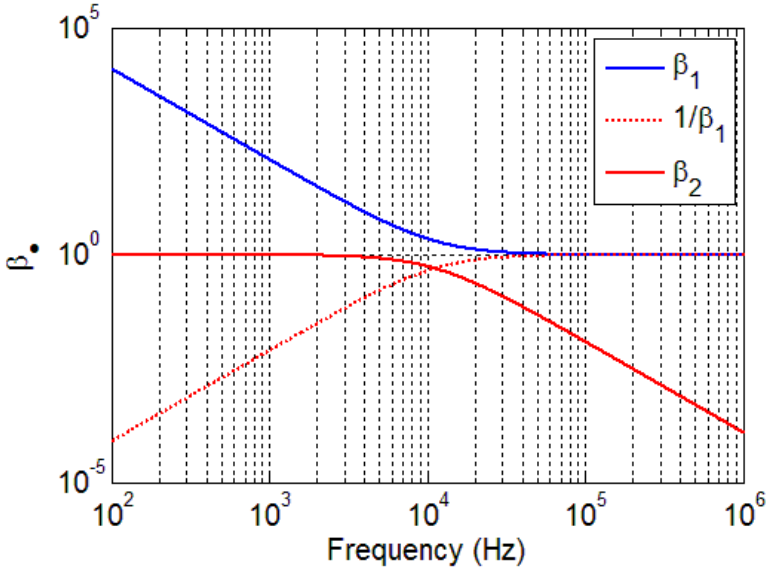

Figure 1.4-6. Typical β_1 and β_2 functions behavior in frequency domain.

Recalling the sample equivalent electrical circuit of Figure 1.4-5 (b), the pole introduced by the parallel impedance Z_S is found at much higher frequencies than the usual measurements span. Therefore in the range of interest the sample impedance can be represented by a single resistor R_S and the expressions for the measured impedance Z_M become

$$R_{M2} = R_{M1} = \beta_1 R_S + 2R_P \,, \tag{1.4.25}$$

$$C_{M2} = \frac{\beta_2}{2} C_P \,, \tag{1.4.26}$$

where the functions β_1, β_2 and α are given in equations (1.4.22), (1.4.23) and (1.4.24), respectively.

The behavior of the measured impedance as a function of frequency is given in Figure 1.4-7, while Figure 1.4-8 depicts the influence of approximations applied to Z_M.

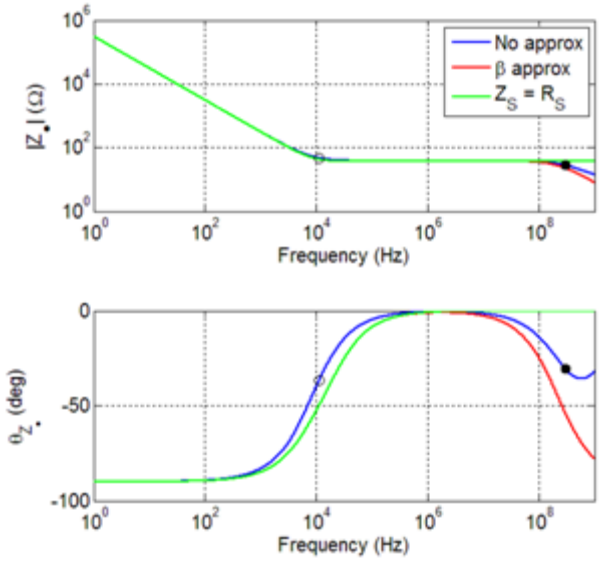

Figure 1.4-7. Bode plot of system electrical impedance using (1.4.25-26) (red) and approximating the sample impedance with its real part (green). The blue line indicates typical EIS data obtained from two gold microelectrodes in contact with standard saline solution.

The errors introduced by the approximations on Z_M have been evaluated on magnitude $\Delta|Z_\bullet|$ and phase $\Delta\theta_{Z_\bullet}$ by using:

$$\Delta|Z_\bullet| = 100\frac{|Z_\bullet| - |Z_M|}{|Z_M|} \,, \tag{1.4.27}$$

$$\Delta\theta_{Z_\bullet} = 100\frac{\theta_{Z_M} - \theta_{Z_\bullet}}{\theta_{Z_M}} \,, \tag{1.4.28}$$

where the reference impedance Z_M is the measured one in the formulation with (1.4.18) and (1.4.19). $Z_\bullet$ represents either Z_{M1} or Z_{M2}, i.e., the parallel equivalent electrical impedance Z_M using (1.4.22), (1.4.23) or (1.4.25), (1.4.26) respectively.

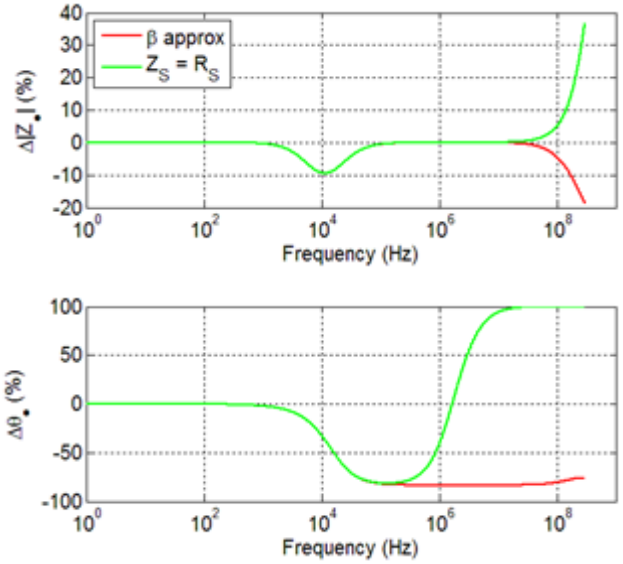

Figure 1.4-8. Percentage error of the two approximations (β functions and purely resistive sample) with respect to the acquired data.

From Figure 1.4-8 it can be seen that there are two frequency ranges where the magnitude of the errors is minimized: one is for frequencies lower than f_z (1.4.9) and the other one for frequencies between f_z and f_p (1.4.10). The influence of C_S is relevant for frequencies higher than f_p. For lower frequencies, the errors induced by the two approximations of Z_M are identical. It is important to avoid the decades of frequencies right around f_z in order to keep the approximations errors on magnitude low.

From equation (1.4.22) and Figure 1.4-6 it can be seen that in order to perform accurate measurements on the sample resistance R_S it is convenient to consider frequencies higher than the zero of function β_1, i.e.,

$$f_\beta = \frac{2}{2\pi R_S C_P} = 2f_z\,, \tag{1.4.29}$$

because in this range the expression of the measured resistance reduces to $R_M = 2R_S + R_P$, so the resistive part of the polarization impedance will add up as a constant factor for every tested frequency.

From (1.4.23) it can be observed that two functions multiply the noticeable parameters of capacitance. Using the same considerations as above, the influence of the reciprocal of β_1 is minimized at high frequencies so C_S, as well as R_S, should be measured for frequencies higher than f_β. Conversely, at lower frequencies the measured capacitance reduces to $C_{M1} = C_P/2$ and so this electrical polarization parameter can be analyzed apart from the sample capacitance.

1.5 Analysis of parasitic elements

The analytic approach described in Section 1.4.2 can be applied to the study of parasitic element of the measurement cell. These parasitic elements can be modeled by simply adding resistive contributions R_{PA} due to connections, e.g. cables, and a capacitive coupling C_{PA} related to the inner structure and materials of the measurement cell, as shown in Figure 1.5-1.

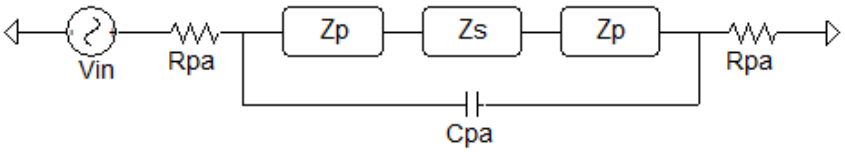

Figure 1.5-1. Schematic representation of electrochemical cell with parasitics elements.

The circuit of Figure 1.5-1 [16] takes into account the electric response of both the electrode/electrolyte interface and the measurement cell. The electrochemical interface is modeled by the classical charge transfer resistance R_{CT} in parallel with a constant phase element Z_{CPE} given by [17]:

$$Z_{CPE} = \frac{1}{(j\omega C_{DL})^n}\,, \tag{1.5.1}$$

where C_{DL} is the classical double layer capacitance and n is an empirical parameter that model electrode surface roughness [14]. The value for n typically range from 0.5 to 1 and it can be obtained by fitting the measured data from the slope of the low frequency impedance plot [18]. A parasitic element C_P is connected in parallel to the electrode/electrolyte interface model in order to take into account the intrinsic coupling effect of the measurement cell [19]. The electrolyte spreading resistance R_S can be evaluated using a spherical approximation as described in [20]. A better estimation for R_S can be obtained by using the formulas described in [21] and [6] (see Section 1.3).

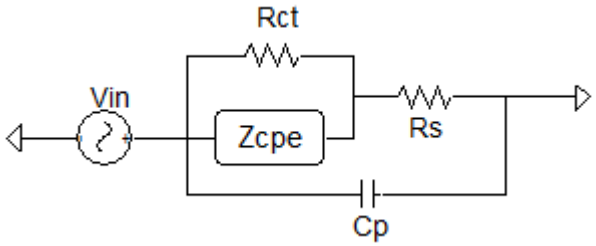

Figure 1.5-2. Equivalent electrical circuit of single electrode/electrolyte interface with purely capacitive parasitic element.

The transfer function of the circuit of Figure 1.5-2 is given by

$$Z_{T,A}(\omega) = \\ = (R_{CT} + R_S)\frac{1 + \left[\left(\frac{R_{CT}R_S}{R_{CT} + R_S}\right)(j\omega C_{DL})^n\right]}{R_{CT}R_S C_P C_{DL}^n (j\omega)^{n+1} + j\omega C_P(R_{CT} + R_S) + R_{CT}(j\omega C_{DL})^n + 1}, \quad (1.5.2)$$

that can be written as

$$Z_A(\omega) = \frac{1 + R_S(j\omega C_{DL})^n}{(j\omega C_{DL})^n\left[j\omega R_S C_P + (j\omega)^{1-n}\frac{C_P}{C_{DL}^n} + 1\right]}, \quad (1.5.3)$$

under the hypothesis $R_{CT} >> R_S$. From the latter formulation can be clearly understood the role played by the parameter n: for n = 0, Z_A becomes the transfer function of the simple parallel between R_S and C_P, while for n = 1 C_{DL} acts as a plain capacitor.

In order to assess a value for C_P it is convenient to derive an explicit formulation for Z_A high frequency pole f_P. From Figure 1.5-3 it can be seen that the influence of n is related to frequencies lower than the pole f_P, so to obtain the high frequency pole expression n can be set to zero for simplicity, obtaining

$$f_P = \frac{1}{2\pi R_S C_P}. \quad (1.5.4)$$

A value for C_P can be derived from (1.5.4) by direct comparison with EIS measurements and by estimation of pole frequency. Typical values for C_P are in the range of few picoFarads. As stated in [22], a direct measurement of cell parasitic capacitance is possible connecting the empty cell to the instrumentation.

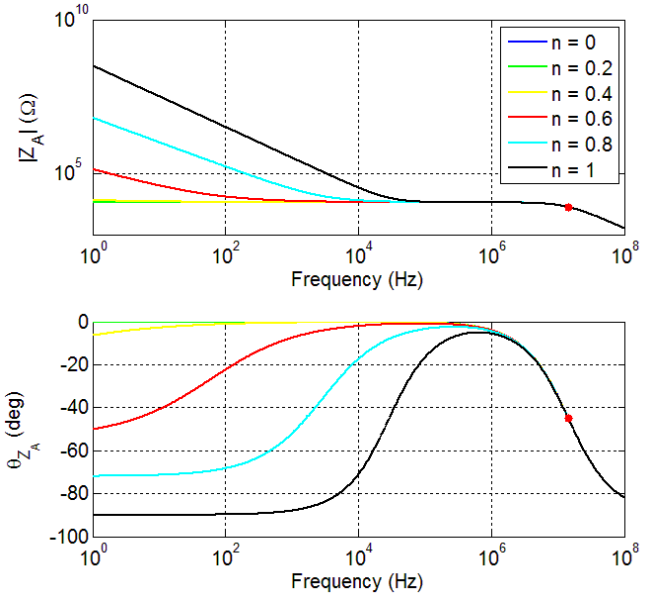

Figure 1.5-3. Impedance (1.5.3) as a function of frequency for different values of parameter n. The red dot indicates f_p frequency.

It is often important to extend the plateau between zero and high frequency pole as much as possible in order to be able to detect the electrolyte characteristics with more accuracy. To do that it is necessary to evaluate a direct formulation for the zero frequency f_Z. From (1.5.3) it can be found that:

$$f_Z = \left| j^{2/n^2} \frac{1}{2\pi R_S^{1/n} C_{DL}} \right| , \qquad (1.5.5)$$

and Figure 1.5-4 depicts the position of zeros and poles of Z_A as n varies.

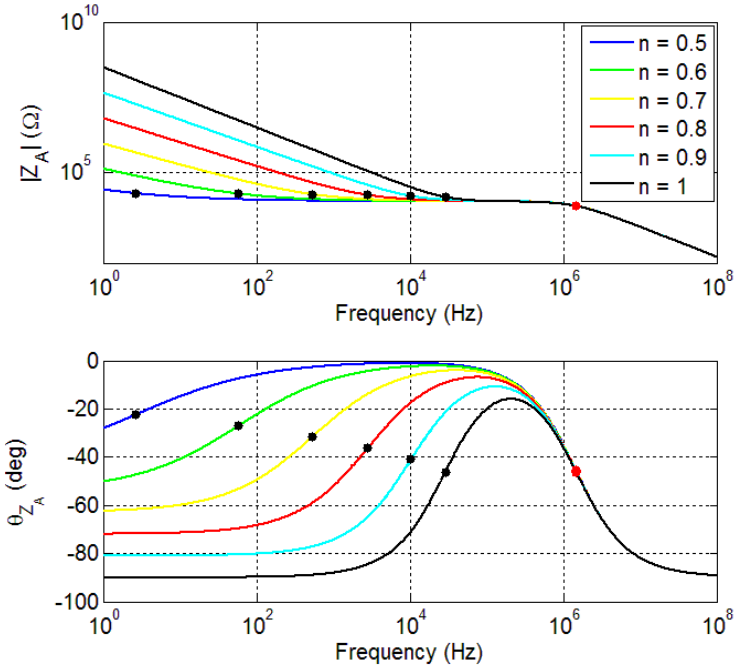

Figure 1.5-4. Impedance (1.5.3) as a function of frequency for different values of parameter n. The red dot indicates f_p frequency, while the black one indicates f_z.

Figure 1.5-5 depicts the typical response of a PBS solution in contact with a gold microelectrode. The data set has been obtained using an Ayanda Multi Electrode Array with electrodes diameter of 30 μm.

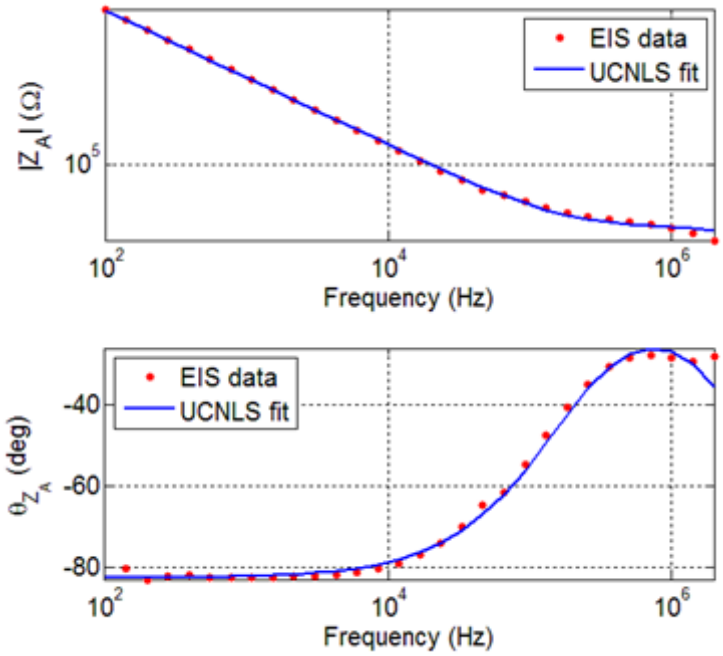

Figure 1.5-5. EIS data of one gold microelectrode in contact with PBS saline solution (red dots) and data fit obtained with impedance (1.5.3).

These data have been interpreted using the transfer function described in (1.5.3) and an unconstrained complex non-linear squares (UCNLS) fit [23], in which the error function δ is given by

$$\delta = \sqrt{\sum_{i}\left(\frac{\mathcal{R}\{Z_{M,i}\} - \mathcal{R}\{Z_{F,i}\}}{\mathcal{R}\{Z_{F,i}\}}\right)^2 + \sum_{i}\left(\frac{\mathcal{I}\{Z_{M,i}\} - \mathcal{I}\{Z_{F,i}\}}{\mathcal{I}\{Z_{F,i}\}}\right)^2}\ , \qquad (1.5.6)$$

where Z_M represents the measured impedance and Z_F the fitted one.

In order to describe in a more proper way the behavior of the EIS response at high frequencies it can be useful to consider a resistance R_{PA} in series with the system of Figure 1.5.2. This resistance could represent the intrinsic resistive path of the measurement bench connection cables. The equivalent electrical circuit is depicted in Figure 1.5-6.

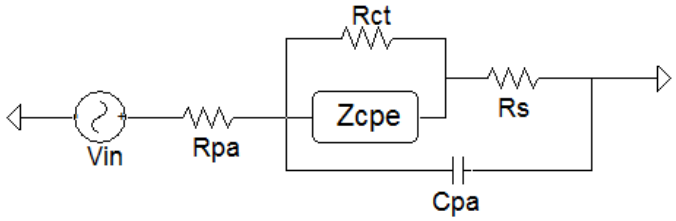

Figure 1.5-6. Equivalent electrical circuit of one electrochemical interface with both capacitive and resistive parasitic elements.

The complete transfer function of this equivalent circuit is given by

$$Z_{T,B} = \\ = \frac{R_{CT} + R_S + R_{PA} + R_{CT}(R_{PA} + R_S)(j\omega C_{DL})^n}{R_{CT}R_S C_{PA}C_{DL}^n(j\omega)^{n+1} + j\omega C_{PA}(R_{CT} + R_S) + R_{CT}(j\omega C_{DL})^n + 1} \\ + \frac{j\omega R_{PA}(R_{CT} + R_S)C_{PA} + j\omega R_{PA}C_{PA}R_{CT}R_S(j\omega C_{DL})^n}{R_{CT}R_S C_{PA}C_{DL}^n(j\omega)^{n+1} + j\omega C_{PA}(R_{CT} + R_S) + R_{CT}(j\omega C_{DL})^n + 1} \qquad (1.5.7)$$

that can be reduced, by using the approximations $R_{CT} >> R_S$ and $R_{PA} << R_S$, to the form of

$$Z_B(\omega) = \frac{[1 + (R_{PA} + R_S)(j\omega C_{DL})^n](1 + j\omega R_{PA}C_{PA})}{(j\omega C_{DL})^n\left[j\omega R_S C_{PA} + (j\omega)^{1-n}\frac{C_{PA}}{C_{DL}^n} + 1\right]}\ . \qquad (1.5.8)$$

Figure 1.5-7 depicts the comparison between (1.5.7) and (1.5.8) as a function of the parameter n.

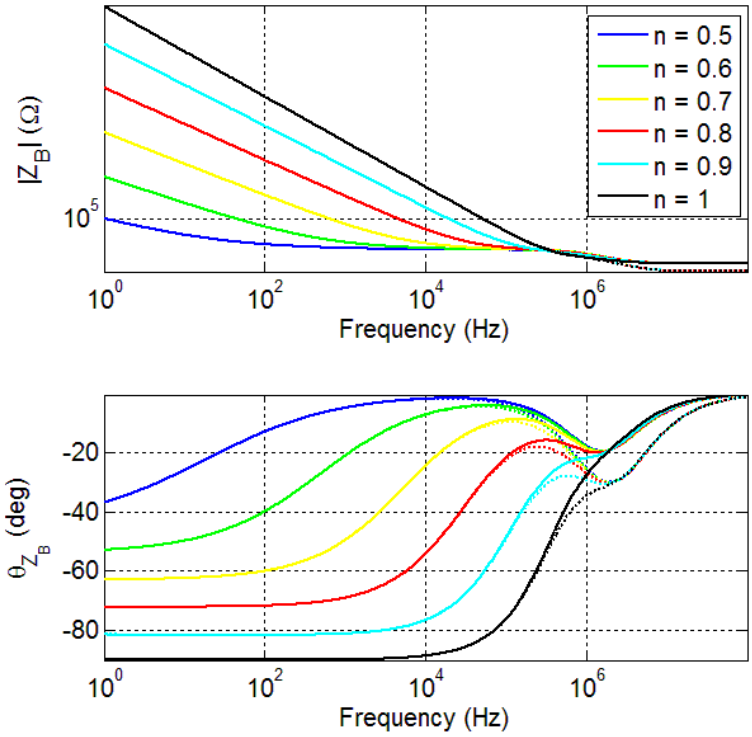

Figure 1.5-7. Comparison between analytic expression (1.5.7) (dotted line) and approximated (1.5.8) (straight line).

The poles/zeros structure of Z_B is obviously very similar to the one of Z_A: the low frequency zero is given by:

$$f_Z = \left| j^{2/n^2} \frac{1}{2\pi (R_S + R_{PA})^{1/n} C_{DL}} \right| , \qquad (1.5.9)$$

while the high frequency one is directly related to the parasitic elements R_{PA} and C_{PA}. Figure 1.5-8 describes the positioning of zeros and poles as n varies.

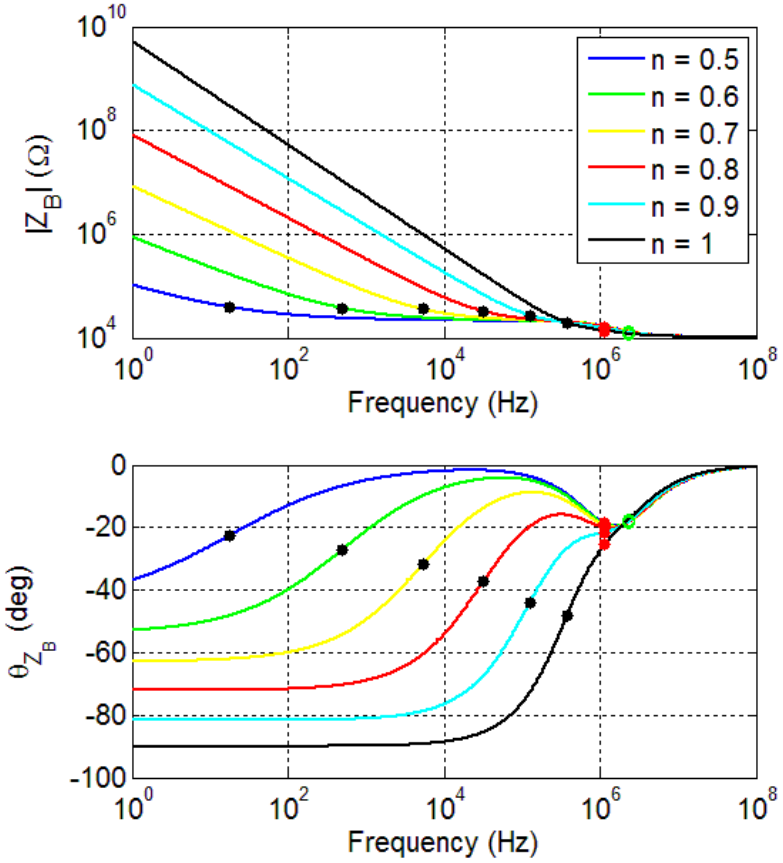

Figure 1.5-8. Location of poles (red dots) and zeros (black and green dots) for (1.5.8).

Using (1.5.2) to fit PBS EIS data of Figure 1.5-5 a better high frequency fit can be obtained, especially for the measured impedance magnitude, than using (1.5.7) as described in Figure 1.5-9.

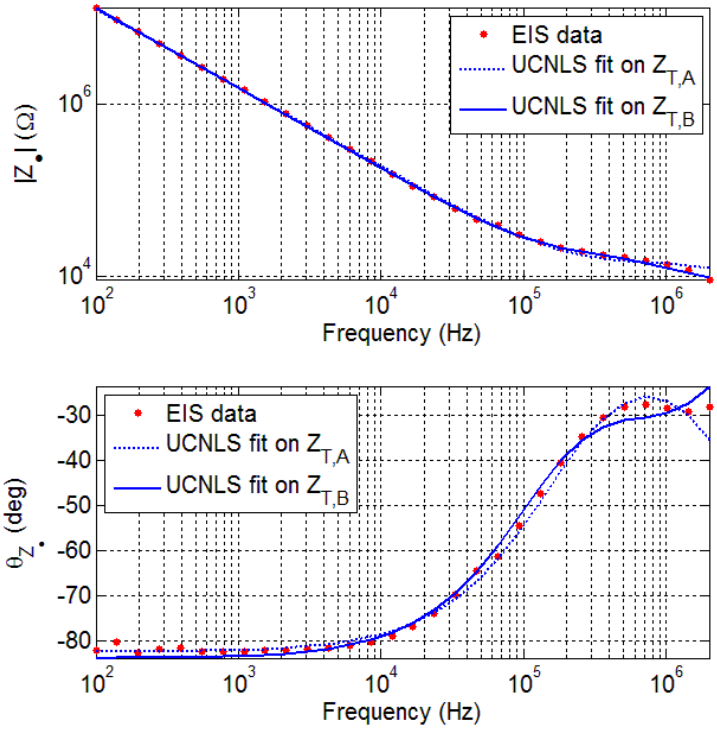

Figure 1.5-9. Comparison between $Z_{T,A}$ (1.5.2) and $Z_{T,B}$ (1.5.7) for EIS data fit.

1.6 Bibliography

[1] Bard, A.J., Faulkner, L.R., 2001. John Wiley and Sons.

[2] Wang, J., 2001. John Wiley and Sons.

[3] Borkholder, D.A., 1998. Stanford University, Stanford, CA.

[4] Geddes, L.A., 1997. Annals Biomed. Eng. 25, 1-14.

[5] Grimnes, S., Martinsen, Ø.G., 2008. Academic Press.

[6] Kovacs, G.T.A., 1994. Academic Press, 121-165.

[7] Macdonald, J.R., 1987. Wiley Interscience, John Wiley and Sons.

[8] Vladikova, D., 2004. Proceedings of Advanced Techniques for Energy Sources Investigation and Testing.

[9] Siu, W.M., Cobbold, R.S.C., 1979. IEEE Transaction on Electron Devices ED-26 (11).

[10] Onaral, B., Sun, H.H., Schwan, H.P., 1984. IEEE Transaction on Biomedical Engineering BME-31 (12).

[11] Yang, G., Long, H., Tian, H., Luo, S., Huang, H., 2008. IEEE Bioinformatics and Biomedical Engineering, 1248-1251.

[12] Carter, S.J., Linker, C.J., Turkle-Huslig, T., Howard, L.L., 1992. IEEE Transactions on Biomedical Engineering 39 (11), 1123-1129.

[13] Stoynov, Z., 1990. Electrochim. Acta 35.

[14] Franks, W., Schenker, I., Schmutz, P., Hierlemann, A., 2005. IEEE Transaction on Biomedical Engineering 52 (7), 1295-1302.

[15] Schwan, H.P., 1968. Annals of the New York Academy of Sciencesw.

[16] Gowrishankar, T.R., Weaver, J.C., 2003. Proc. Nat. Acad. Sci. 100 (6), 3203-3208.

[17] Joye, N., Schmid, A., Leblebici, Y., 2009. Neurocomputing 73, 250-259.

[18] McAdams, E.T., Jossinet, J., 1994. IEEE Transactions on Biomedical Engineering 41 (5), 498-500.

[19] Manzin, A., Boveri, C., Capra, P.P., Durbiano, F., Bottauscio, O., 2009. Sensors and Actuators B 138, 326-335.

[20] Robinson, D.A., 1968. Proceedings of the IEEE 56 (6).

[21] Newman, J., 1966. J. Electrochemical Society 113 (5), 501-502.

[22] Mirtaheri, P., Grimnes, S., Martinsen, Ø.G., 2005. IEEE Transactions on Biomedical Engineering 52 (12), 2093-2099.

[23] Macdonald, J.R., Ross, J., Potter, L.D., 1987. Solid State Ionics 24 (1), 61-79.

Chapter 2. Mesh-based modeling with the Combined Simulation System

2.1 Introduction

Microelectrodes made of noble metals, such as gold and platinum, can be used in aqueous environments [1] to investigate physics and kinetics of processes occurring in systems of biological interest [2]. As described in Section 1.2, electrochemical impedance spectroscopy (EIS) proved to be an effective tool in performing in situ investigations of charge transfer at electrochemical interfaces [3].

One of the main issue of this application is the correct interpretation of EIS measures responses due to the simultaneous presence of faradaic and non-faradaic processes. When an electric signal is applied to the electrode both these charge transport types are present and therefore the data obtained from these stimulations must be interpreted using accurate equivalent electrical circuits and strict working hypothesis (see Section 1.2.1). The equivalent electrical circuits allow to identify the contribution of each fundamental electrochemical process, such as transport of the reactive species in bulk solution, their adsorption on electrodes surface and electrochemical interfacial reactions [4]. Using equivalent electrical circuits when interpreting heterogeneous data is a widely used methodology not only in bioelectrodes characterization [5] but also when electrodes are used to perform electrical measurements on living cells [6] (see Section 5.1).

The concept of impedance network [7] is an approach to biological systems electrical response simulation that can provide noticeable insights than the use of the usual lumped parameters equivalent electrical circuits (LPEEC). With this technique the system to be simulated is subdivided into a connection of impedances whose values are determined from the electrical properties of the specific element, such as density, conductivity and dielectric constant.

The studies about propagation of electromagnetic fields in heterogeneous systems without explicitly solving three-dimensional differential equations have been introduced by Deford in 1985 [26]. The focus of these studies was the estimation of the specific absorption rate (SAR) of human bodies subjected to magnetic fields: in those works a

human body, or a section of it, is modeled as an interconnection of specific impedances with value dependent on both local electric characteristics of tissues, and interfaces between them, e.g., fat, muscles and cartilage (see Figure 2.1-1). The fundamental parameters of electromagnetic fields propagation inside the body, e.g., electric potentials, current densities and SAR, were obtained by analyzing the impedances network with Kirchhoff and Faraday's laws.

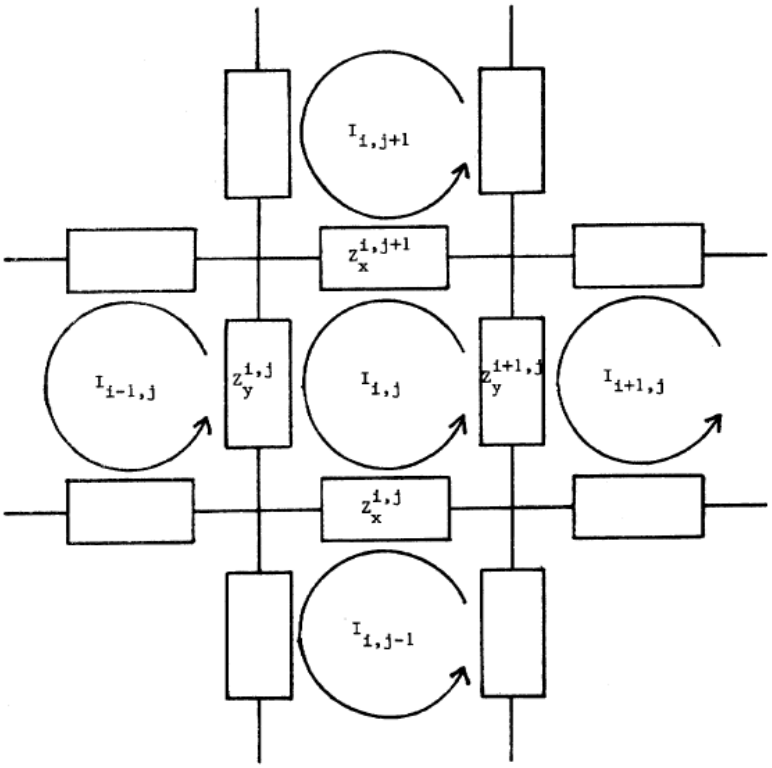

Figure 2.1-1. Mapping of a body region with a finite interconnection of impedances in the (i,j) plane. To each nodes couple corresponds an electrical impedance $Z_y^{i,j}$. The value of $Z_y^{i,j}$ depends on the electric properties of the region between node i and node j [26].

An important application of this approach is given in [8] where a single shell model of cell is meshed with a constant lattice spacing and to each mesh edge is associated an electrical circuit related to the domain it belongs to, i.e. cytoplasm, cell membrane or extracellular medium (see Figure 2.1-2). The focus of this model was the prediction of the electromagnetic field distribution around, and inside, the cell during electroporation process.

Also in this case the problem of system heterogeneity has been overcome using a finite impedances network. Three different kinds of impedances have been used: M_i and

M_e were related to cytoplasmatic region and extra-cellular region, respectively; M_m was used when an impedance connected the intra-cellular region with the extra-cellular one. In fact, this impedance consisted of two impedances similar to M_i and M_e in series to the local electric model for electroporation, where C_m is the membrane capacitance, I_m is the generator of the non-linear ionic conduction current, and the last branch models the rest potential [12].

In 2006, Smith [11] developed an in-depth theoretical study of this approach, and applied the methodology to three-dimensional simulations of cells electroporation including endoplasmatic reticuli [27] and organelles [28].

In these kinds of heterogeneous simulations, i.e., metal electrodes in contact with aqueous electrolytes or living cells electrically stimulated, arise the influence of thin layers like electrodes polarization sheets and cell membranes [9]. The numeric simulation of these systems using finite element methods algorithms often implies the use of large amounts of resources and time, and it suffers of convergence and data preconditioning issues. The Combined Simulation System (CSS) presented in this Section allows to simulate bidimensional systems with appropriate thin layers overcoming these problems by using the features of three well-known programs, i.e. COMSOL Multiphysics, MATLAB and HSPICE, and the information gathered with EIS measurements performed on Ayanda multi electrode array devices.

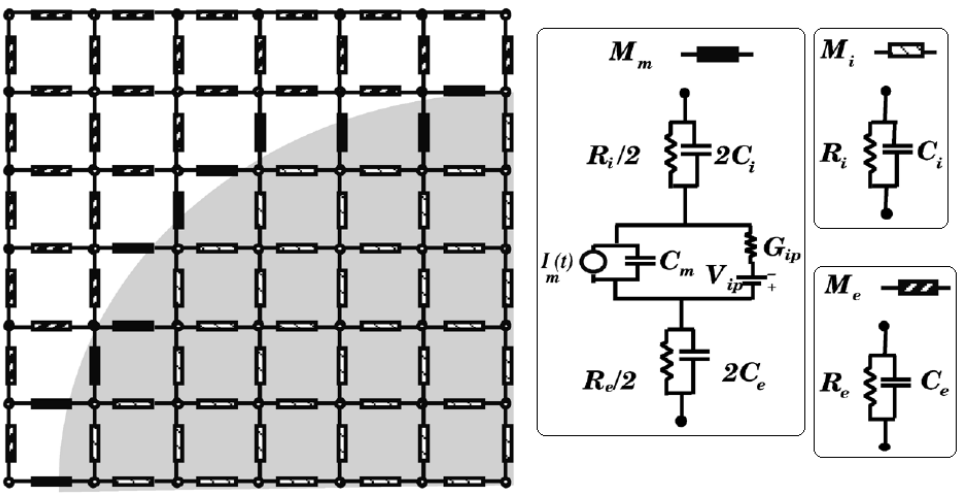

Figure 2.1-2. Impedances network for cell analysis [12].

2.2 Implementation of the Combined Simulation System

Figure 2.2-1 depicts the operational flow of the Combined Simulation System (CSS) and describes how the three commercial software, i.e., COMSOL Multiphysics, MATLAB and HSPICE, work synergically to perform the simulation of electrochemical cell electrical impedance [29].

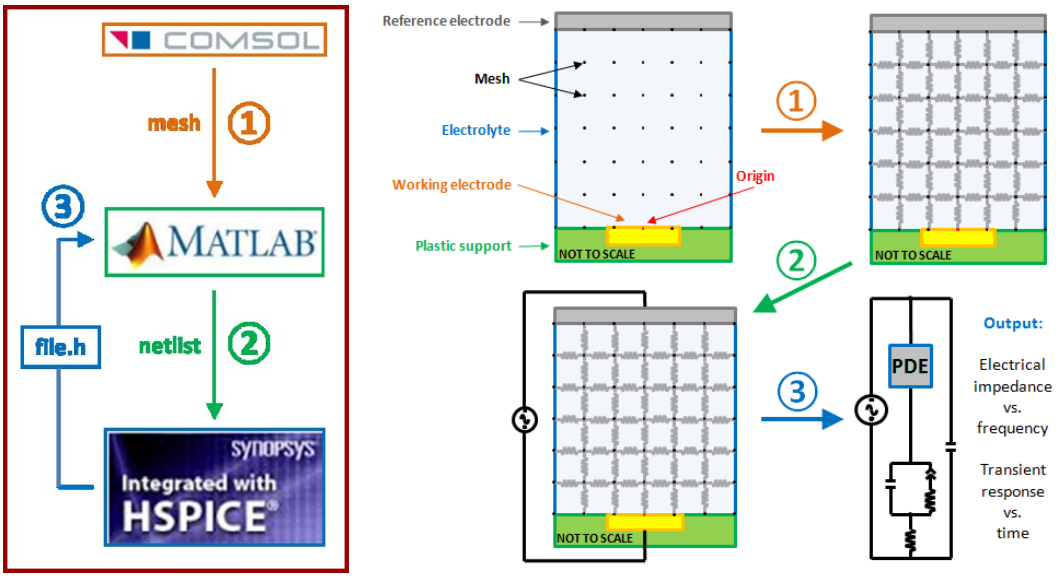

Figure 2.2-1. CSS working principle. Step 1: COMSOL is used to draw and mesh the geometry to be simulated. Step 2: MATLAB creates the netlist of the equivalent pseudo-distributed element (PDE). Step 3: HSPICE simulates the electrical response of the complete system.

With greater detail, the step 1 is focused on the design of the cross-section of the electrochemical cell to be simulated with thin layers if needed. The graphical tool of COMSOL (ver. 3.4) allows to draw the system to be simulated in a very simple and intuitive manner. Moreover, it allows to mesh the designed geometry with great control over the overall number of nodes, their distribution in the various domains and on relative boundaries, and the quality of each mesh element.

The meshing strategy adopted by COMSOL graphical tool is the Delaunay triangulation or, similarly, its dual graph, i.e., the Voronoi diagram [10] (see Figure 2.2-2): let P be a set of n points or sites, the Voronoi diagram of P is the subdivision of the plane into n regions, one for each site in P, such that the region of a site $p \in P$ contains

all points in the plane for which p is the closest site. The region of a site p is called the Voronoi cell of p. The dual graph, i.e., the Delaunay graph, has a node for every Voronoi cell, or equivalently for every site, and it has an arc between two nodes if the corresponding cells share an edge. This means that the Delaunay graph has an arc for every edge of the Voronoi graph, and therefore every mesh arc is intersected by one and only one Voronoi segment. As can be seen from Figure 2.2-2, there is a one-to-one correspondence between the bounded faces of Delaunay graph and the vertices of Voronoi one [10].

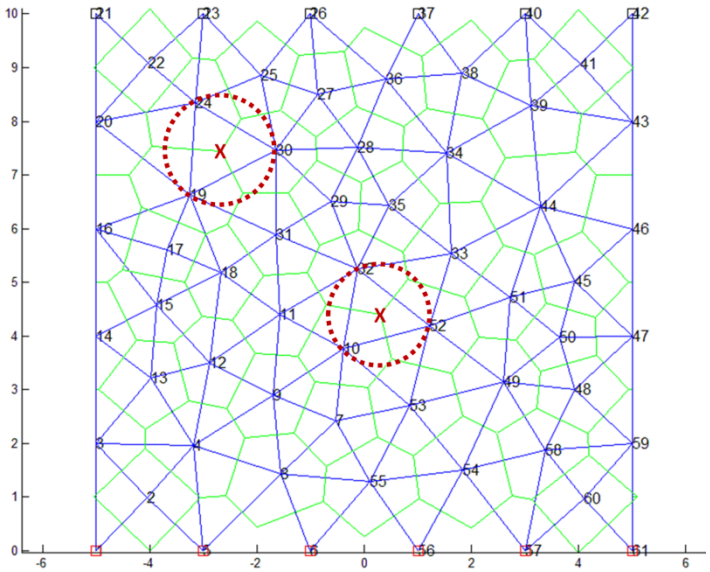

Figure 2.2-2. Example of Delaunay (blue) and Voronoi (green) graphs with nodes numeration. Red circles indicate the relationship between the two graphs, i.e., the circle circumscribed to every Delaunay triangle has the centre (red X) that corresponds to the end of a Voronoi segment

Figure 2.2-3 depicts two cell geometries that have been analyzed using the CSS: one represents a microelectrode/electrolyte/microelectrode system, where the monodimensional working electrode of length 30 μm is located at the center of the square domain lower side. The 1 mm-sided square domain simulates the electrolyte volume. The working electrode is surmounted by a 1 nm-height rectangle that represents the electrical polarization sheath. The 1 mm wide reference electrode is located at the top boundary of the square domain, i.e., 1 mm far from the working one. The second geometry consist of two concentric circles with radius 5 μm and 5 μm + 1 nm respectively, i.e., the classical single shell model for a suspended living cell [6] with

membrane thickness of 1 nm. Here, the working and reference electrodes are the upper and the lower boundary. From Figure 2.2-3 it can be observed that the mesh density underlines the presence of noticeable elements like the microelectrodes or the suspended cells, because the distance between the mesh nodes is a function of the local aspect ratio with respect to the total dimensions. This means that mesh density tends to increase where the geometry exhibits elements smaller than 1/10 of the biggest domain dimension.

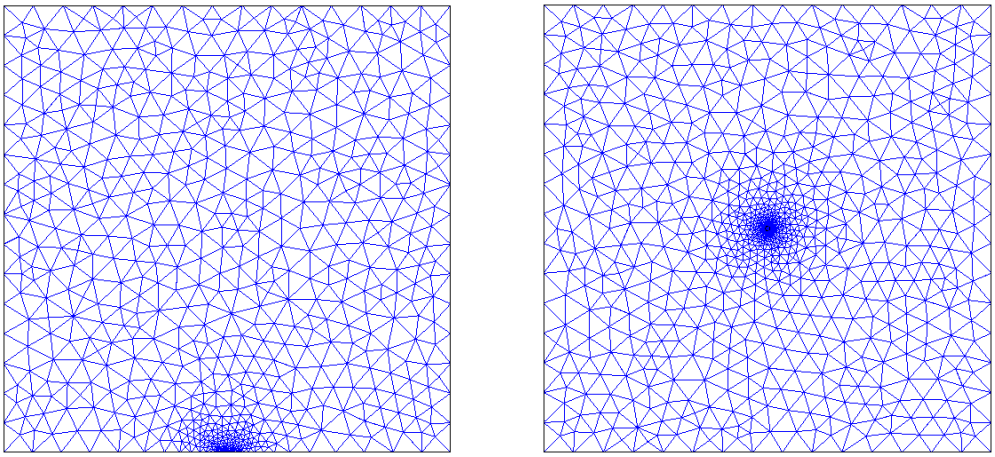

Figure 2.2-3. Example of geometries simulated with the CSS: microelectrode/electrolyte/microelectrode (left) and suspended single cell (right).

Figure 2.2-4 describes how the CSS manages the presence of thin layers: the main assumptions is to simulate thin layers as a single stage of equivalent electrical impedances, and therefore these domains have to be excluded from meshing process. This is accomplished by identifying the boundaries of the thin layers, mesh them with a single vector of nodes and then creating a one-to-one relationship between nodes lying on opposite boundaries. In this way, COMSOL effectively generates the mesh only for broader domains and all the related geometrical information are translated into MATLAB environment, where the complete geometrical mesh is recreated.

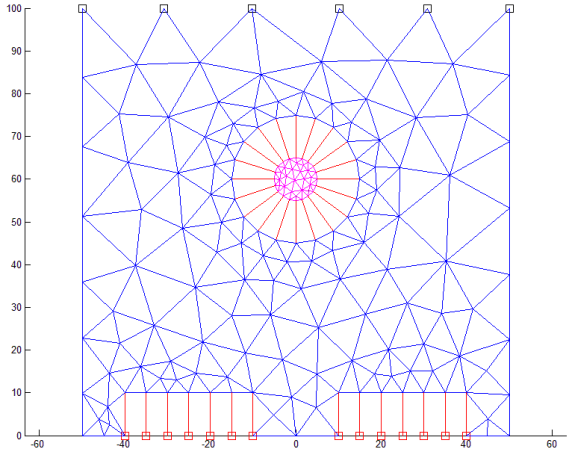

Figure 2.2-4. Example (not to scale) of CSS application to suspended cell simulation. Blue mesh is for extra-cellular medium, magenta is for cytoplasm, red for thin layers, i.e., cell membrane and electrodes polarized interface (with exaggerated size). Electrical stimuli are applied between red (working) and black (reference) squares.

During step 2, MATLAB (MathWorks, 2007) performs the visit of the geometrical mesh as an interconnected graph, in order to translate the geometrical information into electrical circuits: the system associates each mesh arc with a specific user-defined electrical impedance, in order to generate the netlist of a mesh-based pseudo-distributed equivalent electrical circuit, i.e., the Pseudo-Distributed Element (PDE). This task is accomplished through a number of custom data structures that have been implemented to manage all the different aspects of the mesh visit.

- The first data structure is called “acquiredMesh” and it collects all the geometrical information related to each mesh node provided by COMSOL at the end of the meshing process, e.g., vector of spatial coordinates and related domain.
- The second data structure is called “path” and describes the mesh visit performed by MATLAB. This visit has the main rule that each arc can be crossed one and only one time: this restriction is fundamental because the visit is the core of the netlist generation, where between two nodes can exists one and only one equivalent electrical impedance. In this data structure are stored information related to the interconnection of each mesh node with the others, e.g., nodes reachable from the current one and domain of each starting arc. These information can be derived using several custom routine that determine, for example, if an arc has already been

visited, if a node lies on the geometry edge or if an arc connects two equipotential nodes, i.e., two nodes both lying on the same working or reference electrode boundaries. In the latter case, the impedance can be excluded from the netlist because no current will flow between two nodes at the same potential.

- The information related to equipotential nodes are stored in the third data structure called “inOutTable”. This structure simplifies the implementation of the working and reference electrodes, by enabling the use of effective HSPICE functions for stimulation nodes.
- The fourth data structure is called “bones” and stores information related only to those arcs that have been visited once, like starting and ending nodes and relative domains. This means that the data structure is strictly related to all the electrical impedances that will constitute the equivalent electrical circuit.
- The fifth data structure is called “modelsIndex” and stores the information related to each domain of the geometry. In more detail, it contains the information related to the electrical impedance associated to each domain, e.g., topology and type of electric elements, both passive and active. Different kinds of equivalent impedances are stored in a “library” routine from which “modelsIndex” can quickly recall all the information. For example, the Fragment 2.2-1 taken from “library” routine, describes the impedance model param_TH_prc. This model is a parallel between a resistor and a capacitor used inside a thin layer: the parameter n indicates the number of nodes resulting from the meshing of the thin layer boundaries. The values of the resistor and the capacitor can be directly specified by the user, while n is an hidden parameter because it will be evaluated by the CSS during the visit of the mesh.

```
case 'param_TH_prc'
    model.script{1,1} = '.SUBCKT param_TH_prc in out res1=1e3 cap1=1e-12 n=1';
    model.script{2,1} = 'R1 in out ''res1/n''';
    model.script{3,1} = 'C1 in out ''n*cap1''';
    model.script{4,1} = '.ENDS';

    model.param.visible{1,1} = 'res1';
    model.param.visible{2,1} = 'cap1';
    model.param.hidden{1,1} = 'n';
```

Fragment 2.2-1. Example of parallel between divided impedances.

- The sixth data structure is called “bodyNet” and contains text lines that implements HSPICE netlist codes. By using the information stored in “mesh” and “bones”, the geometrical mesh data are translated into an electrical circuit: the mesh nodes become electrical nodes, while mesh arcs become electrical impedances. Each domain can have a different impedance topology, and the values of the electrical parameters can be either specified by the user or determined by the CSS using specific mathematical functions (see Section 2.3).
- The last data structure is defined “dotsTable” and provides an effective map of all the nodes adjacent to the selected one. This structure is widely used when the impedance models specified for a domain rely on some geometrical parameter for the definition of the electrical elements, e.g., the Euclidean distance between two adjacent nodes. For example, the extracellular medium and the cytoplasm domains are typically simulated using parallels between resistors R and capacitors C, automatically evaluated using [11]:

$$R = \frac{1}{\sigma}\frac{l}{A} \quad , \tag{2.2.1}$$

$$C = \varepsilon_0 \varepsilon_r \frac{A}{l} \quad , \tag{2.2.2}$$

where σ and ε_r are the domain conductivity and relative permittivity, respectively, l is the mesh arc length and A = d·v is the local area between the two arc nodes, with d depth of the simulated system and v length of the Voronoi segment that intercepts the mesh arc. Fragment 2.2-2 shows how these relationships can be easily implemented into electrical impedances using HSPICE.

```
case 'param_prc'
    model.script{1,1} = '.SUBCKT param_prc in out sigma1=1 epsr1=1 d=1 v=1 l=1';
    model.script{2,1} = 'R1 in out ''d/(sigma1*l*v)''';
    model.script{3,1} = 'C1 in out ''eps0*epsr1*l*v/d''';
    model.script{4,1} = '.ENDS';

    model.param.visible{1,1} = 'sigma1';
    model.param.visible{2,1} = 'epsr1';
    model.param.hidden{1,1} = 'd';
    model.param.hidden{2,1} = 'v';
    model.param.hidden{3,1} = 'l';
```

Fragment 2.2-2. HSPICE implementation of an electrical model with parameters dependent on mesh local features.

In the last step of the CSS processing, the equivalent complete circuit is simulated using HSPICE (Synopsys, 2003) both in time and frequency domain. The type of analysis is selected from MATLAB interface: the transient analysis (see Fragment 2.2-3) uses a sinusoidal input with adjustable frequency, while the frequency analysis (see Fragment 2.2-4) simulates the electrochemical impedance spectroscopy measurements.

```
%%%%%%%TRANSIENT%%%%%%%%%%%%%%%%
bodyTran{1,1} = '* TRANSIENT ANALYSIS';
bodyTran{2,1} = '*--------------------------------------*';
bodyTran{3,1} = '.PARAM eps0 = 8.854187817e-12';
bodyTran{4,1} = ['.PARAM freq = ' num2str(testFreqs(1,1),'%10.5e')];
bodyTran{5,1} = '.TRAN DATA=sweep_param';
bodyTran{6,1} = '.DATA sweep_param';
bodyTran{7,1} = 'TIME';
```

Fragment 2.2-3. HSPICE syntax for transient analysis. The transient simulation time can be defined through the variable sweep_param.

```
%%%%%%%AC%%%%%%%%%%%%%%%%
bodyAC{1,1} = '* AC ANALYSIS';
bodyAC{2,1} = '*--------------------------------------*';
bodyAC{3,1} = '.PARAM eps0 = 8.854187817e-12';
bodyAC{4,1} = ['.AC DEC ' int2str(noppd) ' ' int2str(fStart) ' ' int2str(fStop)];
temp{1,1} = '*--------------------------------------*';
```

Fragment 2.2-4. HSPICE syntax for frequency analysis. The frequency range can be defined using fStart and fStop variables for boundaries and noppd variable for the number of points per decade.

2.3 Mathematical modeling of electrical impedance local variations

As stated in Section 2.2, the parameters values of the Pseudo-Distributed Element (PDE) equivalent electrical impedances, e.g., basic resistors and capacitors, are not fixed a priori but are determined using specific mathematical functions. These functions are evaluated from a fitting of EIS data using suitable equivalent models, and thanks to these functions two goals can be achieved:

- the independence of the CSS model from the third spatial dimension, i.e., no need to using the depth of the electrochemical cell as a simulation parameter [8, 12];
- understanding the local variations of system electrical impedance, i.e., the variation in equivalent electrical parameters is determined for each mesh arc, starting from the origin of the simulation axes (see Figure 2.2-1).

Figure 2.3-1 shows an example of mesh density impact on CSS result, by comparing it to COMSOL result for the same simulated geometry. This geometry is similar to that describes in Figure 2.2-3, with a single ideal microelectrode with dimensions 30 µm x 15 µm, in contact with a parallelepiped having the same electrical properties of common saline solution, i.e., σ = 1.2 S/m and ε_r = 72.3 F/m [12], and dimensions 1 mm x 1 mm x 15 µm. A simple parallel between resistor and capacitor has been considered as the basic equivalent electrical circuit for the electrolyte PDE, i.e., purely low-pass behavior, and no thin layers have been taken into account for this example. The result shows that by increasing the mesh density, the CSS impedance response is more similar to COMSOL one: having a geometry of 1 mm^2 and about $10x10^3$ mesh elements, the difference between CSS and COMSOL impedance at the cut-off frequency is about 3 %.

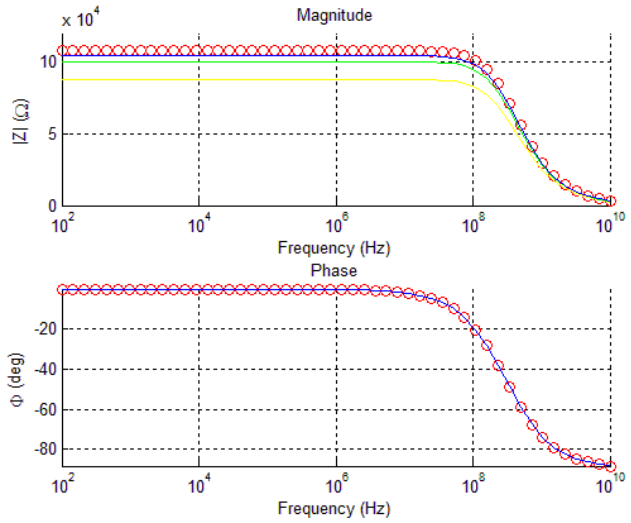

Figure 2.3-1. Effect of mesh density on CSS simulation accuracy with respect to COMSOL (red circles). Mesh composed by 52 elements (yellow), 988 elements (green) and 10636 elements (blue). The percentage difference with COMSOL al low frequency impedance magnitude is 18.5 %, 7 % and 3 %, respectively.

One of the main important parameters of Figure 2.3-1 simulation is the depth of the electrochemical cell, i.e., the size of the system along the orthogonal direction to the plane of the drawn cross-section (see Figure 2.2-1). COMSOL uses this information as a condition to solve its finite-element equations, and therefore this can be improperly used as a simulation parameter if the simulated geometry is a bidimensional cross-section [11]: Figure 2.3-2 shows the influence of the system depth on its electrical impedance.

The CSS provides an electrical simulation of the complete system starting from a bidimensional representation of electrochemical cell cross-section, without the explicit request of the system depth. This is made possible thanks to specific EIS measurements and to appropriate fitting processes, that generate mathematical laws describing the local impedance variation with the bidimensional Euclidean distance from the working electrode as only parameter.

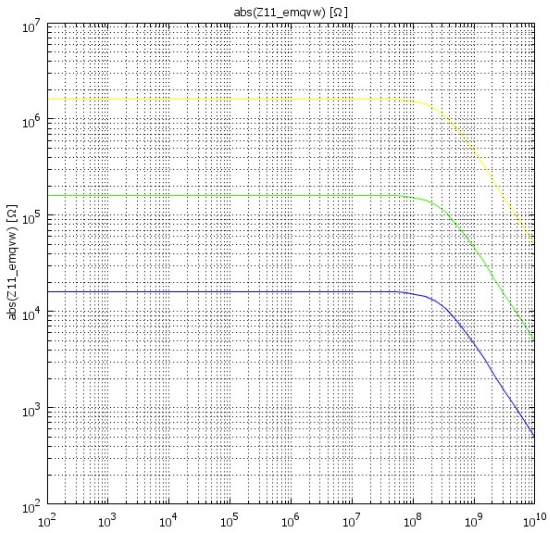

Figure 2.3-2. Effect of cell depth as a COMSOL simulation parameter for electrode/electrolyte system: 1 µm (yellow), d = 10 µm (green), d = 100 µm (blue).

To investigate the modifications of the local electrical impedance with distance between working and reference electrode, Ayanda MEA60 100 Au microelectrodes arrays have been used (see Figure 2.3-4).

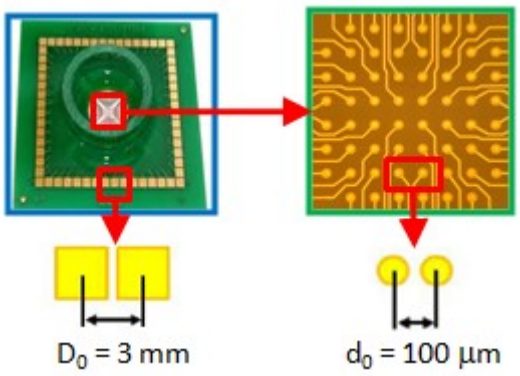

Figure 2.3-4. Ayanda MEA60 100 Au with center-to-center pads distance D0 (left) and the relative microelectrodes matrix with center-to-center microelectrodes distance d0 (right).

Each MEA circular microelectrode has a radius re of 15 µm and a chamber volume of about 1500 µL. Sodium chloride (NaCl) 100 mM and redox mediator potassium ferrocyanide have been used to produce stock solutions of 1 mM $Fe(CN)_6^{4-/3-}$ in NaCl 100 mM.

This electrolyte has been measured with MEA using electrochemical impedance spectroscopy (EIS) technique (see Section 1.2). The electrochemical cells were two kinds

of bipolar set-up: one set-up had MEA microelectrodes as working electrode and different types of external reference electrodes, i.e., silver/silver chloride (Ag/AgCl), 2 mm diameter gold disk or 25 μm diameter gold microdisk. The other set-up had MEA microelectrodes as both working and reference electrodes.

The main steps of the electrochemical characterization process can be summarized as:

- EIS measurements on microelectrodes using external reference electrodes;
- EIS measurements using microelectrodes as both working and reference electrodes;
- evaluation of the electrolyte PDE mathematical laws;
- mathematical laws implementation in the CSS and simulation.

In order to characterize the microelectrode/electrolyte interface, EIS measurements have been carried out on gold microelectrodes using Ag/AgCl external reference electrode and stock solution of 1 mM $Fe(CN)_6^{4-/3-}$ in NaCl 100 mM. This reference electrode has been chosen due to its non-polarizable features [13] that lead to moderate effects on system electrical impedance. EIS stimulation voltages have been set to 235 mV and 10 mV of bias and amplitude, respectively: the former values corresponds to the formal redox potential of the ferri/ferrocyanide couple with respect to Ag/AgCl reference electrode [14], while the latter ensures to keep the system in the linear response domain [3, 15]. The resulting data are shown in Figure 2.3-5: from this figure can be seen that the usual spreading resistance formula for circular electrodes [16] (see Section 1.3), i.e.,

$$R_s = \frac{1}{4\sigma_e r_e} \quad , \tag{2.3.1}$$

is equal to 13.35 kΩ, with r_e microelectrode radius and σ_e = 1.248 S/m electrical conductivity of NaCl 100 mM obtained using the classical approach of conductivity factors [17], is in good agreement with the high frequency value of impedance magnitude.

The same solution has been measured with other two different external reference electrodes, i.e., a gold disk of 2 mm diameter and a gold microdisk of 25 μm diameter, and the resulting data are shown in Figure 2.3-5. As can be seen, the response obtained with the 2 mm diameter gold electrode is comparable with that of the silver-silver chloride reference electrode due to its large exposed metal area [14]. The results

obtained with the 25 μm diameter gold microdisk, that is a dimension comparable to the working electrode, are similar in shape but shifted toward higher impedance magnitudes: this shift can be related to the reference electrode interfacial impedance that become no more negligible [18].

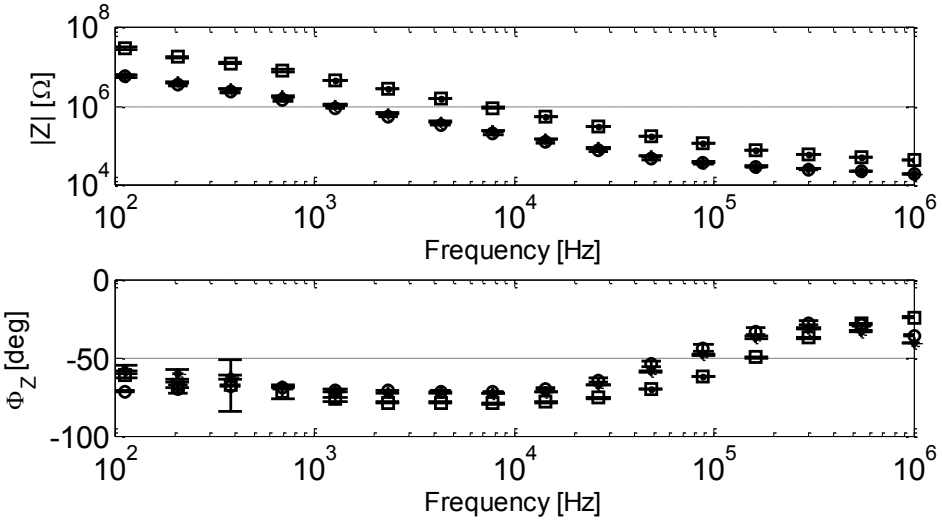

Figure 2.3-5. EIS measurements of stock saline solution (1 mM $Fe(CN)_6^{4-/3-}$ in NaCl 100 mM) with working microelectrode and as reference electrode: Ag|AgCl|KCl 1M (o), 2 mm diameter gold disk (*) and 25 μm diameter gold microdisk (□).

A common lumped-parameters equivalent electrical circuit (LPEEC) used for simulate the electrical response of this kind of EIS measurements is sketched in Figure 2.3-6 (a) [19]: it is composed of the electrolyte spreading resistance R_s, the constant phase element (CPE) with frequency (f)-dependent electric impedance $Z = C_W(j2\pi f)^{-n}$ (see Section 1.3) [5] that accounts for interfacial electrochemical process at microelectrode surface, and the stray capacitance C_p that includes device parasitic effects [20, 21]. Its transfer function, as a function of the angular frequency $\omega = 2\pi f$, can be written as (see Section 1.4)

$$Z_a(\omega) = \frac{1 + (j\omega)^n R_s C_w}{(j\omega)^n C_w \left[1 + (j\omega)^{1-n} \frac{C_p}{C_w} + j\omega R_s C_p\right]} \quad . \tag{2.3.2}$$

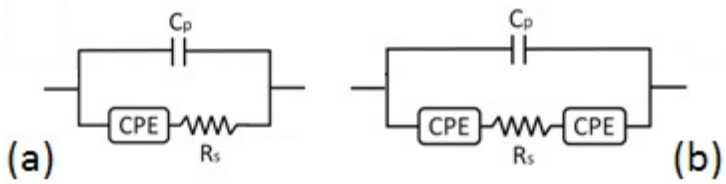

Figure 2.3-6. Equivalent electrical circuits used for EIS data modeling: Ag/AgCl reference electrode (a) [19] and gold reference microelectrode (b) [22].

Equation (2.3.2) describes the behavior of the electrochemical interface generated at a single microelectrode in contact with the stock solution. In order to determine the impedance variations laws as a function of the distance from the working electrode, the electrolyte has been measured using several couples of microelectrodes with different inter-electrodes distances, using the MEA electrode matrix (see Figure 2.3-4). EIS measurements results are shown in Figure 2.3-7, where can be seen that the impedance magnitude increases as the inter-electrode distance increases. Moreover, the impedance magnitude of these EIS data sets always collocates between a lower bound, obtained with Ag/AgCl external reference electrode, and an upper bound, obtained with gold microdisk reference electrode [18].

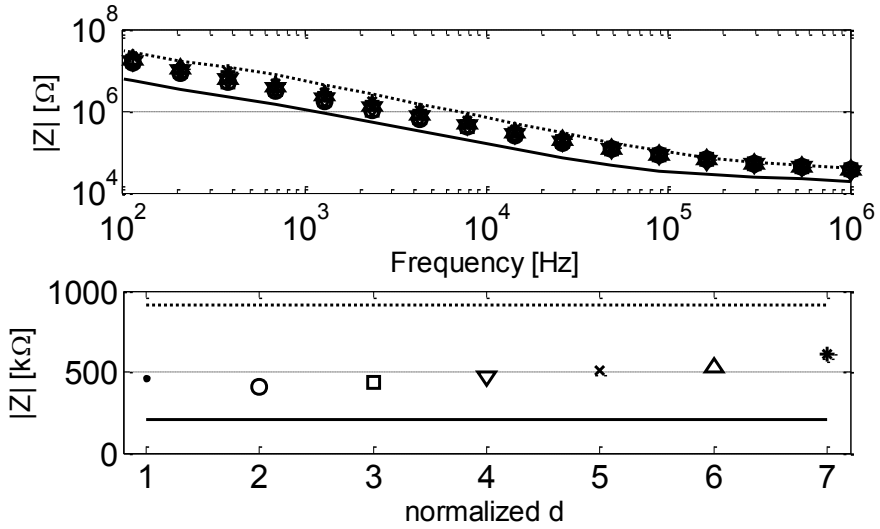

Figure 2.3-7. EIS measurements of microelectrode vs. microelectrode at different inter-electrodes distances: $1d_0$ (·), $2d_0$ (○), $3d_0$ (□), $4d_0$ (▽), $5d_0$ (x), $6d_0$ (Δ), $7d_0$ (*). Straight and dotted lines represents EIS measurements of microelectrode vs. Ag/AgCl and 2 mm-diameter gold disk reference electrode, respectively (upper). EIS data showed at 8 kHz (lower).

EIS data sets of Figure 2.3-7 have been fitted using the LPEEC of Figure 2.3-6 (b): this LPEEC [22] is very similar to the one introduced for the external reference electrodes measurements, but introduces a second microelectrode/electrolyte interface. As described in Section 1.4, its transfer function can be written as

$$Z_b(\omega) = 2\frac{1+\frac{(j\omega)^n}{2}R_sC_w}{(j\omega)^nC_w\left[1+2(j\omega)^{1-n}\frac{C_p}{C_w}+j\omega R_sC_p\right]} \quad . \qquad (2.3.3)$$

As can be seen from the comparison between (2.3.2) and (2.3.3), the presence of a second CPE causes an increase in the measured impedance magnitude with respect to the Ag/AgCl reference electrode data set.

The EIS measurements for microelectrodes couples have been fitted using (2.3.3) and the results of the fitting process are depicted in Figure 2.3-8 for the four LPEEC parameters: as can be seen, the stray capacitance C_p can be considered constant as d varies with low standard deviation (2.9 %), C_W decreases in linear fashion (goodness of fit parameter R^2 = 0.9674) as the inter-electrode distance increases and n exhibits an opposite behavior, i.e., it grows with a power trend (R^2 = 0.9951). The electrolyte resistance Rs has been fitted with the sum of two exponential (R^2 = 0.918), in order to match parameter values trend of a rapid increase followed by a plateau as the distance between electrodes increases, obtaining the interpolation function R_s^*.

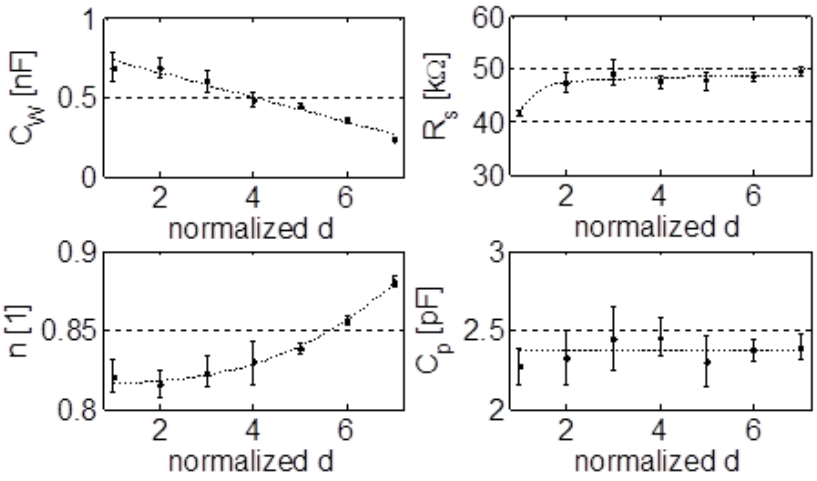

Figure 2.3-8. Behavior of Figure 2.3-6 (b) LPEEC fitted parameters as a function of normalized inter-microelectrodes distance d/d_0. Dotted lines indicates mathematical fit.

At the end of the fitting process, the mathematical incremental laws for PDE implementation have been deduced from the behavior of electrolyte LPEEC R_s as a function of inter-electrode distance d, as depicted in Figure 2.3-8. The main hypothesis is that this trend of variation is still valid even at local level, enabling a differential analysis suitable for mesh application.

The classical Euclidean distance from the center of the working electrode $P_0(x=0,y=0)$ of two given mesh points $P_1(x_1,y_1)$ and $P_2(x_2,y_2)$ is defined as $l_1 = (x_1^2+y_1^2)^{0.5}$ and $l_2 = (x_2^2+y_2^2)^{0.5}$. The CSS implements a basic dipolar LPEEC between P_1 and P_2 that must have the same topology of the complete LPEEC: in this example, as can be seen from Figure 2.3-6, the local LPEEC will be a single resistor ΔR_s. The functions for $\Delta R_s(l_1,l_2)$ have been at first imposed to have the same structure of $R_s(d)$, i.e.,

$$\begin{aligned}\Delta R_s(l_1,l_2) &= k[R_s^*(l_2) - R_s^*(l_1)] = \\ &= k\left[\left(ae^{bl_2} + ce^{dl_2}\right) - \left(ae^{bl_1} + ce^{dl_1}\right)\right] ,\end{aligned} \tag{2.3.4}$$

where $l_1 < l_2$ and a, b, c, d and k are numeric coefficients evaluated from fitting process.

By implementing Eq. (2.3.4) in the CSS as described in Section 2.2, PDEs are created as networks of local LPEEC with parameter ΔR_s that is function of the Euclidean position in the mesh with respect to the center of the working electrode, conventionally considered as origin of the Euclidean axis: Figure 2.3-9 depicts the simulation environment for this example, i.e., a cross-section of MEA devices chamber.

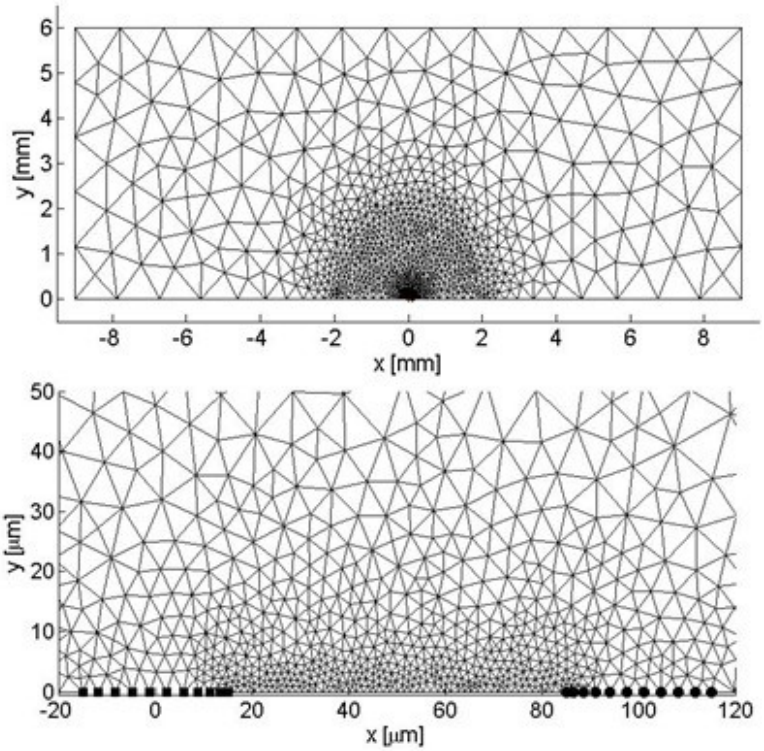

Figure 2.3-9. Mesh of simulated domain: cross-section of MEA chamber (upper); zoom in the working (□)/reference (o) electrodes area for d = d_0 (lower).

The electric parameter R_s in the LPEEC of Figure 2.3-6 (b) can be therefore substituted with a PDE. The values for the electrolyte resistance obtained from the simulation of the resulting circuit are shown in Figure 2.3-10. The picture also describes the percentage difference between the values for R_s obtained with the LPEEC fitting approach and the ones simulated using the PDE, by using the following formulation:

$$\varepsilon_{R_s} = 100 \frac{R_{s,LPEEC} - R_{s,PDE}}{R_{s,LPEEC}} . \qquad (2.3.5)$$

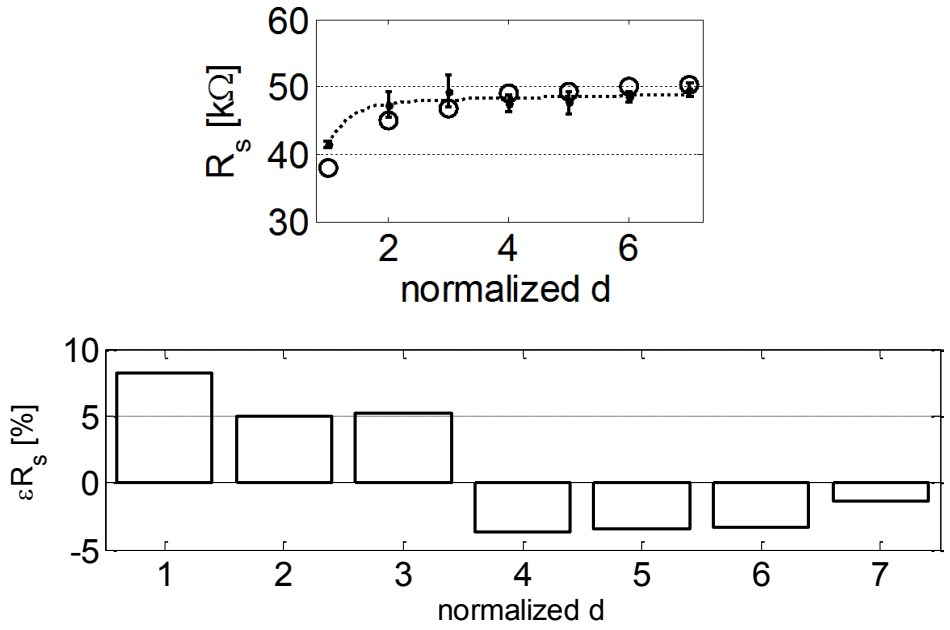

Figure 2.3-10. Values for Rs obtained from LPEEC fit (·) and from PDE simulation using (2.3.4) (o) (upper). Percentage difference εR_s between R_s values determined with LPEEC and PDE approach (lower).

The approximated incremental function (2.3.4) leads to an overall PDE electrical impedance that slightly deviates from LPEEC fitting results (see Figure 2.3-10). The deviations εR_s introduced by CSS approximated incremental law cause a variation in the goodness of EIS measurements fit.

To assess this impact [23], the normalized residual sum of squared errors (NRRS) has been evaluated for LPEEC and PDE fit of Figure 2.3-7 EIS data. The NRRS has been evaluated by applying the error function (1.5.6) on the residual sum of squared errors normalized to the maximum residual of each observation. The results of this evaluation are shown in Figure 2.3-11, from which can be seen that the goodness of fit of the two approaches is comparable even with εR_s variations.

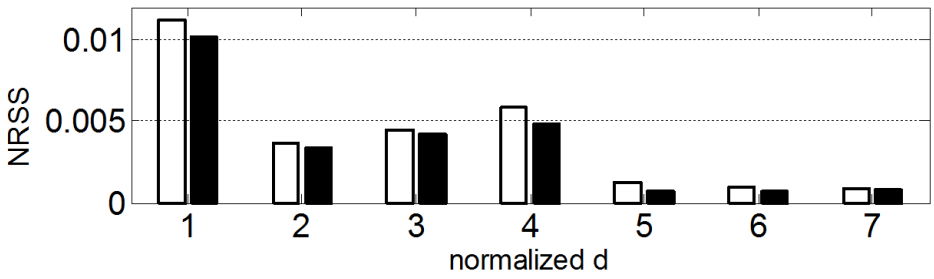

Figure 2.3-11. Normalized residual sums of squared errors for LPEEC (empty bars) and PDE (filled bars)-based fitting process of Figure 2.3-7 EIS data.

Recalling the mesh density influence over impedance response (see Figure 2.3-2), CSS time performance have been evaluated through the simulation of the geometry of Figure 2.3-9 with different mesh densities, i.e., with different numbers of mesh elements. The number of triangular mesh elements is strictly related to the number of basic LPEEC of PDEs, because to each mesh edge corresponds a single basic LPEEC (see Section 2.2). CSS solving time has been compared to COMSOL (AC/DC Module, In-plane electric currents, UMFPACK solver) one for the same simulated geometry. Figure 2.3-12 depicts the outcome of this comparison: as mesh density increases, CSS overall solving time is from 80 to 25 % lower than COMSOL one.

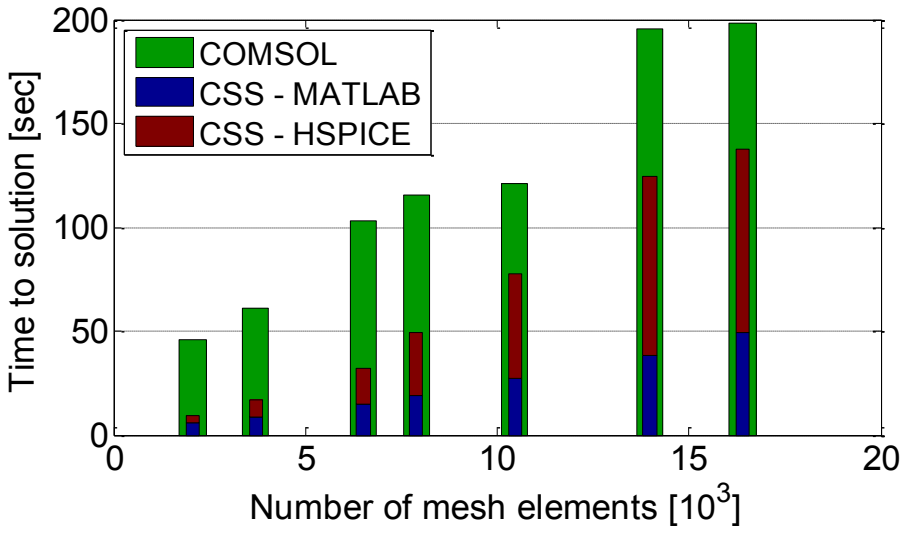

Figure 2.3-12. CSS time performance compared to COMSOL (green bars) as a function of mesh density. CSS solving time has been subdivided into two contributions, one related to mesh processing and netlist creation (blue bars), and the one related to electrical simulation (red bars).

2.4 Example of CSS application

In this section, a complete CSS application will be presented [30]. The simulation process is similar to that introduced in Section 2.3. Moreover, it will be described how the CSS is able to manage the measurement bench parasitic elements.

2.4.1 Experimental set up and modeling of parasitic elements

The experimental set up for this example is similar to that described in Section 2.3. The test devices are Ayanda MEA60 100 Au microelectrodes arrays with minimum inter-electrode distance d_0 = 100 μm and minimum inter-pad distance D_0 = 3 mm. EIS measurements have been performed on microelectrodes matrix using a Solartron SI 1260 Impedance Gain/Phase Analyzer. The electrochemical cells consist of: MEA working microelectrode versus silver/silver chloride reference electrode (CH111, CH Instruments), and MEA microelectrodes as both working and reference electrodes. Micro-positioned conductive probes (Wentworth Laboratories) have been used to contact MEA external pads. Both have been connected to Solartron front-end by standard 95 cm length, 50 Ω BNC connectors (Pomona). A standard solution ASTM D1125 (electrical conductivity σ_e = 0.141 S/m at 25 °C) has been used for EIS measurements.

For CSS implementation the following software has been used: MATLAB 2009 (MathWorks), COMSOL Multiphysics 3.4 and HSPICE 2003 (Synopsys). All simulations have been processed by an HP Pavilion dv6 notebook with AMD Phenom II N620 Dual-Core Processor 2.80 GHz and 4 GB RAM. Lumped-parameters equivalent electrical circuit (LPEEC) fit analysis have been performed using ZVIEW 2.80 (Scribner Associated), with "Data-modulus weighting" option. The simulation domain is the MEA cross-section depicted in Figure 2.3-9.

In order to evaluate the short-circuit parasitic elements [24], EIS measurements have been performed after short-circuiting the microprobes. The resulting Bode diagram is shown in Figure 2.4-2. From this figure can be seen that the self-inductive behavior of

leads impedance starts from about 10 kHz. These data are well fitted by the equivalent electrical circuit of Figure 2.4-1 (a) [25], that consists of a series between a resistor R_S = 0.24 Ω (fitting error: 0.39 %) and an inductance L_S = 1.14 μH (fitting error: 0.74 %).

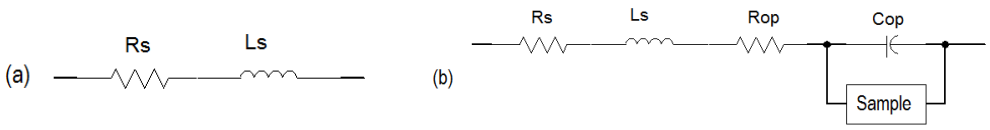

Figure 2.4-1. Short-circuit parasitic LPEEC (a). Structure of LPEEC with both short-circuit and empty-chamber parasitic elements (b). The "Sample" box contains LPEEC of measured systems.

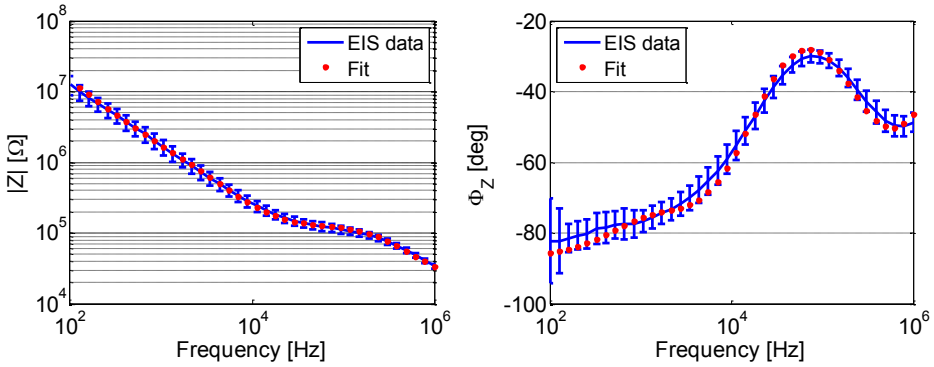

Figure 2.4-2. EIS measurements of short-circuited system with fit obtained from Figure 2.4-1 (a) circuit.

The open-circuit parasitic elements [21] have been evaluated by performing high frequency EIS measurements, i.e., in the 100 kHz – 1 MHz range, on empty MEA devices using microelectrodes as both working and reference electrode. During the measurements, different combinations of distances d and D have been tested, according to devices interconnection patterns, obtaining in this way a map of the open-circuit electric impedance of the system as a function of the inter-electrodes distance d and inter-pads distance D. Figure 2.4-3 depicts an example of EIS data obtained by measuring d = d_0 microelectrodes couples and varying the position of the microprobes along the external connection pads. These sets of electrical impedances Z have been fitted using the LPEEC described in Figure 2.4-1 (b): this circuit takes into account the previously determined short-circuit parameters along with the open-circuit ones, i.e., the resistor R_{op} and the capacitance C_{op} [24] (see Section 1.5).

The empty chamber impedance sensed by microelectrodes couples has been approximated with a single capacitor C_{air}. Values for C_{air} have been determined using COMSOL three-dimensional simulations (AC/DC module, in-plane electric currents): in this case the simulated domain consists of a cylinder of air (electrical conductivity σ_{air} = $5 \cdot 10^{-15}$ S/m, permittivity ε_{air} = 1) with a couple of 30 μm-diameter microelectrodes with variable inter-electrodes distance d on the lower base (see Figure 2.4-4). Table 2.4-1 indicates C_{air} values as a function of d obtained from simulations.

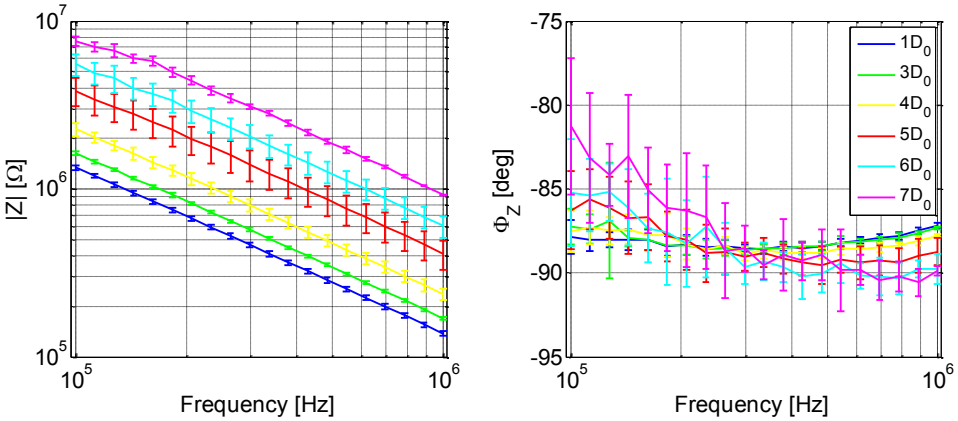

Figure 2.4-3. Empty-chamber EIS measurements as a function of D (d = d_0).

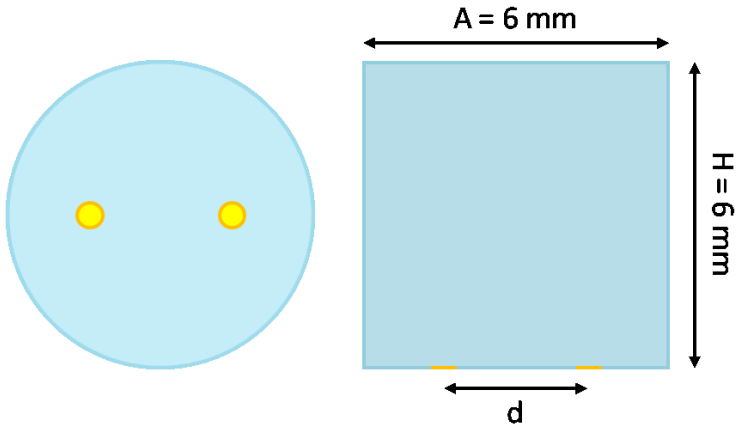

Figure 2.4-4. Schematization of the domain for empty-cell simulation and fitting (left: bottom view, right: front view).

Simulated d	$1d_0$	$2d_0$	$3d_0$	$4d_0$	$5d_0$	$6d_0$	$7d_0$
C_{air} [fF]	0.2862	0.2718	0.2674	0.2653	0.2642	0.2630	0.2652

Table 2.4-1. Simulation results of empty-chamber capacitance.

By fitting empty-cell EIS data using the LPEEC of Figure 2.4-1 (b) and the values for C_{air} listed in Table 2.4-1, it has been possible to determine a distribution of open-circuit equivalent electrical parameters values as a function of d and D (see Figures 2.4-5 and 2.4-6). The analytical functions for C_{op} and R_{op} have been obtained using MATLAB Surface Fitting Toolbox and can be expressed as polynomial sums as follows:

$$P = \begin{bmatrix} p_{00} & p_{01} & p_{02} \\ p_{10} & p_{11} & p_{12} \end{bmatrix} , \tag{2.4.1}$$

$$Q = \begin{bmatrix} 1 & D & D^2 \\ d & d \cdot D & d \cdot D^2 \end{bmatrix} , \tag{2.4.2}$$

$$S = \mathrm{sum}\big(\mathrm{sum}(PQ)\big) . \tag{2.4.3}$$

where P is a 2-by-3 numerical coefficients matrix, Q is a 2-by-3 distances matrix and S = {C_{op}, R_{op}}. With the coefficients P listed in Table 2.4-2 the goodness of fit indicator R^2 for C_{op} is 0.9493 and for R_{op} is 0.8665.

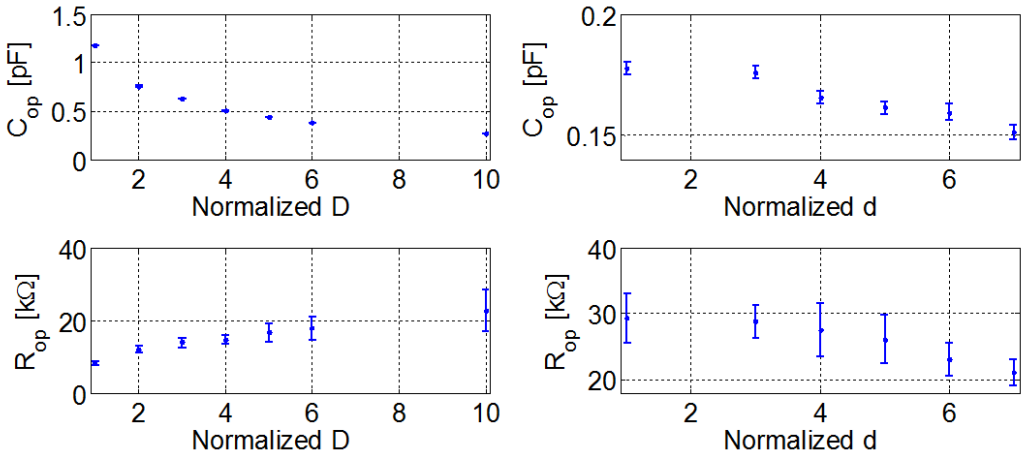

Figure 2.4-5. Example of empty-chamber parasitic elements behavior as a function of D over D_0 with d = 2d_0 (left), and as a function of d over d_0 with D = 15D_0 (right).

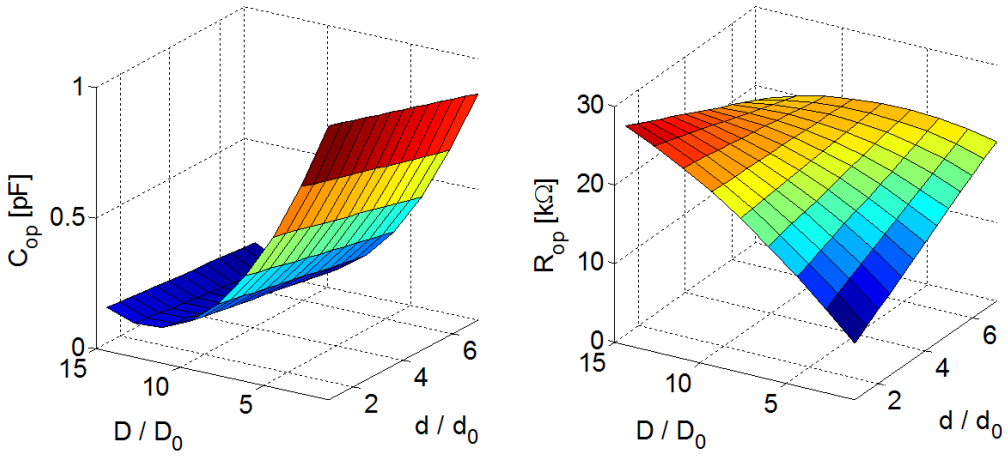

Figure 2.4-6. Empty-chamber parasitic elements of Figure 2.4-1 (b): C_{op} (left), R_{op} (right).

Coefficient	p_{00}	p_{01}	p_{02}	p_{10}	p_{11}	p_{12}
C_{op}	$1.2 \cdot 10^{-12}$	$-6.1 \cdot 10^{-11}$	$8.4 \cdot 10^{-10}$	$-3.2 \cdot 10^{-10}$	$5.2 \cdot 10^{-9}$	0
R_{op}	2539	$8.5 \cdot 10^{7}$	$-5.3 \cdot 10^{6}$	$2.5 \cdot 10^{7}$	$-9.2 \cdot 10^{8}$	0

Table 2.4-2. Coefficients for equation (2.4.1).

2.4.2 Modeling of electrochemical interfaces and electrolyte

In order to retrieve the electrode/electrolyte interface parameters, EIS measurements have been carried out on gold microelectrodes using Ag/AgCl reference electrode and standard ASTM D1125 solution. As described in Section 2.3, the reference electrode has been chosen due to its non-polarizable features [13] that lead to moderate effects on system electrical impedance. EIS stimulation voltages have been set to 0 V and 10 mV of bias and amplitude, respectively. These values ensure to keep the system in the linear response domain [3,15].

The LPEEC used for EIS data processing is described in Figure 2.4-7. The structure of this model is the one depicted in Figure 2.4-1 (b) where the “Sample” impedance has been substituted with the model 1.4.4: it consists of the double layer capacitance C_{dl}, the charge transfer resistance R_{ct}, the electrolyte resistance R_m and the constant phase element CPE with electrical impedance

$$Z(f) = \frac{1}{(j2\pi f)^n C_W} \quad , \tag{2.4.4}$$

where f is the EIS sinusoidal stimulus frequency. R_t represents the ohmic resistance of gold interconnections between contacted pad and corresponding microelectrode [18]. This resistance has been evaluated to be R_t = 1.43 Ω by considering the average values for devices interconnections dimensions [25] and σ_{Au} = $4.5 \cdot 10^7$ S/m for gold electric conductivity.

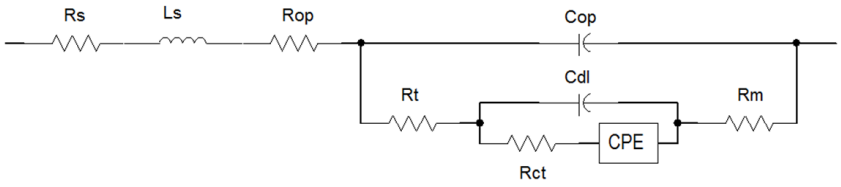

Figure 2.4-7. LPEEC for Ag/AgCl reference electrode set-up EIS data processing.

Figure 2.4-8 shows EIS measurements data and the result of fit process by keeping L_s and R_s to the previously determined values. Fitting results are listed in Table 2.4-3: the fitted value for R_m is in good agreement with the usual spreading resistance formula for circular electrodes [16], i.e. $R_m = (4\sigma_e r_e)^{-1}$ = 118.2 kΩ. Moreover, the fitted value for C_m leads to the common double-layer charge density for gold electrodes of $C_m(\pi r_e^2)^{-1}$ = 0.1 pF/μm^2 [20].

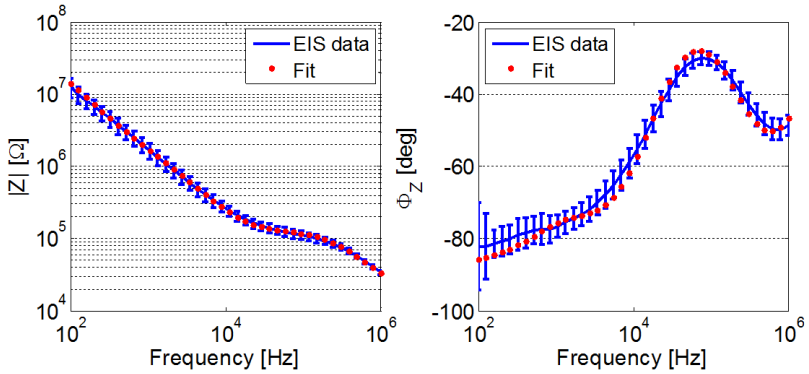

Figure 2.4-8. EIS measurements of ASTM D1125 standard solution with fit obtained using Figure 2.4-7 circuit.

Parameter	C_{dl} [pF]	R_{ct} [MΩ]	C_W [pF]	n	R_m [kΩ]	R_t [Ω]	R_{op} [kΩ]	C_{op} [pF]
Value	68.26	4.09	57.96	0.93	117.8	1.4	17.72	6.28
Fit error [%]	3.4	4.1	2.6	0.8	0.6	-	3.9	1.6

Table 2.4-3. Parameters values for Figure 2.4-7 circuit: fitting of ASTM D1125 standard solution.

With the parameters listed in Table 2.4-3, the behavior of the electrochemical interface at a MEA microelectrode has been investigated. In order to determine the impedance variations laws with the distance from the working electrode l, the standard electrolyte has been measured using several couples of microelectrodes with different inter-electrodes distances d. EIS results are shown in Figure 2.4-9, where can be seen that the impedance magnitude increases as d increases. Electrical stimulus parameters, i.e. bias and amplitude, are the same of the Ag/AgCl reference electrode set-up.

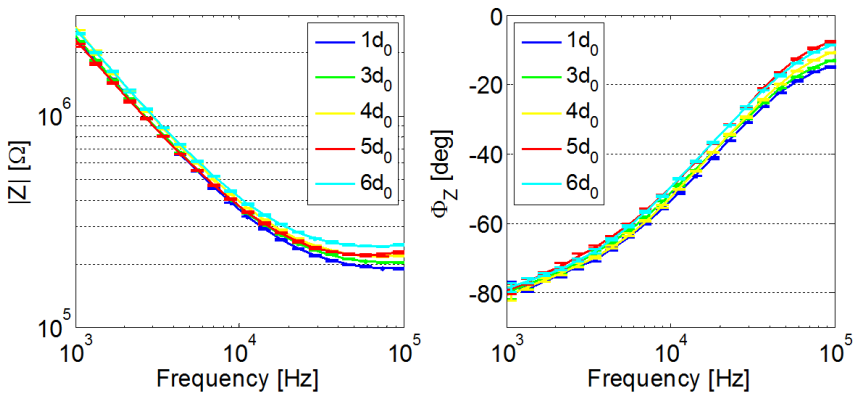

Figure 2.4-9. EIS measurements of ASTM D1125 standard solution as a function of d. These data sets have been obtained by measuring the electrolyte using microelectrodes as both working and reference electrode.

EIS data sets of Figure 2.4-9 have been fitted using a LPEEC with the same parasitic structure of that in Figure 2.4-1 (b) and using as "Sample" impedance model the circuit of Figure 2.4-10 (a) that consists of a double Randles equivalent circuit [22]. The electrolyte is represented by a parallel between the spreading resistance R_m and a capacitor C_m. All the empty-chamber parasitic parameters have been evaluated using (2.4.3) and the short-circuit ones have been fixed to R_s and L_s. The results of fitting process for various d are depicted in Figure 2.4-11, where can be seen that the interfacial parameters C_{dl} and R_{ct} exhibit an increase in their impedance with d, while the

diffusion-related CPE is constant on average with low standard deviation [3], and its values are consistent with those obtained from the Ag/AgCl reference electrode set-up.

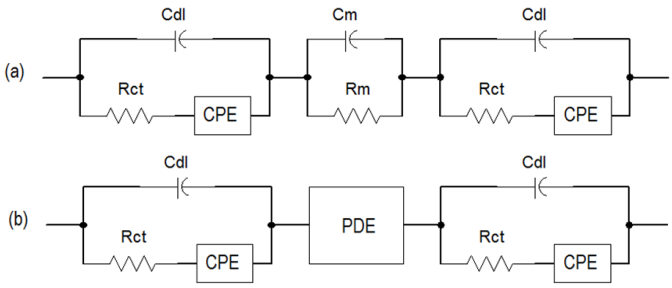

Figure 2.4-10. LPEEC for microelectrode vs. microelectrode EIS measurements fit (a). PDE substitutes electrolyte LPEEC (b).

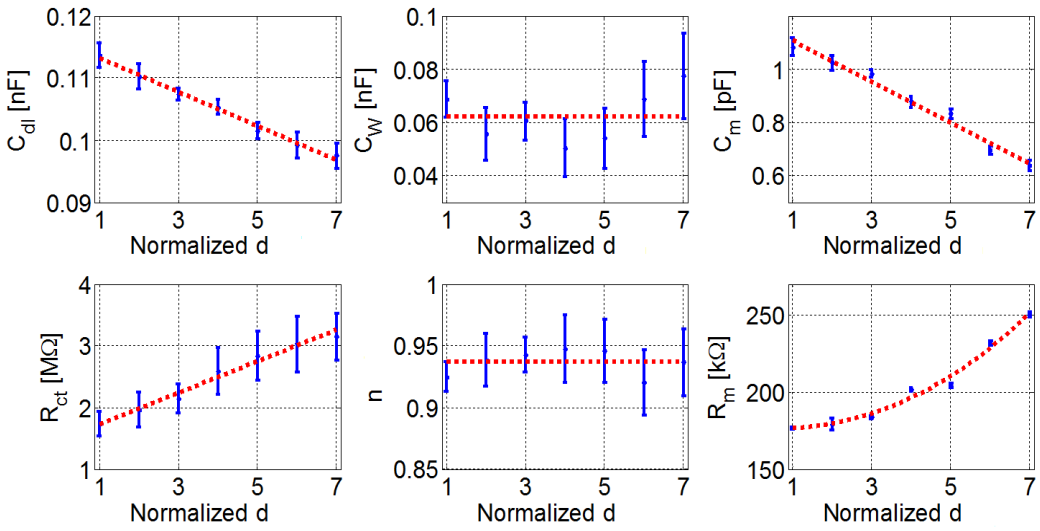

Figure 2.4-11. Behavior of Figure 2.4-10 (a) LPEEC fitted parameters as a function of d over d_0.

The mathematical laws for PDE implementation have been deduced from the behavior of C_m and R_m as a function of d depicted in Figure 2.4-11. Applying the same working hypothesis of Section 2.3, the local variation of the electrolyte equivalent elements can evaluated as

$$\Delta C_m(l_1, l_2) = g_1|l_1 - l_2| + g_2 \ , \qquad (2.4.5)$$

$$\Delta R_m(l_1, l_2) = h_1|l_1 - l_2|^{h_2} + h_3 \ , \qquad (2.4.6)$$

where $\{g_1, g_2\}$ and $\{h_1, h_2, h_3\}$ are numeric parameters listed in Table 2.4-4 for the mathematical fit of C_m and R_m respectively. By implementing (2.4.5) and (2.4.6) in the

CSS, electrolyte PDE is created as networks of basic LPEEC with parameters ΔC_m and ΔR_m that are functions of the Euclidean position in the mesh with respect to the center of the working electrode. The LPEEC of Figure 2.4-10 (a) can be therefore substituted with the one of Figure 2.4-10 (b) in which the electrolyte electrical parameters are expressed by a PDE.

Parameter	C_{dl}=ad+b [F]	R_{ct}=ad+b [Ω]	C_W=a±b [F]	n=a±b	C_m=ad+b [F]	R_m=ad^b+c [Ω]
a	$-0.27\cdot10^{-8}$	$2.5\cdot10^{9}$	$6.2\cdot10^{-11}$	0.9367	$-7.7\cdot10^{-10}$	$1.5\cdot10^{12}$
b	$1.2\cdot10^{-10}$	$1.5\cdot10^{6}$	$0.9\cdot10^{-11}$	0.01	$1.2\cdot10^{-12}$	2.313
c	-	-	-	-	-	$1.7\cdot10^{5}$
R^2	0.9913	0.9789	-	-	0.9798	0.9832

Table 2.4-4. Mathematical fit of Figure 2.4-10. The inter-electrodes distance parameter d is measured in [m].

Figure 2.4-12 describes a comparison between LPEEC fitting results and CSS simulation results for electrolyte parameters: as can be seen the approximated incremental functions (2.4.5) and (2.4.6) lead to an overall PDE electrical impedance that slightly deviates from the correspondent values obtained from usual LPEEC fitting process. Table 2.4-5 lists these variations between fitted and simulated electrolyte parameters in terms of percentage difference.

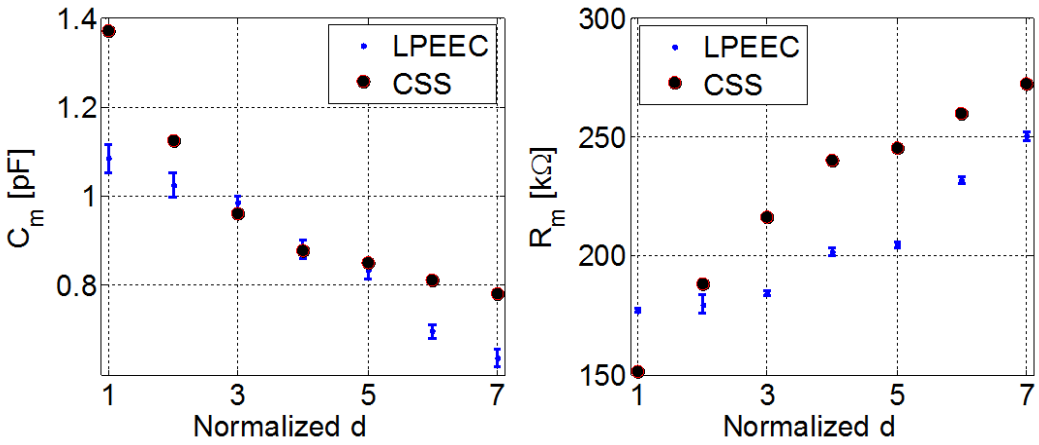

Figure 2.4-12. Electrolyte parameters obtained from LPEEC (blue dots, see Figure 2.4-11) and from CSS (filled circles) as a function of d over d_0: C_m (left) and R_m (right).

	$1d_0$	$2d_0$	$3d_0$	$4d_0$	$5d_0$	$6d_0$	$7d_0$
εC_m [%]	23.6	9.0	0.7	0.1	6.2	12.2	20.6
εR_m [%]	14.2	4.8	16.1	22.2	16.8	13.9	8.5

Table 2.4-5. CSS response deviations as percentage difference (see (2.3.5)).

Recalling Figure 2.3-10, the percentage error listed in Table 2.4-5 indicates that the electrolyte LPEEC used for this modeling example, i.e., a parallel between a resistor R_m and a capacitor C_m, should be simplified for the tested frequencies in a single resistor: in fact, as described in Section 1.4.2, the cut-off frequency of a purely low-pass electrolyte [3, 4] can be found at higher frequencies than 100 kHz (see Figure 2.4-9). This means that the error introduced by the capacitor C_m reflects on the overall fitting impedance, and therefore on the value of R_m.

The deviations εC_m and εR_m introduced by CSS approximated variation laws have an impact on the goodness of EIS measurements fit, both in low and in high frequency. To assess this impact, EIS data of Figure 2.4-9 have been both fitted using the “Sample” model of Figure 2.4-10 (a) and simulated using the evaluated electrolyte PDE. The resulting normalized residual sum of squares (NRRS) [23] (see Section 2.3) plot is shown in Figure 2.4-13.

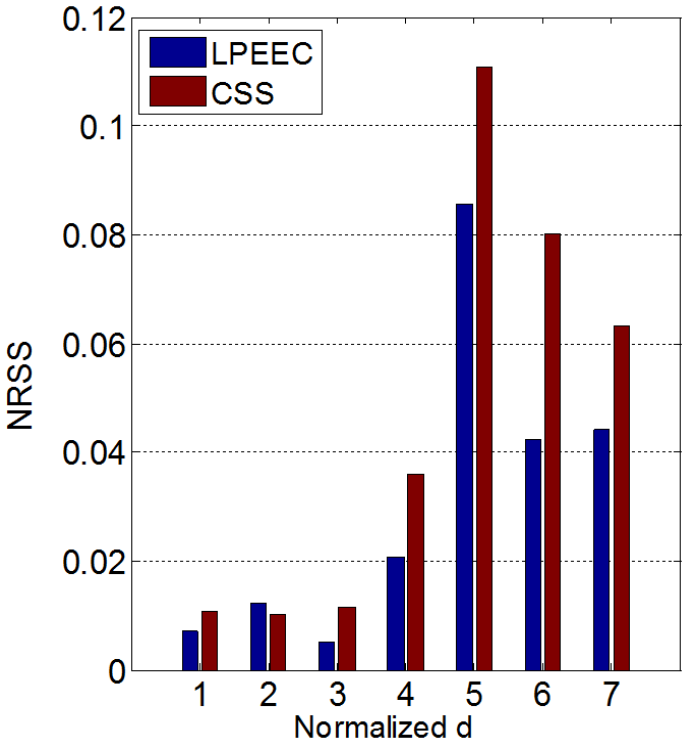

Figure 2.4-13. NRSS for electrical impedance Z simulated using LPEEC approach (blue bars) and CSS (red bars), compared to EIS data of Figure 2.4-9: impedance magnitude (left) and phase (right). Inter-electrodes distance d normalized over d_0.

2.5 Bibliography

[1] Siu, M., Cobbold, R.S.C., 1979. IEEE Trans. Electr. Dev. ED-26 (11), 1805-1815.

[2] Schwan, H.P., Foster, K.R., 1980. Proc. IEEE 68 (1), 104-113.

[3] Macdonald, J.R., 1987. Wiley Interscience, John Wiley and Sons, 27-133.

[4] Gabrielli, C., 1998. Monograph Reference 004/83, Solartron Analytical Instr. Group, Farnborough, Hampshire, UK.

[5] Franks, W., Schenker, I., Schmutz, P., Hierlemann, A., 2005. IEEE Transaction on Biomedical Engineering 52 (7), 1295-1302.

[6] Deng, J., Schoenbach, K.H., Buescher, E.S., Hair, P.S., Fox, P.M., 2003. Biophys. J. 84, 2709-2714.

[7] Deford, J.F., Gandhi, O.P., 1985. IEEE Trans. Electr. Comp. EMC-27 (3), 168-173.

[8] Gowrishankar, T.R., Weaver, J.C., 2003. Proc. Nat. Acad. Sci. 100 (6), 3203-3208.

[9] Cantrell, D.R., Inayat, S., Taflove, A., Ruoff, R.S., Troy, J.B., 2007. Journal of Neural Engineering 5, 54-67.

[10] de Berg, M., Cheong, O., van Kreveld, M., Overmars, M., 2008. Springer-Verlag.

[11] Smith, K.C., 2006. Massachussets Institute of Technology.

[12] Stewart, D.A., Gowrishankar, T.R., Smith, K.C., Weaver, J.C., 2005. IEEE Transactions on Biomedical Engineering 52 (10), 1643-1653.

[13] McAdams, E.T., Lackermeier, A., McLaughlin, J.A., Macken, D., Jossinet, J., 1995. Biosensors & Bioelectronics 10, 67-74.

[14] Bard, A.J., Faulkner, L.R., 2001. John Wiley and Sons.

[15] Onaral, B., Sun, H.H., Schwan, H.P., 1984. IEEE Transaction on Biomedical Engineering BME-31 (12).

[16] Newman, J., 1966. J. Electrochemical Society 113 (5), 501-502.

[17] Grimnes, S., Martinsen, Ø.G., 2008. Academic Press.

[18] Borkholder, D.A., 1998. Stanford University, Stanford, CA.

[19] Price, D.T., Rahman, A.R.A., Bhansali, S., 2008. Biosens. Bioelectron. doi:10.1016/j.bios.2008.10.026.

[20] Kovacs, G.T.A., 1994. Academic Press, 121-165.

[21] Bao, J.Z., Davis, C.C., Schmukler, R.E., 1993. IEEE Transaction on biomedical engineering 40, 364-378.

[22] Gómez, R., Bashir, R., Bhunia, A.K., 2002. Sens. Act. B 86, 198-208.

[23] Polk, B.J., Stelzenmuller, A., Mijares, G., MacCrehan, W., Gaitan, M., 2006. Sens. Actuat. B 114, 239-247.

[24] Xiao, C., Lachance, B., Sunahara, G., Luong, J.H.T., 2002. Anal. Chem. 74, 5748-5753.

[25] Mercanzini, A., Colin, P., Bensadoun, J.C., Bertsch, A., Renaud, P., 2009. IEEE Transactions on biomedical engineering 56, 1909-1918.

[26] Deford, J.F., Gandhi, O.P., 1985. IEEE Transactions on Electromagnetic Compatibility EMC-27 (3), 168-173.

[27] Gowrishankar, T.R., Esser, A.T., Vasilkoski, Z., Smith, K.C., Weaver, J.C., 2006. Biochemical and Biophysical Research Communications 341, 1266-1276.

[28] Smith, K.C., Gowrishankar, T.R., Esser, A.T., Stewart, D.A., Weaver, J.C., 2006. IEEE Transactions on Plasma Science 34 (4), 1394-1404.

[29] Scaramuzza, M., Ferrario, A., De Toni, A., 2010. Ph.D. Research in Microelectronics and Electronics, 1-4.

[30] Scaramuzza, M., Ferrario, A., Pasqualotto, E., De Toni, A., 2012. Procedia Chemistry 6, 69-78.

Chapter 3. Detection of oligonucleotide sequences hybridization

3.1 Introduction to genosensors

Sensor devices for electrochemical analysis and detection of biological processes using both proteins, e.g., enzymes or antibodies, nucleic acids like DNA and RNA, or living cells, have been constantly developed and enhanced. A great attention has been focused on new technologies and materials for the sensor interface, in order to improve sensitivity and integration, to minimize dimension and analysis time, and in particular to reduce manufacturing cost.

DNA diagnostics has become an important area of molecular biology and biotechnology studies. The detection of specific base sequences in human, viral and bacterial nucleic acids is becoming increasingly important in several areas, with applications ranging from the detection of disease-causing and food-contaminating organisms to forensic and environmental research [1].

Conventional methods for the analysis of specific gene sequences are based on either direct sequencing or DNA hybridization methods. Because of its simplicity, the second option is more commonly used in diagnostic laboratories. In DNA hybridization, the target gene sequence is identified by a DNA probe that can form a double-stranded hybrid (dsDNA) with its complementary nucleic acid, i.e., the target sequence (cDNA), with high efficiency and extremely high specificity, even in presence of a complex and heterogeneous sample. DNA probes are single-stranded DNA (ssDNA) labeled to provide detectable signals after successful DNA hybridization [1], that create a self-assembled monolayer on the electrode surface during functionalization process.

Genosensors, or DNA biosensors, are devices that combine a biological recognition agent, i.e., ssDNA also called probe, that confers selectivity, with a transducer that provides sensitivity and converts the recognition event into a measurable electronic signal [1].

A fundamental element for the efficiency of a biosensor is the optimization of the adsorption of the biological probes substrate [2, 3, 4]. In fact, the organization of the probe self assembly monolayer, which, in turn, depends on the electrode surface

physical characteristics, strongly affects the hybridization efficiency [3, 5, 6]. This means that it is important to study the biological probes adsorption process as well as the characteristics of the electrode surface, like the effective surface area or the surface roughness factor [7, 8] (see Section 3.2).

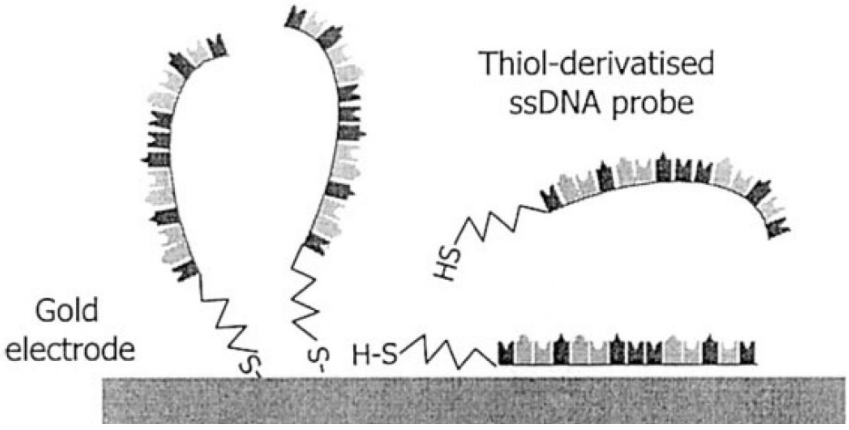

(a)

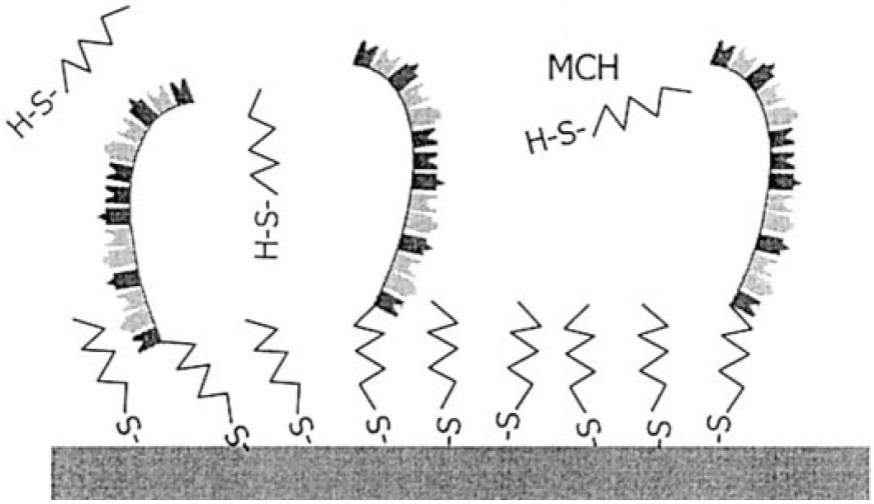

(b)

Figure 3.1-1. Thiol-modified DNA probes immobilization by covalent bonding to a gold surface. Specific and non-specific adsorption (a). Exposure to mercaptohexanol (MCH) solution to minimize non-specific adsorption of probes (b) [1].

The control of the coverage of gold electrode surface can be achieved by creating a mixed monolayer of thiol (HS)-derivatised probe and a lateral spacer thiol, i.e., mercaptohexanol (MCH), using a two-step method [9, 10, 11, 12]. This two-step method consists on electrode functionalization with thiolated single-stranded DNA probes (HS-

ssDNA), and then exposure of the functionalized surface to a MCH solution. An advantage of using this two-step process to form the HS-ssDNA/MCH mixed monolayer is that non-specifically adsorbed DNA is largely removed from the surface. Before exposure to MCH, the HS-$(CH_2)_6$-ssDNA molecules interact with the gold surface through both the nitrogen-containing nucleotide bases and the sulphur atom of the thiol group (see Figure 3.1-1). After exposure to MCH, the new thiol groups compete with the nucleotide bases to interact with the gold surface. Thus, the majority of surface-bound probes are accessible for specific hybridization with complementary DNA [1].

As a result, the self-assembled monolayer of HS-ssDNA and MCH allows to create a more uniform interface and to remove the non-specific adsorbed probes from the surface: to maximize the hybridization efficiency it is essential to minimize the number of nonspecifically adsorbed probes. Moreover, the spatial position of probe sequences affects the hybridization outcomes, as MCH negatively charged hydroxyl head groups orient the flat lying HS-ssDNA strands in perpendicular configuration and reduces the probe surface density to give high freedom for hybridization [13, 14], while the short chains of MCH do not interfere with the hybridization process [15].

3.2 Design and development of a biosensor for DNA hybridization detection

In this Section, the development of an electrochemical biosensor for the detection of short DNA sequences is presented [16]. The biosensor performs amperometric transduction using planar gold electrodes, i.e., working, counter and reference electrode, on polymeric substrate (see Figure 3.2-1).

The sensor layout was designed to be used both for electrochemical impedance spectroscopy (EIS) and voltammetric measurements. The device consisted of four gold coplanar electrodes: a reference electrode, a counter electrode and two working electrodes, both of 1 mm^2 area. An insulator layer was printed on the device in order to define the electrochemical cell and to insulate the conductive tracks.

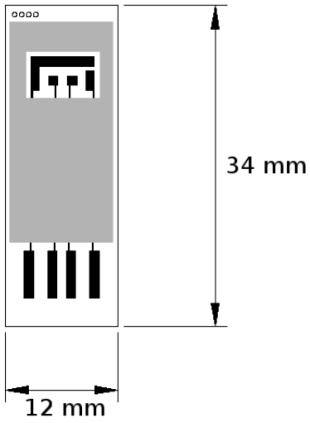

Figure 3.2-1. Biosensor layout (not to scale). Polycarbonate substrate is represented in white, gold electrodes in black and the printed insulator layer in grey [16].

The gold electrodes have been preliminary characterized through cyclic voltammetry (CVM) measurements with solutions of hexacyanoferrate(II)/(III) 1 mM in potassium chloride 100 mM buffer, i.e., 1 mM $Fe(CN)_6^{4-/3-}$ in KCl 100 mM. These measurements were fundamental in order to better understand the interfacial electrochemical processes because they provided information on the charge transfer mechanisms at the non-functionalized interface between electrode and redox solution.

Figure 3.2-2 shows the comparison between CVM measurements obtained with planar gold reference electrode and the standard silver/silver chloride external

reference electrode. The electrochemical behavior of the two electrodes was similar, with an observed potential difference of about 236 mV. To assess the efficiency of the gold electrode as reference electrode, the CVM results have been analyzed as described in Section 1.2.2: recalling (1.2.1), the difference between $E_{p,c}$ and $E_{p,a}$ results ΔE_p = 64 mV, while the ratio between the peaks current (1.2.5) is $I_{p,a}/I_{p,c}$ = 1.043. These values indicate a nearly reversible electrode reaction, and therefore the gold reference electrode can be used for electrochemical detection.

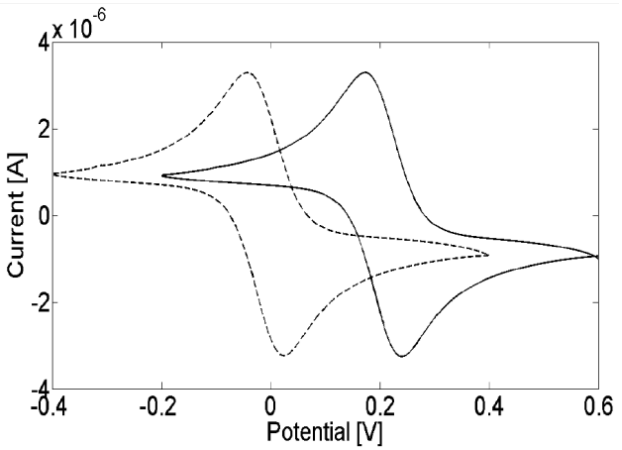

Figure 3.2-2. Cyclic voltammetry of hexacyanoferrate(II)/(III) 1 mM in KCl 100 mM on bare gold electrode. Comparison between the integrated reference electrode (dotted) and a standard silver/silver chloride external reference electrode (solid).

CVM measurements of redox solution at different scan rates v (see Figure 3.2-3) shown no adsorption effects on gold working electrode surface [17]. Moreover, a $v^{0.5}$ dependence for cathodic peak current I_p was found, as required for these kinds of processes (see (1.2.6)).

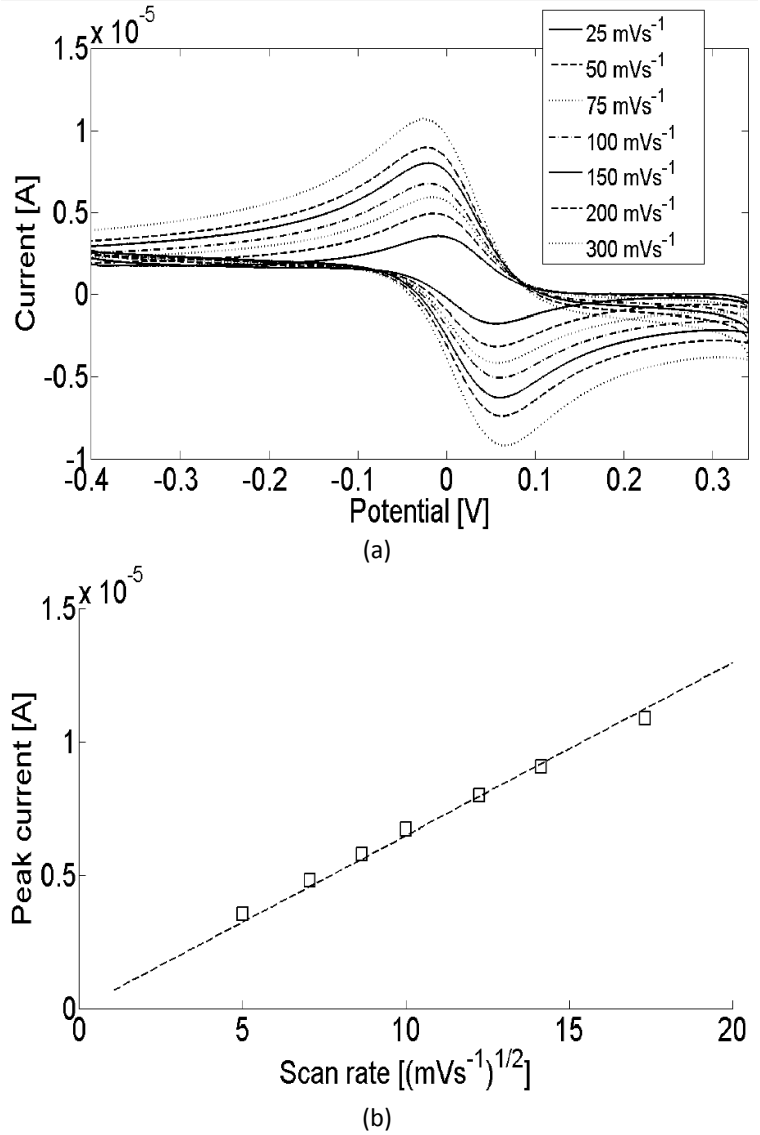

Figure 3.2-3. Cyclic voltammetry of hexacyanoferrate(II)/(III) 1 mM in KCl 100 mM on bare gold electrode at different scan rates, from 25 to 300 mVs^{-1} (a). DPV peak currents versus square root of scan rate: the linear relationship has equation $y = 6.491 \cdot 10^{-7} \cdot x + 2.66 \cdot 10^{-7}$ ($R^2 = 0.9894$).

The electrochemical behavior of a gold planar electrode depends also on the real microscopic surface area, i.e., the electrochemical surface area (ESA) or active surface area, A_{eff}. Usually, this area is different from the geometric one, A_g. The ratio between the two areas, i.e.,

$$R_f = \frac{A_{eff}}{A_g} \quad , \tag{3.2.1}$$

is called the surface roughness. The surface roughness was investigated with a method proposed in [18]. The electrochemical effective surface area was calculated from the quasi-reversible reaction [19] (1.2.6):

$$i_p = (2.69 \times 10^5) A C \sqrt{n^3 D_0 v} \quad , \tag{3.2.2}$$

where the diffusion coefficient $D_0 = 7.6 \cdot 10^{-6}$ $cm^{-2}s^{-1}$ for ferricyanide ion [19] and scan rate $v = 100$ mVs^{-1}. Electrodes with different geometrical area were measured with CVM to obtain a better estimation of the electrode roughness. Figure 3.2-4 depicts the values of the effective surface area A_{eff} calculated from (3.2.1) as a function of the geometrical area. The slope of the fitting regression line $y = 1.52 \cdot 10^{-6}$ ($R^2 = 0.9927$) represents the roughness factor, which is $R_f = 1.52$.

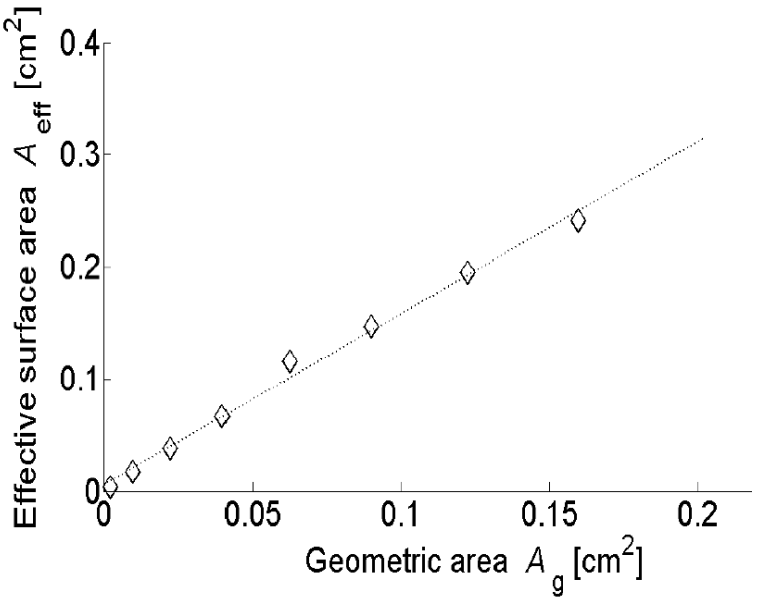

Figure 3.2-4. Relation between the electrode geometric area A_g and effective surface area A_{eff} calculated from CVM measurements. The slope of the fitting curve determines the surface roughness factor R_f.

The functionalization of the working electrode has been performed by chemisorptions of thiol-modified DNA probes with 33 bases. This thiolated probe DNA (HS-ssDNA), had the sequence:

5'-GTA ACA TCA CAG GCT ATT AGT TGC CAA CGT CCT C-3' , (3.2.3)

and was modified on the 5' to obtained HS – $(CH_2)_6$ – ssDNA.

A fundamental aspect of the genosensor development is the control of the probe deposition process: in fact, optimization of probe adsorption on the electrode surface is

fundamental for the hybridization detection efficiency. To assess this important parameter, the DNA probe adsorption was studied both as a function of the concentration and in relation to kinetic aspects.

Figure 3.2-5 (a) and (b) depicts Bode diagrams of electrical impedance Z obtained from EIS measurements of the working electrode functionalized with six different concentrations of DNA probe. From the Bode diagrams can be observed that the impedance magnitude increases as probe concentration increase and that this effect is particularly evident for frequencies below 10 Hz, where the diffusive phenomena dominates over charge transfer process (see Section 1.4). Figure 3.2-5 (c) shows Nyquist diagrams of the same EIS measurements in the range between 1 Hz and 1 MHz: the diameter of the low-frequency impedance semicircle increases with DNA probe concentrations, suggesting a broader electrode coverage of biological material.

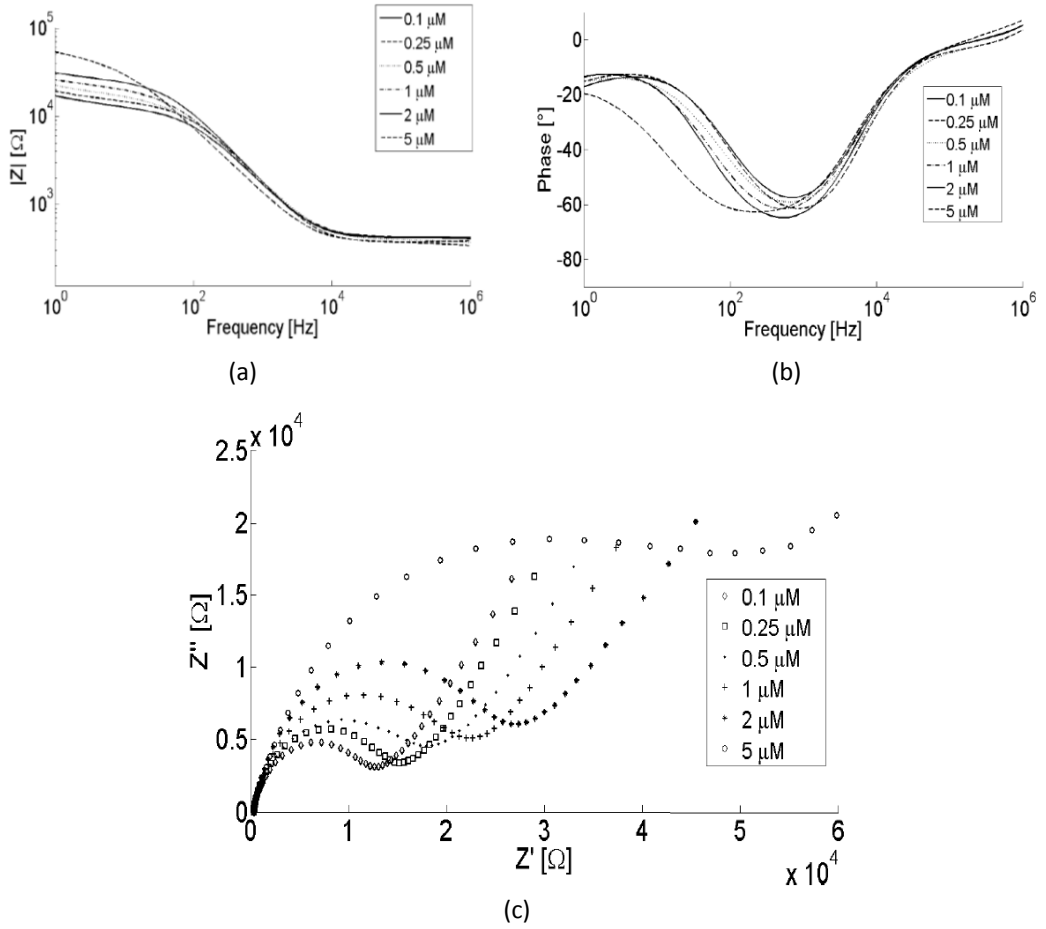

Figure 3.2-5. Bode plot, (a) and (b), and Nyquist plot (c) of EIS measurements of hexacyanoferrate(II)/(III) 1 mM in KCl 100 mM on ssDNA functionalized electrode as function of ssDNA probe concentration.

The pattern of these EIS measurements on the Nyquist plane reflects that of equation (1.4.4), therefore by using this equation for EIS data fitting it has been possible to evaluate the charge transfer resistance R_{ct} [20] as a function of probe concentration (see Figure 3.2-6 (a)): R_{ct} is the parameter that models interfacial charge exchange, therefore its growing values with DNA probe concentrations indicate an increase of adsorption process at the working electrode.

Differential pulse voltammetry (DPV) measurements (see Section 1.2) have been carried out on electrodes functionalized with different concentrations of DNA probe in order to assess the influence of adsorbed molecules on the electrode surface. The results of these measurements are depicted in Figure 4.2-6 (b), where can be seen the lowering of measured current as probe concentration increases, i.e., as R_{ct} grows.

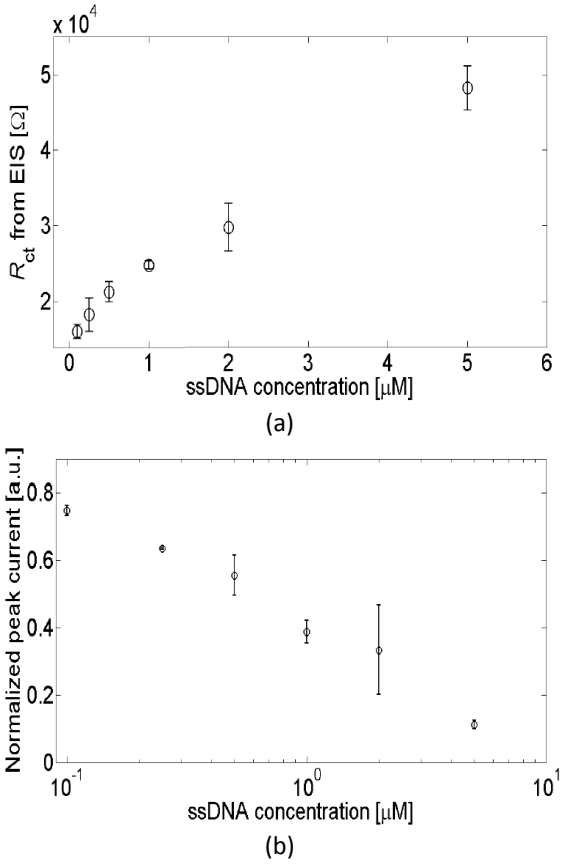

Figure 3.2-6.Charge transfer resistance R_{ct} extrapolated from fitting of Figure 3.2-5 EIS data as function of ssDNA probe concentration (a). Normalized DPV peak currents of hexacyanoferrate(II)/(III) 1 mM in KCl 100 mM on ssDNA modified electrode as function of ssDNA probe concentration (b).

Figure 3.2-7 (a) depicts DNA probe adsorption behavior as a function of functionalization time. DPV measurements have been carried out on working electrodes

functionalized with a solution of DNA probe at the concentration of 2 μM. The functionalization solution has been left in contact with the electrodes for a time variable between few minutes and two hours. During the first 20 minutes a sharp decrease of DPV current peaks can be observed, while after this period the decrease is less sharp but still present. This situation is better described in Figure 3.2-7 (b), where the DPV current peaks are normalized to the non-functionalized gold working electrode DPV peak current: after one hour the normalized current trend reaches the 90 % of its maximum value, that indicates a situation in which the electrode surface is almost completely covered by adsorbed DNA probe.

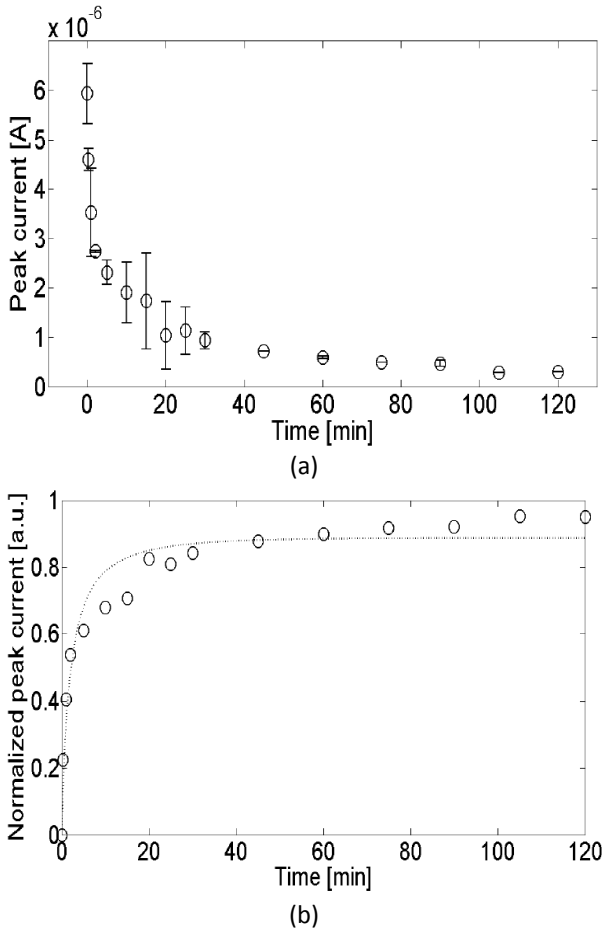

Figure 3.2-7. DPV peak currents (a) and normalized peaks (b) of hexacyanoferrate(II)/(III) 1 mM in KCl 100 mM of ssDNA modified electrodes as function of time adsorption.

After this study on working electrode functionalization protocol, the genosensor has been tested in presence of the target sequence, that had the complementary base sequence of (3.2.3), without the thiol modification, i.e.,

5'-GAG GAC GTT GGC AAC TAA TAG CCT GTG ATG TTA C-3' . (3.2.4)

For these studies, the working electrode was modified with 2 μM DNA probe, while the control electrode has been left non-functionalized, in order to verify the stability of the pseudo reference electrode and to have a direct measurement of the bare gold working electrode. The target sequence (3.2.4) was at a concentration of 20 μM.

Before hybridization, the target solution was heated at 90 °C for 1 minute. Hybridization was obtained by placing 1 μl of target solution directly onto the probe-modified electrodes for 3 hours, in a wet sealed Petri at 65 °C. The hybridization buffer solution was Na_2HPO_4 100 mM, pH 8.5. After hybridization, the electrode surface was washed with 20 μl of KCl 100 mM, to remove non-specific adsorbed sequences, and then was rinsed thoroughly with deionized water [16].

Both EIS measurements and DPV measurements were used to verify the effects of the hybridization process. Figure 3.2-8 depicts impedance modulus and Nyquist plot of both control electrode, working electrode modified with DNA probe and working electrode after hybridization with target sequence. A large impedance variation can be observed for frequencies below 100 Hz. Thus, the interaction between the negatively charged hexacyanoferrate(II)/(III) ions and the DNA backbone induces an increase in the charge transfer resistance R_{ct} [16].

The signal variations, with respect to the non modified gold electrode, obtained with EIS measurements are depicted in Figure 3.2-9: as can be seen, the signal variation is nearly 40 times higher than the DNA probe signal.

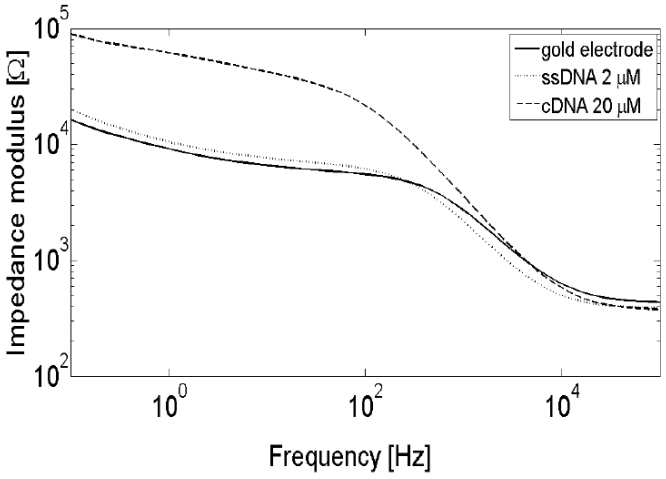

(a)

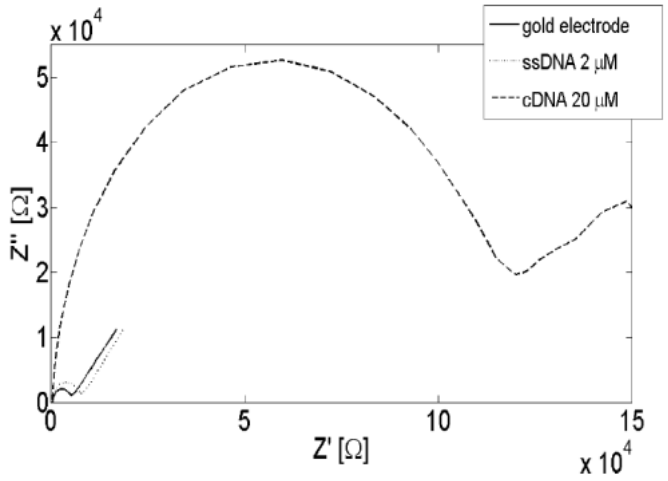

(b)

Figure 3.2-8. Impedance magnitude (a) and Nyquist plot (b) of EIS measurements with hexacyanoferrate(II)/(III) 1 mM in KCl 100 mM on three different surface conditions: bare gold electrode, ssDNA modified electrode and after hybridization with 20 μM complementary target sequence (cDNA).

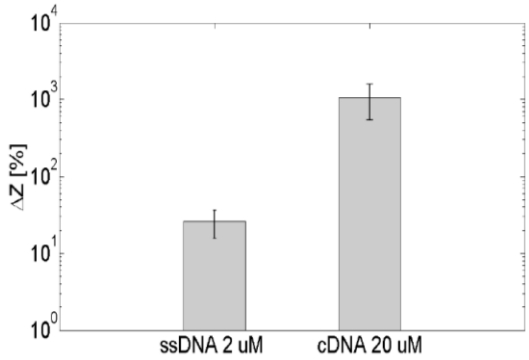

Figure 3.2-9. Comparison between EIS signal variation for 2 μM ssDNA probe adsorption and 20 μM complementary target hybridization. Variation are referred to the non-functionalized gold electrode.

3.3 Optimization of the functionalization protocol

A fundamental aspect concerning the optimization of a DNA hybridization sensor is the accessibility, i.e., the molecular orientation and the surface density of ssDNA probes. A high degree of control over the immobilization of DNA probes is required to enhance the hybridization efficiency. In fact, a too high density of probes reduces the hybridization efficiency while a too low density does not determine a significant change in the electrochemical signal [21, 22]. MCH is used for this purpose, by backfilling the electrode surface after the ssDNA immobilization (see Section 3.1).

In this Section, the same biosensor described in the previous Section has been optimized using a different functionalization process. A self-assembled monolayer obtained from a mixed solution of ssDNA probes and MCH was used to assess the effectiveness of hybridization detection [23].

The electrical characterization of the biosensor has started with the investigation of DNA probe surface density as a function of the ratio between its concentration and MCH concentration in the mixed functionalization solution. The charge transfer resistance R_{ct} was obtained by fitting EIS data with (1.4.4) model as in Section 3.2. EIS data and fitting results are depicted in Figure 3.3-1: the semicircle diameter in the impedance spectrum equals to the charge transfer resistance, and from the Figure its variation with the surface modifications are evident. The corresponding values of the charge transfer resistance were calculated as 32 kΩ (R^2 = 0.9894) for bare MCH, 63 kΩ (R^2 = 0.9930) for MCH/ssDNA mixed solution and 375 kΩ (R^2 = 0.9953) after hybridization with target DNA. These higher impedances are due to the presence of immobilized molecules that introduce a barrier to the electron transfer processes between the redox couples and the electrode surface [19, 24, 25].

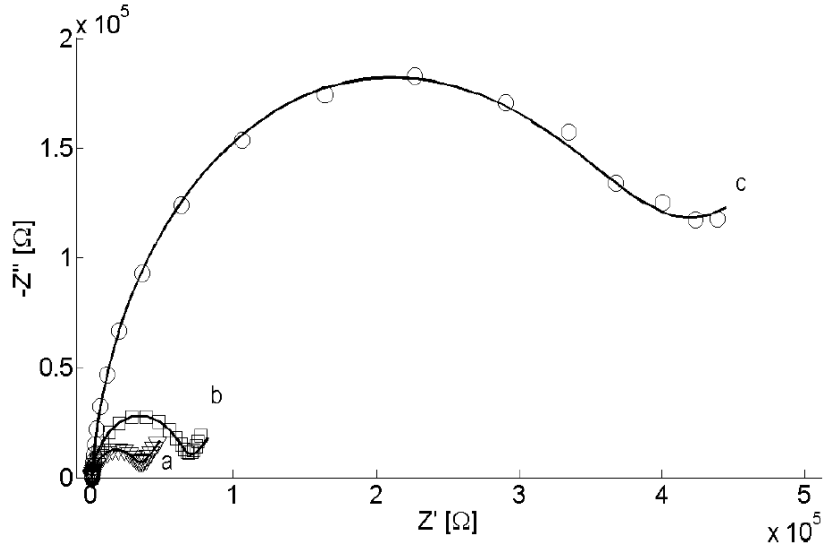

Figure 3.3-1. Nyquist plot of bare MCH immobilized on the electrode (a), MCH solution with 2 μM ssDNA (b) and after hybridization with 1 μM target solution (c). The measurements solution was 1 mM $Fe(CN)_6^{4-/3-}$ in KCl 100 mM. Solid lines represent data fits to (1.4.4) model.

Figure 3.3-2 (a) depicts R_{ct} as a function of the MCH concentration for the pure thiol monolayer, the ssDNA/MCH mixed self-assembled monolayer and after the hybridization with 1 μM target solution. Below 0.2 μM, the R_{ct} value for the simple MCH monolayer is in the order of about 10^4 Ω, which is a value similar to a bare gold electrode. This means that few thiols cover the surface. Above 0.2 μM, R_{ct} increases of more than one order of magnitude. By comparing these results with R_{ct} obtained for the mixed ssDNA/MCH monolayer, it can be observed that below 0.2 μM MCH concentration, the charge transfer increase is mainly due to the presence of ssDNA probes. Conversely, at 20 μM MCH concentration, DNA probes do not significantly affect the surface coverage. In the range between 0.2 μM and 2 μM MCH concentration, the increase of R_{ct} with both pure MCH solution and mixed ssDNA/MCH solution, suggests a more equilibrate presence of both thiols and ssDNA probes, which is important for the hybridization efficiency [26, 27].

Correspondingly, Figure 3.3-2 (b) shows the decrease of the DPV peak currents with the increase of MCH concentration. DPV measurements results are consistent with those obtained from EIS measurements: at high MCH concentrations, the thiols monolayer strongly reduces the current, therefore other variations, e.g., ssDNA probes

or hybridization, are not relevant. The lower the MCH concentration, the higher is the presence of ssDNA probes.

These results show that with a mixed solution of ssDNA probes and MCH it is possible to control the amount of immobilized probes in the self-assembled monolayer that covers the electrode surface. Similar results are reported in [22]. In [25] a two-step electrode functionalization process has been implemented, i.e., first ssDNA immobilization and then MCH solution exposure, showing that ssDNA immobilization is largely unaffected either by the presence nor by different concentrations of MCH solution.

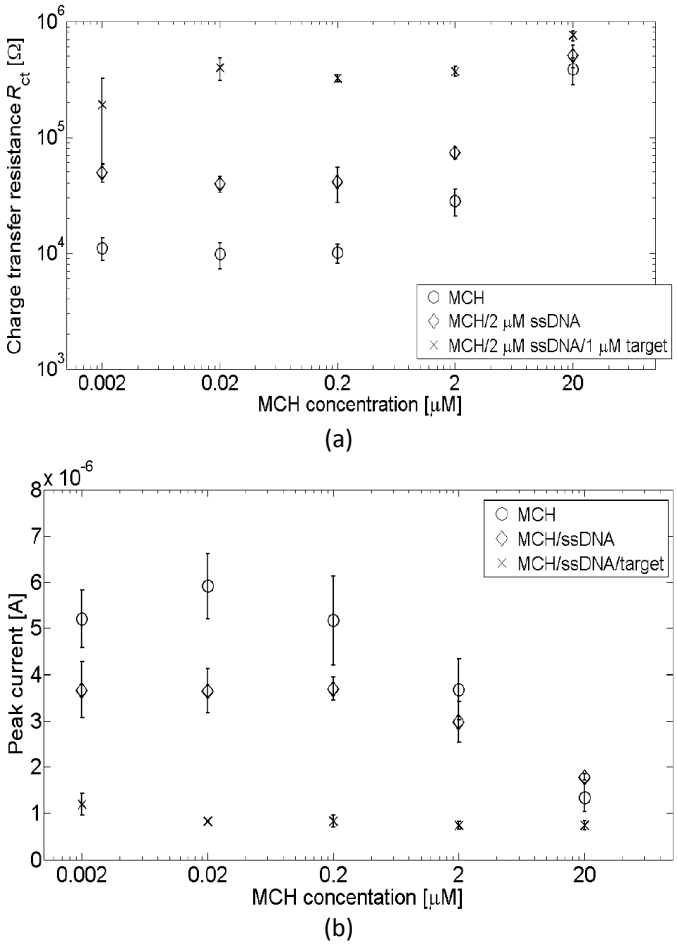

Figure 3.3-2. Charge transfer resistance R_{ct} (a) and DPV peak currents (b) as a function of MCH concentration: bare immobilized MCH, MCH solution with 2 μM ssDNA and after hybridization with 1 μM target solution.

Figure 3.3-2 (a) shows the increase of the charge transfer resistance after the coupling of complementary target sequences. The increase is more evident for MCH

concentration between 0.02 μM and 0.2 μM. A similar behavior is depicted in Figure 3.3-2 (b), where DPV peak currents decrease for MCH concentration of 20 μM is less evident than those for concentration ratio above $c_{ssDNA}/c_{MCH} = 1$.

Figure 3.3-3 confirms these observations: the variation of R_{ct}, evaluated from EIS data, is plotted as a function of MCH concentration in mixed ssDNA/MCH functionalization solution. The ssDNA probes adsorption efficiency is calculated as the percentage change in R_{ct} after the ssDNA/MCH self-assembly monolayer adsorption with respect to the layer of only thiols, i.e., bare MCH. Similarly the variation induced by hybridization is calculated as the percentage change in R_{ct} after the hybridization process with respect to the ssDNA/MCH layer charge transfer resistance.

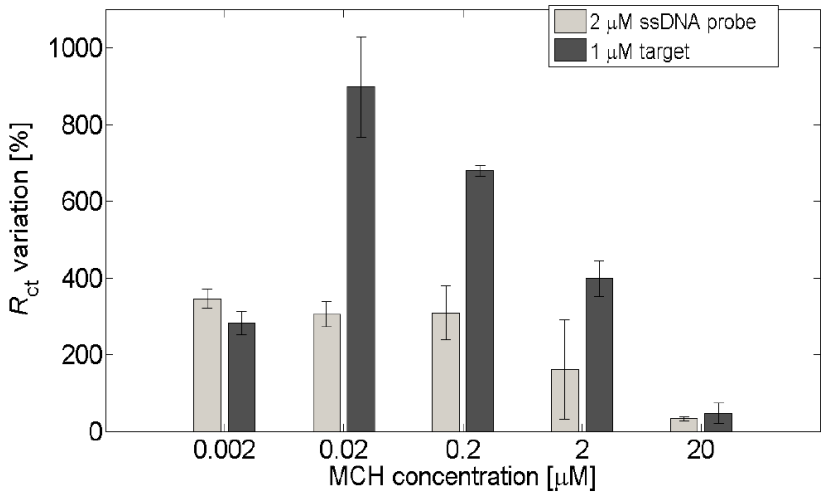

Figure 3.3-3. Charge transfer resistance variation as a function MCH concentration in mixed ssDNA/MCH immobilization solution. Grey bars represent the percentage variation between the pure MCH and ssDNA/MCH self-assembled monolayers. Black bars represent the percentage variation after the hybridization with 1 μM complementary DNA sequences, with respect to the charge transfer resistance of the ssDNA/MCH layer.

The maximum value of the percentage difference can be found for MCH concentration of 0.02 μM, while the variation strongly decreases for thiol density above and below this value. When the concentration of MCH is too low, the hybridization detection sensitivity is reduced because the probes orientation is not controlled and non-specific adsorption of ssDNA probes on the electrode surface can occur. When the MCH concentration is too high, i.e., 20 μM, that corresponds to a concentration ratio of $c_{ssDNA}/c_{MCH} = 0.1$, the R_{ct} variation is reduced to 48 %. This decreased sensitivity of

hybridization detection is due to the high impedance of the self-assembled monolayer (see Figure 3.3-2 (a)), that prevents any further R_{ct} variation.

The kinetics of adsorption of the mixed solution of ssDNA and MCH was monitored with DPV and EIS measurements in 1mM $Fe(CN)_6^{4-/3-}$ in KCl 100 mM solution. Experiments were performed over a period of 120 minutes.

Figure 3.3-4 (b) shows the normalized peak current from DPV measurements as a function of adsorption time. Results are related to two different MCH concentrations, i.e., 2 μM and 20 μM, which correspond to a concentration ratio of $c_{ssDNA}/c_{MCH} = 1$ and $c_{ssDNA}/c_{MCH} = 0.1$, respectively. Figure 3.3-4 (b) shows that the adsorption process is faster with a concentration ratio of 0.1, which corresponds to the highest concentration of MCH solution. In this case, the normalized peak current reach the 95 % of peak variation at 45 minutes and then it remains nearly constant. In the case of concentration ratio $c_{ssDNA}/c_{MCH} = 1$, i.e., a MCH concentration of 2 μM, the adsorption process is slower, and the normalized peak current increases throughout the duration of the experiments. The same behavior is shown in Figure 3.3-4 (a), where the charge transfer resistance R_{ct} has been derived by fitting EIS data using (1.4.4) similarly to Section 3.2 and then plotted as a function of adsorption time. The adsorption kinetics of mixed solution with concentration ratio of 0.1 is faster and induces an higher R_{ct}.

The presence of MCH is very important for the control of ssDNA monolayer [15]. There are differences when the self-assembled monolayer is developed in a two step process [15] or in a one step process with a mixed solution. Considering Figure 3.3-4, it can be observed that:

- an higher concentration of MCH induces a more rapid formation of the self-assembled monolayer;
- as MCH chains and probe DNA sequences are competing in the adsorption, and the MCH chains are shorter, the biological layer will consist mainly of MCH rather than ssDNA probes;
- the monolayer is more uniform and compact, as shown in Figure 3.3-2 by EIS and DPV measurements: an higher R_{ct} value indicates that the electron transfer is inhibited, that corresponds to a lower peak current value measured with DPV. The high value of the charge transfer resistance heavily influences the sensitivity of the sensor.

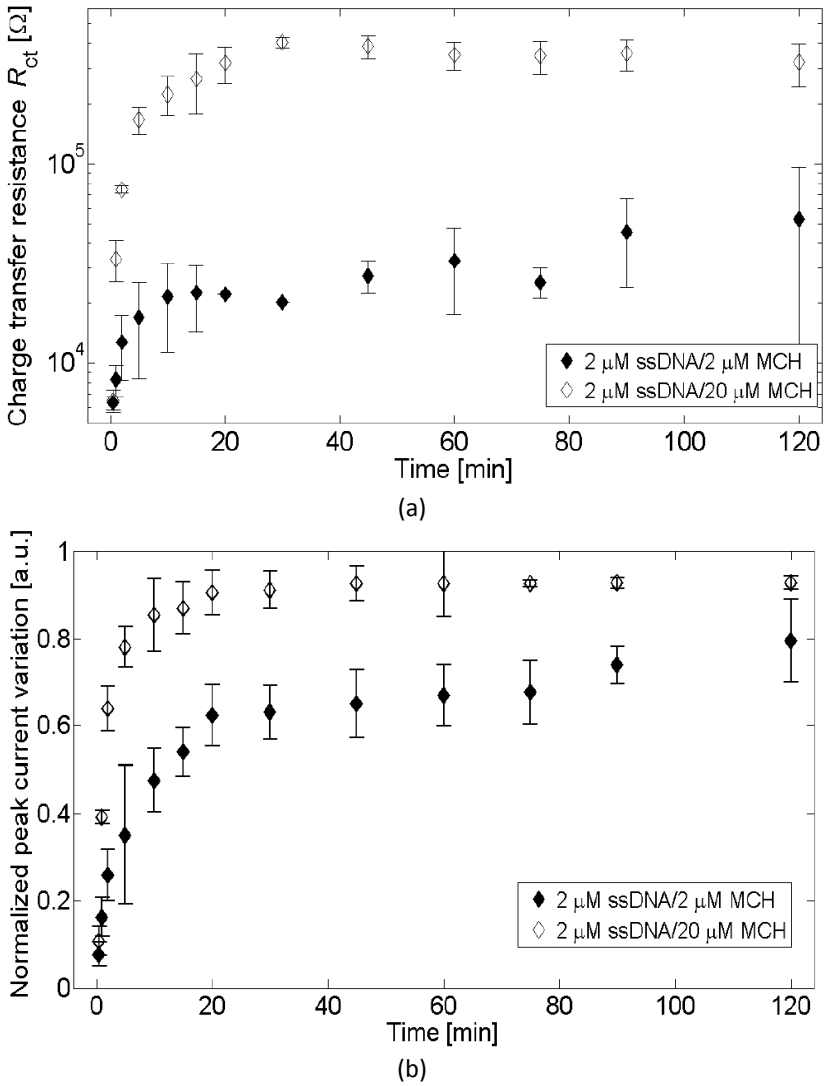

Figure 3.3-4. Adsorption kinetics of mixed solution of ssDNA/MCH. Graphs show kinetics data for a concentration ratio of c_{ssDNA}/c_{MCH} = 1 and c_{ssDNA}/c_{MCH} = 0.1. Charge transfer resistance from EIS measurements as a function of adsorption time (a) and normalized peak currents from DPV measurements as a function of adsorption time (b).

3.4 Bibliography

[1] Pividori, M.I., Merkoçi, A., Alegret, S., 2000. Biosensors and Bioelectronics 15, 291-303.

[2] Hianik, T., Gajdos, V., Krivanek, R., Oretskaya, T., Metelev, V., Volkov, E., Vadgama, P., 2001. Bioelectrochemistry 53 (2), 199-204.

[3] Peterson, A.W., Heaton, R.J., Georgiadis, R.M., 2001. Nucleic Acids Research 29 (4), 5163-5168.

[4] Campuzano, S., Kuralay, F., Nòn, M.J.L.-C., Bartošìk, M., Vyavahare, K., Paleček, E., Haake, D.A., Wang, J., 2011. Biosensors and Bioelectronics 26 (8), 3577-3583.

[5] Gong, P., Levicky, R., 2008. PNAS 105 (14), 5301-5306.

[6] Keighley, S.D., Estrela, P., Li, P., Migliorato, P., 2008. Biosensors and Bioelectronics 24 (4), 906-911.

[7] Carvalhal, R., SanchesFreire, R., Kubota, L., 2005. Electroanalysis 17 (14), 1251-1259.

[8] Hoogvliet, J.C., Dijksma, M., Kamp, B., van Bennekom, W.P., 2000. Analytical Chemistry 72 (9), 2016-2021.

[9] Nuzzo, R.G., Allara, D.L., 1983. J. Am. Chem. Soc. 105, 4481-4483.

[10] Bain, C.D., Troughton, E.B., Tao, Y.-T., Evall, J., Whitesides, G.M., Nuzzo, R.G. , 1989. J. Am. Chem. Soc. 111, 321-335.

[11] Herne, T.M., Tarlov, M.J., 1997. J. Am. Chem. Soc. 119, 8916-8920.

[12] Steel, A.R., Herne, T.M., Tarlov, M.J., 1998. Anal. Chem. 70, 4670-4677.

[13] Dharuman, V., Hahn, J.H., 2007. Sensors and Actuators B 127 (2), 536-544.

[14] Boozer, C., Chen, S., Jiang, S., 2006. Langmuir 22 (10), 4694-4698.

[15] Peterlinz, K.A., Georgiadis, R.M., Herne, T.M., Tarlov, M.J., 1997. J. Am. Chem. Soc. 119, 3401-3402.

[16] Ferrario, A., Scaramuzza, M., Pasqualotto, E., De Toni, A., Paccagnella, A., 2012. Procedia Chemistry 6, 36-45.

[17] Erlenkötter, A., Kottbus, M., Chemnitius, G.-C., 2000. Journal of Electroanalytical Chemistry 481 (1), 82-94.

[18] Trasatti, S., Petrii, O.A., 1991. Pure & Appl. Chem. 63, 711-734.

[19] Bard, A.J., Faulkner, L.R., 2001. John Wiley and Sons.

[20] Alfonta, L., Bardea, A., Khersonsky, O., Katz, E., Willner, I., 2001. Biosensors and Bioelectronics 16 (9-12), 675-687.

[21] Peterson, A.W., Heaton, R.J., Georgiadis, R.M., Nucleic Acids Research 29 (4), 5163-5168.

[22] Keighley, S.D., Li, P., Estrela, Migliorato, P., 2008. Biosensors and Bioelectronics 23 (8), 1291-129.

[23] Ferrario, A., Scaramuzza, M., Pasqualotto, E., De Toni, A., Paccagnella, A., 2012. Journal of Electroanalytical Chemistry.

[24] Campuzano, S., Pedrero, M., Montemayor, C., Fatas, E., Pingarron, J.M., 2001. Journal of Electroanalytical Chemistry 586 (1), 112-121.

[25] Chang, B.-Y., Park, S.-M., 2010. Annual Review of Analytical Chemistry 3 (1), 207-229.

[26] Millan, K.M., Saraullo, A., Mikkelsen, S.R., 1994. Anal. Chem. 66, 2943-2948.

[27] Gong, P., Lee, C.-Y., Gamble, L.J., Castner, D.G., Grainger, D.W., 2006. Analytical Chemistry 78 (10), 3326-3334.

[28] Lao, R., Song, S., Wu, H., Wang, L., Zhang, Z., He, L., Fan, C., 2005. Analytical Chemistry 77 (19), 6475-6480.

Chapter 4. Detection of lactic acid with redox catalytic enzymes

4.1 Introduction to enzymatic biosensors

The ability to monitor enzymatic reactions through the rapid and reliable assessment of their specific substrates concentrations has a growing importance both in clinical analysis and in biotechnological applications. Lactate, i.e., the ionic form of lactic acid, is one of these important substrates due to its relevance in various fields: in clinical analysis it is well-known that its concentration in human blood samples can be related to cardiac or respiratory pathologies [1], and therefore its detection enables early diagnosis of critical situations [2]; in sport medicine, blood lactate concentration is an indicator of the physical effort intensity through the aerobic and anaerobic thresholds [3]; in food processing applications, lactate measurements are an easy and effective way to monitor microbial contamination of dairy products [4].

When dealing with lactate concentration assessment in liquid samples, enzyme-modified electrodes represent common and reliable tools [5]. This kind of biosensors provides high selectivity to a specific substrate and fast response time [6] but the detection performance indicators, e.g. linear range, stability, sensitivity and lifetime, are tightly related to the technique used to bind enzymes to electrodes surfaces [7]. For this reason, an in-depth study of the functionalization protocol is crucial when developing reliable biosensors oriented to mass-production.

The most widely used technique for lactic acid (LA) detection is a colorimetric and chromatographic analysis, which are expensive and time-consuming due to sample pre-treatment. Conversely, both amperometric [8] and potentiometric [9] electrochemical analysis allow high sensitivity and fast response.

The two principal electrochemical enzyme-modified sensors refer to lactate oxidase, LOx (see Figure 4.1-1) and lactate dehydrogenase. The lactate oxidase catalytic reaction pathway is [10, 11]:

$$\text{lactate} + (\text{LOx})_{OX} \rightarrow \text{pyruvate} + (\text{LOx})_{RED} \quad (4.1.1)$$

$$(\text{LOx})_{RED} + (\text{Med})_{OX} \rightarrow (\text{LOx})_{OX} + (\text{Med})_{RED} \quad (4.1.2)$$

$$(\text{Med})_{RED} \rightarrow (\text{Med})_{OX} + e^{-} \quad (4.1.3)$$

where Med indicates the redox mediator. In this pathway, the pyruvate is a product of the catalytic reaction, and is a ketone organic acid. In presence of lactic acid, the redox active sites of lactate oxidase at the electrode surface produces pyruvic acid and gain an electron from the electrode. With redox reactions, this electron is first exchanged between the enzyme and the redox mediator molecule (Med), and then exchanged between the two forms of the mediator, i.e., reduced and oxidized, in the solution bulk. In this way, an electrons current is generated between functionalized working electrode and reference electrode, that is proportional to the number of lactate molecules, i.e., to lactic acid concentration.

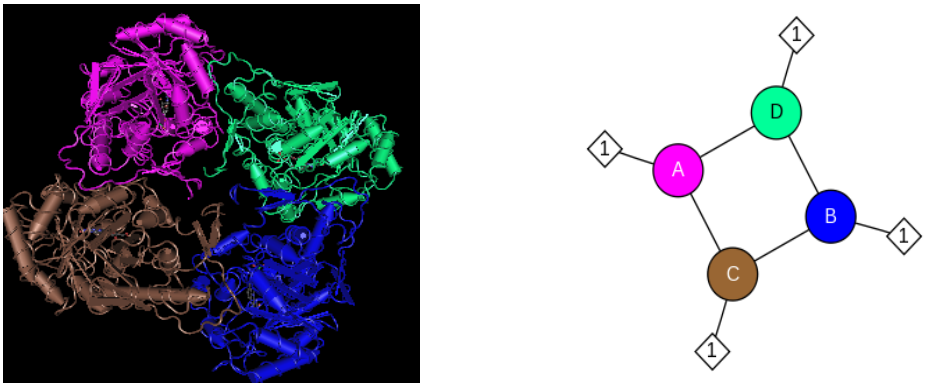

Figure 4.1-1. Structure and interactions of lactate oxidase enzyme [12].

The enzymatic immobilization technique on the electrode surface plays a crucial role in enzymatic biosensors effectiveness. Two different immobilization techniques will be presented, i.e., direct adsorption and covalent binding through a cross-linker [13].

The direct adsorption of LOx enzymes on gold electrode surface relies on electrostatic forces between metal and enzyme electrical charges. As can be seen from Figure 4.1-2, an electrical charge distribution can be identified on enzyme surface: this distribution allows the interaction between electrode and LOx, enabling an easy immobilization way. The drawback of this technique is that there is no control on enzymes position: this means that the functionalization through direct adsorption does not optimize the enzymes spatial displacement, and can therefore happen that a number of enzymes do not expose their redox active sites to the sample. This uncontrollable situation inhibits the redox response, and therefore the amperometric biosensor performance [14].

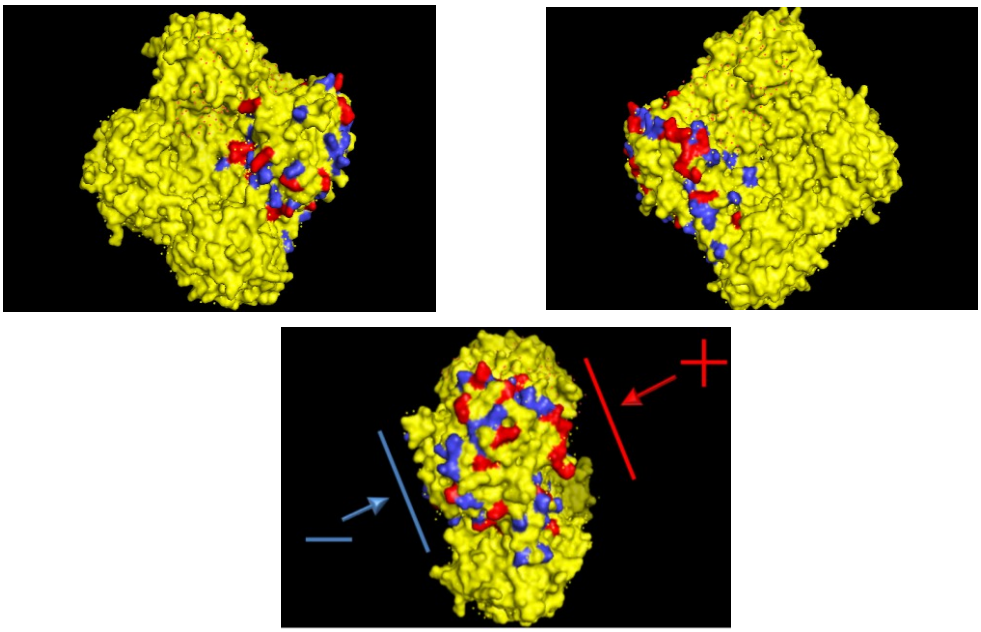

Figure 4.1-2. Superficial charge distribution of lactate oxidase enzymes. Blue dots represent negative charges and red dots positive ones. Red arrow indicates the positively charged side. Blue arrow indicates the negatively charged side of the enzyme by the overall amino acid residues.

To maintain the optimal position of the immobilized enzymes, a proper self-assembled monolayer (SAM) can be created on the electrode surface before the enzymatic functionalization. The SAM molecules, i.e., the cross-linkers, are firmly anchored to the metal surface, and expose a functional group at the other end. The enzymes have few sites that can create a covalent bonding with these groups, so their position on the SAM can be predicted. By choosing the proper SAM molecule with the correct functional group, the enzymes spatial position on the electrode can be controlled in a very effective way, and therefore exposing the maximum number of redox active sites to the sample.

For the cross-linking immobilization technique, DTSP (3,3'-dithiodipropionic acid di(N-hydroxysuccinimide ester, see Figure 4.1-3) has been used. DTSP creates a self-assembled monolayer on the electrodes by disulfide groups adsorption [15] with maximum linkage distance of 1.1 nm [16]. This SAM sets an orientation of bind enzymes

[17] that promotes reduction-oxidation reactions and therefore electrons transfer through the functionalized electrodes surface.

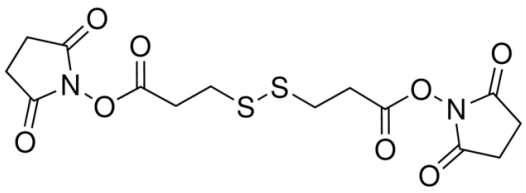

Figure 4.1-3. DTSP molecular structure.

4.2 Directly adsorbed enzymes for lactic acid amperometric detection

4.2.1 Electrical characterization and validation

In this Section, an enzyme-based biosensor for the detection of lactic acid (LA) is presented and electrically characterized. The enzymes immobilization strategy is direct adsorption on the gold electrode surface, i.e., electrostatic binding between gold surface and enzymes superficial electrical charges [14].

Both electrochemical and voltammetric measurements have been carried out in order to evaluate the main features of the system: electrochemical impedance spectroscopy (EIS) measurements EIS measurements have been performed with a Solartron SI1260 impedance analyzer in a frequency range between 1 Hz and 1 MHz, while a potentiostat from CH Instruments (CHI129) has been used for cyclic voltammetry (CVM) measurements. Differently from the integrated electrochemical cell of Figure 3.2-1, for this biosensor both the reference and the counter electrode were external: the former was a standard silver/silver chloride in potassium chloride 1 M reference electrode (CHI111, CH Instruments), while the latter was a platinum wire counter electrode (CHI129, CH Instruments).

During gold electrodes surfaces preliminary electrical characterization, EIS and CVM measurements have been performed with non-functionalized electrodes surfaces, i.e., gold electrodes without any biological coverage. The aim of these measurements was to determine the best trade-off between the signal to noise ratio of interfacial charge transfer and redox mediator concentration (see Figure 4.2-1). From these tests the measurement solution has been chosen as ferri/ferrocyanide redox couple, i.e., $Fe(CN)_6^{4-/3-}$ 1 mM in phosphate buffer solution 100 mM. For CVM measurements, the potential ranged from -0.20 V to +0.70 V, with a scan rate v of 50 mV/s.

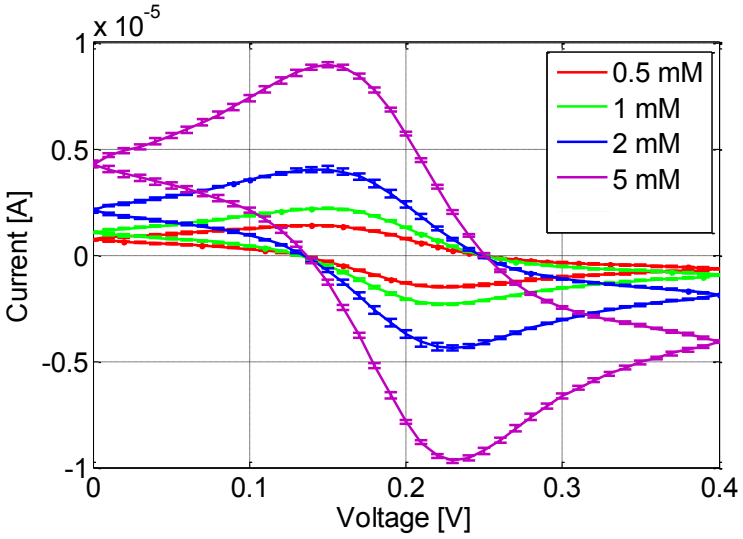

Figure 4.2-1. CVM measurements on 1 mm diameter gold electrodes for different redox mediator concentrations with scan rate of 50 mV/s.

Using the identified measurement solution, different functionalization tests have been performed on gold electrodes surfaces using different concentration of lactate oxidase (LOx) enzymes from Pediococcus species in buffer solutions, ranging from the maximum concentration obtained from producer, i.e., C_{LOx} = 25 mg/mL, down to C_{LOx} = 1 mg/mL, through subsequent dilutions of the maximum concentration stock solution.

The immobilization protocol consisted in the deposition of 1 μL of enzyme solution directly onto the electrodes for 1 hour and then rinsed with de-ionized water [18]. EIS measurements have been performed on the functionalized electrodes to determine the effectiveness of the functionalization protocol: in Figure 4.2-2 is depicted an example of these assessments, where the rinse process after the functionalization step does not affect the functionalized interface.

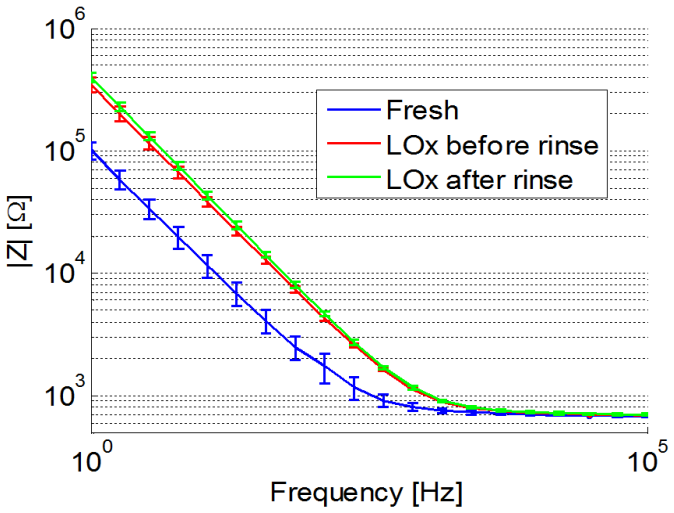

Figure 4.2-2. EIS measurements on functionalized gold electrodes before (blue line, "Fresh") and after (red and green lines) enzymatic functionalization.

Figure 4.2-3 depicts EIS measurements of functionalized gold surfaces with different LOx solutions: as can be seen, increasing the LOx concentration in the solution causes an increase of the measured electrical impedance after functionalization, suggesting that more biological material is immobilized onto the electrode.

The EIS data have been fitted using the model depicted in Figure 4.2-4 in order to assess electrodes enzymatic coverage. The main feature of this model is the weighted contribution of two different electrical impedances to the overall system impedance [19].

By using this model, the simulation approach is to consider the two extreme situation of the electrode interface, i.e., non-functionalized ("fresh") surface and electrode surface saturated with enzymes. The EIS data obtained from these two situations are fitted using the same basic model: a series between a resistor R_s, that represents the buffer spreading resistance (Section 1.3), a constant phase element related to the interfacial electrochemical processes [20] (Z_{fresh} and Z_{LOx} for non-functionalized and fully-covered electrodes, respectively), and the parallel R_{Au} // C_{Au} related to gold surface intrinsic electrical parameters.

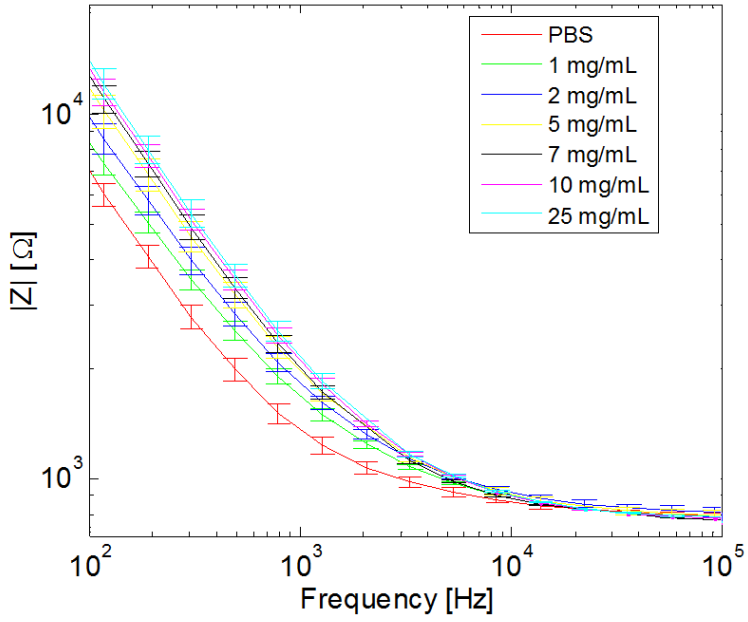

(a)

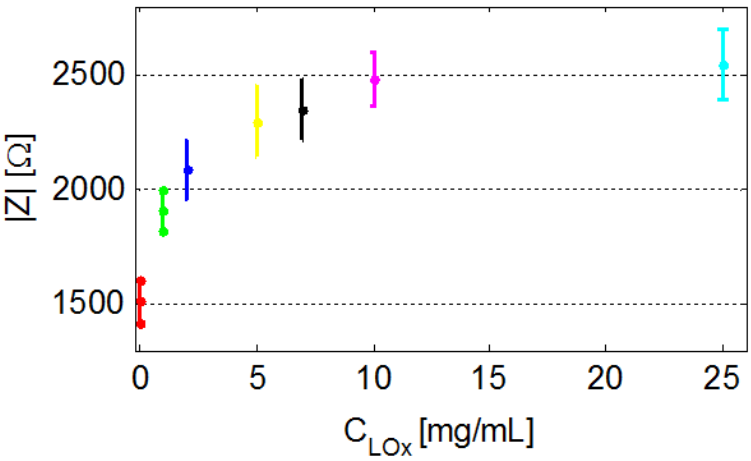

(b)

Figure 4.2-3. EIS measurements on round gold electrodes (1 mm diameter) with different concentrations of immobilized LOx (a). EIS response of |Z| at 1 kHz (b).

To obtain the complete model of Figure 4.2-4, these two similar branches are placed in parallel, sharing the same electrolyte resistance. A numerical multiplier a is used to properly weight the two constant phase elements, in order to fit the EIS data. As a result, all the electrical parameters of Figure 4.2-4 model are fixed and determined from preliminary measurements, and the only fitting parameter is the weight a.

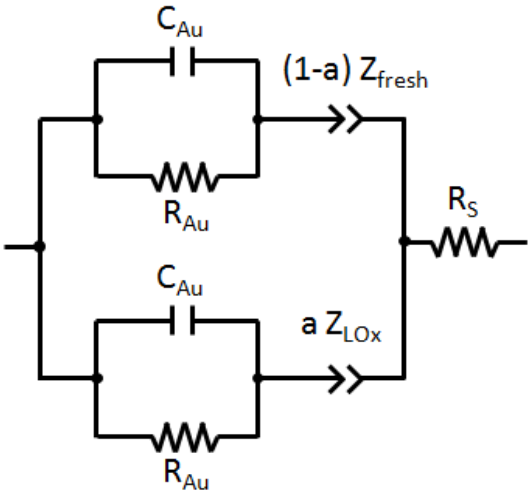

Figure 4.2-4. Equivalent electrical model for electrode coverage studies. Parameter a is the numerical impedance multiplier. Free electrode interface equivalent element Z_{fresh} is multiplied for (1-a), while full enzyme-covered electrode impedance Z_{LOx} for a.

As usual (see Section 1.5), the impedance frequency dependence of the constant phase elements have been modeled as

$$Z_{fresh} = \frac{1}{C_0(j2\pi f)^{n_0}} \quad , \tag{4.2.1}$$

$$Z_{LOx} = \frac{1}{C(j2\pi f)^{n}} \quad , \tag{4.2.2}$$

with values described in Table 4.2-1.

Values for R_{Au} and C_{Au} (see Table 4.2-1) have been obtained using COMSOL Multiphysics 3.4 (AC/DC In-plane electric currents module) to simulate the electrical impedance of the raw gold sensor, with size 2 cm x 1 cm and thickness of 50 nm. Gold electrical parameters have been set to conductivity σ = $4.5 \cdot 10^7$ S/m and relative dielectric permittivity ε_r = 6.9 (see Figure 4.2-5).

Electrolyte spreading resistance R_s value has been obtained by fitting EIS measurements of phosphate buffer solution (PBS, i.e., NaCl 137 mM, KCl 2.7 mM, Na_2HPO_4 10 mM, KH_2PO_4 2 mM with pH 7.4).

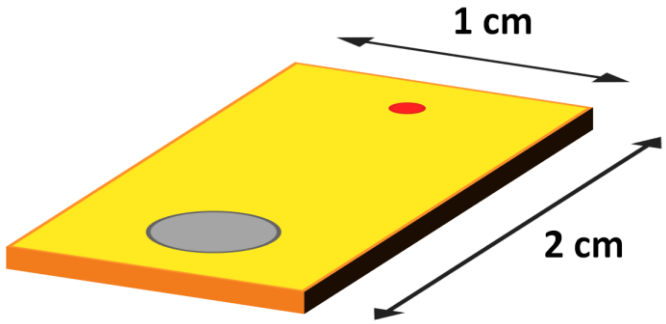

Figure 4.2-5. Biosensor model (not to scale). Grey circle represents the area (1 mm diameter) where the external reference electrode is placed in contact with the sample. Red circle represents the area (100 μm diameter) where the sensor working electrode is connected to the impedance analyzer instrument. Yellow part (50 nm thick) represents gold [14].

To obtain the values of the functionalization parameters of the model, electrodes surfaces have been full covered with 25 mg/mL LOx in PBS 100 mM solution. Functionalization EIS data have been fitted with similar equivalent circuit using (4.2.2), making the weighting parameter a the only fitting variable of the complete electrical model.

The behavior of the weighting parameter as a function of immobilized LOx concentration C_{LOx} has been obtained from EIS measurements: each curve depicted in Figure 4.2-3 (a) has been fitted using the coverage model, obtaining the values described in Figure 4.2-6.

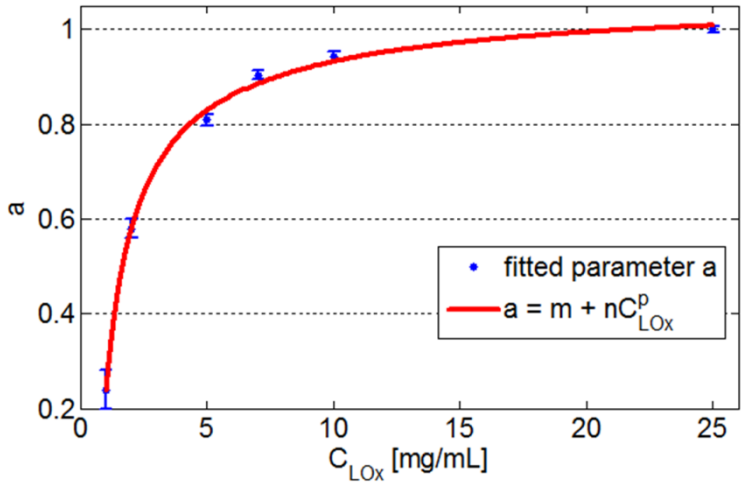

Figure 4.2-6. Variation of weighting parameter a as a function of enzyme concentration C_{LOx}. Fitting parameters are: m = 1.086, n = -0.7414, p = -0.8473. With the described power function the goodness of fit is R^2 = 0.9979.

Table 4.2-2 describes the values of the weighting parameter as a function of C_{LOx} with percentage fitting error. As can be seen from Figure 4.2-6, weighting parameter a trend reaches a saturation level for LOx concentrations above 10 mg/mL, which corresponds to a = 0.94, therefore in this condition an adequate electrode coverage is obtained.

To validate this analysis, biosensor electrical response has been evaluated with CVM measurements in presence of lactic acid 1 mM and 100 mM: Figure 4.2-7 shows CVM reduction currents peaks, and it can be seen that the trade-off between detection efficiency and electrodes coverage can be obtained for C_{LOx} = 10 mg/mL.

Parameter		Value	Error [%]
R_{Au}		0.6078 Ω	-
C_{Au}		2.62 aF	-
Z_{fresh}	C_0	0.44 μF	1.82
	n_0	0.898	0.35
R_s		821 Ω	0.94
Z_{LOx}	C	0.23 μF	1.71
	n	0.888	0.31

Table 1: Electrical parameters for Figure 2 model.

C_{LOx} [mg/mL]	1	2	5	7	10	25
a	0.239	0.579	0.809	0.903	0.942	0.99975
Error [%]	8.46	1.77	0.70	0.49	0.51	0.37

Table 4.2-2. Values for weighting parameter (a) as a function of enzyme concentration (see Figure 4.2-6).

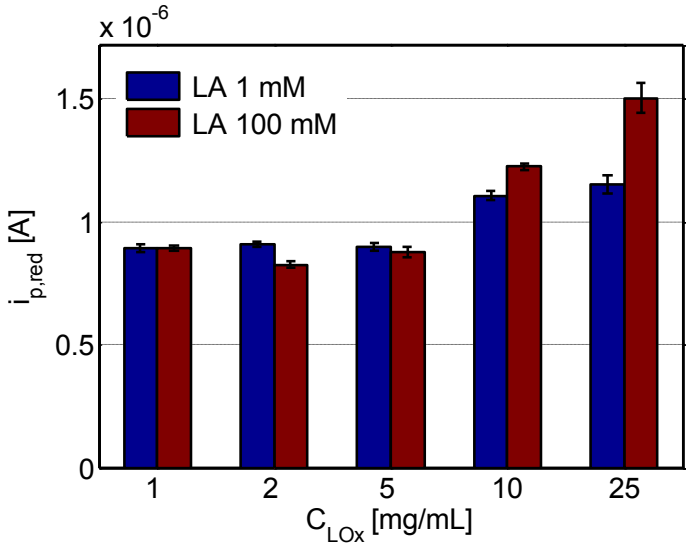

Figure 4.2-7. CVM peak currents with different concentrations of immobilized LOx and 1 mM (blue) and 100 mM (red) LA. For C_{LOx} below 10 mg/mL the target analytes cannot be properly detected.

Once identified the more effective enzyme concentration for the device, the enzymatic biosensor has been tested with LA racemic mixture at different concentrations. First 2 mm diameter gold electrodes have been used to detect LA concentration range between 70 μM up to 1.2 M in order to verify transduction saturation levels. Results of CVM measurements are depicted in Figure 4.2-8.

In order to study sensor lower detection limits and sensitivity, CVM measurements have been carried out in a lower LA concentration range, i.e. down to 1 μM, with 1 mm diameter electrodes. Figure 4.2-9 depicts reduction peaks currents as a function of LA concentration. The sensor linear response range is comparable with similar works in literature [10], with corresponding LA sensitivity of about 6.24 μA mM^{-1} cm^{-2} [21].

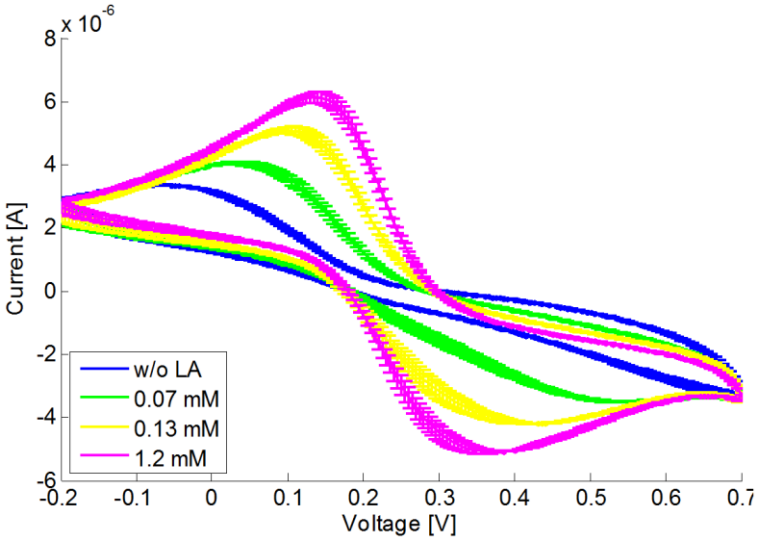

(a)

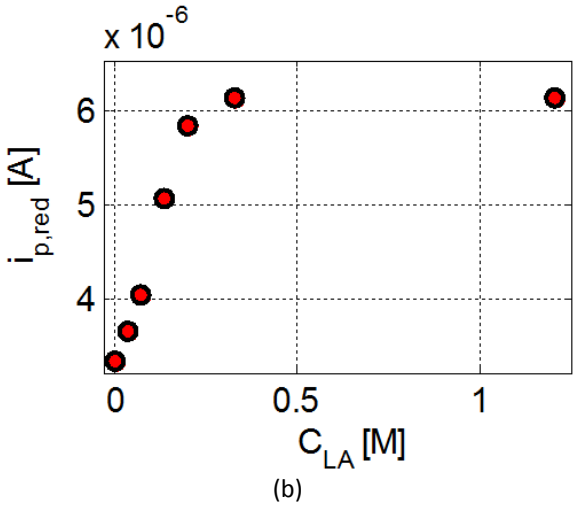

(b)

Figure 4.2-8. CVM response of 2 mm diameter gold sensors with different LA concentration in measurement solution (a). CVM reduction peaks currents as a function of LA concentrations (b). The response saturates for LA concentrations above 300 mM.

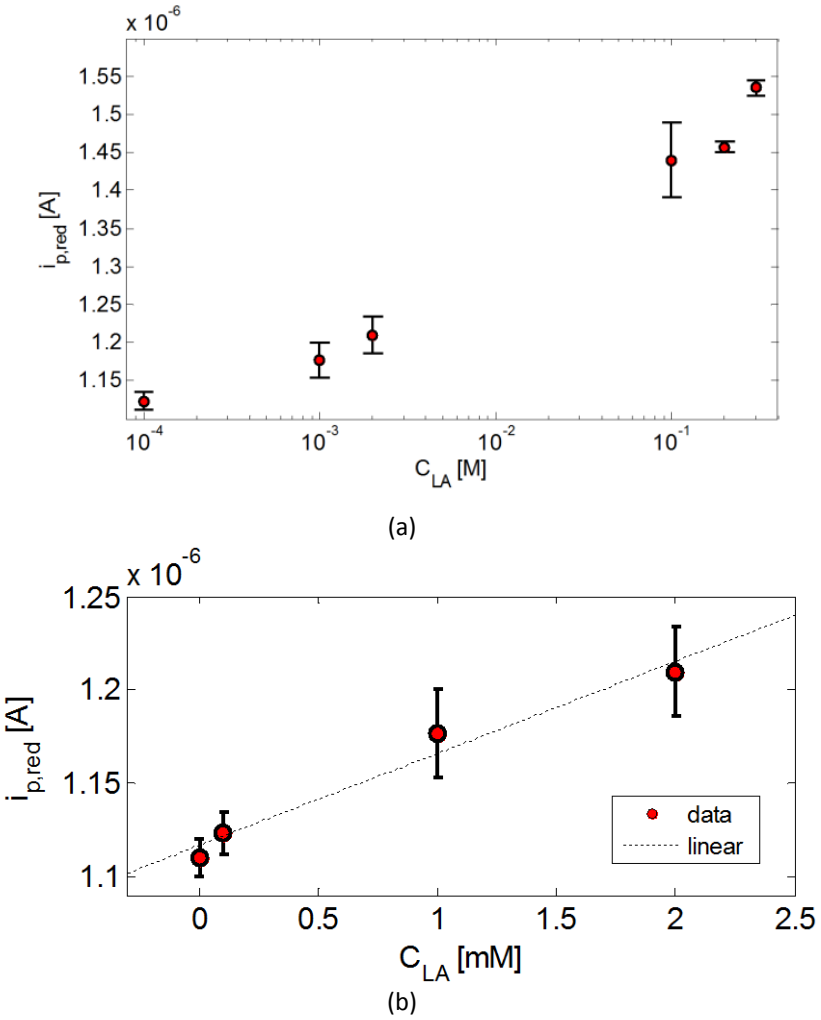

Figure 4.2-9. CVM reduction peaks currents as a function of LA concentrations for round gold electrodes (1 mm diameter). The tested LA concentrations vary from 1 µm up to 300 mM (a). Magnification in milli-molar range (b): regression line: $i_{p,red} = 4.9 \cdot 10^{-2} C_{LA} + 1.1 \cdot 10^{-6}$.

4.2.2 Study of enzymatic functionalization reproducibility

The enzymatic functionalization by direct adsorption of biological material relies on a statistical and poorly reproducible process, affected by temperature and other environmental parameters that influence the final result.

The present Section describes how a suitable electrical model can be used to study the reproducibility of the functionalized layer using EIS measurements.

Figure 4.2-10 describes the Nyquist plot of EIS data depicted in Figure 4.2-3 (a). Recalling Section 1.3, the behavior is compatible with a bare constant phase element at the tested frequencies: in fact, in the complex plane the locus of EIS data are straight lines with angular coefficients that depend on the enzymes concentration. Figure 4.2-11 describes this situation, comparing the behavior of EIS data at a fixed frequency with the fitted angular coefficients as a function of lactate oxidase concentration C_{LOx}. The linear fit has been obtained with the classical model

$$-\mathrm{Im}(Z) = m \cdot \mathrm{Re}(Z) + q \quad , \tag{4.2.3}$$

where m and q are the angular coefficient and the intercept of the fitted line.

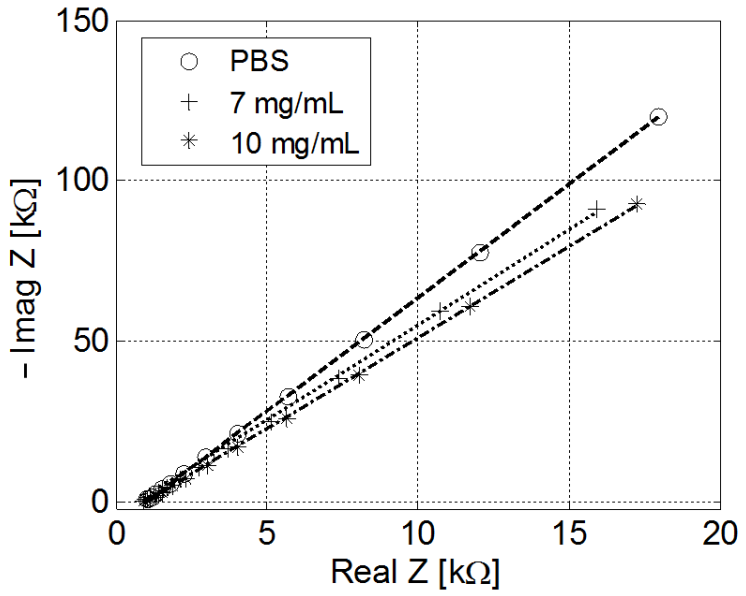

Figure 4.2-10. Nyquist plot of EIS data depicted in Figure 4.2-3.

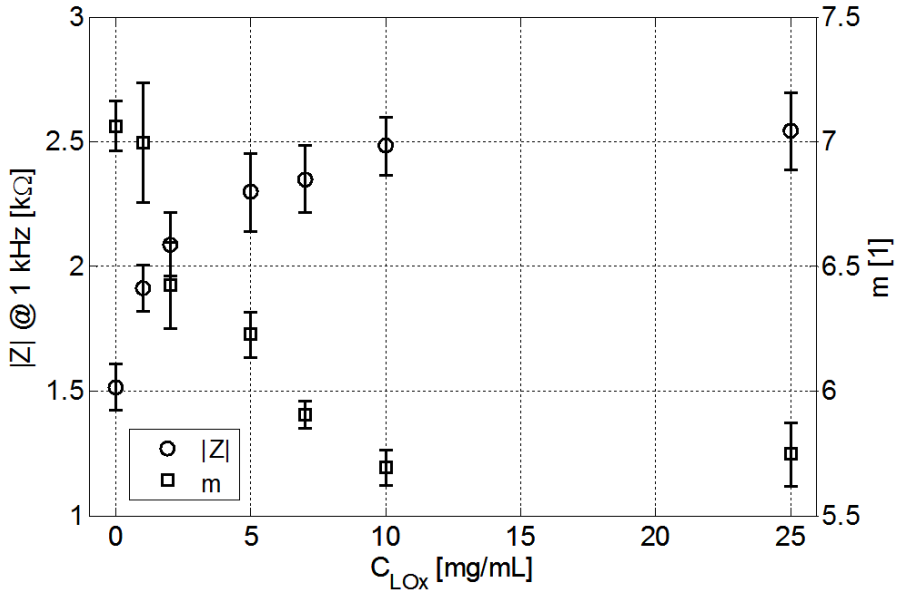

Figure 4.2-11. Plot of impedance magnitude at fixed frequency and angular coefficients obtained from linear fit of Figure 4.2-10 EIS data.

To fit Figure 4.2-10 data, the model (4.2.4) has been used:

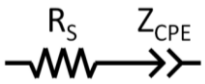

$$Z(\omega) = R_s + Z_{CPE} = R_s + \left(\frac{1}{j\omega C}\right)^n = \\ = \frac{1 + (j\omega)^n R_s C^n}{(j\omega C)^n} \quad , \tag{4.2.4}$$

that is similar to the model (1.4.1) of the ideally polarizable electrode. In this case, diffusion-limited electrochemical reactions at the electrode surface has been taken into account by using a constant phase element (CPE) instead of a simple capacitor (see Section 1.4).

The fitting parameters of (4.2.4) model are the capacitance C and its numeric exponential n. The electrolyte resistance R_s has been evaluated from EIS measurements of non-functionalized electrodes and kept constant during subsequent analysis. The fitting result for C and n are depicted in Figure 4.2-12 (a), while (b) describes the behavior of C^n, its trend fitted with a double exponential function and the normalized C^n with the following formula:

$$\text{normalized } C^n = 1 - \frac{C_{LOx}^n}{C_0^{n_0}} \quad , \tag{4.2.5}$$

where C_0^{n0} is the fit result of non-functionalized electrode and C^n_{LOx} represents the fit results as a function of enzyme concentration C_{LOx}.

The behavior of the fitting parameters, and especially of C^n, resembles that of the weighting parameter a of Figure 4.2-6: in fact, observing Figure 4.2-12 (b) it can be seen that the enzymatic concentration that ensures the broader electrode coverage with the minimum quantity of enzyme is 10 mg/mL, as concluded with Figure 4.2-4 model.

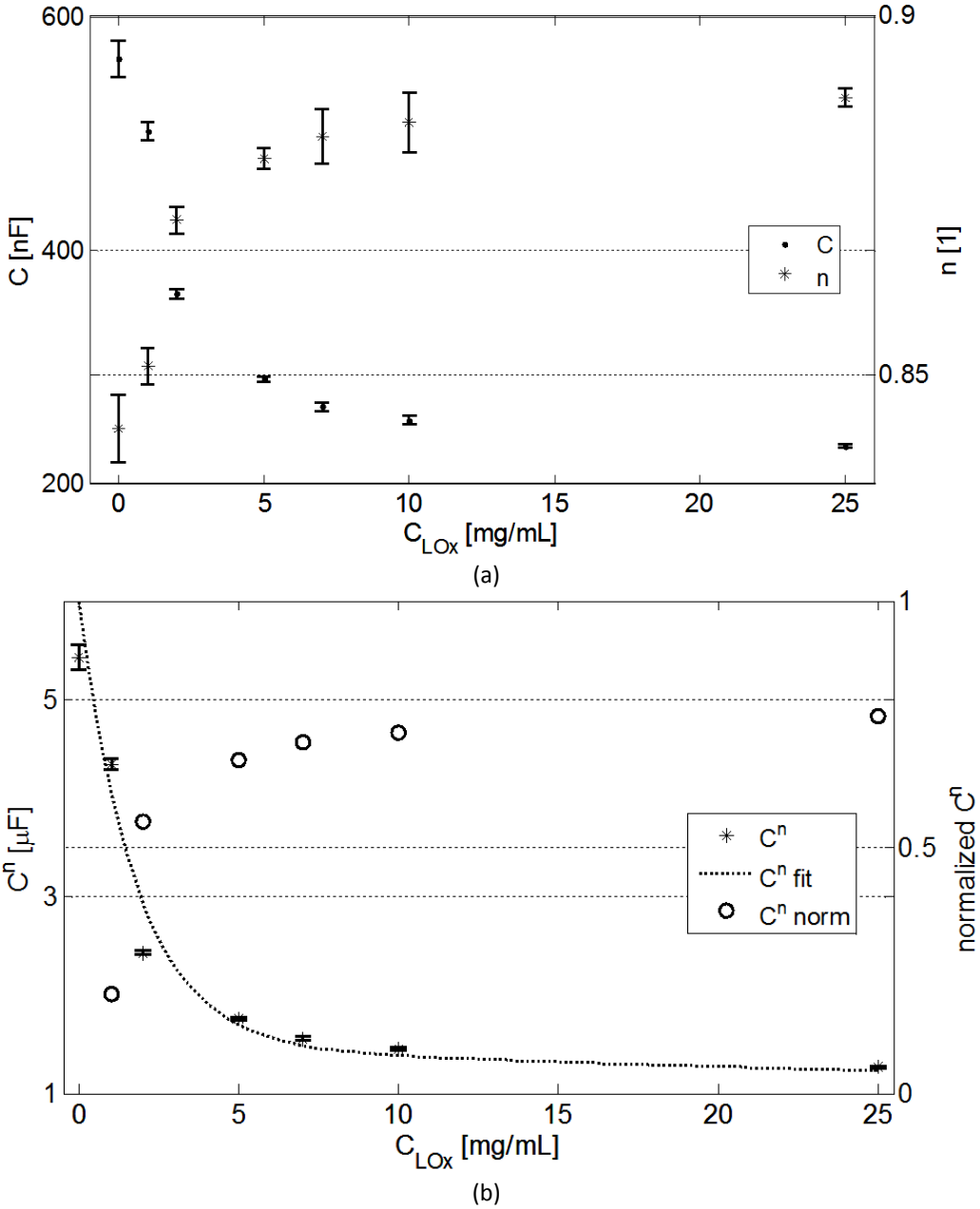

Figure 4.2-12. Fitting parameters of (4.2.4) model (a). C^n parameter with double-exponential fit and normalization (b).

C^n has been used as parameter to assess the reproducibility of the direct adsorption functionalization with lactate oxidase of 35 different biosensors. Each device has been functionalized with the same protocol (see Section 4.2.1) and with the same functionalization solution, i.e., LOx 10 mg/mL in phosphate buffer saline 100 mM. EIS measurements have been performed after functionalization and before lactic acid detection, and the data have been fitted with model (4.2.4).

The distribution of the evaluated C^n is depicted in Figure 4.2-13. A Gaussian function has been used to fit the distribution, obtaining a mean value of C^n = 1.407 μF (R^2 = 0.975). Using the fitted double exponential function of Figure 4.2-12 (b), this value correspond to a LOx concentration of 8.98 mg/mL, i.e., a 10 % error with respect to the nominal concentration used for device functionalization. This error can be imputed to both the poor reproducibility of the functionalization by direct adsorption, and to the control of the substances during the production of the stock solutions. Nevertheless, the presented methodology proved to be suitable for fast and effective assessment of functionalization reproducibility of enzymatic biosensors.

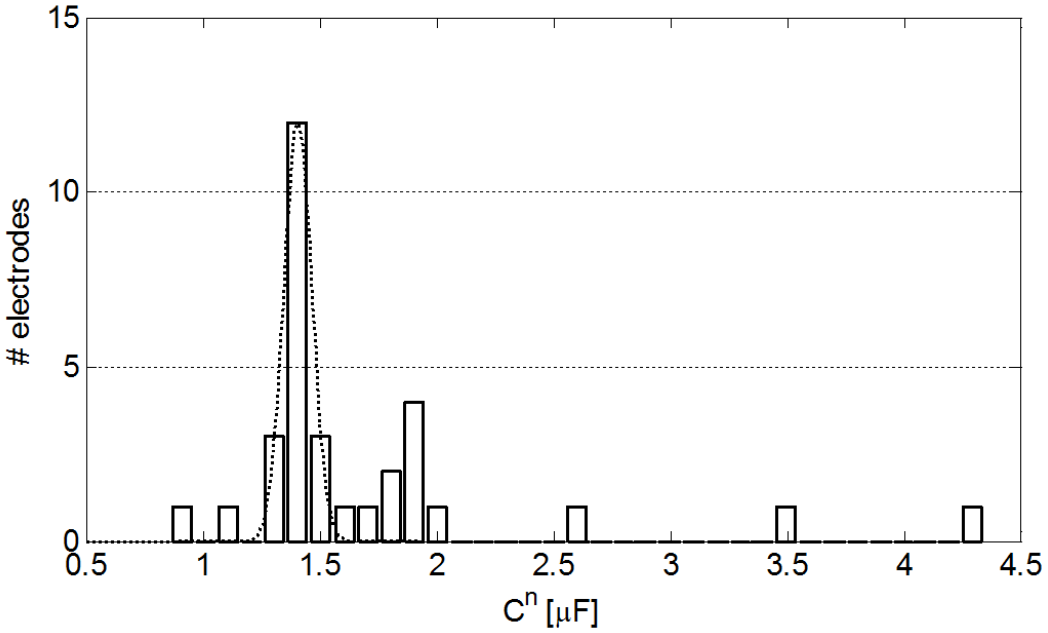

Figure 4.2-13. Distribution of C^n parameter over 35 devices with Gaussian fit (dotted line).

4.3 Enzymatic functionalization using a cross-linker

In this Section, the electrode functionalization process has been modified from immobilization of directly adsorbed LOx enzymes with electrostatic forces, to LOx enzymes immobilized via covalent bonding with a cross-linker.

The system is similar to that described in Section 4.2. Stock solutions of lactate oxidase from Pediococcus species 50 U (molecular weight: 4271.3) have been prepared by dissolving powdered enzymes in 250 µL of phosphate buffer saline (PBS), then aliquoted in volumes of 15 µL and stored at -10 °C. These volumes have been further diluted with 100 mM PBS in order to obtain proper enzyme concentrations just before performing electrodes functionalization. The solution used for electrochemical measurements have been obtained by dissolving redox mediator salts in PBS to obtain 1 mM $Fe(CN)_6^{4-/3-}$ in 100 mM PBS.

The cross-linker is the DTSP (molecular weight: 404.42), i.e., 3,3'-dithiodipropionic acid di(N-hydroxysuccinimide ester), and self-assembled monolayers (SAMs) of different concentrations have been obtained by diluting it in proper volumes of dimethyl sulfoxide (DMSO) 10 %.

The functionalization protocol for directly adsorbed LOx enzymes is similar to that described in Section 4.2: active electrodes surfaces have initially been rinsed with ultra pure water and then 1 µL of enzyme solution has been drop-casted over each surface. Functionalized electrodes have been kept in wet environment for one hour at room temperature, and then rinsed again with ultra pure water to wash away unbounded enzymes. An example of EIS measurements of these steps is depicted in Figure 4.2-2.

For cross-linking deposition, a two-step functionalization method has been performed. After working electrodes rinse with ultra pure water, 5 µL of DTSP solution have been drop-casted over each electrodes. After this, the electrodes have been kept in wet environment for one hour at room temperature and then rinsed with ultra pure water [22]. At this point, the same protocol used for LOx direct adsorption has been followed, i.e. drop-casting of 1 µL of enzyme solution over each DTSP-functionalized electrode, wait for one hour at room temperature and rinse with ultra pure water.

EIS measurements have been carried out in the range from 100 mHz to 100 kHz using a stimulus amplitude of 10 mV, in order to keep the system in the linear response

domain [20], and a DC bias of 235 mV. This DC potential has been determined by cyclic voltammetry measurements of the electrochemical cell filled with 50 µL of measurement solution, i.e. 1 mM $Fe(CN)_6^{4-/3-}$ in 100 mM PBS, using bare gold electrodes without any functionalization. This DC potential corresponds to the formal redox potential of ferri/ferrocyanide couple vs. Ag|AgCl|1 M KCl reference electrode [23].

Using the information obtained from cyclic voltammetry measurements, DPV measurements have been carried out in the range between 0.05 V and 0.45 V, with stimulus amplitude of 50 mV and pulse width and period of 0.2 s and 0.5 s respectively, in presence of measurement solution containing lactic acid 1 mM.

4.3.1 Effects of LOx direct adsorption on gold electrodes

In order to evaluate the effects of the cross-linker, a preliminary direct adsorption study has been carried out as described in Section 4.2.1.

The direct adsorption of LOx enzymes over gold electrodes surfaces has been investigated using EIS measurements for different concentrations of LOx solution used during the functionalization protocol. The results of these measurements are depicted in Figure 4.3-1. For concentrations below 1 U/mL, the measurements behave in good accordance with the classical equivalent electrical model of electrode/electrolyte interface (1.4.4) [24], while for higher concentrations their behaviour tends to an equivalent parallel between a resistor and a capacitor, e.g., (1.4.2), as can be seen from the U-shaped phase diagram [25].

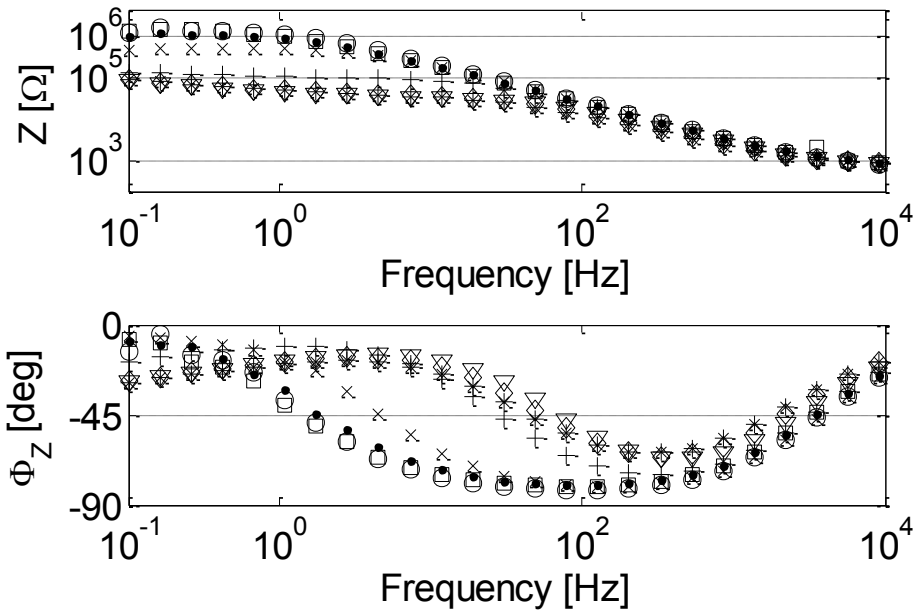

Figure 4.3-1. Bode diagrams of EIS measurements on LOx-modified gold electrodes. LOx concentrations are: 100 U/ml (O), 10 U/ml (□), 5 U/ml (·), 2 U/ml (x), 1 U/ml (+), 0.5 U/ml (*), 0.1 U/ml (◊) and bare electrodes (Δ).

These considerable changes in system impedance for LOx concentrations around 1 U/mL can also be seen from Figure 4.3-2, that shows impedance magnitude and phase variations at fixed frequencies: in about one decade of concentration around 1 U/mL the phase drops of about 50 degrees while the impedance modulus increases of about one order of magnitude. For values of concentrations lower than this threshold the impedance is very similar to that of bare gold electrodes, while for higher values it tends to a plateau regardless of the tested LOx concentration, that is similar to data showed in Figure 4.2-3 (b). As the impedance modulus at low frequency is related to the charge transfer resistance, the high impedance value above the threshold of 1 U/ml indicates a thicker LOx layer [23].

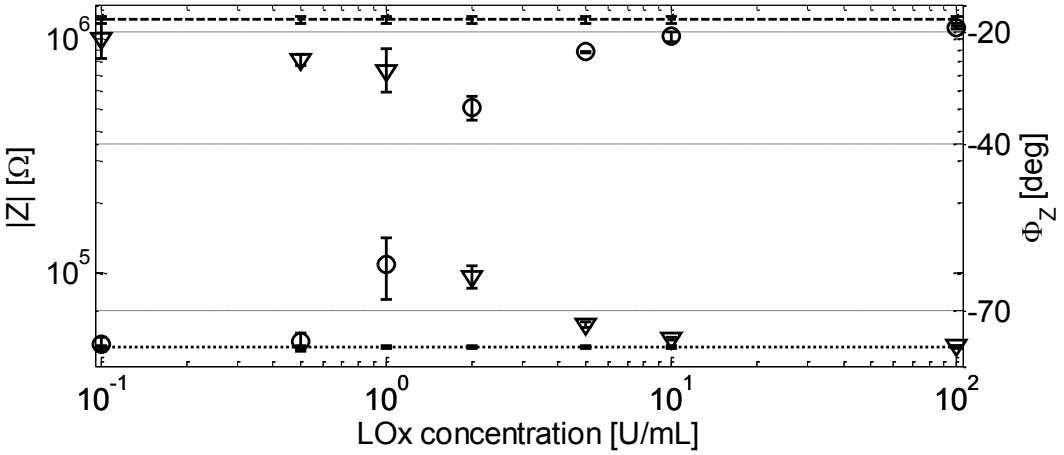

Figure 4.3-2. Magnitude (O) and phase (Δ) of LOx-modified electrodes EIS measurements (with standard deviations) at about 1 Hz and 10 Hz, respectively. Lines indicate magnitude (dotted) and phase (dashed) values for bare gold EIS measurements.

After EIS measurements, these LOx-modified electrodes have been used for the detection of lactic acid 1 mM in solution through DPV measurements, and the results have been compared to control DPV measurements carried out on electrodes functionalized with the same LOx concentrations in contact with measurement solution lactic acid-free. Figure 4.3-3 depicts DPV peak currents (i_p) as a function of LOx concentration: as can be seen, the total amount of flowing current during measurements decreases with the increase of LOx concentration, and the largest drop is located around the same concentrations of Figure 4.3-2. In accordance with EIS characterization, for concentrations above 5 U/mL the voltammetric response of both control and detection measurements reaches a lower plateau in which LOx concentrations has less influence, thus the higher impedance of LOx layer reduces the electrons transfer.

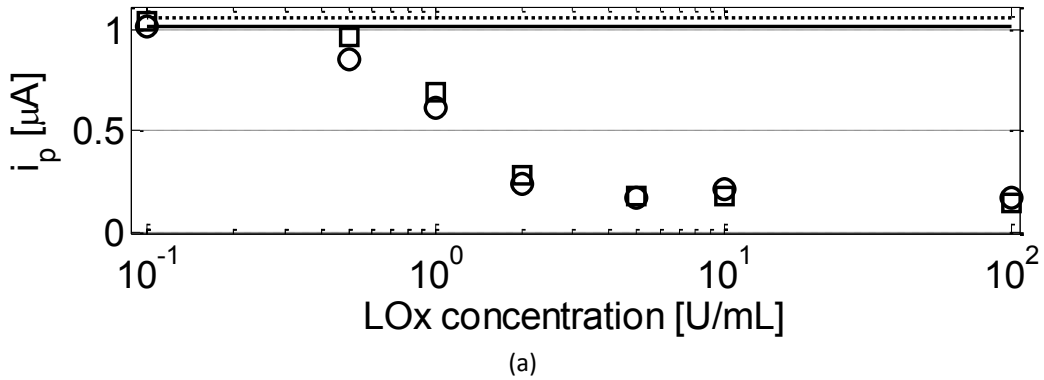

(a)

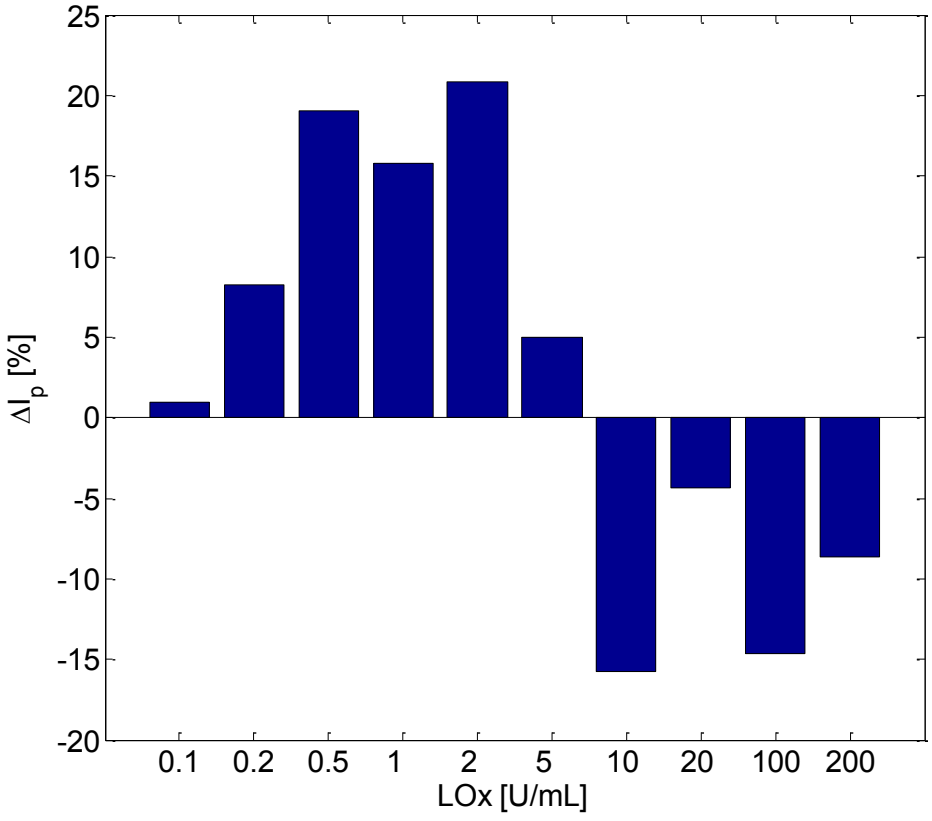

(b)

Figure 4.3-3. DPV peak currents measurements of LOx-modified electrodes in absence ($i_{p,PBS}$, o) and in presence ($i_{p,LA}$, □) of lactic acid 1 mM, respectively (a). Lines indicate bare gold DPV peak current values without (straight) and with (dotted) lactic acid 1 mM. Peak currents percentage variation $\Delta i_p = 100(i_{p,LA} - i_{p,PBS})/i_{p,PBS}$ (b).

The percentage variation between control DPV and detection DPV peak currents (Δi_p) has been depicted in Figure 4.3-3. The highest variation corresponds to a LOx concentration in the range between 0.5 and 2 U/mL, i.e., Δi_p varies from about 15 % to 21 %. In this range the amount of enzyme adsorbed over the electrodes surface is able

to effectively catalyze the reaction with the lactic acid 1 mM solution and increasing LOx concentration above 0.5 U/mL does not affect the electrochemical response [8]. The drop in Δi_p, observed for concentrations above 5 U/mL, can be justified with EIS measurements of Figure 4.3-1: at these concentrations electrodes surfaces are completely covered with disorderly adsorbed enzymes layers with non optimal molecular arrangements that decrease detection efficiency [11].

4.3.2 Effects of cross-linked enzymes on gold electrodes

EIS measurements have been performed on DTSP-functionalized electrodes before exposing the cross-linker to the enzyme, in order to find the optimal DTSP surface coverage. The results of these measurements are shown in Figure 4.3-4: from these Nyquist plots can be seen that the diameter of the high frequency semi-circle increases with DTSP concentration and this corresponds to an increase in the interfacial charge transfer resistance R_{ct} [26] (see models (1.4.3) and (1.4.4)).

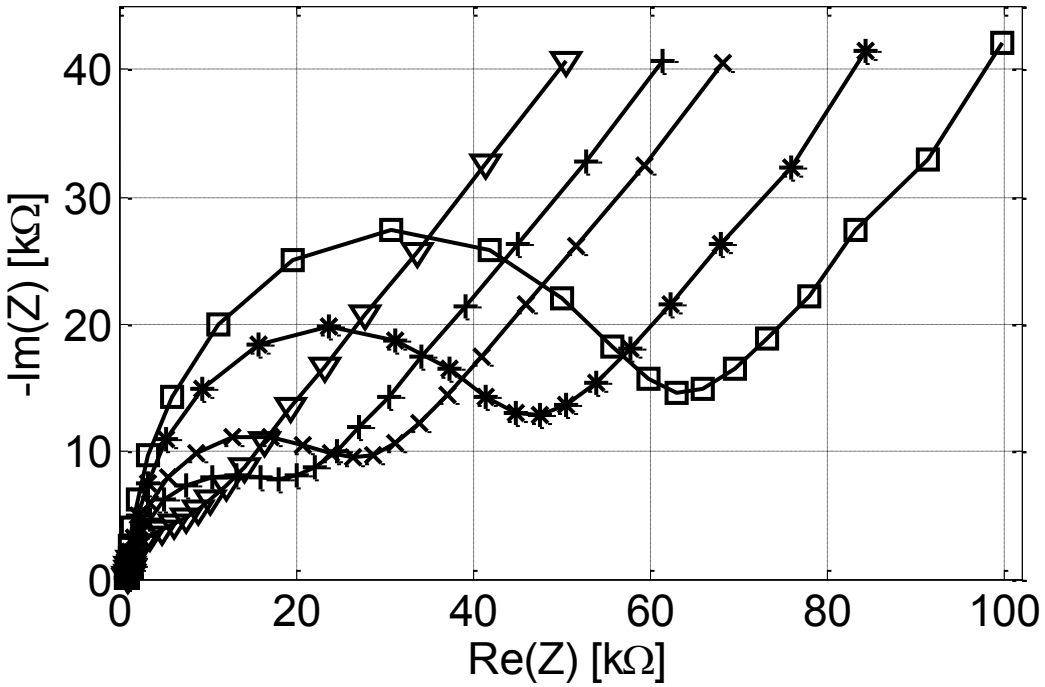

Figure 4.3-4. Nyquist plots of DTSP-functionalized electrodes obtained from EIS measurements. DTSP concentrations: bare electrodes (Δ), 100 nM (+), 1 µM (x), 10 µM (*), 100 µM (□).

Figure 4.3-5 depicts the behavior of impedance magnitude of DTSP-modified electrodes at fixed frequency as a function of DTSP concentration: the impedance modulus grows with a linear fashion for DTSP concentrations below 100 μM and reaches a plateau-like trend for higher concentrations. The fractional coverage approach can be used to determine the parameter ϑ of electrodes coverage by DTSP self-assembled monolayer [27],

$$\vartheta = 1 - \frac{R_{ct}}{R_{ct}^{*}} \ , \tag{4.2.5}$$

where R_{ct} is the charge transfer resistance of the DTSP SAM and R_{ct}^{*} is evaluated from the non-functionalized electrode. The structure of (4.3.1) is similar to (4.2.5), i.e., the normalization of the coverage parameter C^{n}. Fitting EIS data of Figure 4.3-4 with (1.4.4) model, values for ϑ can be obtained that range from 0.4895 for DTSP 0.1 μM to 0.9210 for DTSP 1 mM [28], indicating the almost complete coverage of the electrodes at these concentrations.

The DTSP-modified electrodes have been further functionalized with a fixed concentration of LOx, i.e. 0.5 U/mL. This LOx concentration has been selected from Figure 4.3-3 data set because it represents the lowest tested enzymatic concentration that gives rise to the maximum value of Δi_p. EIS measurements on LOx/DTSP-modified electrodes are shown in Figure 4.3-5 at fixed frequency: as can be seen, EIS data are similar in trend to those obtained for DTSP-modified electrodes, and their higher impedance modulus is consistent with new molecules bind at DTSP SAM surface [10].

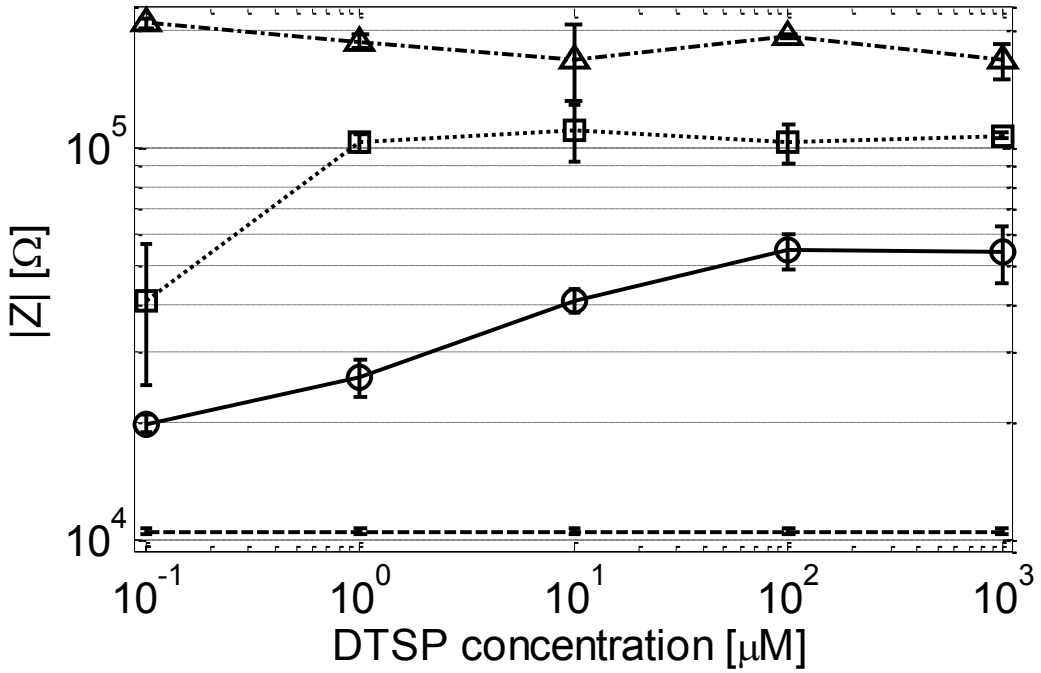

Figure 4.3-5. Impedance magnitudes at 10 Hz obtained from EIS measurements of functionalized electrodes as a function of DTSP concentration: bare gold (straight line), DTSP only (o), 0.5 U/mL LOx/DTSP (□), 200 U/mL LOx/DTSP (Δ).

As a comparison, in the same figure are depicted EIS measurements of LOx/DTSP-functionalized electrodes with 200 U/mL LOx concentration: the impedance magnitude values of these data are in good agreement with those showed in Figure 4.3-1 for LOx-modified electrodes at the same concentration and are independent from DTSP concentration. This can be attributed both to LOx molecular weight, that is about ten times higher than DTSP one (see Section 4.3), and to this particular LOx/DTSP concentration ratio, that is variable between $5 \cdot 10^2$ and $5 \cdot 10^6$.

DPV measurements have been carried out on LOx/DTSP-modified electrodes in presence of lactic acid 1 mM solutions and the resulting Δi_p as a function of DTSP concentration is depicted in Figure 4.3-6. As expected [18], the cross-linker enables a higher enzymatic reaction and a consequent increase in the current detected by the electrochemical cell. In the whole tested DTSP concentration range, the values of Δi_p are more than twice those obtained for direct LOx-modified electrodes, i.e., about 19 % (see Figure 4.3-3), with a peak of 51 % for 1 μM DTSP concentration. This indicates that with the adopted functionalization protocol a SAM capable to bind and properly orientate LOx can be obtained for DTSP concentrations lower than 1 mM [29].

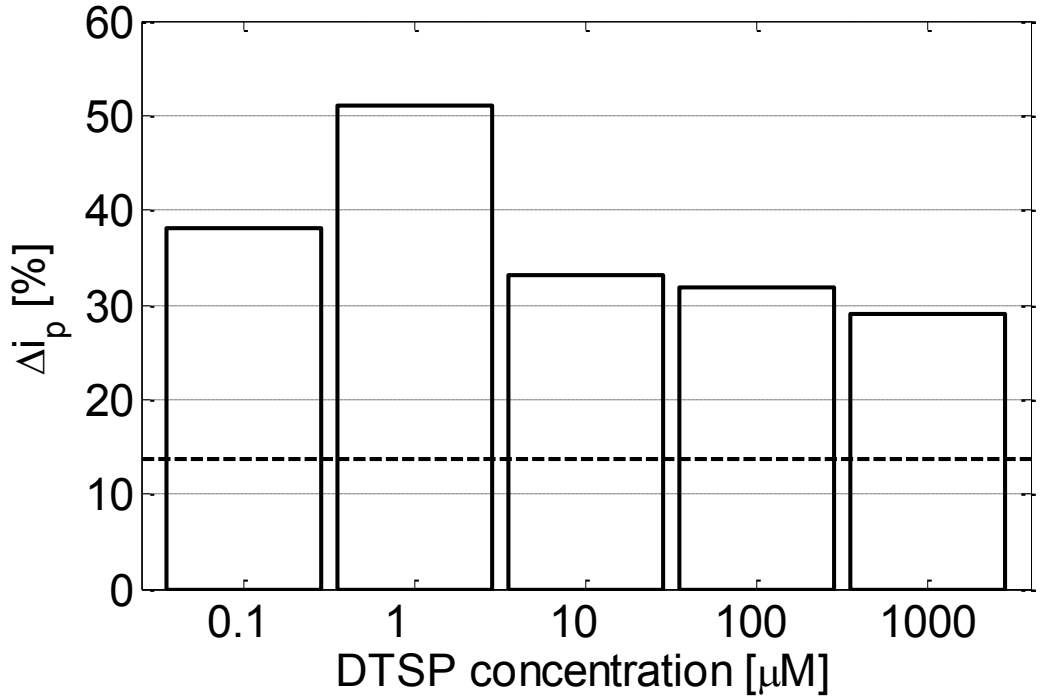

Figure 4.3-6. DPV peak currents percentage variation of 0.5 U/mL LOx/DTSP electrodes in presence of lactic acid 1 mM. The dashed line represents Δi_p achieved with 0.5 U/mL LOx-modified electrodes (see Figure 4.3-3).

4.4 Bibliography

[1] Weil, M.H., Afifi, A.A., 1970. Circulation 41, 989-1001.

[2] Detry, B., Cao, M.L., Frans, A., Robert, A., Clerbaux, T., 1998. Eur. Respir. J. 11, 183-187.

[3] Palleschi, G., Mascini, M., Bernardi, L., Zeppilli, P., 1990. Med Biol Eng Comut, doi: 10.1007/BF02442677.

[4] Palmisano, F., Quinto, M., Rizzi, R., Zambonin, P.G., 2001. Analyst 126, 866-870.

[5] Sung, W.J., Bae, Y.H., 2006. Sens. Actuators B 114, 164-169.

[6] Kumar, S., Kumar, A., 2008. S&T 96, 18-31.

[7] Lillis, B., Grogan, C., Berney, H., Lane, W.A., 2000. Sens. Actuators B 68, 109-114.

[8] Boujtita, M., Chapleau, M., Mum, N.E., 1996. Electroanalysis 8 (5), 485-488.

[9] Lee, H.C., Wu, W.Y., Lin, J.L., Chin, Y.L., Lee, K.Y., Sun, T.P., 2008. Sensors, 898-901.

[10] Gamero, M., Pariente, F., 2010. Biosensors and Bioelectronics 25, 2038-2044.

[11] Casero, E., Vázquez, F., Parra-Alfambra, A.M., Lorenzo, E., 2010. Analyst 135, 1878-1903.

[12] Umena Y., Yorita K., Matsuoka T., Kita A., Fukui K., Morimoto Y., 2006. Biochem. Biophys. Res. Commun., 350, p.249.

[13] Marzouk, S.A.M., Cosofret, V.V., Buck, R.P., Yang, H., Cascio, W.E., Hassan, S.S.M., 1997. Anal Chem. 69, 2646-2652.

[14] Scaramuzza, M., Ferrario, A., Pasqualotto, E., Rosati, G., De Toni, A., Quarta, M., Paccagnella, A., Reggiani, C., 2011. Proceedings of the International Conference on Biomedical Electronics and Devices, pp. 380-383.

[15] Matemadombo, F., Westbroek, P., Nyokong, T., Ozoemena, K., De Clerck, K., Kiekens, P., 2007. Electrochimica Acta 52, 2024-2031.

[16] Leith, D.K., Morse, S.A., 1980. J. Bacteriology 143, 182-187.

[17] Chaki, N.K., Vijayamohanan, K., 2002. Biosens. Bioelectron. 17, 1-12.

[18] Parra, A., Casero, E., Vázquez, L., Pariente, F., Lorenzo, E., 2006. Anal. Chim. Acta, 308-315.

[19] Huang, X., Nguyen D., Greve, D.W., Domach, M.M., 2004. IEEE Sensors Journal 5 (4), 576-583.

[20] Onaral, B., Sun, H.H., Schwan, H.P., 1984. IEEE Trans. Biomed. Eng 31, 827-832.

[21] Jena, B.K., Raj, C.R., 2006. Anal. Chem. 78, 6332-6339.

[22] Darder, M., Takada, K., Pariente, F., Lorenzo, E., Abruña, D., 1999. Anal. Chem. 71, 5530-5537.

[23] Bard, A.J., Faulkner, L.R., 2001. John Wiley and Sons.

[24] Kovacs, G.T.A., 1994. Academic Press, 121-165.

[25] Stoynov, Z., Vladikova, D., 2005. Academic Publishing, Sofia.

[26] MacDonald, J.R., 1987. Wiley Interscience.

[27] Janek, R.P., Ronald Fawcett, W., 1998. Langmuir 14, 3011-3018.

[28] Mena, M.L., Carralero, V., González-Cortés, A., Yáñez-Sedeño, P., Pingarrón, J.M., 2005. Electroanalysis 17, 2147-2155.

[29] Park, B.W., Kim, D.S., Yoon, D.Y., 2011. Korean J. Chem. Eng. 28, 64-70.

Chapter 5. Cells electropermeabilization: experiments and modeling

5.1 Introduction to the electrical modeling of living cells

Figure 5.1-1 (a) depicts the schematization of a living cell. As can be seen, cells are sealed by a thin membrane that both protects them from external environment and preserves the inner electric potential.

The membrane is mainly composed by a double layer of phospholipids that contain both hydrophobic regions, pointed toward cell inside, and hydrophilic regions, pointed toward the outside (see Figure 5.1-1 (b)). All the other small proteins that compose the lipidic structure can travel inside the membrane, acting as ionic channels able to transfer molecules inside or outside the cell: in this sense the cell membrane is said to be semi-permeable, because it is able to either allow a substance to pass, or to limit its amount or to completely block specific substances.

Inside the membrane the cytoplasm can be found, i.e., a saline solution that fills most part of cell volume, in which sub-cellular organelles are anchored to a proteic structure called cytoskeleton. The cytoskeleton performs different tasks, from retaining the shape of the cell, to organizing molecules transport inside it. The liquid phase of the cytoplasm is called cytosol, in which amino acids and simple sugars are diluted to act as reserve for small molecules and organelles.

The cell nucleus is a sub-cellular organelle that contains nucleic acids, and therefore both provides the DNA duplication and RNA transcription and maturation. As the other inner organelles, its internal region is said nucleoplasm, and is separated from the cell cytoplasm by its own phospholipid membrane. The nucleus membrane is contact with the endoplasmatic reticulum, an organelle that consists of cytoplasmatic regions delimited by membranes that act as reservoirs for specific enzymes able to catalyze several different chemical reactions.

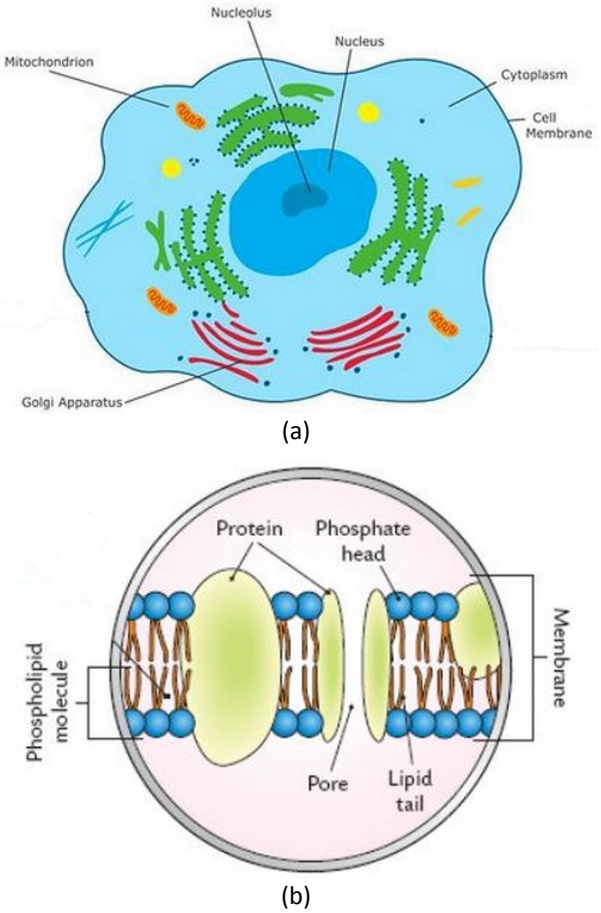

Figure 5.1-1. Schematic representation of a living cell with main intra-cellular structures (a) and of cell phospholipid membrane (b). The membrane acts as a selective barrier for proteins with its pores.

All these basic elements are affected by electromagnetic fields, and each of them reacts with different behavior to the stimulations, depending on the specific electrical parameters.

The first developed cell model has been the single shell model (SSM) [1]: it considers the cell as a conductive sphere covered by a thin low-conductive dielectric layer, i.e., the membrane (see Figure 5.1-2). With a second conductive sphere surrounded by dielectric placed in the SSM, a cell with nucleus can be modeled. This model is called double shell model (DSM) [2].

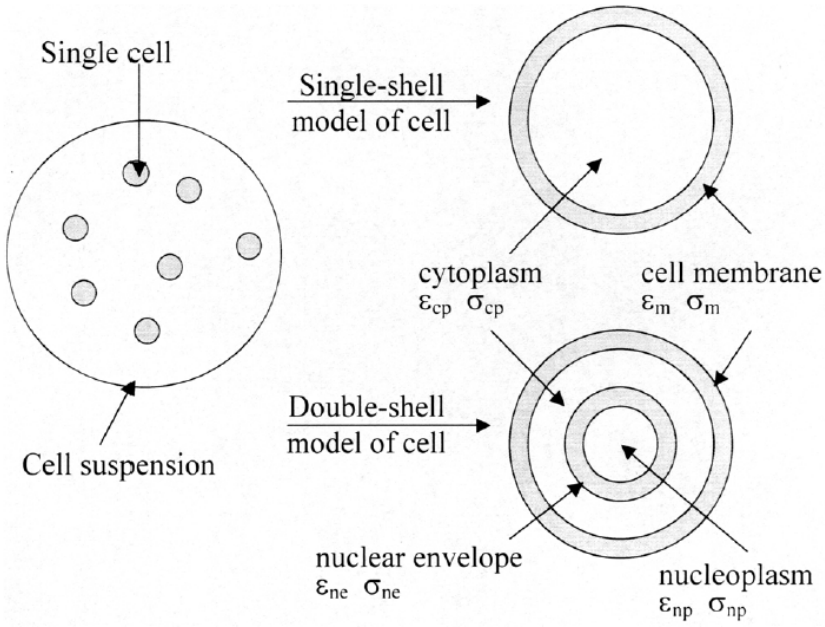

Figure 5.1-2. Single shell and double shell model for suspended living cells. Each different region, e.g., cytoplasm and membrane, is described by its own specific electrical parameters like conductivity σ and permittivity ε [1].

When the cell is suspended in a conductive medium and placed between two electrodes, if a voltage pulse is applied the generated electric field causes a current to flow that stocks electrical charges at the membrane. This implies that the voltage difference between the internal surface of the membrane and the external one changes. If this voltage difference is higher than a critical value, it induces structural and morphological changes in membrane surface, i.e., pores formation and consequent increase in membrane permeability [11]. This process is called electroporation or electropermeabilization [3] (see Figure 5.1-3), and has been widely studied for drug-delivery and biological modification applications, i.e., applications where cells are modified with exogenous material without using biological transfectant vectors like viruses.

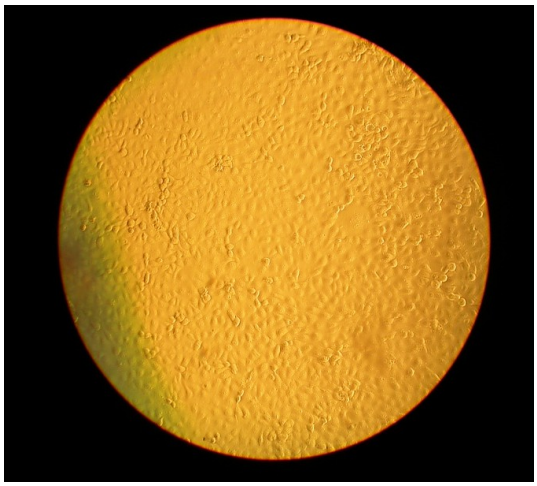

(a)

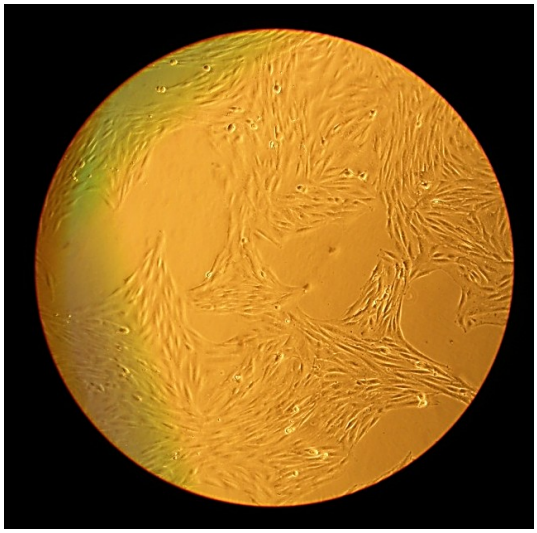

(b)

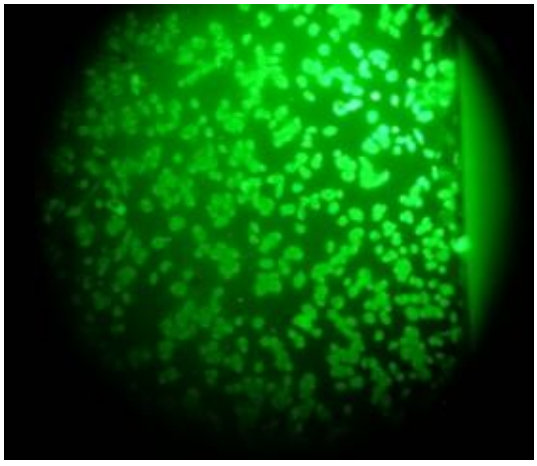

(c)

Figure 5.1-3. Example of adherent cells on gold electrodes surfaces: Chinese hamster ovary (a) and rat muscular (b). Effect of electroporation of adherent cells with fluorescent dye (c): once electropermeabilized, the membrane pores let the small dye molecules enter the cell.

Electroporation is widely used in genetics and molecular biology to promote the delivery of biological active molecules, such as DNA, into cells. Metal electrodes can be used for both stimulating and measuring the resulting effects [4, 5]. Living cells usually grow and attach on the electrode surface, causing an increment of the impedance at the interface with the metal electrode. For this reason, electrochemical impedance spectroscopy (EIS) is an important tool for monitoring cells behaviour [6] and in particular their health, adhesion and electroporation level: for instance, a change of the interface between culture and electrode due to cells proliferation may be detected by an impedance increase, or a decrease in the whole membrane impedance can be used to detect electropermeabilization as pores open [7] (see Section 5.2).

During cells electrical stimulation, if the voltage at the membrane is not too high and the impulse duration is limited, the membrane permeabilization is reversible and the cell survive. The time required to charge the membrane surface depends on both its electrical parameters and on those of the conductive medium. For an ideal SSM, i.e., with a non-conductive dielectric layer of infinitesimal thickness, at low volumetric concentration of suspended cells, the charging time constant is given by [8]

$$\tau_c = C_m \left(\rho_c + \frac{\rho_a}{2}\right)\frac{D}{2} \ , \qquad (5.1.1)$$

where C_m is the density of membrane capacitance, D is the cell diameter, ρ_c and ρ_a are the electrical resistivity of the cytoplasm and the of the medium, respectively. For example [9], for a cell with diameter 10 μm with $\rho_c = \rho_a = 100\ \Omega\cdot$cm and membrane capacitance of 1 μF/cm^2, the charging time constant is 75 ns. During τ_c time, the inner region of the cell is exposed to the applied electric field: in fact, if the angular frequency ω of the applied stimulus is higher that the threshold voltage τ_c^{-1}, the membrane reduces its shielding effectiveness, allowing the electromagnetic field to penetrate with more energy, as described in Figure 5.1-4 [10]. Figure 5.1-5 describes the simulation results of a SSM suspended cell using the Combined Simulation System described in Section 2.1.

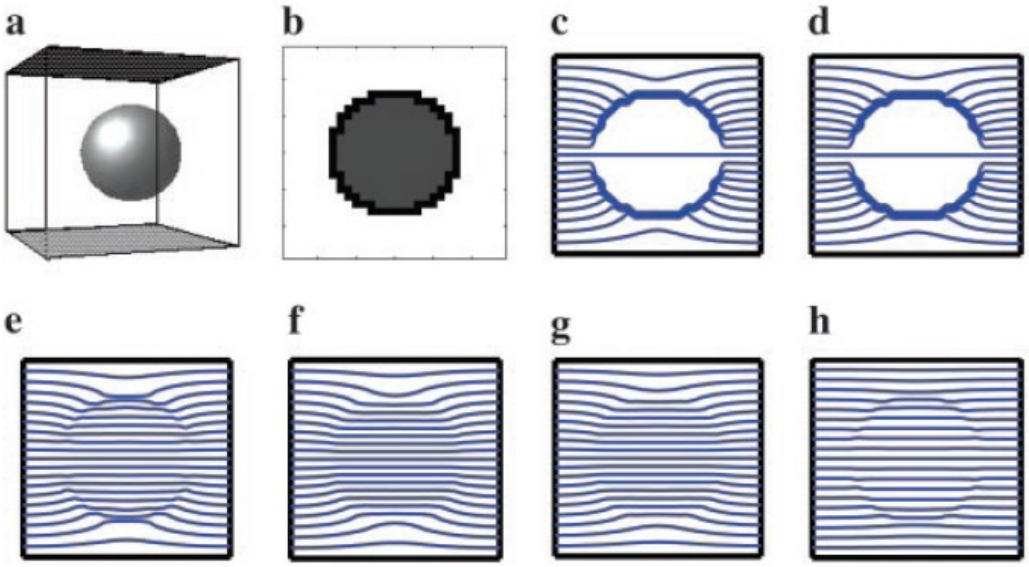

Figure 5.1-4. Cell membrane shielding effect. The electric parameters of the system are $\rho_a = 0.833\ \Omega\cdot m$, $\rho_c = 4\rho_a$, $C_m = 9.2\ mF/m^2$, $D = 10\ \mu m$, therefore (5.1.1) becomes $\tau_c = 172$ ns, i.e., $(2\pi\tau_c)^{-1} = 925$ kHz. Tridimensional cell model (a) and its cross-section (b). Impedance network simulation (see Section 2.1) as a function of applied stimulus frequency: 100 Hz (c), 100 kHz (d), 1MHz (e), 10 MHz (f), 100 MHz (g), 1 GHz (h) [17].

The DSM of Figure 5.1-2 allows to simulate the coupling of electric fields at the cell membrane [27] and their effects on internal structures, as nucleus and organelles, as described in Figure 5.1-6. The application of electric fields to the cell suspension solution generates conduction currents in both the medium and the cytoplasm, and also displacement currents at both cell and organelles membranes.

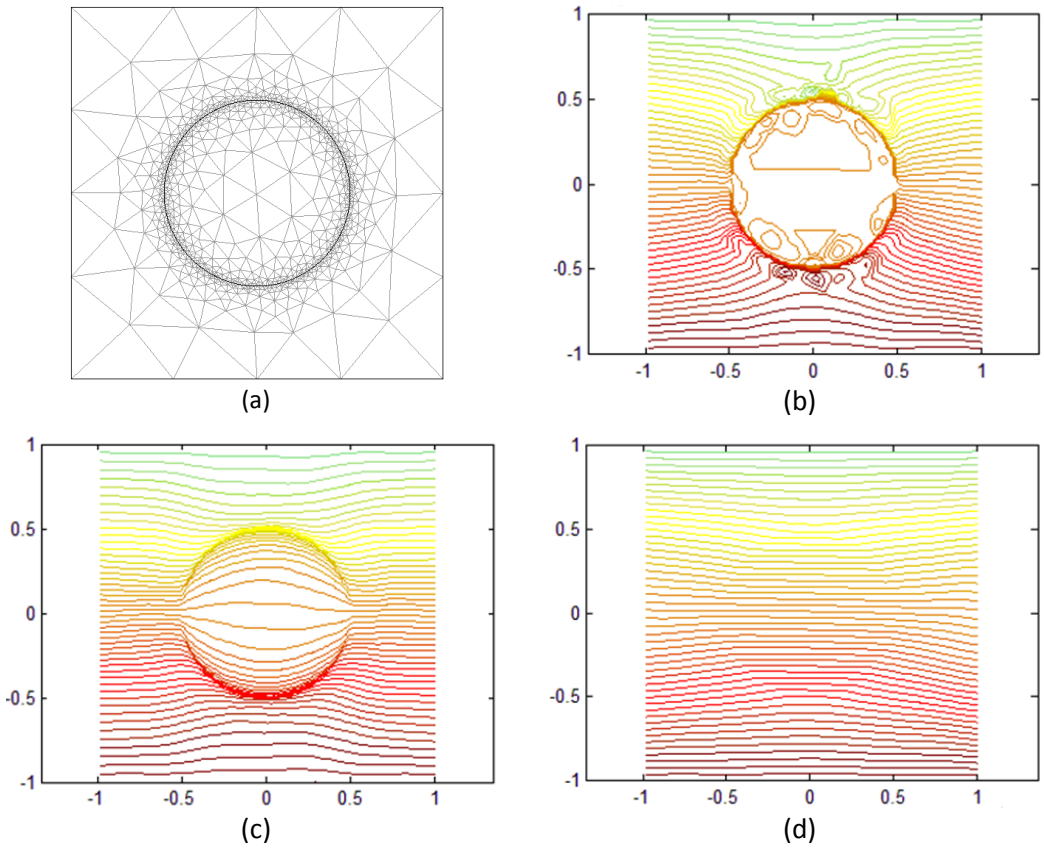

Figure 5.1-5. CSS simulation of Figure 5.1-4 system. Cross-section model (a) and electric field distribution as a function of applied stimulus frequency: 100 kHz (b), 1 MHz (c), 1 GHz (d). See Section 2.1 for details.

These sub-cellular structures are affected by two principal effects when the cell is exposed to electric fields. The first is the increase in the total amount of electrical charge stored at their membranes as the frequency of the stimulus increases: this is due to capacitive coupling between membranes, and it leads to high sub-cellular trans-membrane voltage potentials is the applied electric fields have rising and falling time smaller than the membranes charging tome constants (5.1.1). The second effect is directly related to the first, and is the increase in the amount of energy transferred at the sub-cellular structures through Joule effect: if the pulses total energy is kept constant, the energy transferred to the internal structures by nanoseconds duration pulses will be higher than that generated by microseconds pulses [8].

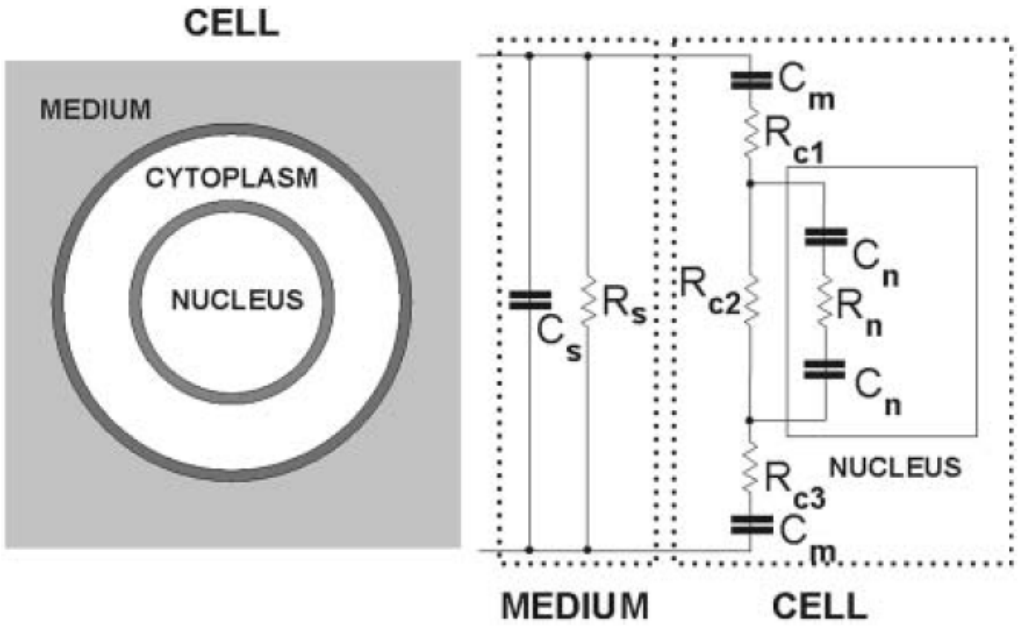

Figure 5.1-6. Electrical implementation of a DSM for an isolated suspended cell [8].

As can be seen from Figure 5.1-6, cells contain conductive electrolytic solutions separated by low-conductivity thin membranes with electroactive macromolecules. Multi-cells systems are very heterogeneous, in terms of both local electrical properties and interaction mechanisms, e.g., ionic channels activity and membrane conductivity variations. Some of these interactions can take place simultaneously, but often dominant interactions can be identified. Moreover, these phenomena depend on the local electric field rather than on the mean electric field applied to the stimulation electrodes. For this reason, the distribution of the applied electric field in cells and organelles is of great interest [10] (see Section 2.1).

Analytical approaches to this problem started with the assumptions that both cytoplasm and extra-cellular medium are purely conductive regions, i.e., with null dielectric permittivity, and that the membrane is a lossy dielectric, i.e., with non-null conductivity and permittivity [11]. These assumptions lead to an analytic description of the trans-membrane electric field caused by the application of an alternated external electric field [12]:

$$U_m(\omega,\theta) = \frac{3}{2} E_e R \cos\theta \frac{1}{1+j\omega\tau_m} \quad , \tag{5.1.2}$$

where E_e is the amplitude of the applied electric field, R is the cell radius, θ is the displacement with respect to the electric field direction and ω is its angular frequency.

The first-order process described in (5.1.2) is characterized by the time constant

$$\tau_m = RC_m \frac{1}{\frac{1}{\frac{1}{\sigma_i}+\frac{1}{2\sigma_e}}+\frac{R}{d}\sigma_m} \quad , \tag{5.1.3}$$

where d represents the membrane thickness, $C_m = \varepsilon_m/d$ is the membrane capacitance, ε_m its dielectric permittivity, and σ_i, σ_e and σ_m are the electrical conductivity of cytoplasm, extra-cellular medium and membrane, respectively.

If the frequency of the applied electric field is about 10 kHz, cytoplasm and extra-cellular medium cannot be considered as perfect conductors, because their capacitive properties acquire greater influence on the overall electrical response. In these conditions, the trans-membrane potential equation becomes [13]

$$U_m(\omega,\theta) = f(\omega)E_e R\cos\theta \frac{1+j\omega\tau_{m2}}{1+j\omega\tau_{m1}} \quad . \tag{5.1.4}$$

The time constants are:

$$\tau_{m1} = \frac{\varepsilon_m}{\sigma_m + \frac{d}{R}\frac{2\sigma_e\sigma_i}{\sigma_e+\sigma_i}} \quad , \tag{5.1.5}$$

$$\tau_{m2} = \frac{\varepsilon_i + 2\varepsilon_e}{\sigma_i + 2\varepsilon_e} \quad , \tag{5.1.6}$$

where ε_i and ε_e indicate the dielectric permittivity of the cytoplasm and of the extra-cellular medium, respectively. The function f(ω) is related to the complex conductivity and permittivity (*) of the various cellular regions:

$$f(\omega) = \\ = \frac{3\sigma_e^*[3R^3\sigma_i^* + (3dR^2 - d^2R)(\sigma_m^* - \sigma_i^*)]}{2R^3(\sigma_m^* + 2\sigma_e^*)\left(\sigma_m^* + \frac{1}{2}\sigma_i^*\right) - 2(R-d)^3(\sigma_e^* - \sigma_m^*)(\sigma_i^* - \sigma_m^*)} \quad . \tag{5.1.7}$$

The analytical approach described by (5.1.2) and (5.2.4) is based on the deep knowledge of each different biological region that constitutes the heterogeneous cells environment: in fact, the peculiarities of each region have to be taken into account to obtained reliable equations, e.g., resistive and capacitive parameters, non-linear conductivity of ionic channels, cells irregular shapes and influence of adjacent cells.

5.2 Electropermeabilization of adherent cells

In this Section, Chinese hamster ovary (CHO) cells adhesion on microelectrodes and electroporation effects have been studied using electrochemical impedance spectroscopy (EIS) measurements [14].

EIS data have been fitted in order to determine the fundamental parameters of the electrode/cell interface. After this, a numeric parameter has been introduced as cell impedance multiplier to take into account the presence of multiple cells on a single microelectrode.

After electroporation experiments on adherent cells, the pre- and post-stimulation EIS data have been compared and fitted, to determine the trend of variation caused by the stimulation as a function of the applied electric stimulus amplitude [15].

5.2.1 Modeling strategy

Chinese hamster ovary (CHO) cells have been grown onto gold surfaces to verify the feasibility of the protocol in term of cells viability and electrode materials biocompatibility. Figure 5.2-1 describes an example of measurement using flow cytometry: from these results it can be seen that cells can grown and proliferate over gold surfaces.

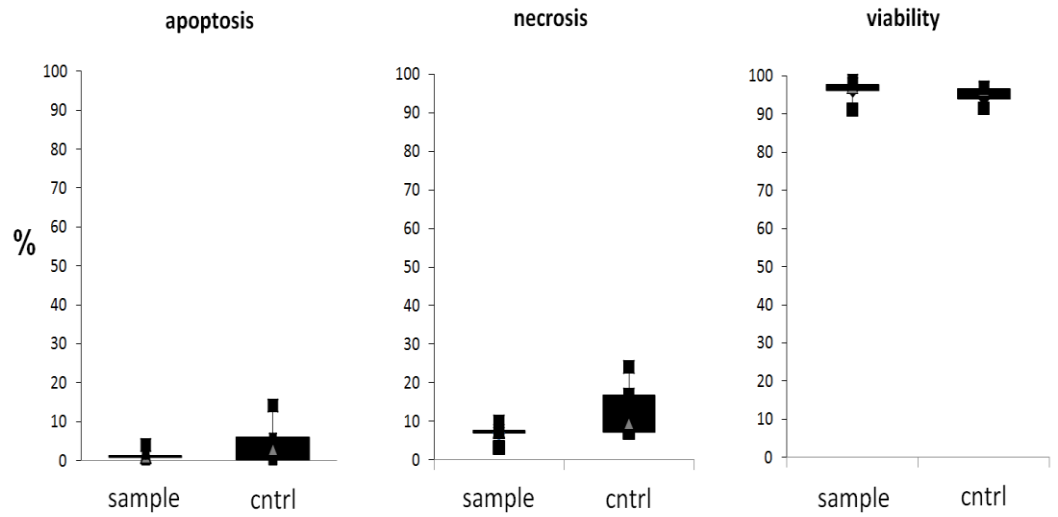

Figure 5.2-1. Flow cytometry analysis of CHO cells plated on gold surfaces. After the cultivation process, the viability of adherent cells is about 95 %.

After the biocompatibility tests, cells have been grown on Ayanda multi-electrode arrays (MEA) described in Section 2.3 (see Figure 5.2-2), using the integrated cultivation chamber.

Both the electrochemical impedance spectroscopy (EIS) measurements and the cells stimulation have been carried out between the individually addressable gold working microelectrodes and a standard silver/silver chloride external reference electrode in buffer solution (see Figure 5.2-3). EIS data have been collected both prior the cultivation process and 2 hours after cells were plated on MEA surface. Measurements were performed in a frequency range of 100 Hz to 1 MHz, using sinusoidal voltage of 10 mV amplitude and 0 V DC bias with an impedance analyzer (SI 1260A, Solartron, UK). The cell viability and electrodes coverage have been observed using an optical microscopy (DM LB2, Leica Microsystems, Wetzlar, Germany).

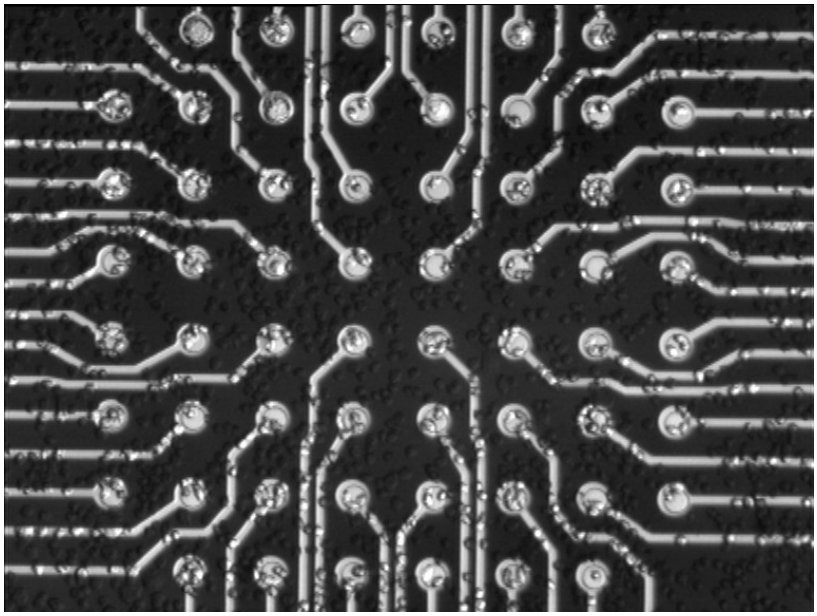

Figure 5.2-2. Example of CHO cells plated on MEA microelectrodes.

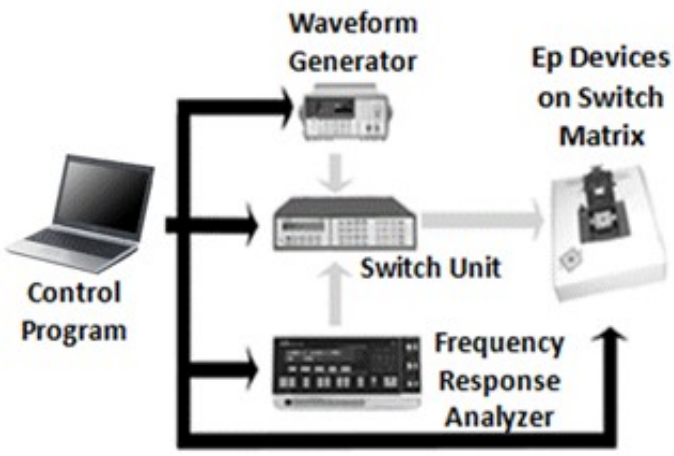

Figure 5.2-3. Electroporation bench set up. The frequency response analyzer is used to perform EIS measurement. The switch unit automatically select one microelectrode in the MEA matrix. The waveform generator is used to apply the stimulation pattern to the target microelectrode.

The cultivation protocol for CHO-K1 cells consisted of a routinely cells suspension in Nutrient Mixture F-12 HAM supplemented with 10 % heat-inactivated fetal bovine serum (FBS), 10 U/ml penicillin and 10 μg/ml streptomycin at 37 °C in a 5 % CO_2 environment. MEA microelectrodes have been carefully wiped and rinsed with deionized water and sterilized with UV light before cell cultivation. 48 hours before EIS measurements, cells are rinsed with phosphate buffer saline (PBS), i.e., NaCl 137 mM,

KCl 2.7 mM, Na_2HPO_4 10 mM, KH_2PO_4 2 mM with pH 7.4, and then incubated with Trypsin for 1 minute at 37 °C. After Trypsin inactivation by complete medium, cells were centrifuged for 5 minutes at 250 g. Cells were then suspended and plated on MEA microelectrodes at a density of 10^5 cells/cm^2 to ensure that each microelectrode was covered at least by one cell (see Figure 5.2-2).

As can be seen from Figure 5.2-4, electrical stimulation for the electroporation consisted of six pulses of 100 µs of different applied voltages, between 0.3 V and 2.4 V, with rise and fall time of 5 ns.

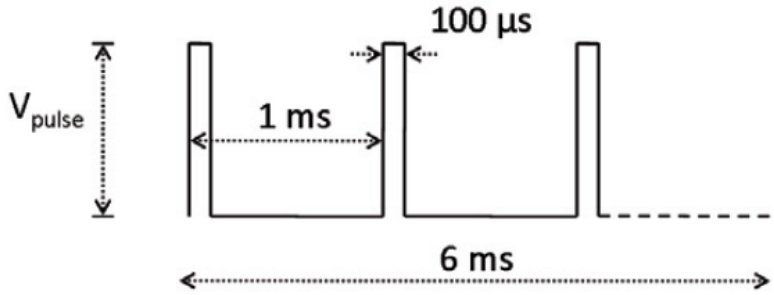

Figure 5.2-4. Stimulation pattern for cells electroporation.

To investigate the features of microelectrodes/electrolyte electrochemical interface, model (1.5.3) has been used to fit preliminary EIS data (see Figure 5.2-5). Recalling Section 1.5, its electrical impedance is given by

$$Z_{el}(\omega) = \frac{1 + (j\omega)^n R_s C_{dl}^n}{(j\omega C_{dl})^n \left[j\omega R_s C_p + (j\omega)^{1-n} \frac{C_p}{C_{dl}^n} + 1 \right]} \quad . \tag{5.2.1}$$

The electrochemical interface model includes the classical elements:

- the charge transfer resistance R_{ct} , which is related to electrons exchange between gold surfaces and buffer electrolyte [16];
- the electrolyte resistance R_s evaluated from a working microelectrode, that has been simulated using the Combined Simulation System (see Section 2.2), that gives results in good agreement with the classical theoretical formulation of the spreading resistance [17], $R_s = (4\sigma_s r_e)^{-1}$, where σ_s = 1.6 S/m is the electrolyte electric conductivity and r_e = 15 µm is the radius of the circular electrode;
- the double layer capacitance $C_{dl,0}$ that has been derived from the usual formulation under the hypothesis of low electrolyte concentration [18]: $C_{dl,0}$ =

$\varepsilon_0\varepsilon_{r,e}A/L_D$, where ε_0 is the vacuum permittivity, $\varepsilon_{r,e}$ = 80 is the electrolyte relative permittivity, the electrode active area is $A = \pi r_e^2$ and L_D = 1 nm is the Debye length for PBS at given concentration (see Section 1.1). With these values $C_{dl,0}$ = 500 pF.

The electrode/electrolyte interface electrical model usually contains the impedance $Z_{CPE} = (j\omega C_{dl})^n$ in order to take into account the electrode surface roughness [18] (see Section 1.3), with n empirical parameter between 0 and 1. To estimate a value for C_{dl} it can be considered that, for n = 1, $Z_{CPE} = j\omega C_{dl,0}$ and therefore $C_{dl} = C_{dl,0}^{1/n}$. The value of n for gold microelectrodes is typically 0.9 [19] and so C_{dl} = 46 pF;

- from (5.2.1), that is valid under the hypothesis that $R_{ct} >> R_s$, and recalling Section 1.5, the electrochemical interface basic model allowed to estimate the value of the capacitance C_p which is related to the parasitic elements of the measurement device. The influence of C_p arises at high frequencies, where it determines a pole in the transfer function [1] at the frequency $f_p = (2\pi R_s C_p)^{-1}$ (1.5.4). From comparison with the performed EIS measurements, that show a pole at about 2 MHz, C_p can be estimate of about 9 pF.

All the electrical parameters of the microelectrode/electrolyte interface have been evaluated by fitting EIS data of cell-free electrodes prior cultivation protocol.

Concerning CHO cells modeling, a single shell model has been used [8] (see Figure 5.1-2): membrane and cytoplasm parameters, i.e., R_m, R_c and C_m, have been evaluated under the approximation of spherical thin layer as described in [21], obtaining the values listed in Table 5.1-1. The cytoplasm has been approximated with a sphere of 5 µm-radius [17] with an electric conductivity of 0.464 S/m as described in [18].

To complete the model of Figure 5.2-5, two aspects have to be considered. The first is the capacitive effect of the junction between the cell and the microelectrode, i.e., C_{hd}, which represents the cell membrane-electrolyte interface. The second one is the seal resistance, R_{seal}, which is the electrical resistance between the cell and the electrode. The complete model is well-known and has been widely used in literature [19, 21].

5.2.2 Electropermeabilization experiments and fitting results

In this Section, the electrical impedance of a single CHO cell has been considered constant and it has been evaluated analytically from the above-mentioned theoretical considerations. This basic impedance has been multiplied by a numerical correction parameter β related to microelectrode cell coverage, i.e., β has been considered as a fit parameter taking into account the number of cells grown onto a single microelectrode. The complete transfer function of Figure 5.2-5 (a) system can be therefore described as

$$Z(\omega) = Z_{el}(\omega) + \beta \frac{Z_{cell} R_{seal}}{Z_{cell} + R_{seal}} \quad , \tag{5.2.2}$$

where $Z_{cell}(\omega) = Z_{Chd} + R_c + 2\cdot(R_m \,//\, Z_{Cm})$.

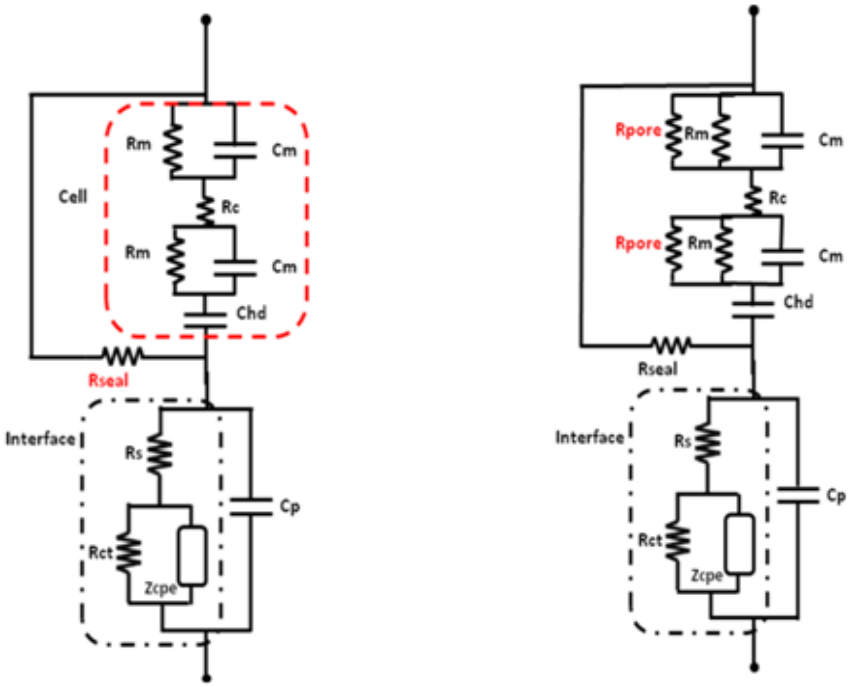

Figure 5.2-5. Cell/electrode interface model for cells adhesion studies (a). Cell/electrode interface model for cells electroporation studies (b).

EIS measurements have been performed on plated MEAs to monitor cells coverage and adhesion over microelectrodes and the effects of electroporation on membrane pores.

Parameter	Analytical value	Reference	Fitted value
R_{ct} [x 10^{12} Ω]	1.83	[19]	1.97 ± 2.1%
R_s [kΩ]	11	[21]	14.45 ± 1.1%
C_P [pF]	9	[1]	2.79 ± 11.9%
C_{dl} [pF]	41	[22]	20.7 ± 6.9%
n	-	[16]	0.9055 ± 0.5 %
C_{hd} [pF]	17	[17, 23]	-
R_m [GΩ]	4.244	[17, 24]	-
C_m [pF]	0.785	[10, 17]	-
R_c [x 10^5 Ω]	1.83	[10, 17]	-

Table 5.1-1. Parameters of Figure 5.2-5 model.

Concerning adherent cells experiments, the EIS measurements have been performed two hours after cells plating on the chip. Figure 5.2-6 shows the Bode diagrams of electrical impedance magnitude and phase for cell-free electrodes and for electrodes with different covering levels, i.e., with different area covered by cells, in a frequency range between 100 Hz and 1 MHz.

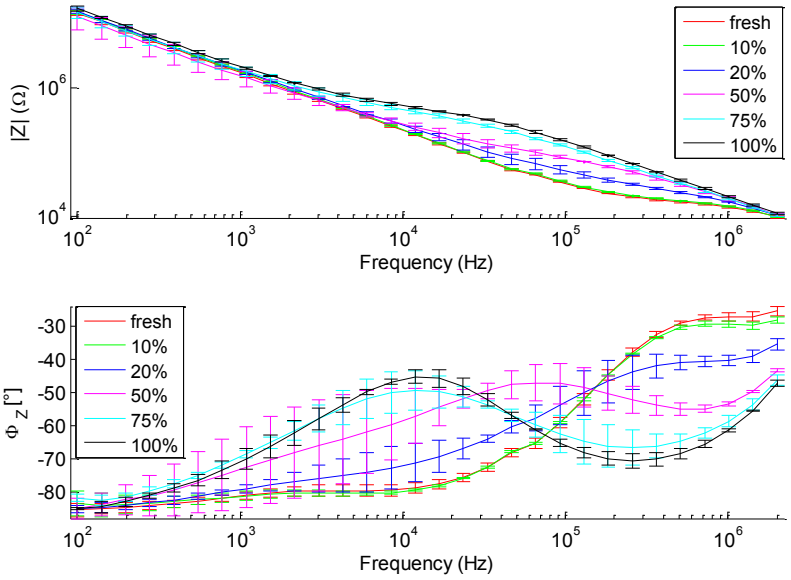

Figure 5.2-6. Bode plots of six different electrode coverage conditions. The "fresh" data (blue) corresponds to cell-free electrode condition.

A strong difference between cell-free and cell-covered impedances can be seen in the frequency range from ~10 kHz to ~800 kHz, where the variation of the impedance magnitude Δ|Z| is from 4.11 % to 336 % at 130 kHz, while the phase signal |Φ| has a variation from 27.4 ° to 65.4 ° at 718 kHz. Below few kHz the measured and fitted impedance of cell-electrode interface is similar to that of the free electrode. EIS data plotted in Figure 5.2-6 arise from 31 independent measurements of different microelectrodes, averaged for groups based on the covering level. In the case of cell-free electrodes, and also in the case of one cell over the electrode, the standard deviation is about 2 % – 8 %, depending on the frequency. For electrodes with more than one cell the standard deviation is higher, about 5 % – 20 %, due to both variable cells displacement over the electrodes and non-uniform cells morphological shape. When the microelectrodes are completely covered with cells, i.e., 100 % coverage level, impedance measurements have less dispersion and standard variation is lower, about 3 % – 10 %.

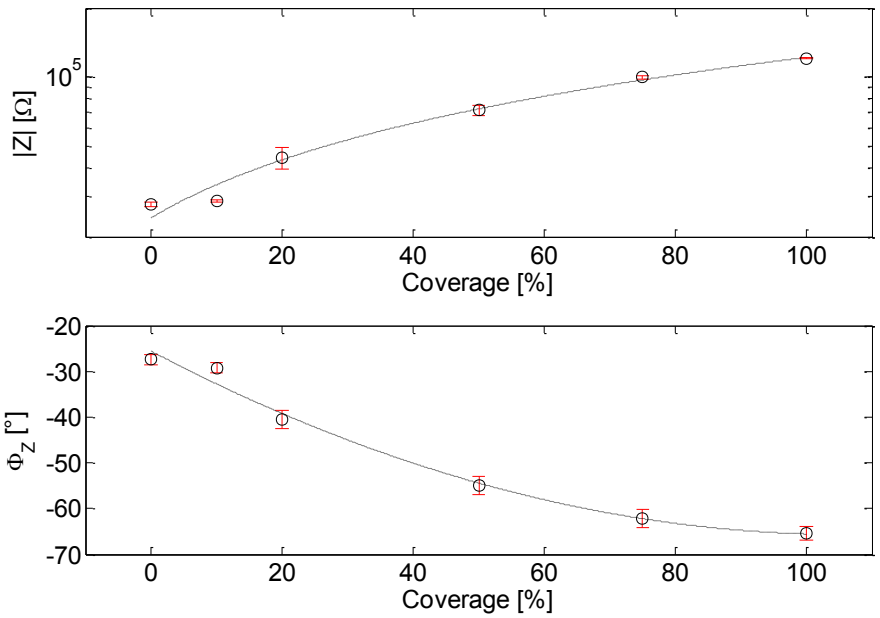

Figure 5.2-7. EIS impedance magnitude and phase variation as a function of microelectrode surface coverage.

Figure 5.2-7 compares the magnitude and phase of different microelectrodes as a function of the surfacial covering percentage due to cells presence. The effect of cells adhesion over the microelectrodes consists of a higher impedance magnitude and a lower phase at high frequencies [23, 25, 26]: this means that a cell adds an impedance in

series to the electrode, increasing the resistance from the electrode to the solution. The electrode coverage percentage has been optically estimated (see Figure 5.2-2).

A MATLAB code based on least squares method has been developed to fit experimental data of Figure 5.2-6 with the electrical model shown in Figure 5.2-5 (a). The resulting constants and derived parameters are summarized in Table 5.2-1. Considering cell-free gold electrode model in PBS solution, the electrolyte resistance R_s is equal to 14.447 kΩ with a standard deviation of 1.1 %, the charge transfer resistance R_{ct} results 1.97×10^{12} Ω (± 2.1 %) and the constant phase element, Z_{CPE}, gives a value of 2.07×10^{-11} F (± 6.9 %) for C_{dl}, with n = 0.9055 (± 0.5 %). The stray capacitance C_p which represents the whole parasitic capacitance of MEA substrate and measurements cell, results in 2.792 pF (± 11.9 %). The effect of this parasitic capacitance is to increase the impedance phase at high frequency.

From Figure 5.2-7 it can be seen that the presence of one or more cells over microelectrodes active surface implies a change in cell-electrode interface equivalent model. Once the parameters for cell-free electrode have been fixed with cell-free EIS measurements fit, the complete model of Figure 5.2-6 (a) can be used to fit experimental data, in order to obtain the parameters β and R_{seal} related to the microelectrode-cell interface.

Four EIS data sets (see Figure 5.2-8), each consisting of 5 independent experiments, have been collected in different conditions: no cell, one, two or three cells over the electrode surface. In this model, the cell is considered to be at a fixed distance from the electrode, i.e., tens of nanometers, and its impedance Z_{cell} is put in series with the impedance of the free electrode Z_{el} (5.2.1).

The values of C_{hd} is taken from [15], while β and R_{seal} have been considered fitting parameters. Figure 5.2-8 shows the fitting curves and EIS experimental data of four different microelectrodes surface coverage, with β = 0 meaning cell-free electrode. As expected, the sealing resistance R_{seal} increases, in accordance with β, from few MΩ to more than ten MΩ, as reported in Table 5.2-2. When increasing the electrode coverage, β reaches a value four times higher than the value of one cell coverage: the higher the electrode surface coverage, the lower the current flowing from the microelectrodes to the solution through the gap between the cell membrane and the electrode surface [26], i.e., a higher sealing resistance.

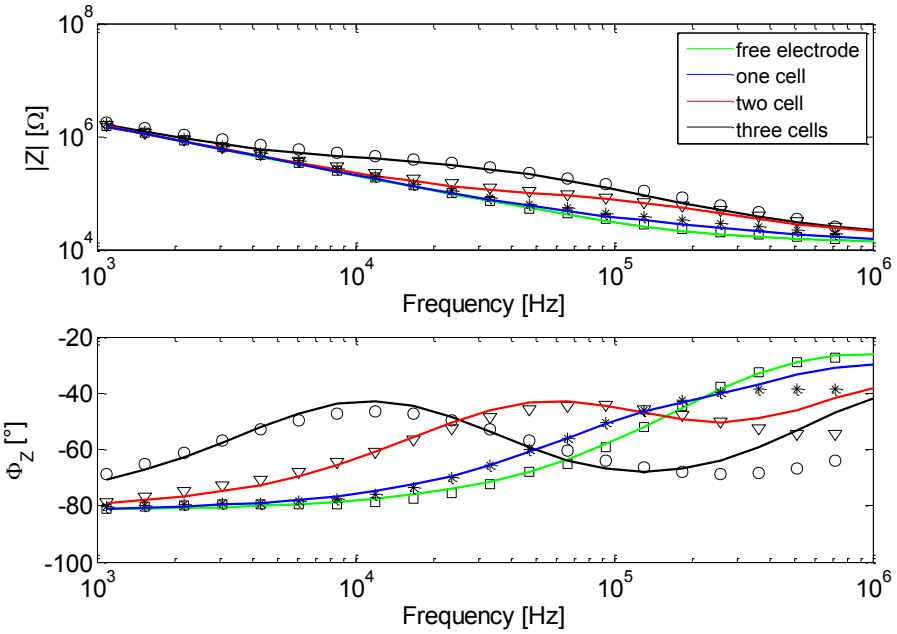

Figure 5.2-8. Experimental EIS data (markers) and fitting curve (solid lines) of both free electrodes and electrodes covered with one (*), two (▽) or three (□) cells. For this fitting process, the cover factor β and the resistance R_{seal} were the only parameters.

# cells	0	1	2	3
β	0	0.0054	0.0194	0.0222
R_{seal} [MΩ]	-	1.72	3.22	13.81

Table 5.2-2. Coverage parameters obtained from the fitting of Figure 5.2-8 EIS data.

Figure 5.2-9 describes the variations of impedance magnitude $\Delta|Z|$ and phase $\Delta\Phi_Z$ of Figure 5.2-8 EIS data, evaluated as usual:

$$\Delta|Z| = 100\frac{|Z_{cell}| - |Z_{free}|}{|Z_{free}|} \quad , \tag{5.2.3}$$

$$\Delta\Phi_Z = \left|\Phi_{Z_{free}}\right| - \left|\Phi_{Z_{cell}}\right| \quad , \tag{5.2.4}$$

where Z_{free} is the cell-free electrode impedance and Z_{cell} is the cell-covered electrode impedance. As can be seen from Figure 5.2-9, EIS measurements showed a significant variation in a frequency range between 10 kHz and 800 kHz. The variation of impedance magnitude increases with the number of cells and consequently with the electrode coverage. The variation is about 41 % for one cell, 163 % for two cells and 313 % for three cells over the electrode surface. At the same time, the frequency of maximum

variation decreases at low frequency, from 180 kHz to about 66 kHz. The phase variation ranges from −40 ° to about +40 °.

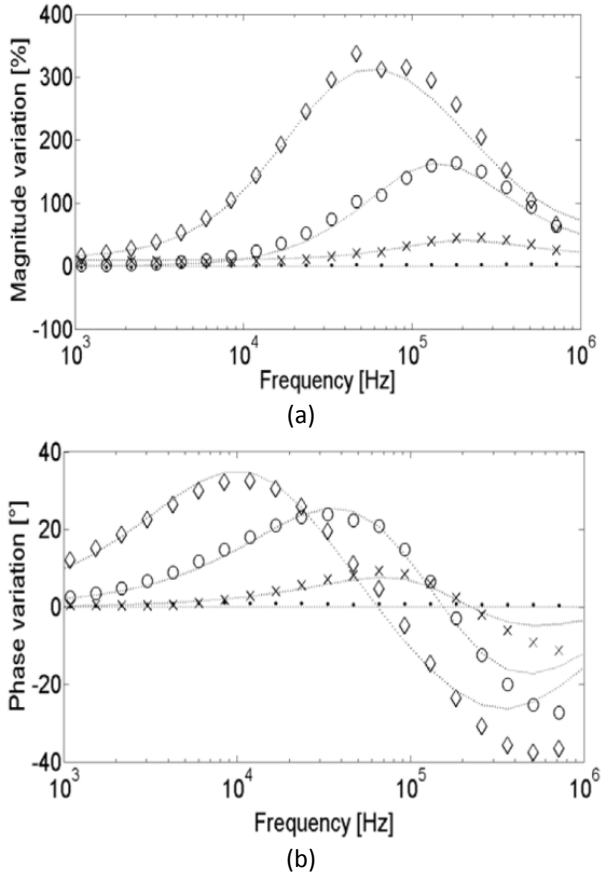

Figure 5.2-9. Variation of EIS impedance magnitude (a) and phase (b) of Figure 5.2-8 for different electrodes coverage: cell-free electrode (·), one cell (x), two cells (o), three cells (◊).

After the characterization of the cell-based system, electroporation experiments have been performed on plated CHO cells [15]. Cells have been stimulated with six pulses of 100 µs of different applied voltages V_{pulse}, between 0.3 V and 2.4 V (see Figure 5.2-4). Membrane resistance changes have been monitored through electrochemical impedance spectroscopy measurements. The stimulation process was mainly composed by three steps: preliminary EIS measurement of target microelectrode (Z_{pre}), voltage stimulation of target electrode, post-stimulation EIS measurement (Z_{post}). Figure 5.2-10 shows an example of cells electroporation through microelectrodes.

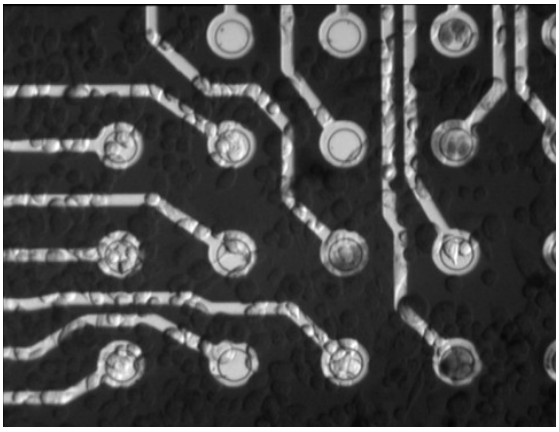

Figure 5.2-10. Example of cells electroporation using microelectrodes. The transfected cells over the selected microelectrodes become opaque, and therefore optically hide the underlying electrodes.

Figure 5.2-11 depicts, for fixed frequency, the impedance magnitude variation as a function of the applied voltage. This variation has been determined by direct pre- and post-stimulation EIS measurement and then evaluating $\Delta|Z| = |Z_{post}| - |Z_{pre}| / |Z_{post}|$, similarly to (5.2.3). As can be seen, a threshold value exists between 0.9 V and 1.2 V. After this, the impedance magnitude considerably decreases as the applied stimulus voltage increases.

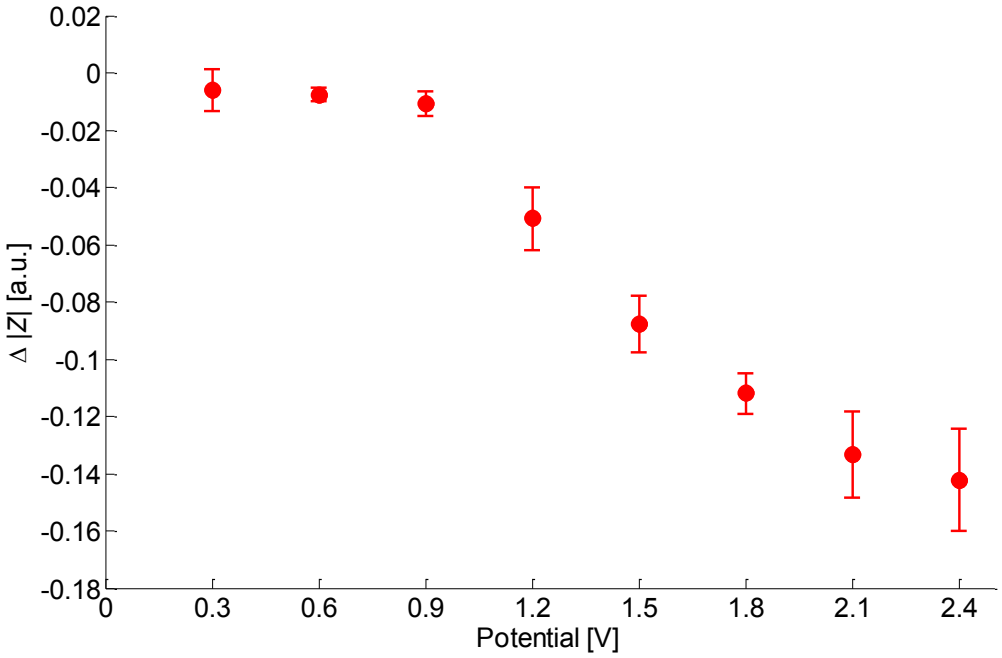

Figure 5.2-11. EIS impedance magnitude variations as a function of stimulus voltage V_{pulse}. The variation has been evaluated comparing pre- and post-r electrical stimulation EIS measurements.

The collected EIS data have been fitted using the model of Figure 5.2-5 (b): the resistance R_{pore} modulates the impedance of the cell membrane, enabling the indirect assessment of membrane permeabilization. R_{pore} was the only fitting parameter, because all other electrical parameters have been fixed to values of Table 5.2-1. The results of this fit are shown in Figure 5.2-12: as expected, R_{pore} exhibits a threshold behavior, presenting a variation of three order of magnitude after the critical applied voltage.

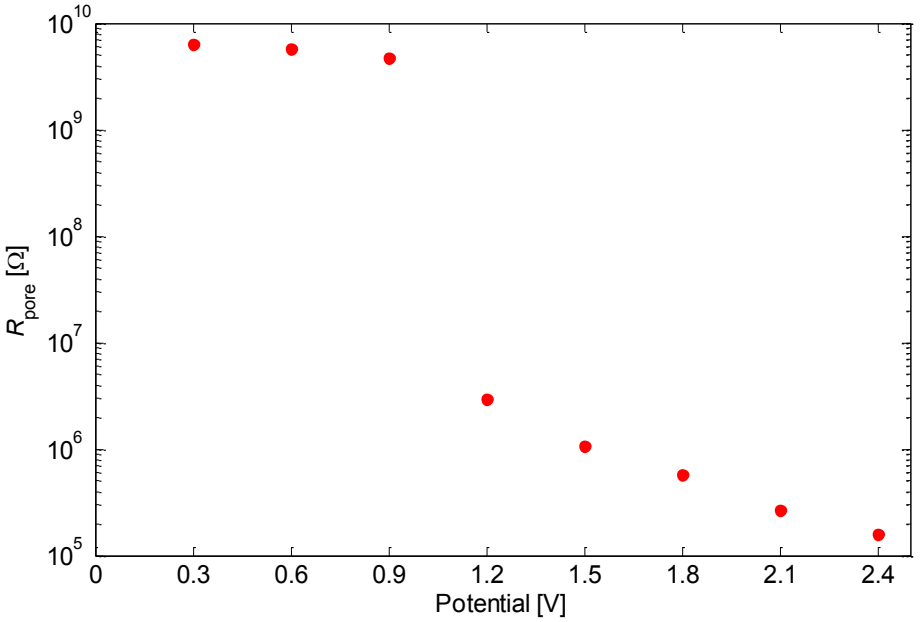

Figure 5.2-12. R_{pore} fitting values as a function of applied stimulus voltage.

5.3 Bibliography

[1] Feldman, Y., Ermolina, I., Hayashi, Y., 2003. IEEE Transaction on Dielectrics and Electrical Insulation 10, 728-753.

[2] Polevaya, Y., Ermolina, I., Schlesinger, M., Ginzburg, B., Feldman, Y., 1999. Biochimica et Biophysica Acta 1419, 257-271.

[3] Weaver, J.C., Chizmadzhev, Y.A., 1996. Bioelectrochemistry and Bioenergetics 41, 135-160.

[4] Morimoto, T., 1990. Eur. Surg. Res. 22, 86-92.

[5] Silver, I.A., 1987. Biol. Sci. 316, 161-167.

[6] Price, D.T., Rahman, A.R.A., Bhansali, S., 2009. Biosensor and Bioelectronics 24, 2071-2076.

[7] Mossop, B.J., Barr, R.C., Henshaw, J.W., Yuan, F., 2007. Annals Biomed. Eng. 35, 1264-1275.

[8] Deng, J., Schoenbach, K.H., Buescher, E.S., Hair, P.S., Fox, P.M., Beebe, S.J., 2003. Biophysical Journal 84, 2709-2714.

[9] DeBruin, K.A., Krassowska, W., 1999. Biophysical Journal 77, 1213-1224.

[10] Gowrishankar, T.R., Weaver, J.C., 2003. PNAS 100 (6), 3203-3208.

[11] Tsong, T., 1991. Biophysical Journal 60 (2), 297–306.

[12] Qin, Y., Zhan, S., Su, J., Zhang, Z., 2008. IEEE Bioinformatics and Biomedical Engineering, 1165-1168.

[13] Kotnik, T., Miklavčič, D., 2000. IEEE Transactions on Biomedical Engineering 47 (8), 1074-1081.

[14] Pasqualotto, E., Ferrario, A., Scaramuzza, M., De Toni, A., Maschietto, M., Vassanelli, S., 2011. Ph.D. Research in Microelectronics and Electronics.

[15] Pasqualotto, E., Ferrario, A., Scaramuzza, M., De Toni, A., Maschietto, M., 2012. Procedia Chemistry 6, 79-88.

[16] Macdonald, J.R., 1987. Wiley & Sons.

[17] Borkholder, D.A., 1998. Stanford University.

[18] Bard, A.J., Faulkner, L.R., 2001. Wiley & Sons.

[19] Franks, W., Schenker, I., Schmutz, P., Hierlemann, A., 2005. IEEE Trans. Biom. Eng. 5, 1295-1302.

[20] Campbell, R.M., Crichton, B.H., Fouracre, R.A., Timoshkin, I.V., Given, M.J., 2006. IEEE Conference Record of 2006 Power Modulator Symposium.

[21] Joye, N., Schmid, A., Leblebici, Y., 2009. Neurocomputing 73, 250-259.

[22] Massobrio, P., Massobrio, G., Martinoia, S., 2007. Neurocomputing 70, 2467-2476.

[23] Spegel, C., Heiskanen, A., Skjolding, L.H.D., Emnéus, J.,2008. Electroanalysis 20 (6), 680-702.

[24] Scaramuzza, M., Ferrario, A., De Toni, A., 2010. PRIME Conference, 1-4.

[25] English, A.E., Squire, J.C., Bodmerand, J.E., Moy, A.B., 2007. IEEE Transactions on Biomedical Engineering 54, 863-873.

[26] Ghosh, P., Keese, C., Giaever, I., 1993. Biophysical Journal 64, 1602-1609.

[27] Foster, K.R., 2000. IEEE Transaction on Plasma Science 28 (1), 15-23.

Chapter 6. Electrical transduction of hand force activity

6.1 Introduction to hand force measurement systems

The measurement systems for force exerted by human hands have the typical shape of a glove connected to an external data processing unit. Carpaneto et al. [1] have focused the system on the transduction of thumb activity by using a matrix of 64 piezoresistive electrodes (Interlink electronics). The thumb distal phalanx is bounded on the transduction matrix by using an external plastic element covered with silicon rubber. The aim of the system is to assess the contact force and its distribution during the grasp process of cylindrical and spherical objects [2]. These tests have been carried out following specific protocols based on functional neuromuscular stimulation. An analogue instrument has been developed by Beebe et al. [3] using a single silicon-based transducer in the thumb area. These sensors are developed by properly dope silicon areas inside microelectronic industrial processes.

Tarchanidis et al. [4] developed a combined measurement system able to detect both the force exerted by the thumb and the bending of each finger, by using five strain gauges. Similarly, Sato et al. [5] have integrated in the same acquisition and analysis system both a glove for force detection and distribution assessment (Sensor Glove MKIII), and a commercial glove for accurate measurement of fingers and wrist position (Cyber Glove, VRLogic). The glove for force detection had 103 sensing points, distributed along a matrix of 13 x 15 positions. Each sensing spot was embedded in the glove fabric using electrically conductive wires and a layer of force-sensitive conductive rubber.

The force sensing systems are often used to generate biofeedback loops where the information related to the force exerted is used as control signal for local or remote actuators.

For example, in haptic interface applications the force sensors are applied to specific aids intended to either manipulate virtual object or to remote drive anthropomorphic robots. Some examples of these applications are robotic interfaces [6] and surgical medicine [7].

Castro et al. [8] applied polymeric force sensors to distal phalanx of thumb, fore and middle fingers, in order to implement a biofeedback system that modulates a neuromuscular electrical stimulus in response to the force applied by the subject during the execution of specific tasks. This kind of biofeedback systems are oriented to the development of neuroprosthesis that the subject could drive directly with its neural electrical pulses [9]. Bouzit et al. [10] implemented a measurement system of hands force based on a similar biofeedback loop. The fingers position is monitored through five small pneumatic pistons connected between the palm and each distal phalanx (Rutger Master III). Inside each piston is placed a infra-red sensor that measures the piston position during finger movement. On the palm, where the five pistons are connected together, Hall-effect based sensors measure the adduction, abduction and bending angles. A software model collects all the different data and generates a reconstruction of hand movements and position.

Turner et al. [11] have developed a glove able to send and receive information from a remote robotic arm. This glove enables the user to drive the robotic arm by moving hand and fingers. The robot is provided with force sensors in each of its mobile parts, whose outputs are sent directly to the pneumatic actuators of the user glove: these actuators allow or inhibit glove fingers movement, communicating in this way both the shape and the hardness of the material investigated by the robot.

6.2 Measurement system overview

The aim of the force measurement system is to implement a tool able to quantitatively assess the effectiveness of a functional rehabilitation protocol by using a biofeedback loop based on patient reactions: the force exerted during functional tasks execution is transduced into electrical signals that are processed and visualized back to the patient, in order to stimulate the perception of its own force (see Figure 6.2-5). In fact, by looking at the real-time visualization window (see Figure 6.2-1) the patient can learn how to functionally modulate the force exerted by its hand, trying to overcome or manage its impairment.

The force transduction system consists of the following main elements:

- Graphical interface.

  The software interface of the system intended to be used both by the patient during task execution and by occupational therapists as a tool to improve the rehabilitation protocol: in fact, the system interface has a main control view through which therapists can control the rehabilitation tasks options, and an analysis view that allows clinicians to compare different exercise results.

  The graphical interface allows to store patient data, e.g., name and anamnesis, and to select a specific task to deliver to the patient. The implemented tasks are those used in the daily rehabilitation protocols that have been codified by Sollerman [12] (see Section 6.3). Moreover, a free acquisition can be selected, i.e., the patient will perform hand movements without the purpose to achieve a specific grip execution, in order to collect data not strictly related to a specific functional task.

  The real time hand activity is showed using histograms, one for each sensor embedded in the glove. Sensors output voltage are also mapped in a color-base scheme allowing an intuitive understanding of the patient activity. This representation, in particular, proved to be very meaningful to patients, enabling them to modulate the exerted force through the functional task execution.

The patient execution and performance are stored in databases, and using this historical data the clinicians could assess the performance of the delivered rehabilitation protocol.

After the task execution, the analysis view (see Figure 6.2-2) allows to immediately compare different treatment sessions performed in different periods with the database of standard grips.

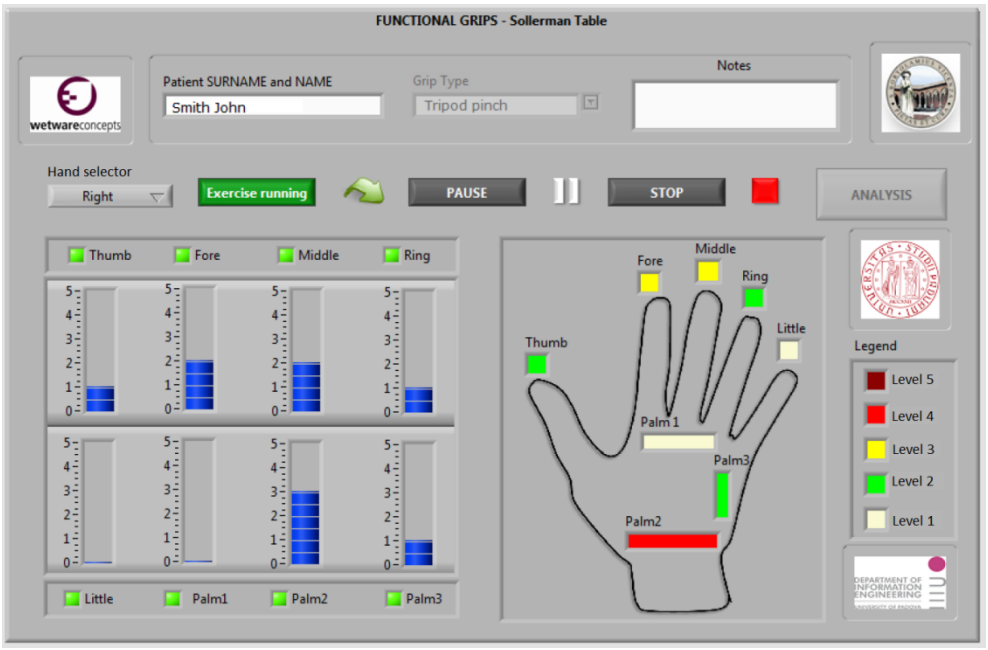

Figure 6.2-1. Real-time visualization view. Histograms graphs on the left provide the-time monitoring of sensors output, while the color map on the right enables an intuitive comprehension of applied force intensity. For sensors displacement insights see Section 6.3.

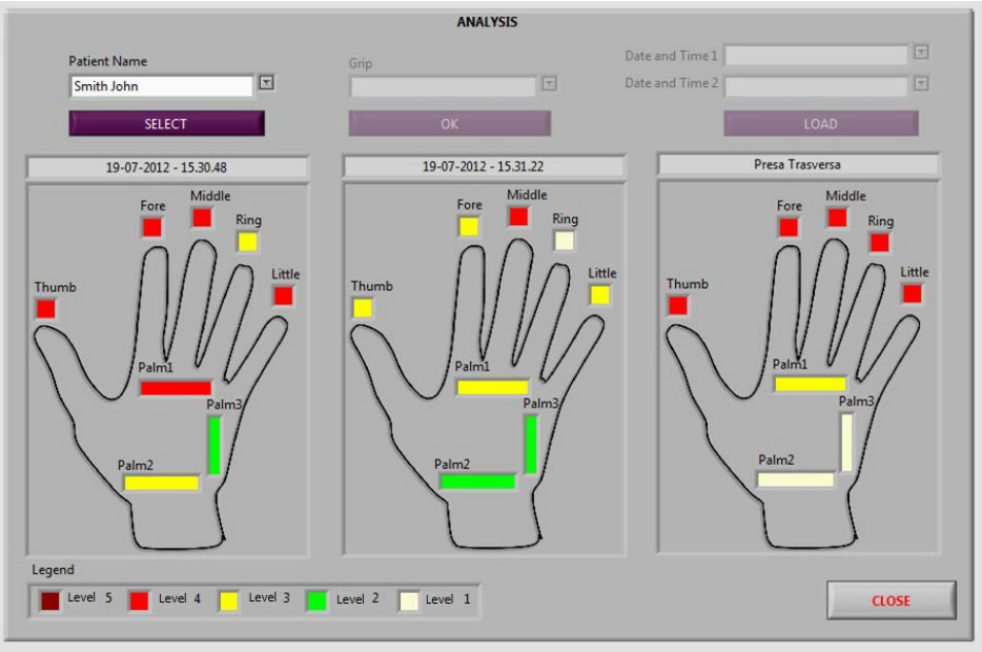

Figure 6.2-2. Analysis view. In this menu different execution of the same task can be compared: leftmost color map depicts the most recent task execution, the central one is an earlier execution loaded from the patient database, and the rightmost color map shows the same task executed by a non-pathological hand.

- Sensorized glove (see Section 6.3).

  The glove is made of 2 mm-thick neoprene and it is shaped to be wearable for different types of pathological hands, i.e., upper extremity hypertonicity or flaccidity. To allow an easy wearing process, some material has been removed from glove fingers and fabric straps have been added in order to wrap the glove around the subject hand rather than try to insert the hand inside the glove.

Figure 6.2-3. The sensorized glove.

The sensors included in the glove structure are piezoresistive transducers that produce electrical signals related to the force applied to their surface [13] (see Section 6.3). The transduction principle is the piezoresistive one: the sensors change their electrical resistance in response to the applied force, i.e., force sensing resistors (FSRs). Once worn the glove, the sensors materials, size and thickness maintain the comfort and the flexibility of a bare neoprene glove, ensuring a sufficient sensibility at fingertips to perform functional tasks.

- Sensors driving circuits and data acquisition.

  The sensors driving circuits have been designed to properly amplify the sensors calibration curve in the working range of applied force. The structure of the driving circuits (see Figure 6.2-4) consists of a de-coupling operational amplifier, that provides a constant supply voltage from computer USB as the FSR varies its resistance, i.e., R_{FSR}, and a voltage amplifier that amplifies the output of a voltage divider between the FSR and a fixed resistor R_1. The equation of the voltage output is

$$V_{OUT} = \frac{R_1}{R_1 + R_{FSR}}\left(1 + \frac{R_B}{R_A}\right)V_{CC} \quad . \tag{6.2.1}$$

  The output of each sensor driving circuit is connected to a commercial data acquisition system (National Instruments NI6008, see Table 6.2-1 for

electrical properties), that interacts with the software through a USB connection.

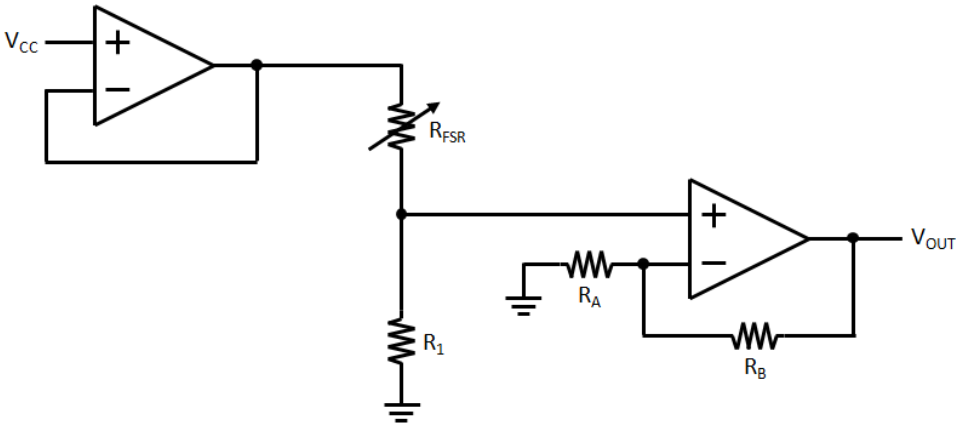

Figure 6.2-4. Force sensors driving circuit. Typical values for the discrete elements are: R_{FSR} = 100 Ω up to 10 MΩ, R_1 = 120 Ω, R_A = 33 kΩ, R_B = 68 kΩ, V_{CC} = 3.5 V.

DC Supply voltage [V]	4.10 to 5.25 (USB)
Supply current [mA]	80 (maximum 500)
Number of acquired force signals	8
Sampling frequency per channel [Hz]	1000
Buffer length per channel [samples]	500
Input resolution [bit]	12
Max sampling rate [kS/s]	10
Timing accuracy [Hz]	± 0.1
Input range [V]	± 10
Channel input resistance [kΩ]	144 (small signals)

Table 6.2-1. Data acquisition system features.

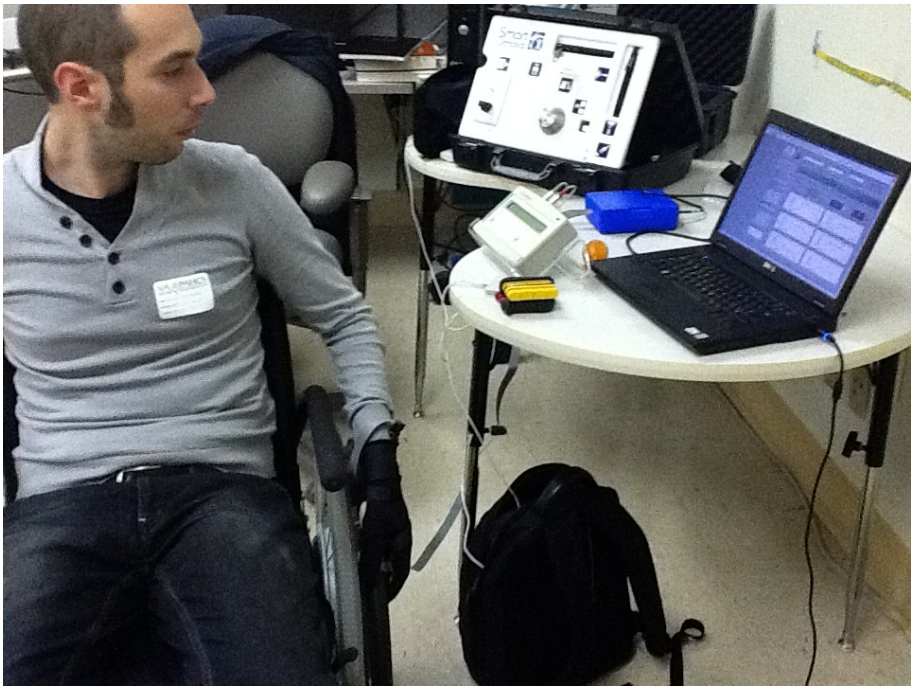

(a)

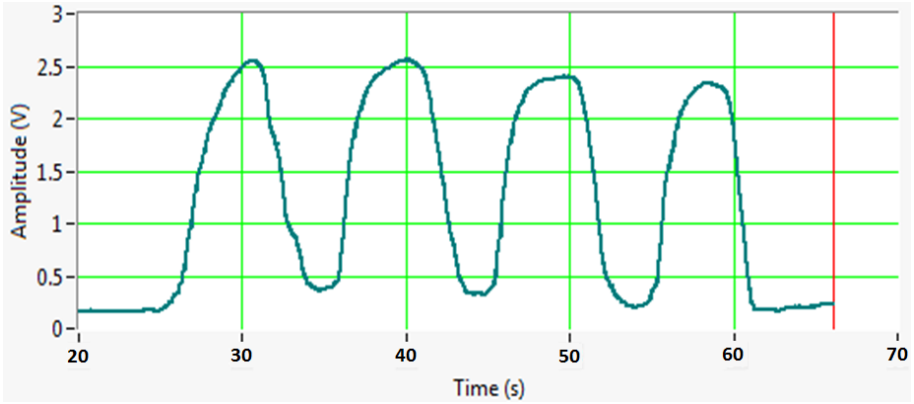

(b)

Figure 6.2-5. Example of glove application for monitoring the force exerted using a wheelchair (a). Sensors output example for this application (b).

6.3 The force-sensing glove

Force sensors detect the contact force between the object on the sensor surface and the surface itself. One of the main transduction principles for applied forces is the piezoresistive effect [13], that is particularly suitable for electronic transduction applications: the force sensing resistors (FSRs) [14] are constituted by a piezoresistive conductive polymer whose electrical resistance varies when it is subjected to deformation, i.e., to an applied force.

The piezoresistive effect describes changes in the electrical resistivity of a semiconductor when mechanical stress is applied, i.e., when it experiences a strain or a deformation. This effect provides an easy and direct transduction mechanism between the mechanical and the electrical domains [15]. The classical resistance value of a resistor with length L and cross-sectional area A is given by

$$R = \rho \frac{L}{A} \quad . \tag{6.3.1}$$

The resistance value is determined by both the bulk resistivity ρ and the geometrical dimensions. Piezoresistors are resistors whose resistivity changes with applied strain, e.g., monolithic sensors based on doped silicon [3]. In the microscopic description of a piezoresistive behavior under normal strain, the resistivity depends on the mobility of charge carriers, while in the macroscopic description of a semiconductor material the change Δ in resistance R is linearly related to the applied strain:

$$\frac{\Delta R}{R} = G \frac{\Delta L}{L} \quad , \tag{6.3.2}$$

where L is the geometrical dimension and ΔL quantifies its variation. The proportional constant G in the above equation is called piezoresistor gauge factor. Terms can be rearranged to get to an explicit expression for G:

$$G = \frac{\Delta R/R}{\Delta L/L} = \frac{\Delta R}{\varepsilon R} \quad , \tag{6.3.3}$$

with $\varepsilon = \Delta L / L$.

The resistance is typically measured along the material longitudinal axis. However, externally applied strain may contain three vector components, one for each directions of the tridimensional space. A piezoresistive element may behave differently in relation to force direction. The change of measured resistance under the longitudinal stress

component is called longitudinal piezoresistivity and similarly the one under transverse strain component is called transverse piezoresistivity [15]. The total resistance variation is the sum of the changes in the longitudinal and transverse stress components [15].

A widely adopted piezoresistive material, e.g., Velostat (3M), can be made of conductive polymers due to the fact that they can offer high electrical conductivity properties which can be tuned by using both the methods of organic synthesis and by advanced dispersion techniques. Thus, piezoresistive polymer is normally supplied by a polymeric sheet on which the piezoresistive film has been applied by screen printing technique. The piezoresistive film consists of both electrically conducting and non-conducting particles suspended in matrix [14]. Applying a force to the surface of the piezoresistive film causes particles to come in contact with the conducting electrodes and change the overall resistance of the film.

For the sensorized glove prototype, commercial FSRs (Interlink electronics) have been used (see Figure 6.3-1). These FSRs are based on robust polymeric film and exhibit a decrease in resistance as the applied force increases. According to manufacturer data sheets, the range of force sensitivity ranges from the actuation force, i.e., 0.1 N, up to 10 N. Figure 6.3-2 depicts the voltage output of Figure 6.2-4 driving circuit once connected to a sensor.

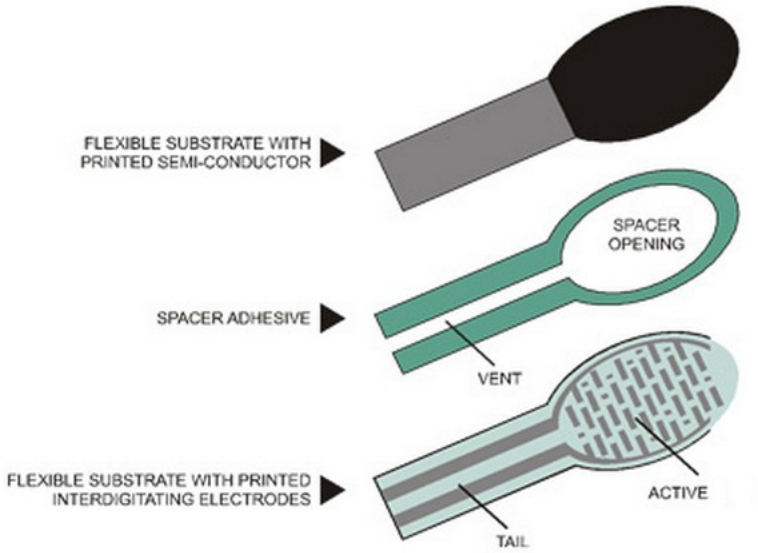

Figure 6.3-1. Schematization of a force-sensing resistor.

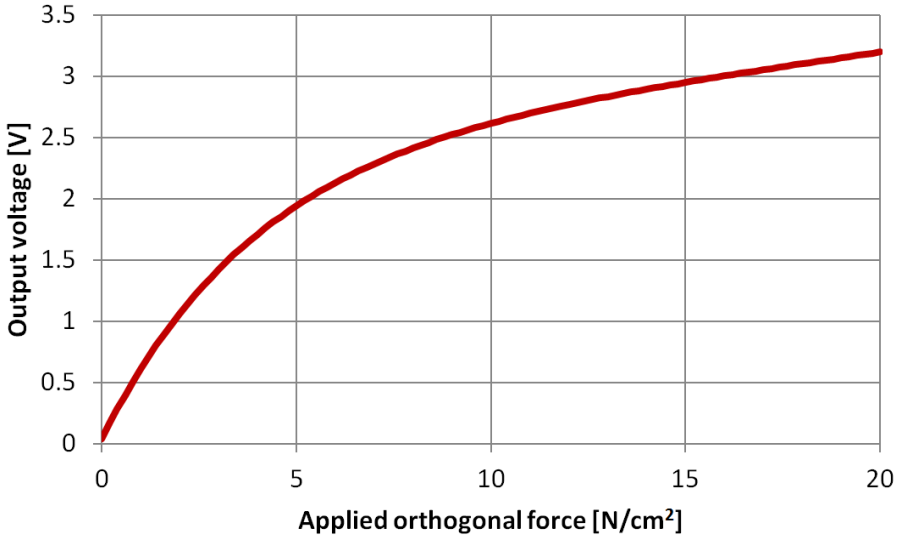

Figure 6.3-2. Typical output response of a force sensor as a function of applied force.

The sensorized glove prototype has been optimized to transduce the force from standard prehension patterns. These patterns have been identified and codified by Sollerman [12] as (see Figure 6.3-3):

1. pulp pinch: the object is held between the thumb and the index;
2. lateral pinch: the object is held between the thumb and the radial side of the index;
3. tripod pinch: the object is surrounded by the thumb, index and middle;
4. five-fingers pinch: the object is held between the thumb and the four fingers together, without contacting the palm;
5. diagonal volar grip: the object is held with the thumb against the four fingers, contacting the palm. Object main axis is parallel to the hand one;
6. transverse volar grip: similar to diagonal grip, but object axis is transverse with respect to hand one;
7. spherical volar grip: the object is surrounded by thumb and four fingers and is in contact with the palm;
8. extension grip: the object is held between the thumb and the four fingers, with the interphalangeal joints extended. The object is not in contact with the palm.

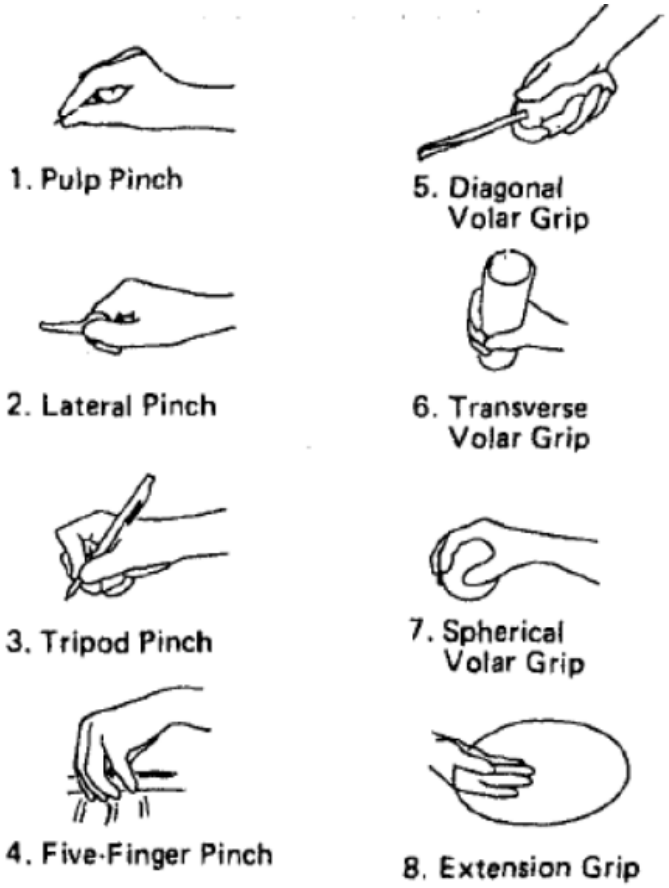

Figure 6.3-3. Standard hand grips [12].

The work of Sollerman has been so relevant that nowadays it represents a fundamental part of the standard for clinical practice related to functional rehabilitation.

In order to monitor in real time the execution of Sollerman tasks, the optimal displacement of force sensors on the glove has been identified using a protocol proposed by Kamakura et al. [16]. Following this protocol some daily objects, e.g., dices, knives, jars, have been colored with paint and have been used to perform functional static grips. As a result, the wet paint stained the hands only on specific contact area. These tests have been performed both with normal and pathological hands (see Figure 6.3-4), and the results are in good agreement with those originally obtained with the protocol [16]. All the various contact areas displacement has been analyzed in order to define the subsets of contact areas shared by the most part of functional static grips, obtaining the displacement depicted in Figure 6.3-5.

Task [12]	Control Non-pathological hand	Subject 1 Good mobility	Subject 2 Poor mobility
Tripod		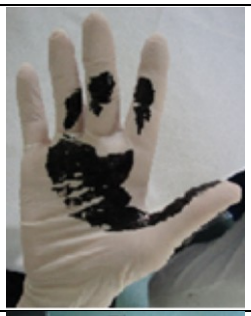	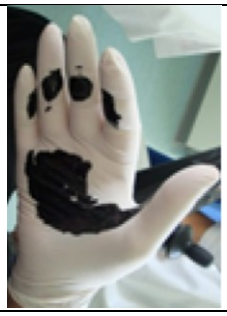
Transverse		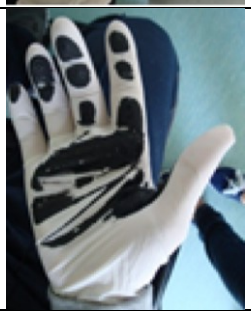	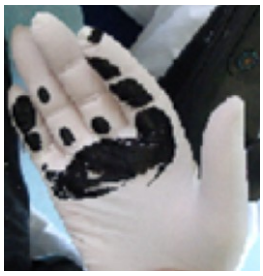

Figure 6.3-4. Example of hand grip tests performed by three subjects: Control has normal hand mobility, Subject 1 suffered of a mild impairment and Subject 2 suffered of an acute impairment.

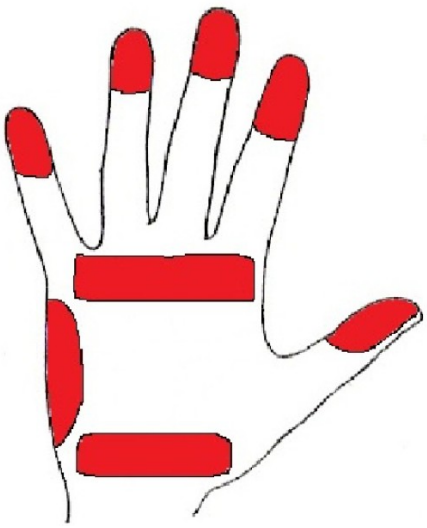

Figure 6.3-5. Schematization of sensors displacement as defined from Figure 6.3-4 tests and glove worn by non-pathological hand.

The commercial FSRs have been integrated in the neoprene glove in correspondence of the functional grips contact areas. Due to neoprene features of elasticity and plasticity, embedded sensors exhibit changes in their transduction curve. In order to

electrically characterize the embedded FSRs, quantitative measurements of forces exerted by a finger wearing the glove were recorded using a peculiar sequence, i.e., the finger wearing the sensorized glove belonged to a normal female subject, who exerted on the sensor a slowly increasing force up to its maximum. Referring to Figure 6.3-6:

- empty glove (from 0 to about 8 s). The stand-off resistance is about 215 kΩ. The resulting trend is almost constant and the value recorded is higher than the working range;
- wearing the glove (from 8 s to about 40 s). During the first 2 s the FSR resistance stabilizes at the contact value, i.e., about 20 kΩ. Between 10 and 40 seconds, the subject has been warned to stand still. The fluctuations in FSR value depends on involuntary finger or body movements, e.g., respiration and heart beat;
- force application (from 42 s to 60 s). The FSR value decreases from the contact value to its minimum of about 540 Ω. The sensor output range for functional applications is more than one order of magnitude when glove is correctly worn;
- release (from 60 to 61 s). During this phase the finger ends the force exertion and relaxes back to rest position;
- rest (from 62 s to 80 s). The subject has been instructed to stand still. The FSR value is higher than the previous contact value. This can be imputed to both hysteresis of the sensor and neoprene substrate plasticity;
- taking out the finger (from 80 s to 84 s). The finger is removed from the glove and the FSR value reaches the sand off one.

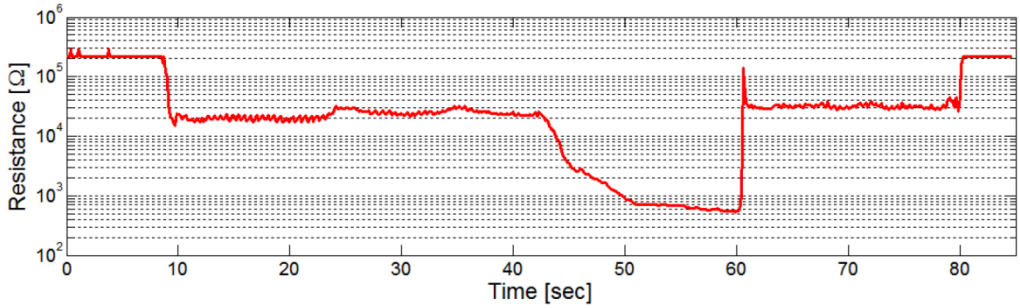

Figure 6.3-6. Example of embedded sensor behavior during a functional test: wearing the glove, exertion of force, pulling out the hand from the glove.

6.4 Monitoring functional tasks with the sensorized glove

In order to correctly wear the glove, fingers have to be accurately inserted and positioned against sensors, then the glove palm side has to be fasten through the wrist fabric strap. An example of force data acquired during this phase is depicted in Figure 6.4-1.

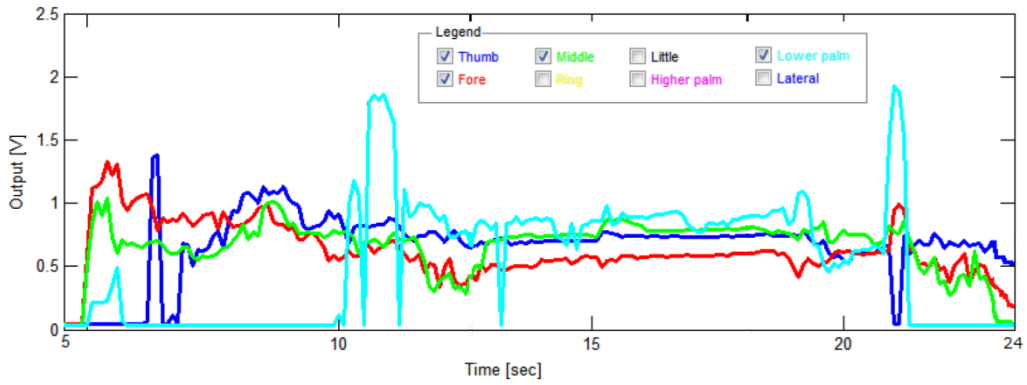

Figure 6.4-1. Glove wearing phases for fingers and palm.

To correctly wear the sensorized glove, the fore and the middle fingers have to be set in place prior to other fingers. Therefore these two sensors show the first force peaks during the wearing phase. After these, the thumb and other fingers are carefully inserted in the glove. The last step is to fasten the fabric strap around the back of the hand, in order to prevent further movements of glove fingers and consequent variations in sensors positioning (see Figures 6.2-3).

During the rest phase, the subject was warned to stand still, and therefore the sensors reaches the respective contact values. These values are affected by involuntary movements of hands or of the whole body, e.g., respiration. Their values are strictly related to piezoresistive sensor physical size, i.e., length and width. During the last period of Figure 6.4-1, the hand has been taken out the sensorized glove, and a palm sensor peak can be observed when the fabric strap is unfasten to let the subject hand out.

Once the glove has been correctly worn, some functional tasks have been performed in order to assess the functionality of the sensorized glove prototype. These preliminary tests have demonstrated that the system can help in distinguishing grips executed in

accordance to Sollerman standards, i.e., a lateral pinch, a transverse grip type 1 and a tripod grip (see Figure 6.3-3). Sensors output for each grip have been divided in two sub-graphs in order to separate the outputs of sensors mainly involved in a correct hand grip, as defined by Sollerman [12], from all the other sensors of the glove.

Figure 6.4-2 depicts the outcome of the lateral pinch execution. The lateral pinch correct execution according to Sollerman static grip standards consists in grabbing the object with thumb fingertip and index lateral proximal/medial phalanges, while a wrong pinch can involve the use of the index lateral distal phalanx. A single task starts with the contact between fingers and object, that becomes a firmly static pinch for about 3 s, then the object is released. Observing the four lateral pinch executions of Figure 6.4-2, a main difference between the first couple of executions can be noticed with respect to the second one: during the pinch process of the first couple, thumb sensor voltage is lower than the fore sensor one, while for the second couple the situation is opposite. These values suggest that only the second couple of executions are compatible with Sollerman standard.

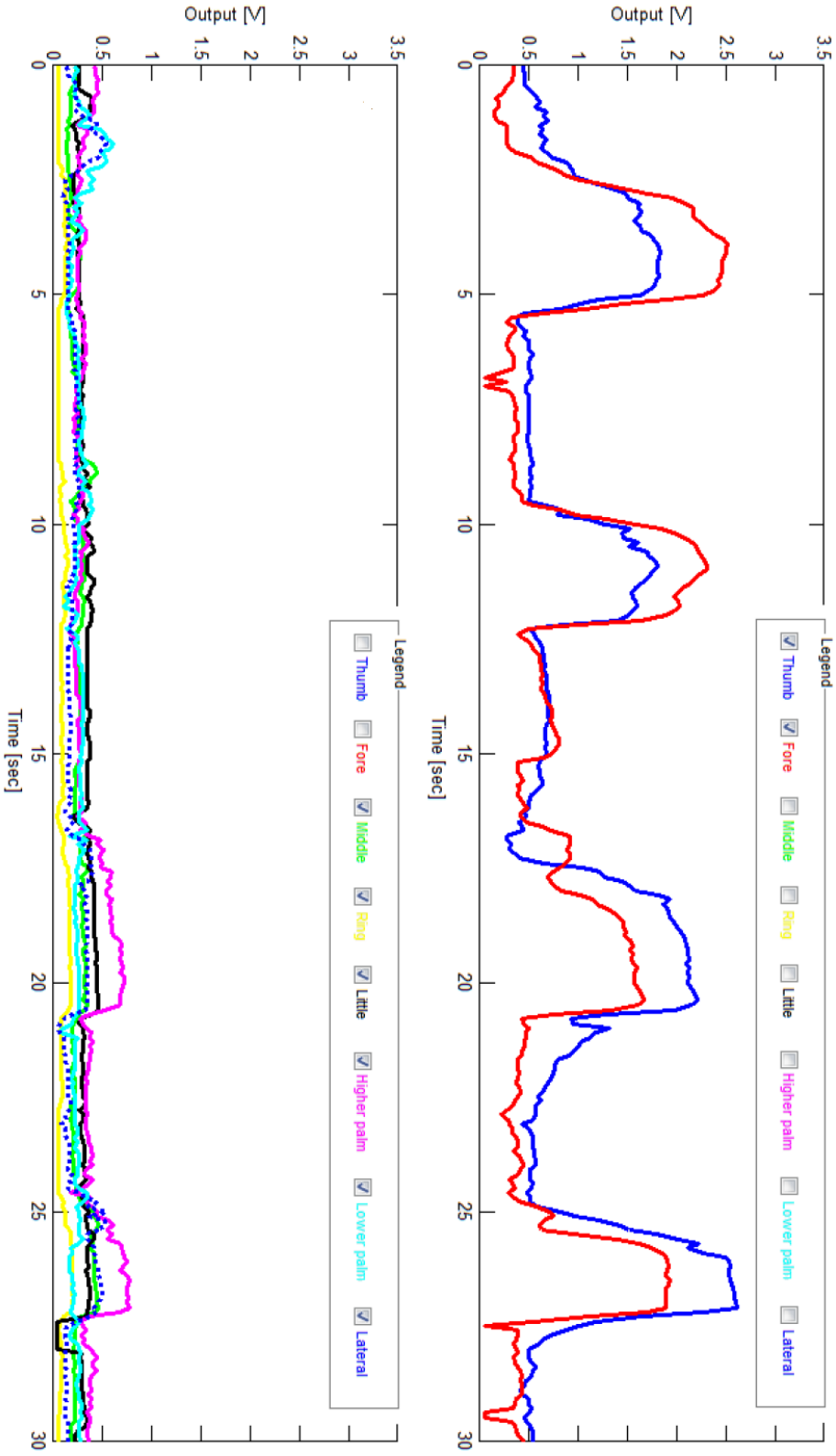

Figure 6.4-2. Series of four lateral pinches.

Figure 6.4-3 describes the sensors output voltage during the execution of a series of four five-fingers pinch (see Figure 6.3-3). The expected output for this grip is the activation of the five fingertip sensors, while palm and lateral sensors should not be relevant. As can be seen, fore, middle and ring fingers exert most part of the force, while thumb and little fingers have a lower output value. The detected fingers behavior is therefore congruent with the correct static grip sequence execution. By observing palm and lateral sensors output it can be seen that the upper palm sensor generates a signal very similar to the fingers one, and this suggests that the upper palm area is actively involved in task execution. In fact, the subject exhibited a compensation movement, i.e., an involuntary strategy to achieve grip purpose that could involve the ipsilesional hand or impaired hand segments (see Figure 6.4-4). This types of movements are not included in Sollerman standard and have to be mitigated by functional rehabilitation. Therefore, the five-fingers grip executions reported in Figure 6.4-3 has been identified as not correct due to the compensation movements.

(a) (b)

Figure 6.4-4. Example of five-fingers pinch: non-pathological (a) and with palm compensation (b).

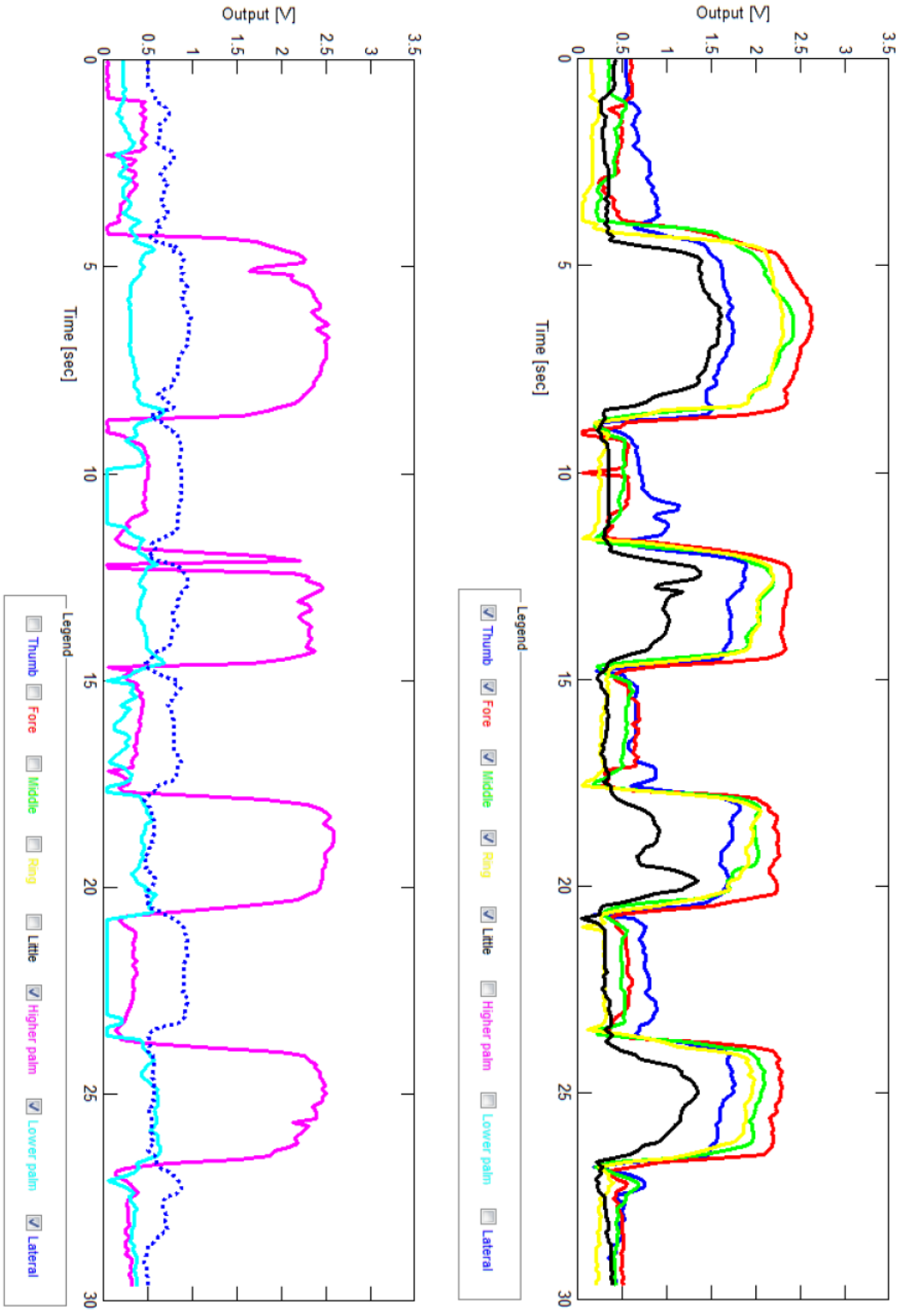

Figure 6.4-3. Series of four five-fingers pinches.

Figure 6.4-5 depicts the sensorized glove response for a tripod dynamic grip. To perform this grip, a jar cap has to be repeatedly screw and unscrew. According to Sollerman standard, only thumb, fore and middle fingers sensors should detect activation, while all the other sensors output voltage should not be relevant. As can be seen, the task has been correctly executed. Moreover, thumb, index and middle fingers sensors show a dynamic trend related to the unscrew-screw process: in fact the first unscrew peaks, at about 10 s, have higher magnitude and last longer than the following two peaks. This is due to the fact that the jar cap was firmly closed. Then, the cap has been released and grabbed in correspondence of each voltage peak. Each time the cap is released, the sensors voltage output reaches the correspondent contact value. Similarly, during the screwing phase, i.e., from about 20 s to 30 s, the voltage peaks increase their magnitude as the cap jar is closed. In the intermediate phase, the subject held the cap using the correct fingers and exerting an adequate force intensity.

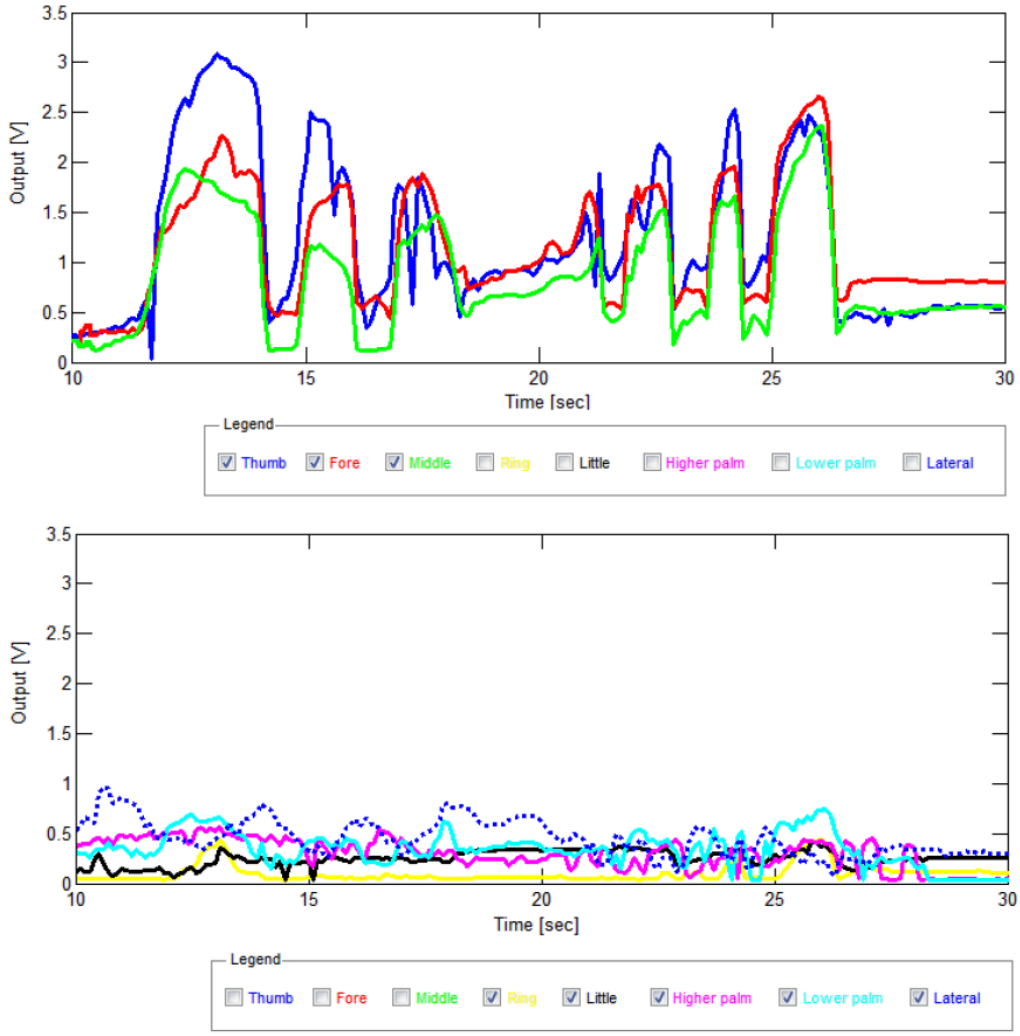

Figure 6.4-5. Tripod dynamic pinch, i.e., unscrewing and re-screwing a jar cap.

6.5 Synchronization between hand force data and electro-encephalic signals

In the neurological and neuro-rehabilitative research and clinical practice, the collection of electro-encephalic data represents a fundamental part of the activities. These data can be gathered using specific electroencephalographic equipments based on sensorized caps, electronic amplifiers and optimization software filters.

The possibility to correlate electroencephalographic (EEG) data with data of other sources, like the measurements of the force generated by hands or arms, would enhance both the capability of conducting research and the clinical methods, adding value to the comprehension of the neuro-physiological phenomena. This integrative approach would allow developing novel and more effective rehabilitation protocols, able to monitor and track over time the patients response to therapy in a quantitative way.

The M.A.K.I. system is a platform that implements the possibility to collect data from force sensors and correlate them with EEG data. This synchronization system allows to collect in parallel different readout coming both from hand and from brain physiological activities. This is made possible by using the event-driven control signals, i.e., triggers, generated by the neurological instrumentation, in combination with system internal processing for incoming signals synchronization. The M.A.K.I. software analyzes and compensates in post processing potential delays and errors of data signaling, generating a matrix of time-correlated data as a function of the time course of the task.

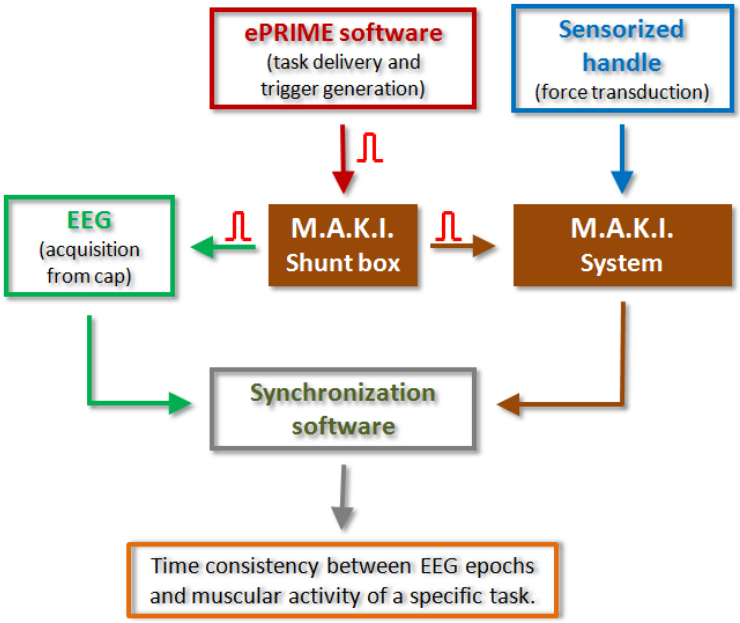

Figure 6.5-1. Workflow diagram of the system for force and EEG data synchronization. The trigger signals generated by the commercial software ePRIME and the internal M.A.K.I. timing routines enable data time correlation.

The main application is to synchronize signals coming from sensorized ergonomically designed handle grips to transduce the force generated by fingers and from 64-channels EEG instrumentation, in order to study the grasping motion correlated with the respective neurophysiologic processes. For this application, a commercially available software (ePRIME, Psychology Software Tool) has been used to deliver tasks to the patient, with computer parallel port generating trigger signals. These signals are generated coherently with significant events, such as visual stimulation or at beginning of a resting phase. These triggering signals are used by EEG instrumentation to track time during cap sensors output acquisition. In this way EEG epochs are related with the stimuli delivered to the patient. Using a specific shunt hardware, the M.A.K.I. system is able to collect ePrime trigger signals and coupling them with force signals collected by the sensorized handles (see Figure 6.5-2).

Figure 6.5-2. Examples of sensorized handles for thumb-index pinches with different sizes.

The preliminary delivered protocol is based on a series of acoustic stimuli generated at random intervals. When the sound is generated, the subject has to exert force on the handle. Electro-encephalic data are collected during the whole experiment and synchronized to force ones during the post processing analysis (see Figure 6.5-3).

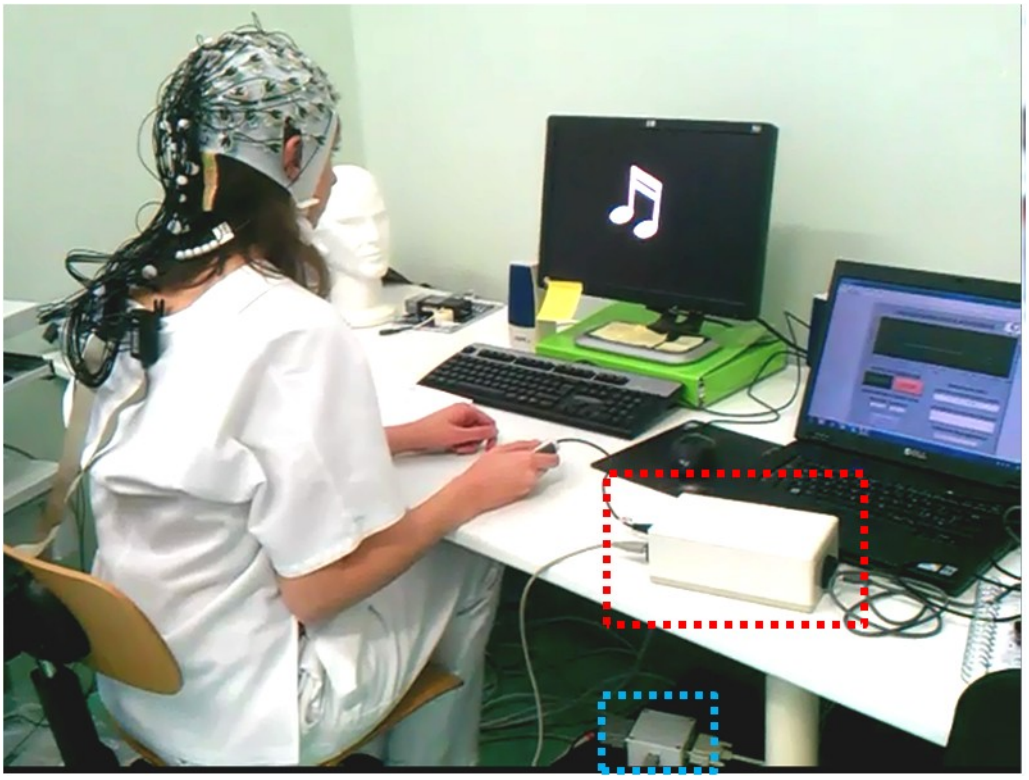

Figure 6.5-3. Example of M.A.K.I. system application. When the note appears on the screen, a sound is generated. The subject in informed to exert force on the handle when it hears the sound. Synchronization system is highlighted in red, while triggers shunt circuitry in blue.

Figure 6.5-4 shows a typical outcome of these experiments: in the graph only four EEG sensors are shown in order to facilitate the comprehension. The typical force

pattern is depicted in Figure 6.5-5: as can be seen, the trigger acquired by EEG instrumentation and the one sampled by the M.A.K.I. system are synchronized.

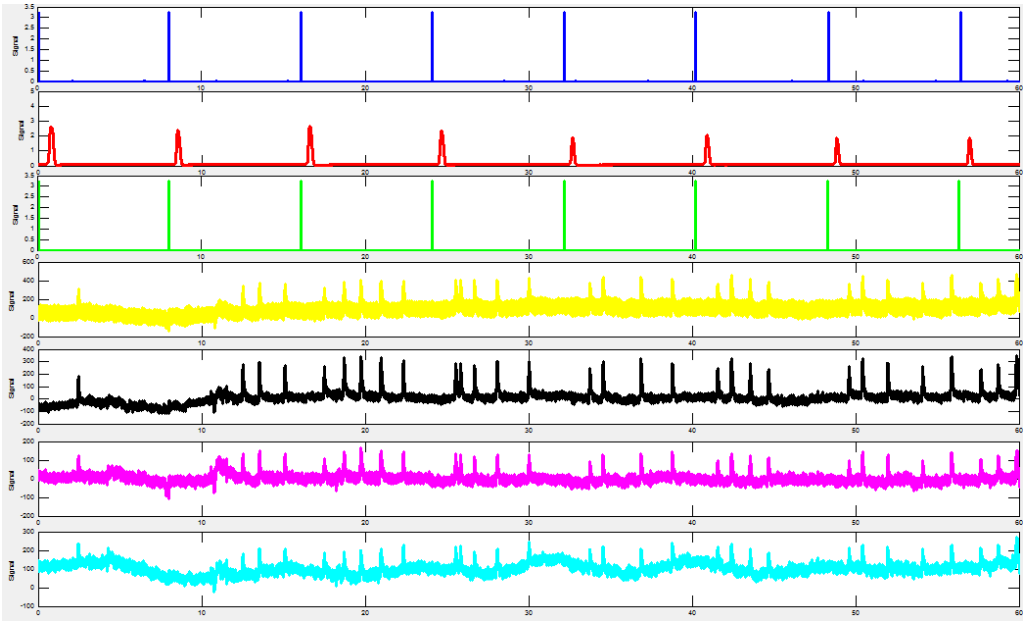

Figure 6.5-4. Post-processing synchronization results. From the topmost signal: trigger acquired by M.A.K.I. system (blue) [V], force signal from handle (red) [N/cm2], trigger generated by EEG instrumentation (green) [V], EEG sensors (yellow, black, magenta, cyan) [mV]. Time window: 60 s.

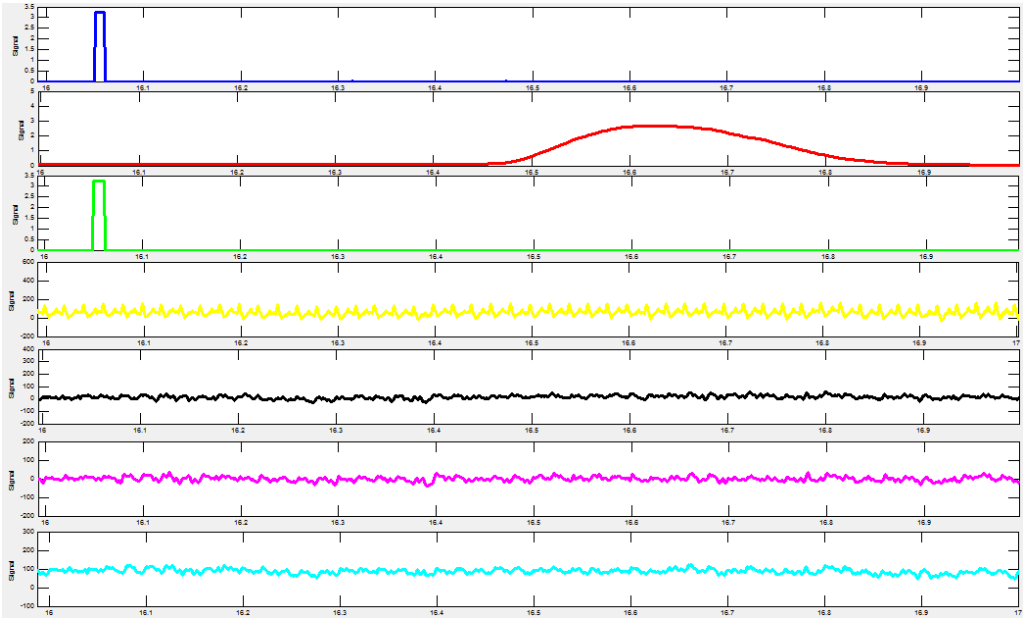

Figure 6.5-5. Zoom of Figure 6.5-4 data. The activation of first and third signal, i.e., blue and green traces, defines the acoustic signal generation. The red signal describes the subject force response to the stimulation. Time window: 1 s.

6.6 Bibliography

[1] Carpaneto, J., Micera, S., Zaccone, F., Vecchi, F., Dario, P., 2003. IEEE Transactions on neural systems and rehabilitation engineering 11 (4), 346-353.

[2] Schreuders, T.A.R., Roebroeck, M.E., Goumans, J., van Nieuwenhuijzen, J.F., Stijnen, T.H., Stam, H.J., 2003. Physical Therapy 83, 806-815.

[3] Beebe, J.D., Denton, D.D., Radwin, R.G., Webster, J.G., IEEE Transactions on Biomedical Engineering 45 (2), 151-159.

[4] Tarchanidis, K.N., Lygouras, J.N., 2003. IEEE Transactions on instrumentation and measurement 52 (3), 984-989.

[5] Sato, S., Shimojo, M., Seki, Y., Takahashi, A., Shimizu, S., 1996. IEEE International workshop on robot and human communication.

[6] Burdea, G.C., 1999. IEEE Transactions on robotics and automation 15 (3), 400-410.

[7] van der Meijden, O.A.J., Schijven, M.P., 2009. Surgical Endoscopy 23, 1180-1190.

[8] Castro, M.C.F., Cliquet Jr., A., 1997. IEEE Transactions on rehabilitation engineering 5 (2), 140-147.

[9] Crago, P.E., Nakai, R.J., Chizeck, H.J., 1991. IEEE Transactions on biomedical engineering 38 (1), 17-27.

[10] Bouzit, M., Burdea, G., Popescu, G., Boian, R., 2002. IEEE/ASME Transactions on mechatronics 7 (2), 256-263.

[11] Turner, M.L., Gomez, D.H., Tremblay, M.R., Cutkosky, M.R., 1998. Proceedings of the ASME IMECE Haptics Symposium.

[12] Sollerman, C., Ejeskär, A., 1956. Scandinavian Journal of Plastic and Reconstuctive Surgery and Hand Surgery 29 (1), 167-176.

[13] Tiwana, M.I., Redmond, S.J., Lovell, N.H., 2012. Sensors and Actuators A 179, 17-31.

[14] Fraden, J., 2004. Springer.

[15] Chang, L., 2006. Pearson Prentice Hall.

[16] Kamakura, N., Matsuo, M., Ishii, H., Fumike, M., Yoriko, M., 1980. The American Journal of Occupational Therapy 34 (7), 437-445.

Conclusions

Equivalent electrical circuits modeling techniques have been used to analyze electrochemical impedance spectroscopy measurements data obtained from biosensors. By using lumped-parameters models to fit the frequency-dependent electrical impedance of sensing devices it has been possible to study processes occurring during biosensors detection activities:

- for the genosensor described in Chapter 3, the equivalent electrical models analysis enabled the assessment of the DNA probes functionalization layers, and the consequent optimization of the functionalization protocol, in order to maximize the detection currents;
- for the enzyme-based biosensor of Chapter 4, it has been possible to study the effectiveness of enzymatic functionalization layers in promoting the redox reactions related to lactic acid. By using proper electrical models, two enzymatic immobilization techniques have been studied and compared, i.e., directly adsorption and cross-linking. Moreover, the equivalent circuits models allowed to identify fit parameters related to the repeatability of the functionalization protocol;
- for the cells-based biosensors presented in Chapter 5, the equivalent electrical modeling approach enabled to monitor the growing process of adherent cells. It also allowed to optimize the electroporation protocol by giving insights about the cell membrane electropermeabilization process.

The pseudo-distributed elements model described in Chapter 2 proved to be suitable for the simulation of microelectrodes/electrolytes systems electrical impedance. The possibility to take into account the effects of devices parasitic elements, e.g., shunt capacitors and wires self-inductance, enables a better estimation of electrochemical cell equivalent parameters. The mesh-based pseudo-distributed elements allowed to retain the geometrical information related to biosensors size and layout, confirming the feasibility of this approach for simulating the electrical response of in-flow electrodes and microfluidic biosensors.

The hand force measurement system described in Chapter 6 has been used to monitor the execution of common functional rehabilitation tasks. The quantitative

assessment of subjects performance has been carried out with the piezoresistive sensors embedded in the sensorized glove fabric. The biofeedback loop constituted by the subject, the sensorized glove and the real time force visualization software contributed to enhance the subject perception of exerted force. Moreover, the acquired force data have been synchronized with electro-encephalic data acquired by a 64 channels electroencephalograph. This result has been achieved with a specifically designed acquisition hardware and with custom post-processing data analysis software routines.